Arborescent Copolymers: Synthesis, Properties & Metallic Nanoparticle Templating

by

Jason Matthew Dockendorff

A thesis
presented to the University of Waterloo
in fulfillment of the
thesis requirement for the degree of
Doctor of Philosophy
in
Chemistry

Waterloo, Ontario, Canada, 2011

AUTHOR'S DECLARATION

I hereby declare that I am the sole author of this thesis. This is a true copy of the thesis, including any required final revisions, as accepted by my examiners.

I understand that my thesis may be made electronically available to the public.

Abstract

Graft copolymers with a dendritic (arborescent) architecture and unimolecular micelle properties have been synthesized and examined for their solution properties as well as their ability to serve as templates for the preparation of metallic nanoparticles. The research focused on two types of arborescent copolymers, namely core-shell (CS) and core-shell-corona (CSC) architectures. Copolymer amphipolarity was provided by a hydrophobic polystyrene (PS) component and a polar poly(2-vinylpyridine), P2VP, phase. The CS copolymers were obtained by grafting P2VP onto linear or branched PS substrates to yield PS-*g*-P2VP unimolecular micelles. These copolymers exhibited solubility with limited aggregation in aqueous environments after protonation with HCl. Coordination of the coronal P2VP phase with $HAuCl_4$ was achieved, and the resulting polymer-stabilized metallic nanoparticles had a spherical morphology.

The tri-layered copolymers were synthesized in similar fashion, by grafting PS-*b*-P2VP block copolymers onto linear or branched PS substrates to afford a CSC morphology with a PS core, a P2VP inner shell, and a PS corona. While the grafting reaction proceeded with lower than expected grafting yields as compared to grafting reactions of homopolymer side-chains, significant P2VP content and molecular weight increases were achieved. It was determined that aggregation of the block copolymer side-chains hindered the coupling reaction of the reactive centers with the substrate. After purification of the PS-*g*-(P2VP-*b*-PS) arborescent copolymers, in part by developing a cloud-point centrifugation purification technique, the spherical copolymers were successfully loaded with various metallic compounds.

The uptake of compounds such as $HAuCl_4$ by the P2VP phase of the copolymers induced intramolecular phase segregation for copolymers of generations (G) 2 and above. Phase segregation produced some unique and intricate morphologies different from the ones observed previously for other unimolecular metal scaffolds. Intramolecular toroidal, nodular, and cylindrical morphologies were observed for the G2, G3, and G4 arborescent copolymers, respectively. Templates of generations 0 and 1 displayed a spherical morphology similar to their PS-*b*-P2VP intermolecular micelle analogues when loaded with metals. Phase segregation is believed to be mediated mainly by the characteristics of the PS core, the length of the P2VP segments having less influence on the morphologies obtained. Reduction of the metallic salts was performed using various agents and protocols. Stronger reducing agents yielded smaller and more narrowly distributed gold nanoparticles, while other reduction methods also removing the polymer scaffold resulted in larger nanoparticles.

Acknowledgements

Firstly, I gratefully acknowledge the support, guidance, knowledge, expertise, wisdom, and patience of Prof. Mario Gauthier during the course of this work; he was vital to the success of this research and the development and advancement of my skills. I would also like to thank my collaborators at the Deutsches Wollforschungsinstitut (DWI) of the Rheinisch-Westfälische Technische Hochschule (RWTH), University of Aachen, Germany, for their assistance, support, and interest in the research. I would particularly like to acknowledge Dr. Ahmed Mourran of the DWI; his expertise had a significant impact on the work and his enthusiasm was a great motivator. In addition, I would like to thank the following individuals for their positive influence and technical advice pertaining to my research:

Mr. Toufic Aridi
Prof. Jean Duhamel
Dr. Mark Ingratta
Prof. Guojun Liu
Prof. Martin Möller
Prof. Linda Nazar
Dr. Gabriel Njikang
Dr. Howard Siu
Dr. Steven Teertstra
Mr. Greg Whitton
Dr. Chris Dockendorff
Prof. Eric Fillion
Dr. Christine Keyes
Dr. Firmin Moingeon
Dr. Abdul Munam
Mr. Olivier Nguon
Prof. Leonardo Simon
Prof. Shirley Tang
Mr. Dale Weber
Dr. Zhongshun Yuan

Finally I wish to thank the following groups and agencies for financial support: The Natural Sciences and Engineering Research Council (NSERC), the Ontario Centres of Excellence (OCE), the University of Waterloo, The Institute for Polymer Research, the DWI, the Garg Foundation, and the German Academic Exchange Service (DAAD).

Dedication

I dedicate this work to my loving parents and wife for their unwavering support, encouragement, guidance, and positive influence.

"Everything is theoretically impossible, until it is done. One could write a history of science in reverse by assembling the solemn pronouncements of highest authority about what could not be done and could never happen."

Robert Heinlein

Table of Contents

List of Figures

List of Tables

List of Schemes

List of Appendices

List of Abbreviations and Symbols

2VP	2-Vinylpyridine
AA	Acrylic acid
A_D	Dendrimer surface area
AEPZ	*N*-Aminoethylpiperazine
AFM	Atomic force microscopy
AIBN	Azobisisobutyronitrile
ATRP	Atom transfer radical polymerization
A_z	Surface area occupied per end-group
b	Block
BA	*tert*-Butyl acrylate
BC	Branch cells
BICs	Block ionomer complexes
BR	Branching ratio
CH	Cyclohexane
C_e	Coupling efficiency
CMC	Critical micelle concentration
CMM	Couple-monomer methodology
CS	Core-shell
CSC	Core-shell-corona
D	Diffusion coefficient
D(t)	Autocorrelation function
DAB	Diaminobutane
DHBA	Dihydroxybenzyl alcohol
DIB	1,3-Diisopropenylbenzene
DMA	*N*,*N*-Dimethylacetamide
DMF	*N*,*N*-Dimethylformamide
DMM	Double-monomer methodology
dn/dc	Refractive index increment
DP	Degree of polymerization

DPE	1,1-Diphenylethylene
DRI	Differential refractive index
DVB	Divinylbenzene
EDA	Ethylenediamine
EGDMA	Ethylene glycol dimethacrylate
EO	Ethylene oxide
Equiv	Equivalents
F	Functionalization level
f	Number of coupling sites or monomer functionality
f_w	Branching functionality
G	Generation
g	Graft
$\|g_1(\tau)\|$	First-order correlation function
$\|G_2(\tau)\|$	Second-order correlation function
G_y	Grafting yield (%)
h	Hour(s)
HPLC	High performance liquid chromatography
HV	High-vacuum
HYPAM	Hyperbranched polyamidoamine
I_o	Intensity of incident light
IPECs	Interpolyelectrolyte complexes
I_θ	Intensity of scattered light at angle θ
k	Arbitrary plotting constant (light scattering)
K	Optical constant (light scattering)
k_B	Boltzmann's constant
LLDPE	Linear low density polyethylene
MAA	Methacrylic acid
MALLS	Multi-angle laser light scattering
MBA	*N,N*'-Methylene *bis*-acrylamide
M_{br}	Branch molecular weight

M_c	Molar mass of core
Meq	Milliequivalents
M_{fm}	Molecular weight of functionalized monomer
M_n	Number-average molecular weight
M_{RU}	Molar mass of repeat units
MW	Molecular weight
M_w	Weight-average molecular weight
MWD	Molecular weight distribution
M_Z	Molar mass of terminal groups
n	Refractive index
N_A	Avogadro's number
N_b	Branching multiplicity
n-BuLi	*normal*-Butyllithium
N_o	Number of monomer units
n_o	Refractive index of solution
p	Extent of reaction or conversion
P(θ)	Particle scattering function or factor
P2VP	Poly(2-vinylpyridine)
P2VPLi	Living poly(2-vinylpyridinyl) lithium
P4VP	Poly(4-vinylpyridine)
PAA	Poly(acrylic acid)
PAMAM	Polyamidoamine
PB	Polybutadiene
PCL	Poly(ε-caprolactone)
PDI	Polydispersity index
PEG	Poly(ethylene glycol)
PEO	Poly(ethylene oxide)
PIP	Polyisoprene
PMMA	Poly(methacrylic acid)
PMDETA	*N,N,N',N'',N''*-Pentamethyldiethylenetriamine

PMS	Poly(α-methylstyrene)
P*n*BA	Poly(*n*-butyl acrylate)
PPV	Poly(*p*-phenylenevinylene)
PS	Polystyrene
PSLi	Living polystyryllithium
P*t*BMA	Poly(*tert*-butyl methacrylate)
PTFE	Polytetrafluoroethylene
PTP	Proton-transfer polymerization
q	Quaternization or scattering vector (light scattering)
r_b	Bulk polymer radius
r_g	Radius of gyration
r_h	Hydrodynamic radius
r_{h1}	Hydrodynamic radius from first-order analysis of the correlation function
r_{h2}	Hydrodynamic radius from second-order analysis of the correlation function
ROMBP	Ring-opening multi-branching polymerization
ROP	Ring-opening polymerization
RU	Repeating unit
R_θ	Rayleigh ratio
SCROP	Self-condensing ring-opening polymerization
SCVP	Self-condensing vinyl polymerization
SEC	Size exclusion chromatography
sec-BuLi	*sec*-Butyllithium
SEM	Scanning electron microscopy
SLS	Static light scattering
SMM	Single-monomer methodology
$[\langle s \rangle_z^2]^{1/2}$	Root mean squared radius of gyration
T	Temperature
TEM	Transmission electron microscopy
tert-BuLi	*tert*-Butyllithium
TFA	Trifluoroacetic acid

THF	Tetrahydrofuran
TMEDA	*N*,*N*,*N'*,*N'*-Tetramethylethylenediamine
TPE	Thermoplastic elastomer
TRIS	Tris-(2-hydroxymethyl)methyl
UV	Ultraviolet
VS	Vinyl sulfonyl
X_n	Number-average degree of polymerization
X_w	Weight-average degree of polymerization
Z	Number of surface groups
α	Branching coefficient
α_{Fr}	Degree of branching
β	Optical factor (light scattering)
Γ	Correlation function decay constant
η_o	Viscosity
θ	Angle of observation
λ	Wavelength
μ_k	Decay moment
ρ	Density
χ	Flory-Huggins interaction parameter

Chapter 1

Foreword

1.1 Opening Remarks

A unique class of branched macromolecules such as the dendritic polymers offers an intriguing topic of investigation. This is not only because these are the most recently discovered macromolecules family, but most importantly due to the vast array of architectures that can be created, and the many applications in which these polymers can potentially offer benefits or provide new functions.

With reference to the work described in this Thesis, well-defined polymers with arborescent 'tree-like' architectures were synthesized by anionic polymerization and grafting.[1,2] The synthetic methods used allow the targeting of specific molecular weights and afford polymers with narrow molecular weight distributions, traits which are paramount to establishing structure-property relationships. Further, in contrast to the other dendritic polymer families, high molecular weight polymers can be obtained in relatively few steps, which is beneficial to the areas of investigation described herein. The methods employed allow the formation of copolymers, and with careful tailoring of the polymer characteristics, unique phase or unimolecular micellar properties can be observed.

This Thesis presents interesting and novel properties of relevance not only to arborescent polymers, but also to copolymers in general.

1.2 Research Objectives and Thesis Outline

The research presented in this Thesis focuses on arborescent copolymers with amphipolar properties. The comprehensive investigation of the novel copolymers presented herein spans from synthesis and fundamental characterization, to more specific application-based research focusing on the unimolecular micelle properties of these copolymers and their use as templates for the construction of metallic nanoparticles.

Background information on dendritic polymers (Chapter 2) and polymeric templating of nanoparticles (Chapter 3) is first presented to provide a strong foundation for the subsequent research-based chapters. Chapter 4 reports on the solution properties of unimolecular micelles created from polystyrene-*g*-poly(2-vinylpyridine) arborescent copolymers, for which partial results have been published in Reference 1. Building on the dissolution protocols developed for the arborescent polyelectrolytes, these species were examined for their ability to coordinate various metals in aqueous environments, as also described in Chapter 4. The synthesis and the characterization of a novel family of arborescent copolymers with a core-shell-corona (CSC) architecture are then presented in Chapter 5. The CSC architecture was obtained by grafting block copolymers of polystyrene (PS) and poly(2-vinylpyridine) (P2VP) onto linear or branched PS substrates, to afford the PS-*g*-(P2VP-*b*-PS) arborescent species. The inherent unimolecular reverse micelle properties of these arborescent CSC copolymers led to an investigation of their use as templates, or scaffolds, for metallic nanoparticle construction in non-polar environments, as presented in Chapter 6. In analogy to established templating methods using multi-molecular micelles of PS-*b*-P2VP,[3] the arborescent copolymers were loaded (coordinated) with various metals, but in our case intriguing morphology transitions were observed due to intramolecular phase

separation yielding intricate nanomorphologies. Preliminary results from these studies have been published in Reference 2. The Thesis concludes with Chapter 7, providing an overall summary of the completed body of work, original contributions to knowledge, and suggestions for future work.

Each chapter of this Thesis, including also the introductory chapters (Chapters 2 and 3, that could be published as review papers), is organized in manuscript format. Included within each chapter is an introductory section providing background pertinent to the specific topic considered, experimental methods, results, discussion, and conclusions. In accordance with the University of Waterloo Thesis Regulations, this Thesis includes a main abstract in the preliminary pages, but each research chapter (Chapters 4 – 6) also includes an analogous Overview section. Further abiding by the Thesis Regulations, one list of references is provided at the end of the document, but it is organized and numbered according to each individual chapter.

Chapter 2

Introduction: Dendritic Polymers

2.1 Introduction

Dendritic species represent the most recently discovered class of branched macromolecular architecture. Major developments in linear, cross-linked, and branched architectures date back roughly to the 1930s, 1940s, and 1960s, respectively. The first synthetic dendritic species were reported in 1978;[1] however, much of the work in this area only began to build momentum in the mid-1980s. A chronology of the key developments in dendritic polymers is provided in Table 2.1.

Table 2.1 Dendritic molecule discoveries in the literature.[2]

Year	Authors
Cascade growth and dendrimers	
1978	Vögtle[1]
1982	Maciejewski[3]
1983	de Gennes[4]
1985	Tomalia,[5] Newkome[6]
1990	Fréchet/Hawker,[7] Miller/Neenan[8]
Random hyperbranched polymers	
1988	Odian/Tomalia[9]
1990	Kim/Webster[10]
1991	Fréchet/Hawker[11]
Dendrigraft polymers	
1991	Gauthier/Möller,[12] Tomalia/Hedstrand/Ferritto[13]

Dendritic patterns can be found all around us in nature and within us. The drainage pattern of rivers and their tributaries, plant roots and foliage, and neurons within our body are but a few examples of unique branched systems ranging in size from kilometers down to

micrometers. Molecular dendritic species recreate fractal-like patterns on the nanometric scale. Dendritic macromolecules can be divided into three subclasses on the basis of their structural characteristics: dendrimers, hyperbranched polymers, and dendrigraft polymers (including arborescent polymers). Dendrimers should ideally have a perfect branched structure, hyperbranched polymers rely upon statistical branching giving a highly imperfect structure, while the architecture of dendrigraft polymers is best described as semi-controlled. A second subclass of controlled structures is the dendrons, which are dendritic fragments formed by a monofunctional initiator or core.

A graphical comparison of the structure of dendrons, dendrimers, hyperbranched polymers, and dendrigraft polymers is provided in Figure 2.1. The stepwise synthesis of dendrimers involves multiple cycles of protection, condensation, and deprotection reactions to produce strictly controlled branched structures and extremely narrow molecular weight distributions (MWD): The polydispersity indices (PDI = M_w/M_n) attained for such molecules can be less than 1.01. The preparation of dendrigraft polymers also relies on stepwise, generation-based synthetic procedures but uses polymeric building blocks rather than small molecules and branching points randomly distributed on the coupling substrate. Under appropriate reaction conditions, usually involving ionic polymerization and grafting, low polydispersities can also be achieved for these systems (PDI ≈ 1.05 – 1.10). The completely random branching process used in the synthesis of hyperbranched polymers, typically resulting from the condensation of non-protected polyfunctional monomers, provides the least defined structures, a PDI > 2 being obtained in most cases.

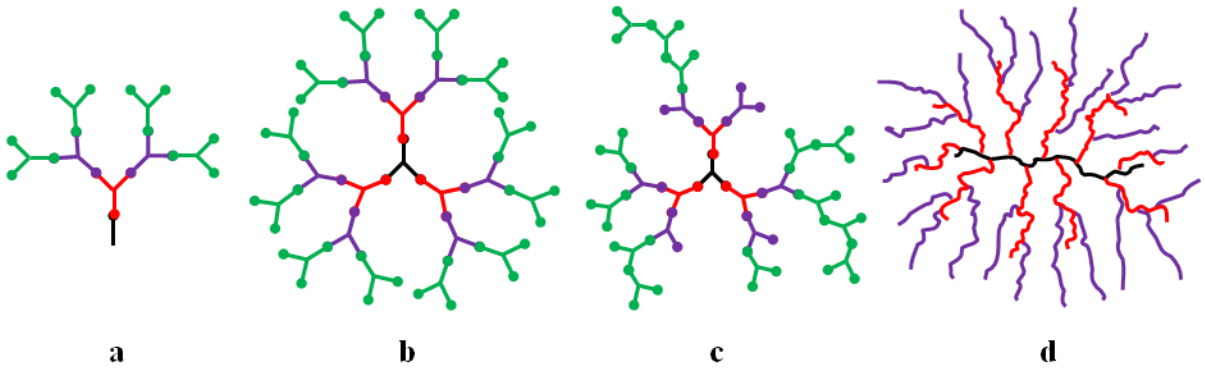

Figure 2.1 Structure of four types of dendritic polymers: (a) Dendron, (b) dendrimer, (c) hyperbranched polymer, and (d) dendrigraft polymer.

Each color in Figure 2.1 represents the branching levels derived from building blocks introduced in successive generations, these being small molecules for dendrons, dendrimers, and hyperbranched polymers (Figure 2.1a – c), and polymeric segments for the dendrigraft polymers (Figure 2.1d). Dendrons are closely related to the dendrimers of Figure 2.1b, the main distinction being the number of functional groups available on the substrate serving as core in the first reaction step. It should also be noted that hyperbranched polymers can be obtained from polymeric segments (e.g. macromonomers) as well as small molecules.

Dendritic macromolecules constructed from small-molecule monomers incorporate three major components: a core, repeating branch cell units, and a corona or outer shell. The branch cells (BC), also known as repeating units (RU), are defined in terms of a branching angle, rotation angles, repeating unit lengths, and terminal groups. The covalent assembly of these branch cells can take place in a symmetrical manner, as in dendrimers, or into random irregular patterns for hyperbranched polymers. The size, shape, and functionality of the

dendritic species depend on the synthetic strategy employed and can be different for each generation and/or each subclass of dendritic species.

The unique architecture of dendritic polymers affords distinct physical properties to these molecules as compared to their linear polymer analogues. For example, as shown in Figure 2.2, branched molecules have a much lower intrinsic viscosity than their linear analogues. Their compact and dense molecular configuration also leads to enhanced solubility at high molecular weights.

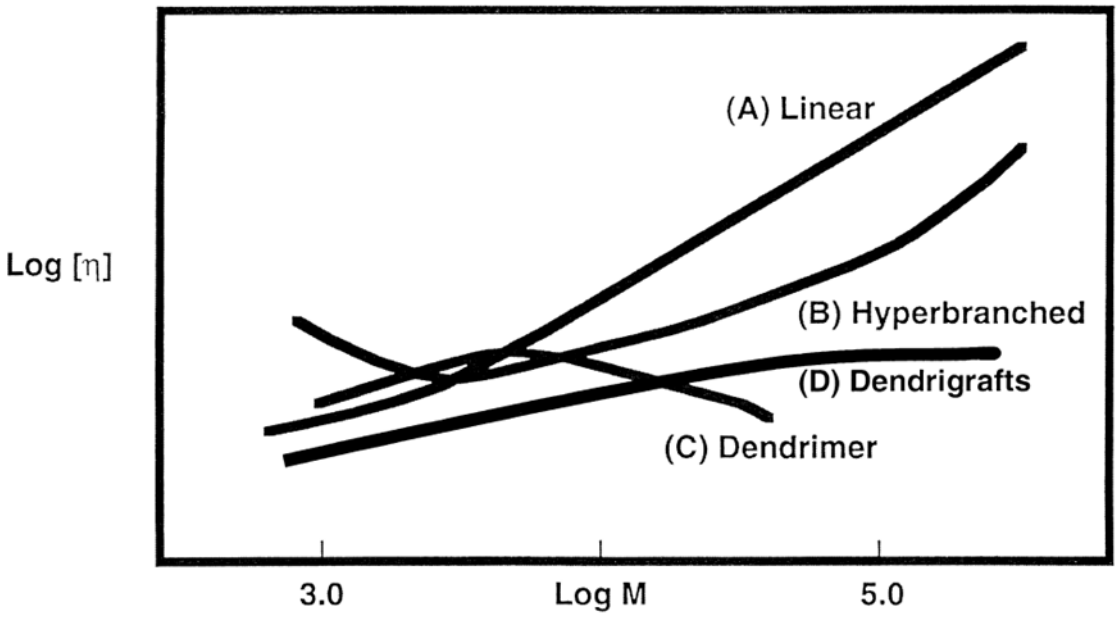

Figure 2.2 Molecular weight dependence of intrinsic viscosity [η] for polymers with (A) linear, (B) hyperbranched, (C) dendrimer, and (D) dendrigraft architectures.[14]

Some of the procedures used to synthesize dendritic molecules can be quite involved, and many different methods have been reported. The following three sections of this Chapter will provide an overview of some of the pioneering work yielding each of the three main

subclasses of dendritic polymers, namely dendrimers, hyperbranched polymers, and dendrigraft polymers. The general characteristics and properties of these materials will also be considered, as well as some of the more recent work including potential applications for these extremely versatile materials.

2.2 Dendrimers

The word dendrimer is derived from the Greek words for tree- or branch-like (dendron) and part (meros). The strictly controlled structure of ideal dendrimers results from the layered assembly of branch cells surrounding the core, which is attained through sequential reaction cycles. This can be achieved in two different ways, namely by divergent (core-first) or convergent (arm-first/core-last) methods.

2.2.1 Synthetic Strategies and Properties

The divergent approach begins with a multifunctional core onto which polyfunctional monomers of the AB_n-type are added. Dendrimers result when the branching multiplicity (subscript n) of the monomer unit is at least 2. Following the addition of these small molecule building blocks, the subsequent layer can be added after deprotection of the end-groups and another monomer condensation reaction. The structure resulting after the first addition cycle is known as a generation 1 (G1) dendrimer. Further reaction cycles are employed to prepare dendrimers of the desired generation, size, or molecular weight.

The convergent approach uses monomers similar to the divergent strategy and provides branched molecules with the same characteristics and predictability; however, wedge-like dendrons are first synthesized and subsequently anchored on a core to complete the dendritic structure. The number of dendrons that can be coupled with a core is governed by the core functionality. Convergent growth of the dendron occurs through selective protection of one of the functional groups followed by a condensation reaction, resulting in directional growth. The dendron unit is interesting in itself, and it has been investigated as its

own entity, but deprotection and coupling with a multifunctional “anchor” core is required to complete the dendrimer structure.

A comparison of the divergent and convergent strategies for the synthesis of a generation 2 (G2) dendrimer is provided in Scheme 2.1, where functionality A selectively reacts with functionality B, and P represents a protecting group for the associated functional group.

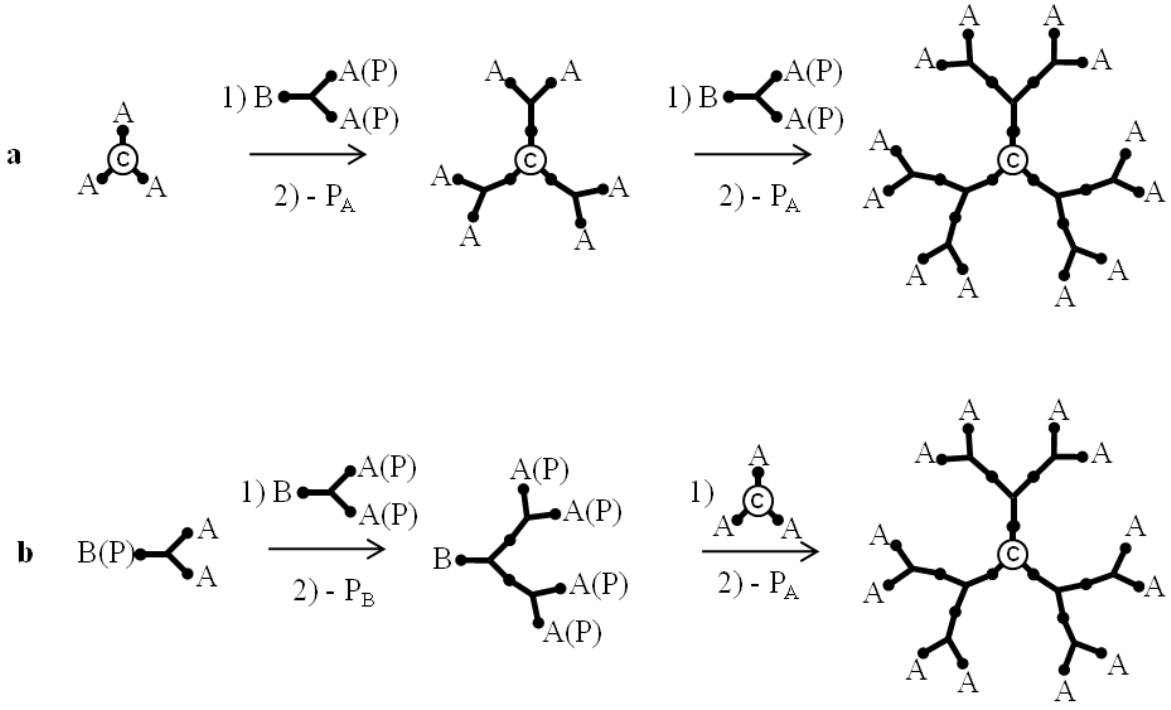

Scheme 2.1 Synthesis of a G2 dendrimer by (a) divergent and (b) convergent strategies.

The divergent synthesis (Scheme 2.1a) begins with an unprotected trifunctional initiating core ($N_c = 3$). The G0 core can be coupled with a partially protected monomer, $BA_2(P)_2$, having a branching multiplicity (N_b) of 2. The G1 dendrimer results after removal of the protecting group on the A functionality (- P_A). Coupling of this substrate with the

protected monomer yields what is referred to as a half-generation dendrimer (G1.5), and the G2 dendrimer is obtained upon deprotection. The convergent synthesis starts by coupling a partially protected monomer, $B(P)A_2$, with a complementary protected monomer, $BA_2(P)_2$, to yield a dendron. Deprotection of the B group (- P_B) at the focal point of the dendron allows selective coupling with the G0 core (A_3) to obtain the G1.5 dendrimer. Deprotection of the terminal A functionalities provides the G2 dendrimer. Specific details on the chemistry for the functionalization, condensation, and protection processes will be discussed subsequently.

The radial core-to-surface direction of the synthesis for the divergent strategy, and surface-to-core direction for the convergent method should yield identical architectures, albeit some differences in properties have been observed for molecules obtained by both methods and deemed to have identical compositions. This can be explained in terms of the degree of structural perfection attained in each case. The divergent strategy requires the reaction of an exponentially increasing number of functional groups over successive generations. Considering the large number of reactions required for the complete conversion of all terminal groups, the probability of attaining a perfect structure is reduced. This contrasts with the small number of coupling reactions involved in each cycle of a convergent synthesis. A lower degree of surface congestion also exists for the synthesis of individual dendrons, which favors complete reactions.

While the convergent strategy facilitates monomer coupling for upper generations independently of surface packing, the coupling of large dendrons to the anchor core is also more difficult due to steric hindrance making the focal point less accessible. Reduced coupling efficiency of the dendrons with the core has a more profound effect on the homogeneity of the dendritic species generated as compared to a reduced coupling efficiency

for small molecule monomers on the periphery of dendrimer in a divergent approach. The extent of surface congestion by terminal dendrimer groups can be estimated from the ratio of the dendrimer surface area (A_D) to the number of surface groups (Z) according to Equation 2.1, corresponding the surface area occupied per end-group (A_z).

$$A_z = \frac{A_D}{Z} = \frac{4\pi r^2}{N_c N_b^G} \tag{2.1}$$

The generation at which the area available per end-group approaches the actual dimensions of the end-group is the point where incomplete reactions should become significant, resulting in an imperfect structure. This dense or critical packing state was predicted by de Gennes for polyamidoamine (PAMAM) dendrimers.[4] It was thus predicted that the onset of deviation in molecular weight from the ideal structure would occur around generation 9 or 10 for dendrimers, while molecular weight deviations were experimentally observed for generations as low as 4, but these nonetheless became more predominant from generations 9 or 10 as expected. Surface crowding effects and surface functionalization can play important roles in the application of dendrimers as scaffolds or containers: For example, a densely packed surface may inhibit loading of the dendrimer and rather favor surface coordination. Conversely, the flexible and more open structure of lower generation dendrimers should enhance their ability to house materials within their interior.

2.2.2 General Characteristics

The size, shape, and molecular weight of a dendrimer depend on the molecular weight and the branching multiplicity of the monomer, as well as its generation number. Molecular weights can range from the hundreds or thousands for low generations, to over 10^5 g/mol for

generations 10 and above. The corresponding diameter of these structures ranges from ca. 1 to above 10 nm. Different generations of dendrimers derived from a trifunctional core are compared in Scheme 2.2.

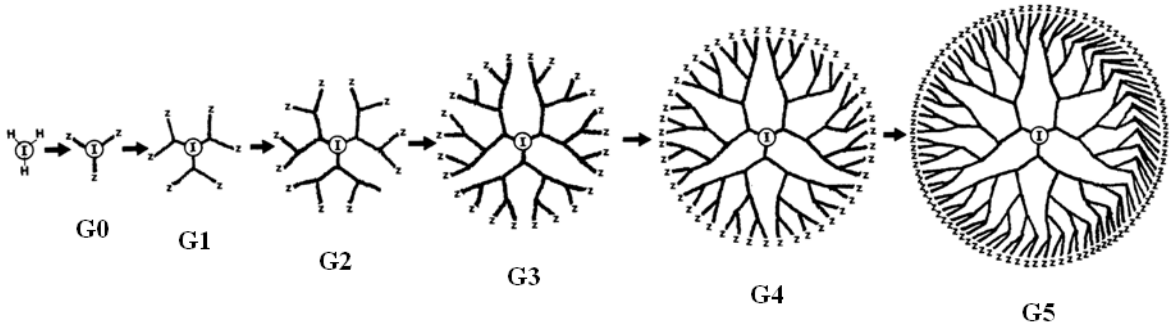

Scheme 2.2 Dendrimer generations derived from a trifunctional core and a monomer with a branching multiplicity of 2.[15]

The three-dimensional topology of dendrimers displays a transition from ellipsoidal to spherical for increasing generations.[16] The onset of the morphogenesis is reliant on the core multiplicity and the synthetic strategy (divergent or convergent) used. Increased core multiplicity (N_c = 3 or 4 vs. N_c = 2) forces a shape change at least one generation earlier. The convergent method has a similar effect due to the more perfect structure (increased crowding) attained for a particular generation. The most significant transformations occur between generations 3 and 5, after which the dendritic species adopt either spheroidal or slightly ellipsoidal geometries. An increase in generation number also brings enhanced surface group congestion, until a maximum known as the dense packing state is reached. Beyond this point only a fraction of the end-groups can participate in the next cycle of monomer addition.

Targeting a specific molecular weight and number of functional groups in dendrimer synthesis is relatively easy due to the uniform structure of the molecules, inasmuch as complete reactions are possible. The molecular weight (MW) and the number of terminal functional groups (Z) of dendrimers are well-defined functions of the core multiplicity (branching functionality N_c), the branch cell multiplicity (N_b), and the generation number (G) of the molecules. The number of functional groups can be calculated according to Equation 2.2.

$$Z = N_c N_b^G \tag{2.2}$$

The number of end-groups is directly related to the number of covalent bonds formed in each reaction cycle, which increases according to a power law. The total number of branch cells (BC) in the structure can be calculated from Equation 2.3. The total number of branch cells is analogous to the degree of polymerization commonly cited for linear polymers, and is also equivalent to the number of covalent bonds formed in the dendrimer:

$$BC = N_c \left[\frac{N_b^G - 1}{N_b - 1}\right] \tag{2.3}$$

The overall molecular weight of the dendrimer can be calculated by factoring in the molar mass of the various components including the core (M_c), the repeat units (M_{RU}), and the terminal groups (M_Z), as expressed in Equation 2.4.

$$MW = M_c + N_c \left[M_{RU}\left(\frac{N_b^G - 1}{N_b - 1}\right) + M_Z N_b^G\right] \tag{2.4}$$

2.2.3 Common Structures

2.2.3.1 Dendrimers Synthesized by a Divergent Strategy

The concept of branched macromolecules derived from repetitive reaction cycles of multifunctional small molecules was first introduced in 1978.[1] Vögtle thus reported a cascade-type divergent synthesis for low molecular weight polypropylenimine by the cyanoethylation of various amines cited in Reference 1, using acrylonitrile in glacial acetic acid at reflux for 24 h. Subsequent reduction of the cyano functionalities with cobalt(II) chloride hexahydrate and $NaBH_4$ in methanol converted the terminal cyanoethyl groups to primary propylamine functionalities, which were subjected to further cyanoethylation and reduction reactions to obtain the upper generation cascade polymers.

The yield of the cyanoethylation and reduction reactions in Vögtle's work was less than ideal, varying from 76 % for the zeroth generation to 35 % for the G1 product. These low yields resulted in ill-defined structures and prevented the synthesis of the upper generation structures. This procedure was nevertheless improved upon in the early 1990s after optimizing the cyanoethylation and hydrogenation reactions, by working in aqueous solutions at 80 °C and through hydrogenation with Raney cobalt, respectively.[17,18] In this case diaminobutane (DAB) served as multifunctional core to generate DAB-*dendr*-$(CN)_x$ and DAB-*dendr*-$(NH_2)_x$ dendrimers after the cyanoethylation and hydrogenation reactions, respectively. The reaction sequence for the divergent synthesis of polypropylenimine dendrimers is shown in Scheme 2.3.

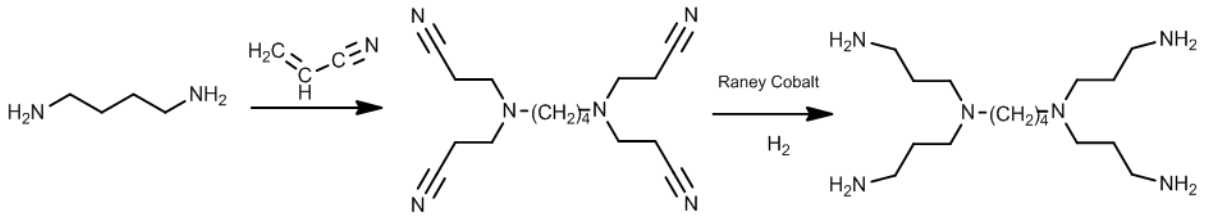

Scheme 2.3 Preparation of polypropylenimine dendrimers.

Polyamidoamine (PAMAM) dendrimers, synthesized subsequently, are likely the most widely investigated and used dendritic polymers to date. The first dendrimers commercialized in that family were the Starburst® systems. These species were developed in the mid-1980s by Tomalia,[5] at about the same time when Newkome developed similar dendritic architectures named Arborols.[6] A major incentive for development of these molecules was the creation of covalently bonded (unimolecular) micelles comparable to the well-known multi- or intermolecular micellar systems.

PAMAM dendrimers are versatile in that their terminal groups can be easily modified for targeted functionality or reactivity. These compounds are synthesized by the condensation of amines and acrylates. An initiating core containing one or more amine functionalities is first reacted with an excess of methyl acrylate, resulting in an alkyl ester branch addition at each amino hydrogen (Scheme 2.4). This ester-terminated product is referred to as the G0.5 dendrimer. Amidation of the ester with ethylenediamine (EDA) causes branch extension with terminal amino groups. This amine-terminated dendrimer is referred to as a G1 PAMAM dendrimer. Repetitive cycles of Michael addition of the acrylate ester and amidation with EDA leads to successive generations of dendrimers. Functional group modification chemistry can also be performed on the terminal ester or amine groups. Thus treatment of the half-

generation (ester-terminated) PAMAM dendrimers with alkali metal hydroxides yields carboxylate functionalities.

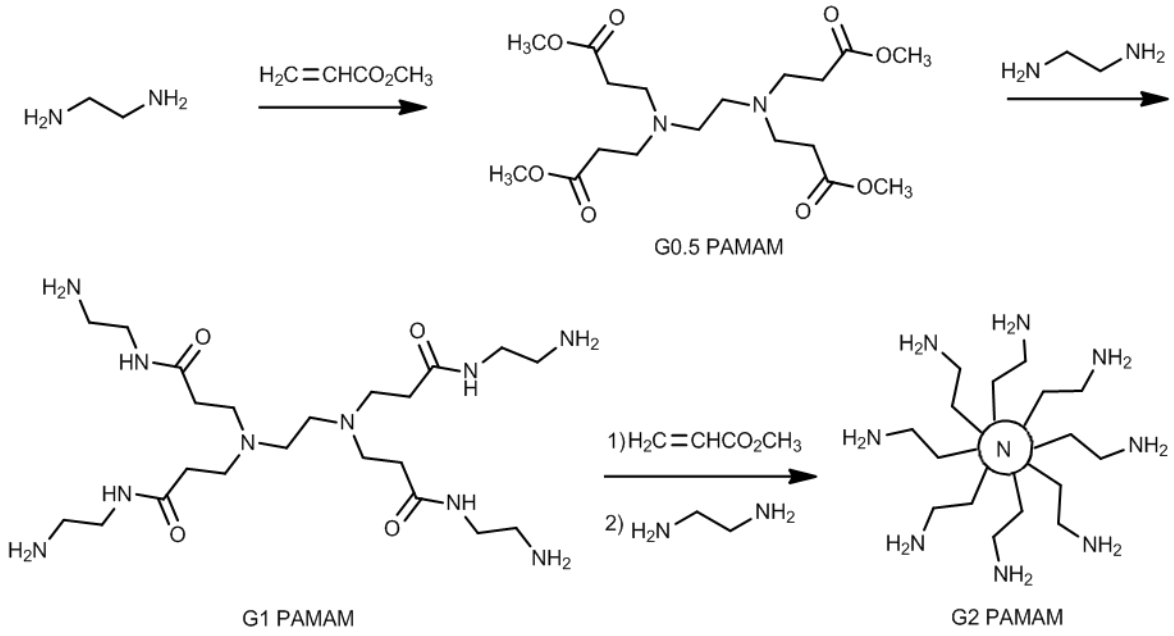

Scheme 2.4 Divergent PAMAM dendrimer synthesis starting from a diamine (EDA) core.

2.2.3.2 Dendrimers Synthesized by a Convergent Strategy

Hawker and Fréchet made a major contribution to the dendritic polymer chemistry field by developing a convergent approach to dendrimer synthesis in 1990.[7] Dendritic fragments (dendrons) of benzyl ether were thus created by coupling phenols with benzylic halides. This approach represents a surface-to-core method, where the monomers are assembled from the peripheral units towards the core. Benzyl bromide was first coupled with dihydroxybenzyl alcohol (DHBA) in the presence of potassium carbonate and 18-crown-6 as a phase transfer catalyst in acetone as shown in Scheme 2.5. Following isolation and purification of the

product, the G1 dendritic benzyl alcohol was converted to a benzylic bromide by treatment with carbon tetrabromide and triphenylphosphine. Further cycles of DHBA monomer coupling were performed to obtain subsequent dendron generations. To obtain a symmetrical dendrimer, the dendritic wedges carrying a bromide functionality at their focal point can be coupled with a polyfunctional core such as l,l,l-tris(4′-hydroxypheny1)ethane.

A convergent strategy such as this, with only one final coupling step for the dendron wedges, facilitates high yield reactions leading to well-defined structures. The symmetry of the molecules can be controlled through the functionality of the anchoring core.

In fact Newkome was really the first one to report a convergent dendron synthesis for the preparation of arborols, but the generation number and the molecular weight attained were limited.[6] The synthesis of arborols started from a trifunctional branch cell formed by treating an alkyl halide with triethyl sodium methanetricarboxylate. Subsequent reduction of the ester with $LiAlH_4$ yielded a triol. The formation of the second tier through another cycle of esterification was attempted by tosylation with tosyl chloride in pyridine and treatment with the methylsodium triester, but the yield was very low due to inefficient nucleophilic attack at the three terminal sites as a result of steric crowding. To solve this issue, extension of the ester was performed prior to tosylation and coupling with the methylsodium triester to afford the nonaester. The third generation of this cascade molecule, obtained through amide functionalization with tris(hydroxymethyl)aminomethane, was completely water-soluble. The reaction scheme for Newkome's synthesis of a 27-arm arborol is shown in Scheme 2.6.

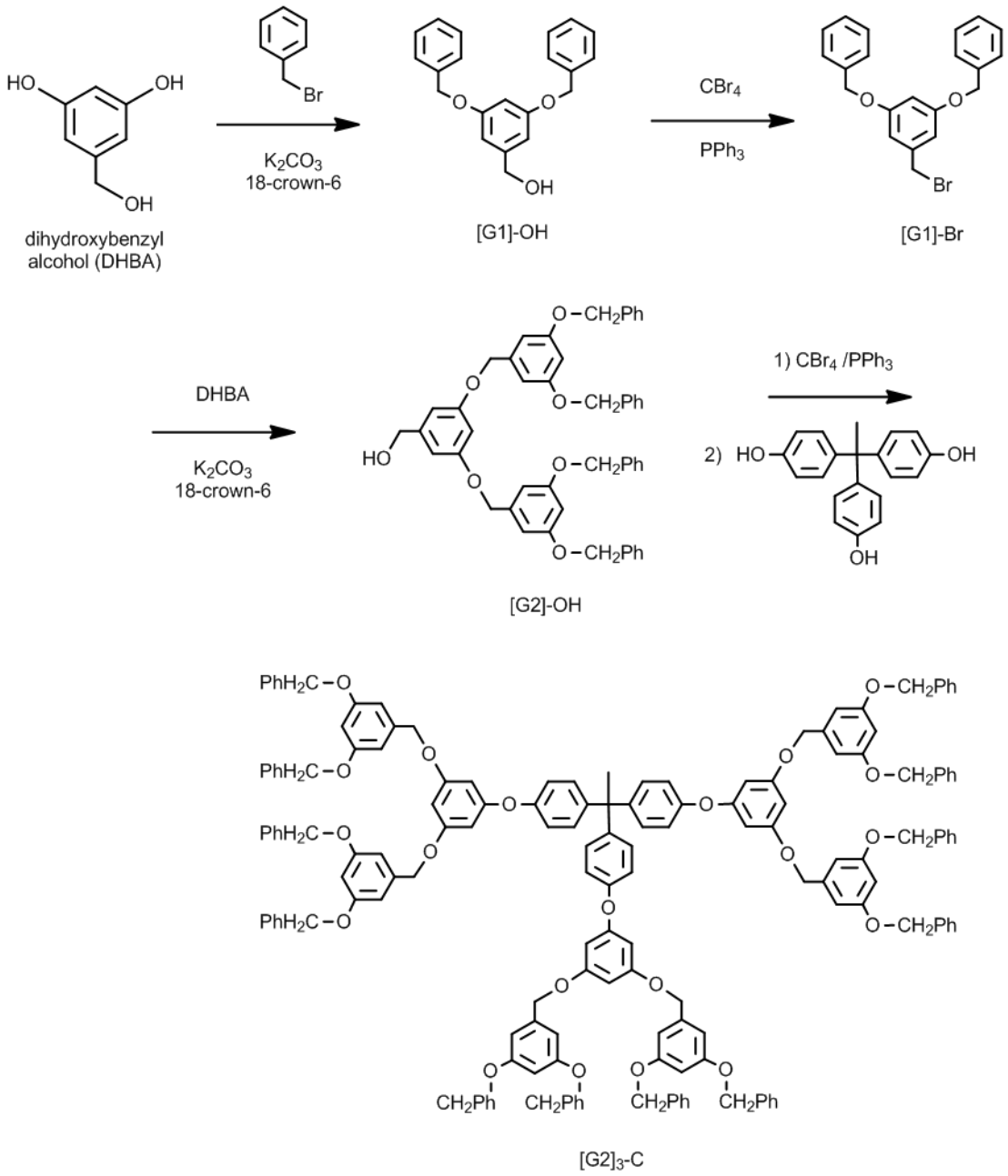

Scheme 2.5 Synthesis of a Fréchet benzyl ether dendrimer by a convergent approach.

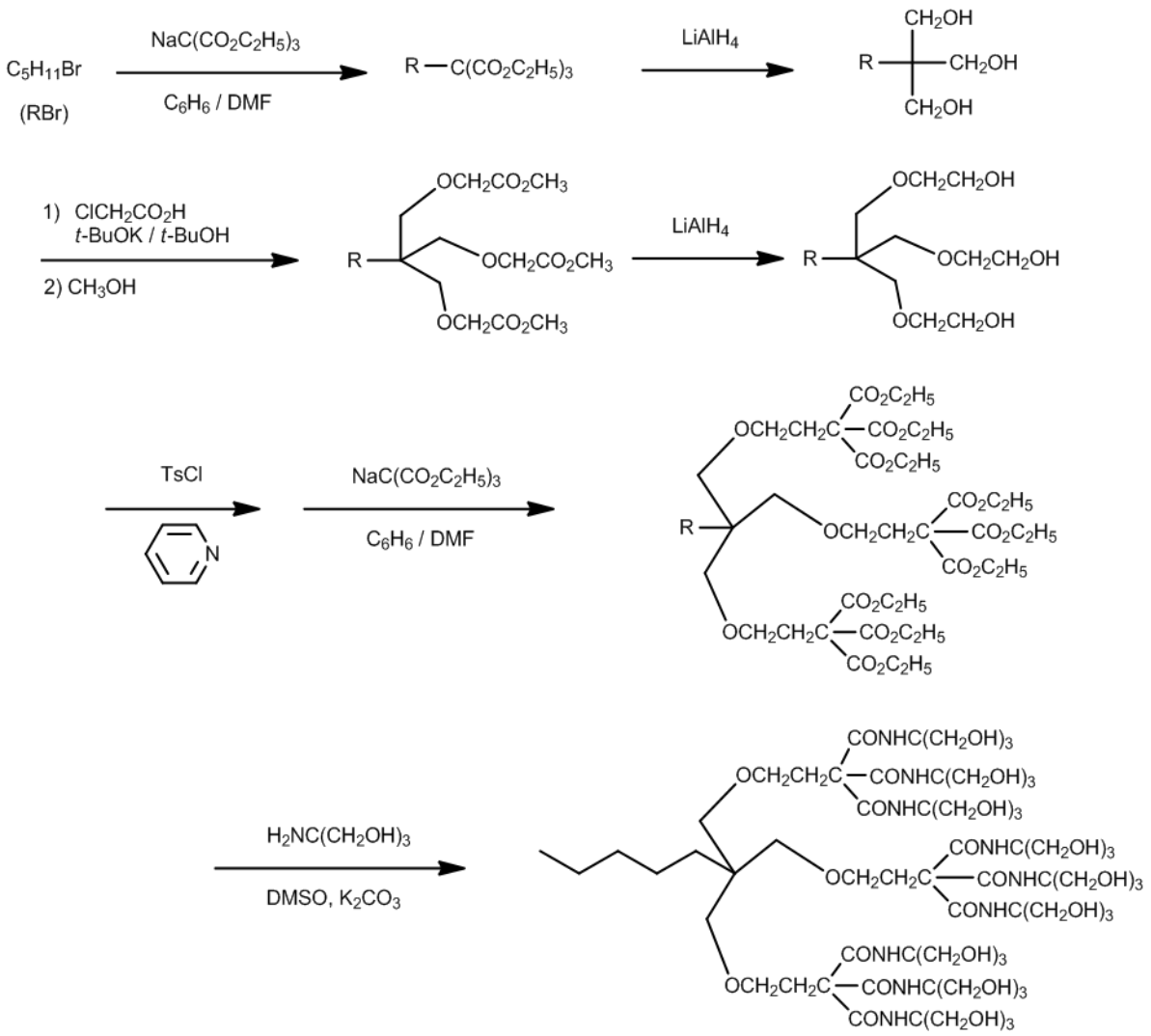

Scheme 2.6 Arborol synthesis according to Newkome.

2.2.4 Applications and Recent Trends

Considering the extensive control achieved over the size, shape, and surface functionality of dendrimers, it is not surprising that these molecules have a wide range of potential applications. Upon examination of the structural features of a dendrimer, one can visualize sector-specific uses as shown in Figure 2.3.

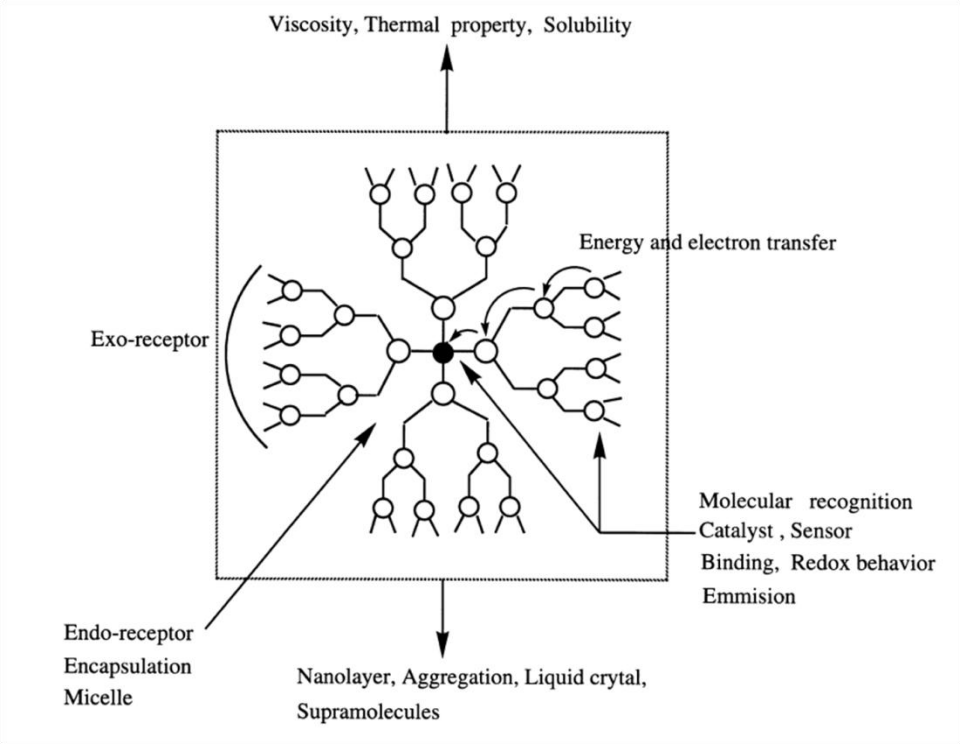

Figure 2.3 Structural features and potential uses of dendrimers.[19]

The first application examined, and one of the primary motivations for dendrimer syntheses, was as unimolecular micelles. In contrast to common micellar structures formed through intermolecular association or aggregation, dendrimers are covalently bonded structures unaffected by their surrounding environment. Consequently, the ability of amphiphilic dendrimers to encapsulate guest compounds should be independent of changes in concentration, solvent, and pH, among others. A strong incentive for dendrimer micelles is in catalysis. Considering the structure and functionality control attained, catalytic sites can be introduced specifically within the core, on the periphery of dendrimers, or both, as illustrated in Figure 2.4.

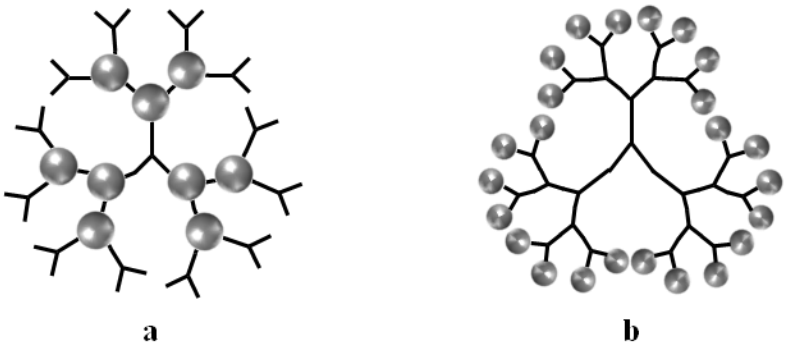

Figure 2.4 Internal (a) and peripheral (b) dendrimer functionalization.

The preparation of metallodendrimers, incorporating metallic species within their structure, is a relatively facile process given the ease and versatility of dendrimer functionalization which can be tailored for metal coordination. For example, the PAMAM dendrimers discussed earlier can coordinate different transition metals through their nitrogen atoms. Metals able to coordinate with the PAMAM structure include among others Cu,[20,21] Au,[22] Pd,[23] Pt,[24] Ag,[25] Co,[26] as well as bimetallic systems such as Pd-Au[27] and Pt-Ru.[28] Dendritic catalyst selectivity, activity, and stability can vary on the basis of steric effects, the location of the catalyst, and the architecture of the dendritic support.[29,30]

Coronal functionalization of the dendrimers with metals is typically performed by a divergent approach, i.e. with the metal binding process occurring in the final step. Catalysis on the periphery of dendrimers provides easily accessible sites; however, steric crowding of the reactants can influence the activity level observed. In theory, such a system should have a performance comparable to homogeneous (non-supported) systems.[31] A higher loading level (catalyst/dendrimer) is possible with peripheral loading, as there is a larger number of terminal groups as compared to junctions within the dendrimer skeleton; however, core-

functionalized metallodendrimers offer isolated catalytic sites which can be attractive for certain applications. In many cases, reduction of the noble metal salts is necessary after loading into the dendrimer. Alternately, the reduction of surface-bound metals could result in encasement of the dendritic structure, and potentially eliminate some of the inherent benefits that the core may have, or create a barrier to core loading. Careful selection of the surface functionality and the degree of functionality are critical. In both core- and periphery-functionalized metallodendrimers, isolation of the catalyst from the crude product is conveniently achieved by nanofiltration. Several reviews have been published on this topic.[31,32]

Examples of peripherally functionalized catalysts include carbosilane dendrimers with Ni at their peripheral functional sites serving in the Kharasch addition of polyhalogenoalkanes to terminal carbon-carbon double bonds, which displayed regioselectivity.[33] Polypropylenimine dendrimers have likewise been end-functionalized with palladium, rhodium, iridium, and Pd-Ni bimetallic catalysts for use in the Heck reaction and hydroformylation.[34] Polyamidoamine dendrimers supported on silica were complexed with rhodium for heterogeneous catalysis in the hydroformylation of styrene and various other olefins. The highly active catalyst yielded branched chain aldehydes with high selectivity from aryl olefins and vinyl esters. The catalyst was easily recovered, and no significant loss in selectivity or activity was observed upon reuse.[35]

Core-functionalized metallodendrimer catalysts are sometimes referred to as ‘dendrizymes’ by analogy to biological systems and due to the observed influence of the generation number on selectivity. Ferrocenyldiphosphine core-functionalized carbosilane dendrimers have thus been prepared as Pd ligands for the homogeneous catalysis of allylic

alkylation reactions, and displayed variations in product selectivity for the largest dendrimers investigated.[36] Fréchet-type polyether dendrons were complexed with Pt for use as SO_2 sensor, and with Ni for the Kharasch addition of CCl_4 to methyl methacrylate.[37] The dendron wedges, when functionalized at their focal point, displayed adequate catalytic activity with easy recovery and good stability.

Mimicking biological species is a major investigation area for dendrimers, particularly for PAMAM-based structures due to their similarities in size, shape, and chemical make-up with globular proteins. Thus the immunodiagnostic capabilities of dendrimers have been investigated,[38] as well as *in vitro* and *in vivo* gene delivery[39] and gene expression.[40] These species possess an exterior barrier controlled through end-group functionalization, as well as void spaces within their interior, much like liposomes. The tailored unimolecular micelle characteristics of dendrimers, with an open interior (in contrast to typical micelles), allows them to entrap guest molecules of various sizes and to selectively release them under certain conditions.[41] These characteristics have led to the development of macromolecular drug delivery systems from dendrimers. In analogy to other complexation processes, drug molecules can be loaded inside or attached at the periphery of the molecules, to form dendrimer-drug conjugates. In the latter category, it has been demonstrated that PAMAM dendrimer–platinate conjugates have anti-tumor activity.[42] More recently, it was shown that the encapsulation or complexation of camptothecin (a plant alkaloid known for its anti-cancer potency) with PAMAM dendrimers increased its solubility, which represents a step towards the effective delivery of this drug to cancerous cells.[43] PAMAM dendrimer–glucosamine conjugates have even been shown to prevent scar tissue formation.[44] Lastly, dendrimers have been investigated for light-harvesting applications.[45] Their branched

architecture provides an interesting framework in which energy transfer can occur from peripheral chromophores to an energy sink located at the core of the molecules. This property can be exploited in light-emitting diodes, frequency converters, fluorescent sensors, or as a mimic for the natural photosynthesis process.

2.3 Hyperbranched Polymers

Hyperbranched polymers also possess a dendritic architecture, but with imperfect branching. The basic structural features present in these molecules are the same as in dendrimers, namely a core surrounded by layers of branch cells capped with terminal units. The one-pot syntheses used to create these tree-like structures also rely upon AB_n-type monomers (Scheme 2.1), but without protecting groups preventing simultaneous condensation reactions. The resulting polymers typically have broad MWD ($M_w/M_n > 2$), with multiple isomers and geometries. Because they are created in a single reaction step, hyperbranched polymers are more economical to produce than dendrimers as their synthesis is less time- and resource-intensive. This trait represents a major draw for industry and the development of commercial applications for dendritic polymers.

2.3.1 General Features

Many methods have been reported to synthesize hyperbranched polymers. These materials were first reported in the late 1980s and early 1990s by Odian and Tomalia,[9] Kim and Webster,[10] and Hawker and Fréchet.[11] As early as 1952, Flory actually developed a model for the polymerization of AB_n-type monomers and the branched structures that would result, identified as random AB_n polycondensates.[46] Condensation step-growth polymerization is likely the most commonly used approach; however, it is not the only method reported for the synthesis of statistically branched dendritic polymers: Chain-growth and ring-opening polymerization methods have also been applied, among others. In a one-pot (or concurrent) method the monomers simply add in alternate fashions into patterns which can be modeled

statistically. Structures can be grown in the presence or the absence of a central core, as illustrated in Scheme 2.7 for a simplified system.

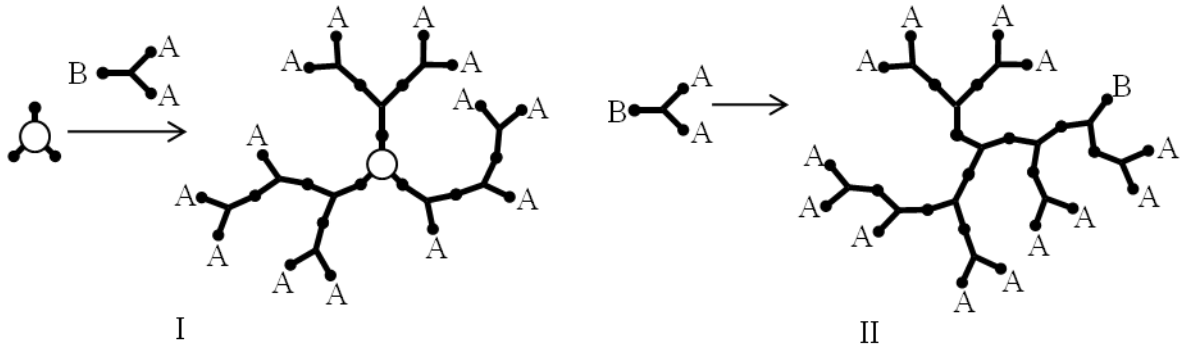

Scheme 2.7 Core (I) and non-core (II) methods for the synthesis of hyperbranched polymers.

Ideally no intermolecular reactions should occur between the branched structures, but this is difficult to avoid in many cases and is a drawback to this method. For such an ideal (and simplified) case with an AB_2-type monomer the branching coefficient (α), representing the probability that a branch unit has reacted, and is thus connected to another branch unit, is equal to the fraction of B groups reacted (p_B), if it is assumed that the two B moieties are equally reactive. The probability or fraction of A groups having reacted (p_A) can then be considered to represent the extent of reaction, which leads to the relation between the extent of reaction (p), the branching coefficient (α), and the functionality of the AB_x monomer (f) given by Equation 2.5.[46]

$$\alpha = p_B \text{ and } p_A = p_B(f-1) \text{ therefore } \alpha = \frac{p_A}{f-1} = \frac{p}{f-1} \qquad (2.5)$$

Fréchet proposed to use the ratio of the number of fully branched monomer units to the total number of monomer units contained within the polymer (N_o) to describe the degree of structural perfection of hyperbranched polymers derived from AB_2-type monomers.[11] In a dendrimer with a perfect structure two types of monomer units are present in equal proportions, the terminal (T), and the dendritic (D) units, and thus the degree of branching is equal to 1. In a hyperbranched structure some of the dendritic units are unreacted, leading to the formation of a third monomer unit described as a linear (L) segment. The degree of branching (α_{Fr}) attained under these conditions can be expressed by Equation 2.6 where D, T, and L represent the total number of each type of unit.

$$\alpha_{Fr} = \frac{D + T}{D + T + L} = \frac{D + T}{N_o} \tag{2.6}$$

The different types of dendritic monomer units are shown in Figure 2.5, where the dendrimer (Figure 2.5a) contains three dendritic and six terminal groups while the hyperbranched structure (Figure 2.5b) has two dendritic, three linear, and five terminal units, yielding branching functionalities (as defined by Fréchet[11]) of 1 and 0.7, respectively.

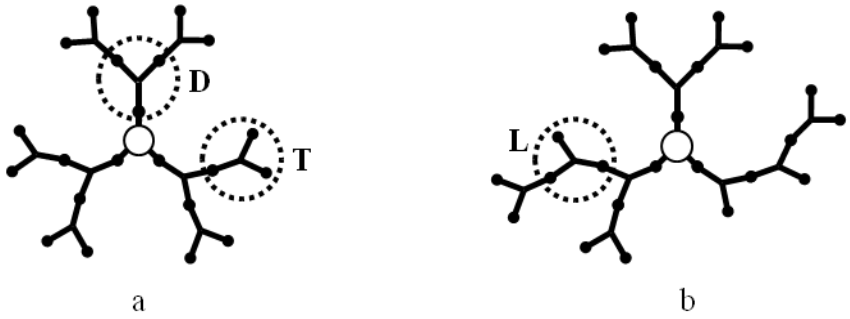

Figure 2.5 Structural units in a dendrimer (a, α_{Fr} = 1) and a hyperbranched polymer (b, α_{Fr} = 0.7): dendritic (D), linear (L), and terminal (T).

The relative amounts of each of the three types of monomer units can, in some cases, be determined by NMR analysis or by other spectroscopic methods. In situations where the units cannot be differentiated by these methods, selective labeling and/or degradation can be performed followed by spectroscopic analysis. It should be noted that Equation 2.6 does not tend towards zero for linear polymers as it should. This discrepancy prompted the development of a corrected expression for branching functionality (α′, Equation 2.7) by two different groups in 1997.[47,48] Expressions for the universal degree of branching were also derived for higher order functionalities and can be found in the respective references.

$$\alpha' = \frac{2\mathrm{D}}{2\mathrm{D} + \mathrm{L}} \tag{2.7}$$

In his original 1952 article,[46] Flory also predicted the influence of branching on the degree of polymerization (X) and polydispersity, as shown in Equation 2.8, which is derived from Equation 2.5.

$$\mathrm{PDI} = \frac{X_\mathrm{w}}{X_\mathrm{n}} = \frac{1 - \alpha^2(f-1)}{1 - \alpha(f-1)} \tag{2.8}$$

It is apparent that the breadth of the MWD is highly dependent on the extent of reaction (conversion) attained in these reactions, as the PDI increases with the conversion. At relatively low conversions the MWD for an AB_n system corresponds to a Flory distribution ($M_\mathrm{w}/M_\mathrm{n} \approx 2$); however, the polydispersity trends towards infinity as full conversion is approached. For trifunctional monomers, including equally reactive A_3 monomers and ABC monomers with reactivity differentials, the MWD also depends on the degree of

polymerization (DP) but in a different way: The PDI is proportional to DP in an A_3 system, while for an ABC system it is proportional to $(DP)^{½}$.[49,50]

Unfortunately, the one-pot reaction scheme for the preparation of hyperbranched polymers offers no option for molecular weight control, which ultimately leads to gelation. Intramolecular side reactions such as cyclization resulting from 'backbiting' processes are also common in these reactions. One technique developed to avoid or reduce side reactions uses a slow monomer addition protocol, by adding monomer throughout the reaction. This method has been termed 'concurrent slow addition'.[51–53] The copolymerization of AB monomers with AB_2 monomers has also been employed to control the molecular weight and reduce the PDI in these reactions.[51,54] Multifunctional initiators (B_y monomers), when used in batch-wise or concurrent slow addition protocols, have also shown promise in controlling the breadth of the MWD.[55,56]

2.3.2 Synthetic Strategies and Common Structures

Hyperbranched polymers can be synthesized by either single- or double-monomer methods. Falling in the single-monomer methodology (SMM) are common polymerization techniques including the polycondensation of AB_n monomers, self-condensing vinyl polymerization (SCVP), self-condensing ring-opening polymerization (SCROP), and proton-transfer polymerization (PTP). The double-monomer methodology (DMM), as the name suggests, relies on monomer pairs which can be subdivided into two strategies: $A_2 + B_3$ reactions and the couple-monomer methodology (CMM). Many combinations of compatible monomers have been successfully applied to these strategies. Considering the broad scope of this topic, only a few examples of the pioneering work and some of the simpler methods will be

provided for the different strategies. A more detailed review on synthetic strategies for the preparation of hyperbranched polymers was provided by Gao and Yan.[57]

2.3.2.1 Single-monomer Methodology

Kim and Webster reported the first example of a single-monomer polycondensation technique using 3,5-dibromophenylboronic acid and aqueous sodium carbonate in the presence of a Pd catalyst.[10] A general scheme corresponding to this reaction and the resulting hyperbranched structure obtained are shown in Scheme 2.8.

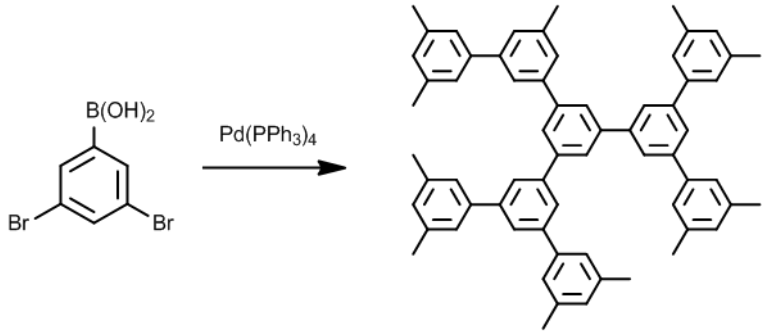

Scheme 2.8 Hyperbranched polyphenylene synthesis by the single-monomer polycondensation method.

The single-monomer polycondensation scheme has also been used to synthesize hyperbranched polyethers,[58] polyesters,[59] polyurethanes,[60] polysiloxysilanes,[61] as well as polycarbonates.[62] Higher order monomers including AB_3, AB_4, AB_5, and AB_6 have also been applied in single-monomer polycondensation syntheses of hyperbranched polymers.[63,64]

Self-condensing vinyl polymerization requires a monomer with a vinyl group, but also with a pendant moiety that can act as an initiating site for other vinyl pendants. This type of monomer is referred to as an inimer (initiator + monomer). Fréchet developed both free

radical[65] and cationic[66] SCVP methods for the synthesis of hyperbranched molecules using inimers. These techniques all depend upon the same principle: New initiating species are formed from a specific functionality within the inimer molecules. Once activated, this site can propagate through vinyl groups on other monomers or inimers. As propagation continues, macromonomers formed from inimers in the reaction eventually react with the propagating center, resulting in branching.

In Fréchet's cationic method, 3-(1-chloroethyl)-ethenylbenzene is activated with $SnCl_4$ to yield a cationic initiating site from the chloroethyl functionality. This site can propagate through vinyl-containing species, producing chains with pendant initiating sites that form branches once they become active and participate in chain propagation. Similar reaction sequences are involved in the radical systems, for example with a styrenic inimer containing a benzylic nitroxide functionality.[65] In this case the hyperbranching process begins with the thermolysis of the benzylic nitroxide, producing radical species which propagate through the pendant vinyl group of the styrene moieties. Residual nitroxides can also cleave along the polymer backbone to form radical sites and propagate branch growth. The cationic and radical hyperbranching processes are illustrated in Scheme 2.9a and b, respectively.

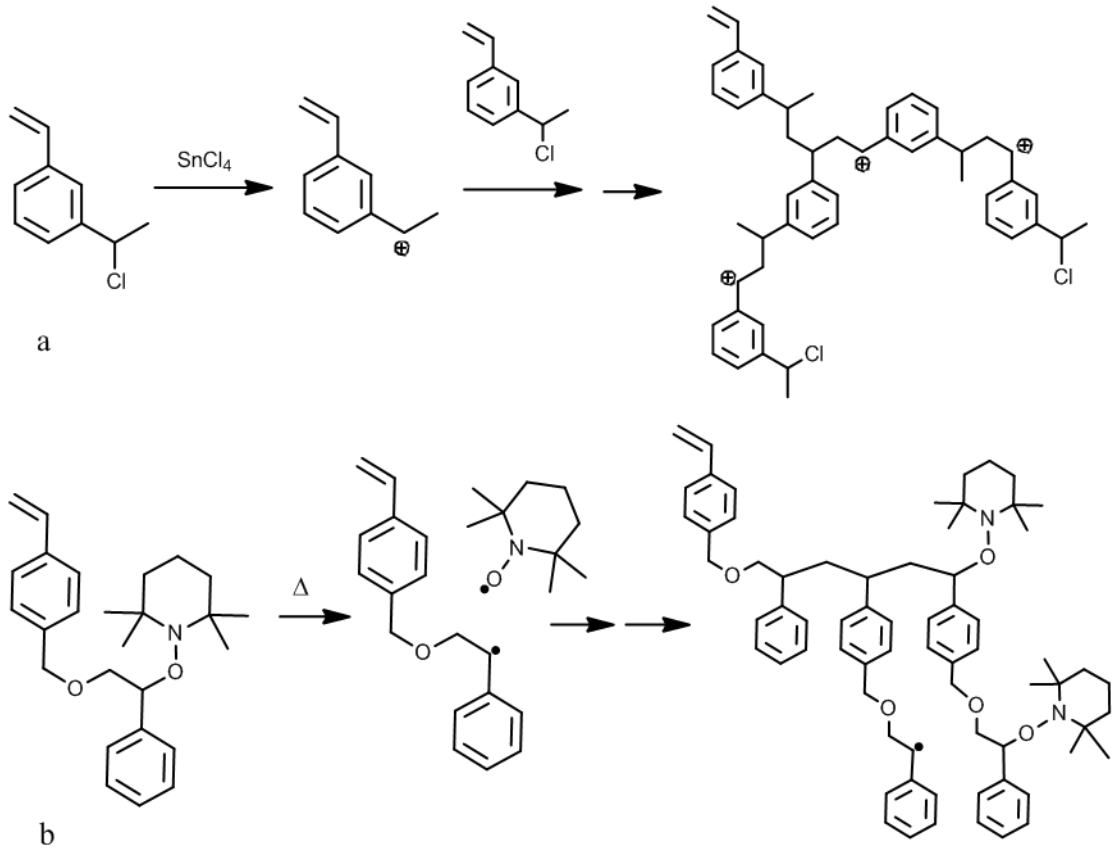

Scheme 2.9 Formation of hyperbranched polymers by (a) cationic and (b) radical SCVP.

The degree of branching attained in SCVP reactions is governed by the reactivity difference between chain growth through the vinyl groups and step growth addition at the initiating site. In some cases the degree of branching attained can be controlled by adjusting the reaction conditions used. The radical SCVP procedure requires additional considerations, however, since side reactions leading to gelation are more probable at longer reaction times.

Polymerization by the inimer technology has received much attention from Kennedy and Puskas, specifically for the synthesis of hyperbranched polyisobutylenes and copolymers thereof in a one-pot method.[67] While this convergent approach complicates the structural

analysis of the branched polymers, fragmentation of the resulting polymer is possible in some cases to allow such analysis.[68] Branching ratios (BR) can be calculated directly from the molecular weight of the branched polymer as per Equation 2.9, to give an indication of the number of branches contained within the molecules, as the ratio of the measured M_n for the polymer obtained to the theoretical M_n (M_n^{theo}).

$$\mathrm{BR} = \frac{M_\mathrm{n}}{M_\mathrm{n}^\mathrm{theo}} - 1 \tag{2.9}$$

The theoretical M_n is calculated by assuming that all the inimer molecules in the reaction act solely as monofunctional initiator and not as a branching agent. This quantity is calculated from the mass of monomer (m_m) and the moles of inimer (n_i) in the reaction as described by Equation 2.10.

$$M_\mathrm{n}^\mathrm{theo} = \frac{\mathrm{m_m}}{\mathrm{n_i}} \tag{2.10}$$

Self-condensing ring-opening polymerization (SCROP) and ring-opening multi-branching polymerization (ROMBP) are similar to SCVP; however, in these cases the inimer is a cyclic monomer carrying an initiating functionality. A good example of this approach is shown in Scheme 2.10, where hyperbranched polyesters are formed from inimers containing an alcohol functionality and a caprolactone group.[69]

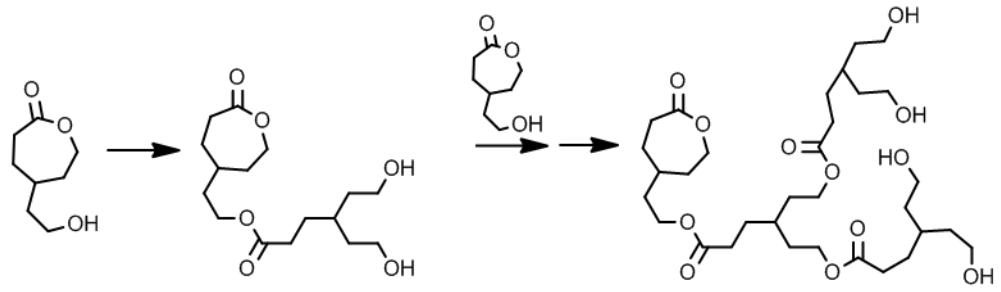

Scheme 2.10 SCROP of hydroxyl-functionalized caprolactone.

The dominant contribution of simultaneous chain growth from all the chain ends, controlled by the deprotonation level of the initiator, leads to relatively narrow MWD ($M_w/M_n \approx 1.1 - 1.4$) while maintaining branching levels typical of random polycondensation reactions (degree of branching $\alpha' \approx 0.5$, Equation 2.7).[70] The SCROP technique has also been used to synthesize hyperbranched polyglycerols,[70] polyethers,[71] and polyamines.[72]

Proton-transfer polymerization (PTP), which began to gain momentum in the late 1990s, relies on a reaction sequence of the type shown in Scheme 2.11 (I), where a catalytic amount of initiator is added to the monomer for proton abstraction. Following coupling with another neutral monomer unit, a thermodynamically favorable proton transfer reaction occurs from another free monomer unit to the dimer. The activated monomer can then couple with another monomer unit or with an existing branched species. The proton-transfer step does not propagate to a significant extent as it is a kinetically slower process. Specific monomers that have been investigated for the PTP method are shown in Scheme 2.11 (II).

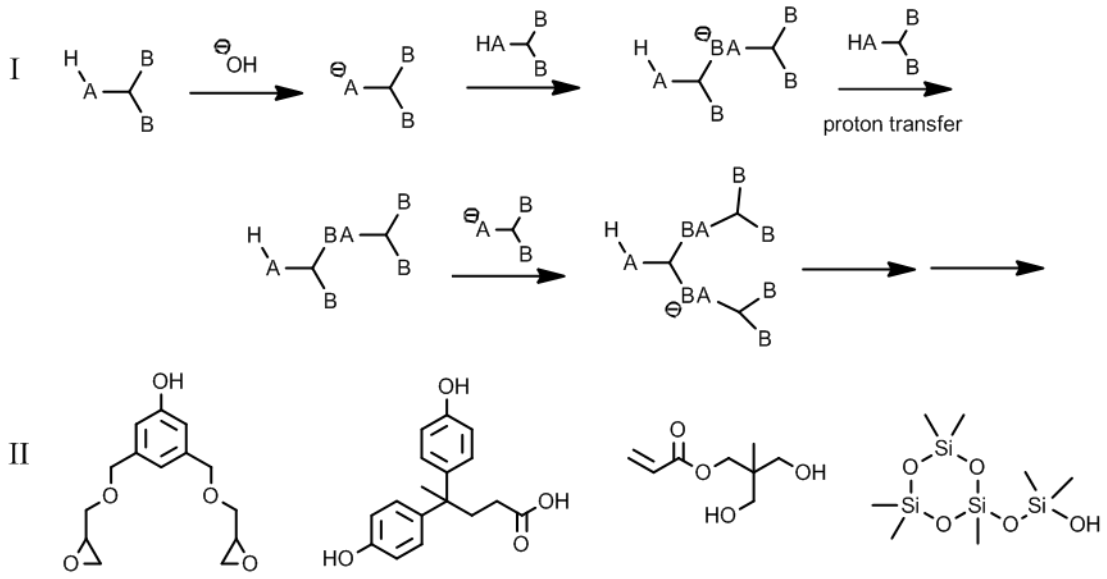

Scheme 2.11 Generalized PTP synthetic scheme (I) and examples of monomers used in PTP syntheses (II).

2.3.2.2 Double-monomer Methodology

The most versatile approach to hyperbranched polymer synthesis is likely the double-monomer method (DMM), due to the wide range of monomers and chemical functionalities to which it can be applied. The two categories of DMM reactions only differ in terms of the reactivity of the functional groups involved: In $A_2 + B_3$ reactions all the moieties within each monomer have the same reactivity, while varying degrees of reactivity describe the couple-monomer method (CMM).

The chemistry behind the $A_2 + B_3$ method is analogous to the previously described AB_n reactions but the compatible reactive sites are separated on two different monomers. A significant obstacle in this approach is the occurrence of gelation, commonly observed for the direct polycondensation of A_2 and B_3 monomers. This problem can be minimized through slow monomer addition, capping agents, reaction quenching by precipitation, or the addition

of catalysts or condensation agents prior to reaching the critical conversion point. A few of the less exotic monomer combinations that have been used in $A_2 + B_3$ reactions are depicted in Figure 2.6. These examples include monomers with the following chemical functionality combinations: aromatic diamine and triacid (Figure 2.6a),[73] diepoxy and trihydroxy (Figure 2.6b),[74] trisbromophenyl and diboronic acid (Figure 2.6c),[75] and diiodophenyl and triethynylphenyl (Figure 2.6d).[76]

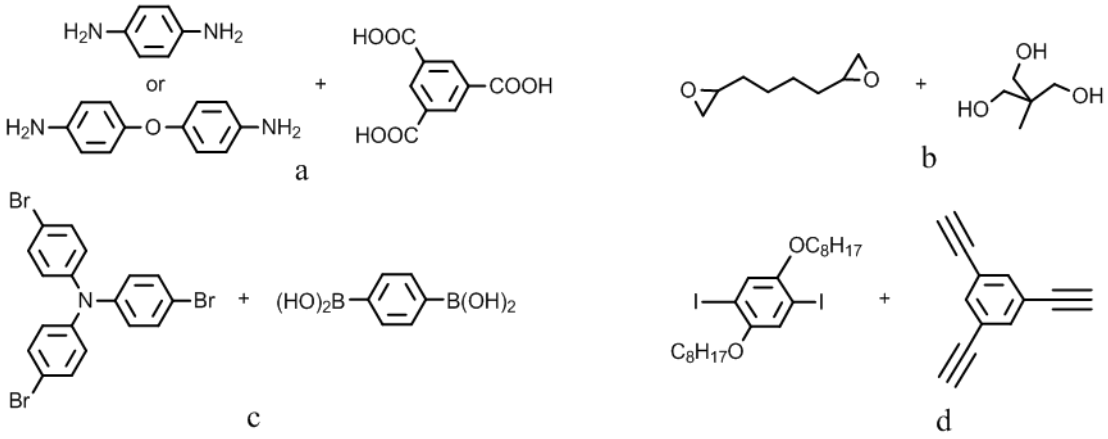

Figure 2.6 Examples of monomer combinations for the $A_2 + B_3$ double monomer synthesis of hyperbranched polymers.

The couple-monomer method (CMM) provides improved control over the branching process through reactivity tailoring, resulting in soluble (non-gelled) hyperbranched polymers in most cases. Gelation can be avoided through careful monomer selection whereby the reactivity of the functional groups differs. Many different monomer combinations have been reported fulfilling this requirement, two of which are $A_2 + B'B_2$ and $A_2 + CB_n$ systems. In the first case both A groups have the same chemistry and reactivity, and likewise for the B groups; however, B′ has the same chemical make-up as B but differs in reactivity. In the $A_2 +$

CB_n system the A groups and B groups have equivalent reactivity, but C differs in chemical structure and reactivity. Examples of monomers corresponding to each of these CMM classes are provided in Figure 2.7.

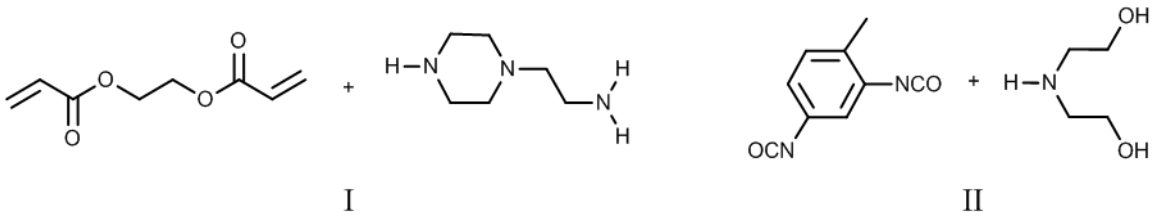

I II

Figure 2.7 CMM monomers for $A_2 + B'B_2$ (I) and $A_2 + CB_n$ (II) reactions.

The first example, Figure 2.7(I), is an $A_2 + B'B_2$ system with two equally reactive vinyl groups (A_2) and three amine functionalities, where the tertiary amine is unreactive under the conditions used. The primary and secondary amines differ in terms of reactivity and are bi- and mono-functional, respectively (B_2B'). In the $A_2 + CB_n$ case, Figure 2.7(II), the isocyanate groups are considered to be equally reactive based on the CMM naming conventions (A_2), as are the hydroxyl groups (B_2), the third functional group being a secondary amine (C). Higher order functionalities have also been investigated. A hyperbranched analogue of the commercially available PAMAM dendrimers (HYPAM) has thus been synthesized by a one-pot method shown in Scheme 2.12.[77] This approach can be described as an $A_6 + B_6$ reaction of tris(2-aminoethyl)amine tris(2-di(methyl acrylate)aminoethyl)amine.

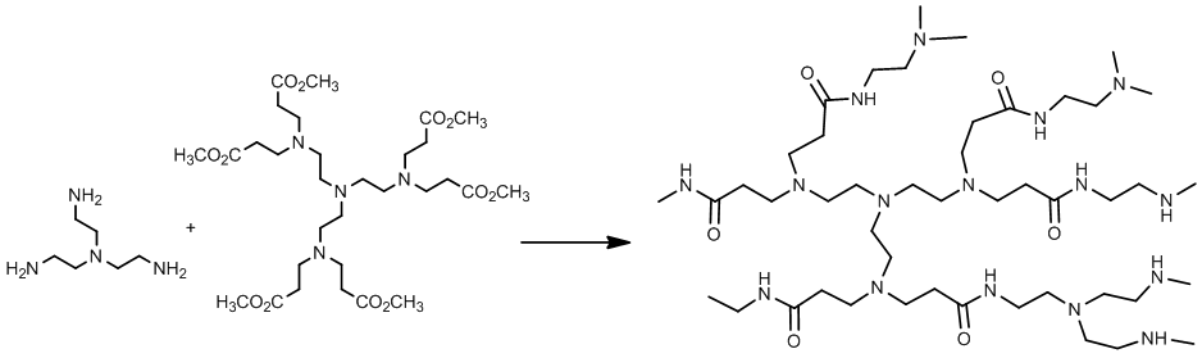

Scheme 2.12 Synthesis of hyperbranched PAMAM (HYPAM).

2.3.3 Applications and Recent Trends

The comparable architecture and chemical functionality of dendrimers and hyperbranched polymers lead to similar applications for these two families of dendritic polymers. The main benefit in using hyperbranched polymers to replace dendrimers lies in their simpler synthesis, provided that the perfect structure of dendrimers can be sacrificed for their broadly distributed hyperbranched analogues. The one-pot syntheses require less time and resources, resulting is less expensive processes which make hyperbranched polymers excellent candidates for commercial applications. Pertinent to the hyperbranched architecture are applications as electronic, magnetic and catalytic materials, as well as numerous uses in the biomedical field; some of these will be considered herein.

The incorporation of transition metals in hyperbranched polymers has received considerable attention. Like dendrimers, hyperbranched materials can be loaded with metals within their interior, on their exterior, or throughout the whole molecule, the exact location of the coordination sites depending on the functionality of the polymer, as shown previously in Figure 2.4. Salazar thus modified hyperbranched polyglycerol with hydroxyl end-groups to a

structure containing tertiary amines on its periphery.[78] The hyperbranched polyamines were coordinated with copper chloride and were successfully used as catalysts in the oxidative coupling reaction of phenylacetylene. Similarly, NCN-pincer platinum(II) carboxylates were complexed with hyperbranched polyglycerols to form endo-receptors to catalyze the coupling reaction of methyl vinyl ketone and ethyl α-isocyanopropionate by Michael addition.[79,80] These systems displayed improved performance due to the enhanced accessibility of the catalytic sites and the high local reagent concentration; the catalysts could be isolated from the reaction product in high yield (> 97 %) by dialysis. Other mainstream hyperbranched polymers such as polyethylenimines[81] and polyamidoamines[77] have also been used to stabilize various transition metals for catalytic applications. These molecules contain multiple metal-coordinating sites, both internal and peripheral, due to their high nitrogen content. The terminal primary amine groups of these polymers can also serve as functionalization sites to enhance the stability of the metal-polymer complexes under different solvency conditions. Thus in the case of hyperbranched polyethylenimines, the aqueous solubility of the polymers loaded with transition metals (Cu, Ag, Au, Pt) was ensured by encapsulating the structure with a carbohydrate shell.[81]

The post-polymerization functionalization method to incorporate transition metals into hyperbranched polymer structures can target the interior cavities and the functional groups of the molecules alike. One of the more exotic applications proposed for a metal-loaded hyperbranched polymer is a combination of a semiconductor polymer of conjugated poly(*p*-phenylenevinylene) (PPV) and colloidal semiconducting CdS nanocrystals at various locations within the structure.[82] This was accomplished by incorporating alkoxy substituents within the monomer prior to the hyperbranched polymer synthesis, to provide coordinating

sites for cadmium. The deposition of cadmium within the branched structure increased the dispersion of the nanoparticles and reduced their aggregation within the PPV-CdS hybrid, in addition to providing efficient energy transfer. The unique photochemical activity displayed by these nanostructured CdS materials make them excellent candidates for power conversion in hybrid photovoltaic systems.[83] Using a similar approach, a scaffold containing triple bonds acting as ligand sites was used to template the deposition of cobalt carbonyl, $Co_2(CO)_8$. The cobalt-containing hyperbranched polyynes were synthesized by Häußler et al. for the preparation of nanostructured magnetoceramics.[84] The cobalt was incorporated in the core of the hyperbranched polyynes through cobalt-triple bond coordination within the hyperbranched backbone. The structural units of the polymers used to template CdS and cobalt deposition are compared in Figure 2.8.

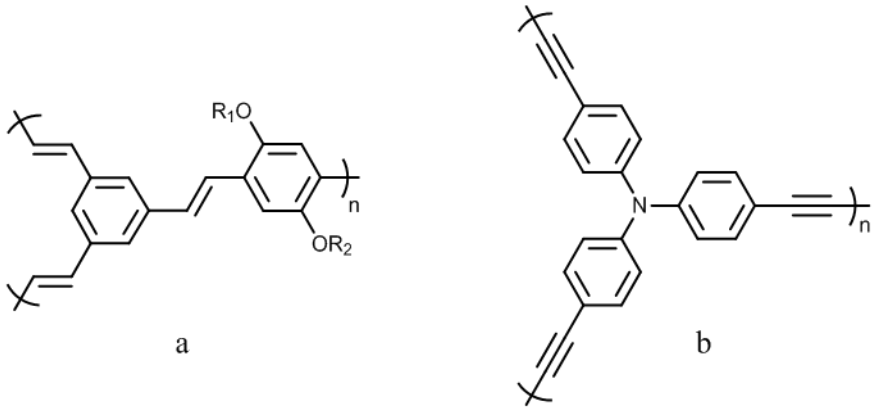

Figure 2.8 Conjugated hyperbranched polymers used to template (a) CdS and (b) cobalt deposition.

The incorporation of metals within dendritic structures during the synthesis of the molecules has been achieved using metal-containing AB_2 monomers. Onitsuka used this

approach in the synthesis of hyperbranched polyynes from Pt-functionalized monomers.[85] These displayed liquid crystalline properties under the influence of a magnetic field, similarly to the analogous one-dimensional linear structures.[86] The predetermined location of the metal within the monomer ensures its even and regular distribution throughout the entire polymer structure. An analogous Pt-containing dendrimer structure has also been reported.[87] The formation of a hyperbranched structure from the platinum-acetylide monomer proceeds as shown in Scheme 2.13.

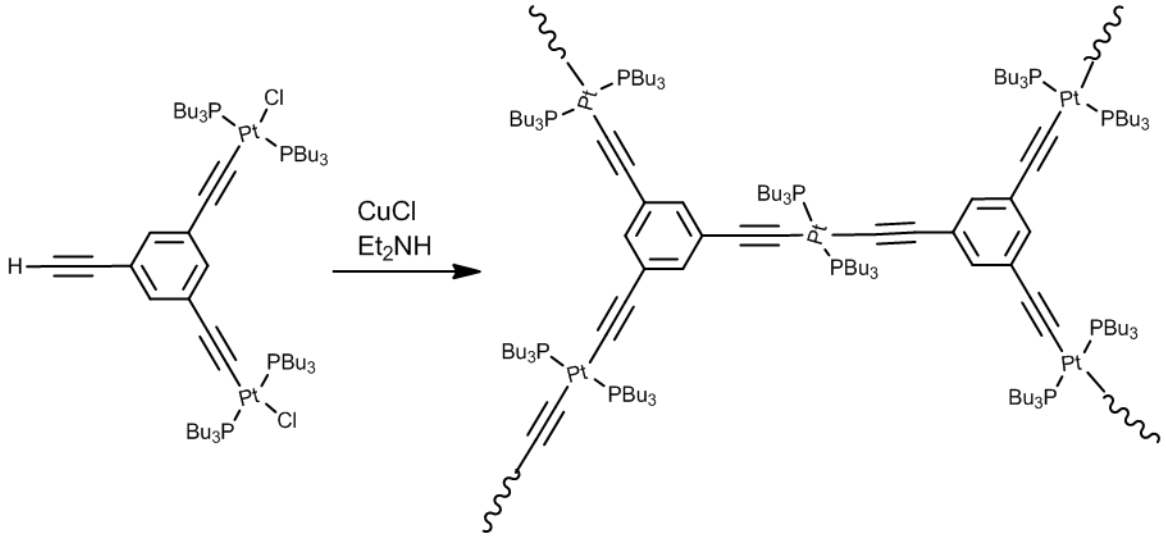

Scheme 2.13 Synthesis of a hyperbranched polymer from a platinum-containing acetylide monomer.

Hyperbranched polymers are also gaining interest as biomaterials, specifically as hosts for bioactive molecules such as drugs, labels, or probes. Hyperbranched polyglycerols are one of the candidates considered for this application as their synthesis is well-established and controlled, but more importantly they are biocompatible and biodegradable. End-group

functionalization is also a versatile method which can be easily adapted for enhanced biocompatibility, for site targeting, or to serve as binding sites for guest molecules.[88] Similar polymers have been applied to protein immobilization[89,90] or to support cell growth.[91] Hyperbranched polyisobutylene (PIB)-based copolymers have likewise received significant attention as biomaterials, with specific interest as coatings in arterial stents.[92,93] This is due to the fact that a linear triblock copolymer analogue, poly(styrene-*b*-isobutylene-*b*-styrene) (SIBS) has received approval from the United States Food and Drug Administration (FDA) for use as medical device coating. More specifically, copolymers of PIB and styrenic monomers were shown to display thermoplastic elastomeric (TPE) properties and are being assessed for their degree of biocompatibility.[94,95] The TPE properties of these materials arise from microphase-separation of the polystyrene chain segments within the polymer matrix providing physical cross-links, in analogy to the common block copolymer TPE. Consequently, these materials behave like covalently cross-linked (vulcanized) rubbers at room temperature, but they can be processed like thermoplastics at temperatures above the glass transition temperature of the polystyrene segments.

2.4 Dendrigraft Polymers

2.4.1 General Characteristics

These macromolecules have a dendritic architecture reminiscent of dendrimers and hyperbranched polymers, but are derived from polymeric building blocks rather than small molecule monomers. While the molecular weights attained for dendrigraft polymers can be much higher than for the other dendritic polymer families, their MWD typically remains relatively narrow ($M_w/M_n < 1.1$), and thus they are referred to as semi-controlled dendritic structures.[96] Synthetic schemes have been developed for the preparation of dendritic graft polymers by different methods including anionic, cationic, radical, and ring-opening polymerization. Three distinct methodologies can be distinguished in the literature, namely divergent *grafting onto*, divergent *grafting from*, and convergent *grafting through* techniques.

The divergent approach relies upon successive grafting reactions starting from a linear substrate (equivalent to the core in dendrimer syntheses). In the divergent *grafting onto* method polymeric side-chains are coupled with the substrate, while in the divergent *grafting from* method the side-chains are grown from initiating sites on the substrate. Successive grafting reactions lead to consecutive generations of branched polymers in both cases. The convergent *grafting through* methodology is a one-pot technique whereby building blocks are produced and coupled *in situ* to yield branched structures in a single reaction step. This represents the main advantage of the *grafting through* methods, in analogy to the hyperbranched polymer syntheses, as it requires less time, effort and resources to obtain high molecular weight dendritic structures. The *grafting onto* and *grafting from* methods, in

contrast, involve distinct steps of substrate functionalization, grafting, and product isolation for each generation.

2.4.2 Synthetic Strategies, Common Structures, and Properties

2.4.2.1 Divergent *Grafting Onto* Strategy

The first dendrigraft polymer syntheses were reported independently by two research groups in 1991. Gauthier and Möller developed a divergent anionic *grafting onto* method for the preparation of branched polystyrenes (PS) denominated arborescent polymers.[12] The term *arborescent* referred to the tree-like architecture of the molecules, with symmetric long branches. Tomalia et al., on the other hand, employed cationic polymerization in a similar divergent *grafting onto* scheme to synthesize branched polyethylenimines,[13] initially called Comb-burst® polymers. The term *dendrigraft polymers* has meanwhile become widely accepted to designate arborescent, Comb-burst®, and other related dendritic graft polymer architectures collectively. The divergent *grafting onto* strategy is represented schematically in Figure 2.9. Specific details of the anionic and the cationic grafting methods developed by Gauthier and Möller and by Tomalia et al., respectively, will be discussed in the subsequent sections.

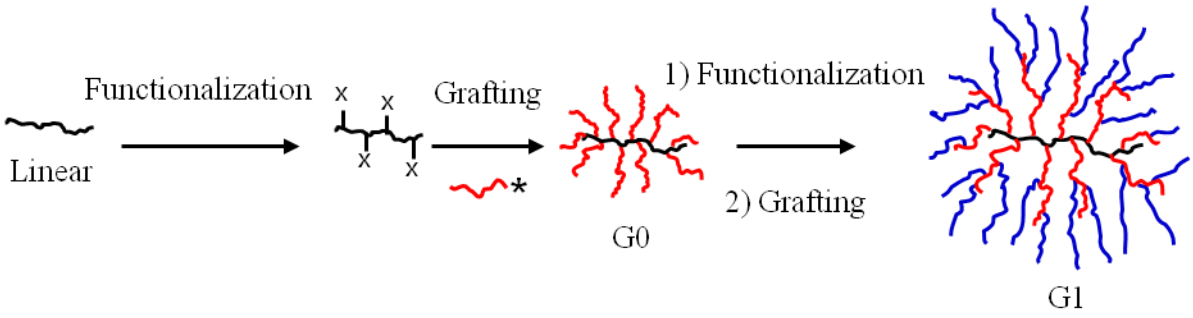

Figure 2.9 Schematic representation of the generation-based synthesis of dendrigraft polymers by a divergent *grafting onto* method.

Arborescent Polymers. The first grafting technique developed for the synthesis of arborescent polymers used chloromethyl coupling sites located on the phenyl pendants of PS substrates. Coupling 'living' polystyryl anions with the chloromethyl sites on the substrate thus resulted in a comb-branched, or generation 0 (G0) arborescent PS structure. Repetition of the functionalization and grafting reactions led to arborescent polymers of generations G1, G2, G3, etc. Efficient coupling with the substrate required 'capping' of the living chains with a single 1,1-diphenylethylene unit to suppress metal-halogen exchange side reactions. One of the major problems encountered in this approach was associated with the use of hazardous chloromethyl methyl ether for the introduction of the chloromethyl coupling sites on the substrate. This issue was solved in 2001, when Li and Gauthier developed an alternate grafting method based upon acetyl coupling sites (derived from acetyl chloride).[97] In this case, the living PS chains were capped with a few 2-vinylpyridine units prior to coupling with the acetylated substrate, and LiCl was added to suppress proton abstraction from the acetyl groups leading to chain termination. The synthetic paths for the preparation of G0

arborescent PS using both chloromethyl and acetyl coupling sites are compared in Scheme 2.14.

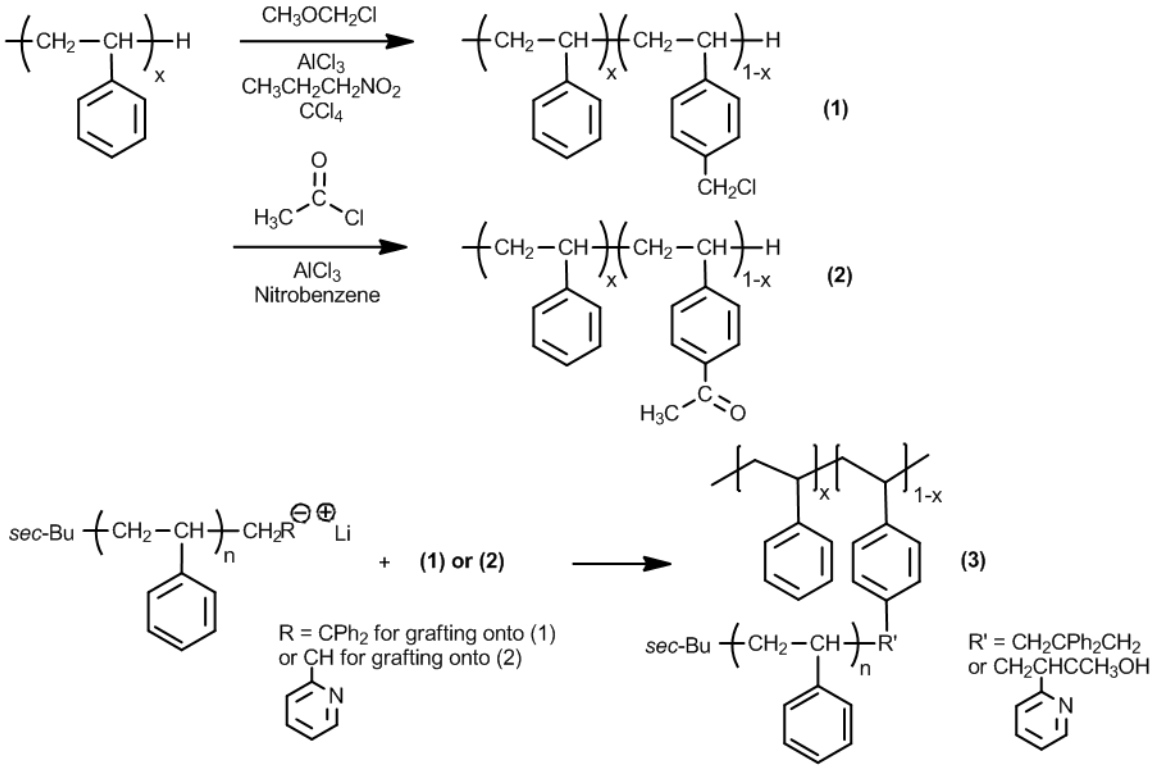

Scheme 2.14 Arborescent polystyrene synthesis: Linear substrate functionalization by chloromethylation (1) or acetylation (2), and coupling with living polystyrene to yield a G0 molecule (3).

The scope of the grafting methods initially developed for polystyrene was expanded over the years to the synthesis of arborescent copolymers, mainly by grafting a polymer with a different composition in the final reaction cycle. Copolymers with core-shell morphologies were thus synthesized by grafting living poly(2-vinylpyridine) (P2VP) chains onto chloromethylated or acetylated PS substrates.[98,99] Polystyrene-*g*-polyisoprene[100] and polystyrene-*g*-poly(*tert*-butyl methacrylate)[101] copolymers were also synthesized by a similar

approach. Alternatively, molecules with an inner P2VP shell embedded between a core and a corona of polystyrene were obtained by grafting a PS-*b*-P2VP block copolymer onto arborescent PS substrates.[102]

Depending on the molecular weight of the side-chains and the functionalization level of the substrate used in the reaction, very high overall molecular weights can be achieved in only a few grafting cycles. If the number of coupling sites (f) available per side-chain on the substrate and the molecular weight of the side-chains (M_{br}) remain constant for each cycle, the molecular weight (M) of an arborescent polymer can be calculated according to Equation 2.11.

$$M = M_{\mathrm{br}} + M_{\mathrm{br}}f + M_{\mathrm{br}}f^2 + M_{\mathrm{br}}f^3 + \ldots = \sum_{\mathrm{x}=0}^{\mathrm{G}+1} M_{\mathrm{br}}f^{\mathrm{x}} \qquad (2.11)$$

Three key parameters characterize the success of a grafting reaction: The grafting yield (G_y), defined as the fraction of side-chains generated in the reaction becoming attached on the substrate; the branching functionality (f_w), corresponding to the number of chains added in a grafting reaction; and the coupling efficiency (C_e), which is the fraction of coupling sites grafted with side-chains. Arborescent polymers are typically synthesized from linear polymer building blocks having a molecular weight of about 5000 g/mol and substrates with target functionalization levels of ca. 25 – 30 mole %. This provides a large number of coupling sites on the substrate (10 – 15 per side-chain), while minimizing steric hindrance effects which would become more important at higher grafting densities. The grafting of coronal side-chains has been investigated for both long (30,000 g/mol) and short (5000 g/mol) chain segments, resulting in either star-like or crew-cut[103] architectures, respectively.

For increased side-chain lengths, the grafting yield and the coupling efficiency decrease due to enhanced steric crowding by the longer chains. The same effect also comes into play when grafting onto substrates of the upper generations. The small molecules used in the substrate functionalization process can easily diffuse on the periphery and the interior of the branched structures. The ability of polymeric chains to diffuse to the coupling sites located within the interior of the branched substrates decreases as their size increases, however, which reduces the grafting yield and the coupling efficiency. Typical values of grafting yield and coupling efficiency thus range from upwards of 90 % in G0 polymer syntheses, down to ca. 20 % for G4 polymers. Narrow MWD are maintained over successive grafting reactions, and the PDI sometimes even decreases marginally as a result of averaging of the side-chain length distribution. The molecular weight of these polymers can range from ca. 5×10^4 g/mol for G0 to over 10^7 g/mol for G4 polymers, but also depending on the length of the side-chains and the grafting density used in the synthesis.

The spherical topology of arborescent polymers is a consequence of the molecular weight of the polymer chains used in their synthesis: A prolate spheroid having at most a 3:2 axis ratio is expected for a G0 molecule (if it were to adopt a fully extended chain conformation) when grafting side-chains having the same molecular weight as the linear substrate (e.g. 5000 g/mol for both components). This changes to an increasingly spherical topology over successive grafting cycles, however (5:3 axis ratio for a G1 polymer, 7:5 for G2, and so on). This topology is reflected in the dilute-solution properties of arborescent polymers in terms of their scaling behavior (molecular weight dependence) for the second virial coefficient (A_2), the z-average translational diffusion coefficient (D_z), and the radius of gyration (r_g), which are all comparable to rigid spheres.[104] More recently it was shown

through small-angle neutron scattering measurements that the chain segment density of arborescent polymer molecules becomes relatively constant at their center after a few grafting cycles, but decreases according to a power law within their corona.[105]

Comb-burst® Polymers. The divergent *grafting onto* method suggested by Tomalia et al. for the synthesis of Comb-burst® polymers yields a molecular architecture similar to the arborescent systems, but these polymers are produced through cationic polymerization of 2-ethyl-2-oxazoline.[13] The side-chains inherently contain protected coupling sites which are activated by deacylation under acidic conditions. The secondary amine sites generated along the substrate polymer can be coupled with living poly(2-ethyl-2-oxazoline) in a predetermined molar ratio to control the branching density. Another possibility is through partial deacylation of a fraction of the secondary amine sites. Depicted in Scheme 2.15 is the cationic synthesis of Comb-burst® poly(2-ethyl-2-oxazoline), by initiation of the polymerization with methyl tosylate, as well as substrate activation and grafting to yield a G0 polyethylenimine (3).

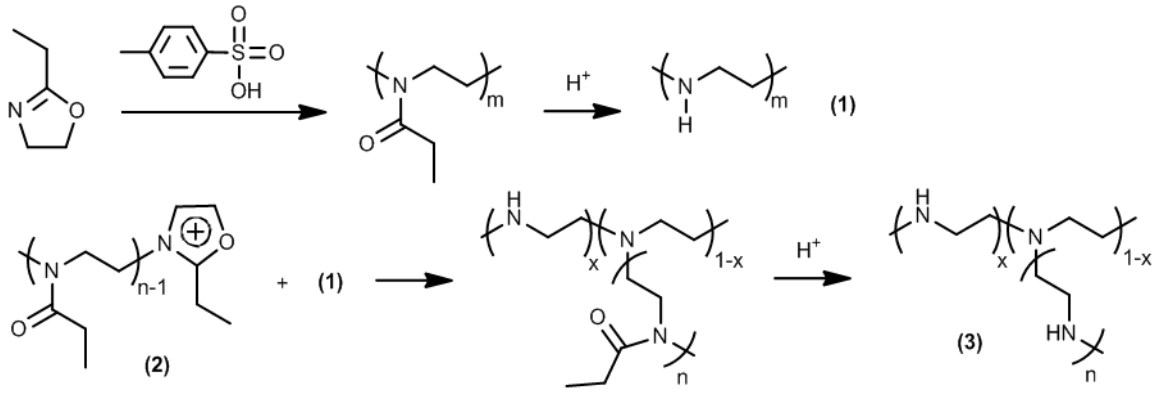

Scheme 2.15 Grafting of living poly(2-ethyl-2-oxazoline) (2) onto a linear polyethylenimine (1) to yield a G0 Comb-burst® polyethylenimine (3).

The number of repeating units (N_{RU}) and the molecular weight (M) of Comb-burst® polymers can be predicted from the number of coupling sites on the branches (N_b) and the core (N_c), the molecular weight of the core (M_c), the molecular weight of the repeating units (M_{RU}), and the molecular weight of the end-groups (M_z), according to the expressions in Equation 2.12.

$$N_{RU} = N_c\left(\frac{N_b^{G+1} - 1}{N_b - 1}\right) \quad M = M_c + N_c\left[M_{RU}\left(\frac{N_b^{G+1} - 1}{N_b - 1}\right) + M_Z N_b^{G+1}\right] \tag{2.12}$$

A series of Comb-burst® polyethylenimine was thus synthesized with a side-chain degree of polymerization increasing from 10 to 20 for the first two generations, and then maintained constant at 100 for the subsequent generations.[106] A geometric increase in molecular weight was observed as predicted by Equation 2.12, with grafting yield variations similar to those observed for arborescent systems.

2.4.2.2 Divergent *Grafting From* Strategy

In a divergent *grafting from* method, polymer chains are grown from a substrate acting as a polyfunctional initiator. This approach is particularly advantageous for the preparation of copolymers with core-shell morphologies, as these can be obtained simply through the addition of different monomers in the side-chain growth process. As with the *grafting onto* method, variations in the dimensions of the initiating core relatively to the side-chains, as well as the location of the initiating sites, can produce different topologies. Spherical molecules result when the core has dimensions comparable to the side-chains and the latter are evenly distributed around the core. If the degree of polymerization of the side-chains in the first grating cycle (G0 polymer synthesis) is significantly lower than that of the core,

cylindrical structures will result. A G0 (comb-branched) molecule exhibiting this topology is commonly referred to as a polymeric brush.

The divergent *grafting from* method suffers from a significant drawback in terms of structural characterization. In the *grafting onto* techniques, a sample of the side-chains can be removed for analysis prior to the grafting reaction. Unfortunately this cannot be done in the *grafting from* approaches, in analogy to hyperbranched polymer syntheses. Characterization of the side-chains is only possible if they can be cleaved from the substrate after the reaction. Another drawback of this method is that it often yields broadly dispersed products, due to the increased probability of side reactions and the influence of steric hindrance resulting in the retardation of propagation for some of the chains.

This approach was first developed by Six and Gnanou for the synthesis of star-like dendritic poly(ethylene oxide).[107] Analogous results have also been obtained using dendrimer-like multifunctional initiators;[108,109] however, we will focus on methods starting from linear macroinitiator substrates in this section. One such method was reported for the synthesis of arborescent polyglycidols, starting from a linear polyglycidol macroinitiator with anionic ring-opening polymerization.[110] The linear substrate was obtained by initiating the polymerization of glycidol acetal with potassium *tert*-butoxide, and treatments with formic acid and KOH/methanol/dioxane to deprotect the hydroxyl functionalities. The initiating sites were activated by treatment with potassium *tert*-butoxide, and glycidol acetal monomer was added to grow branches from the substrate and produce a G0 structure. Further reaction cycles led to arborescent polyglycidols of generations up to G2. The synthesis of a G0 arborescent polyglycidol starting from the polymerization of the acetal monomer is illustrated in Scheme 2.16 as an example.

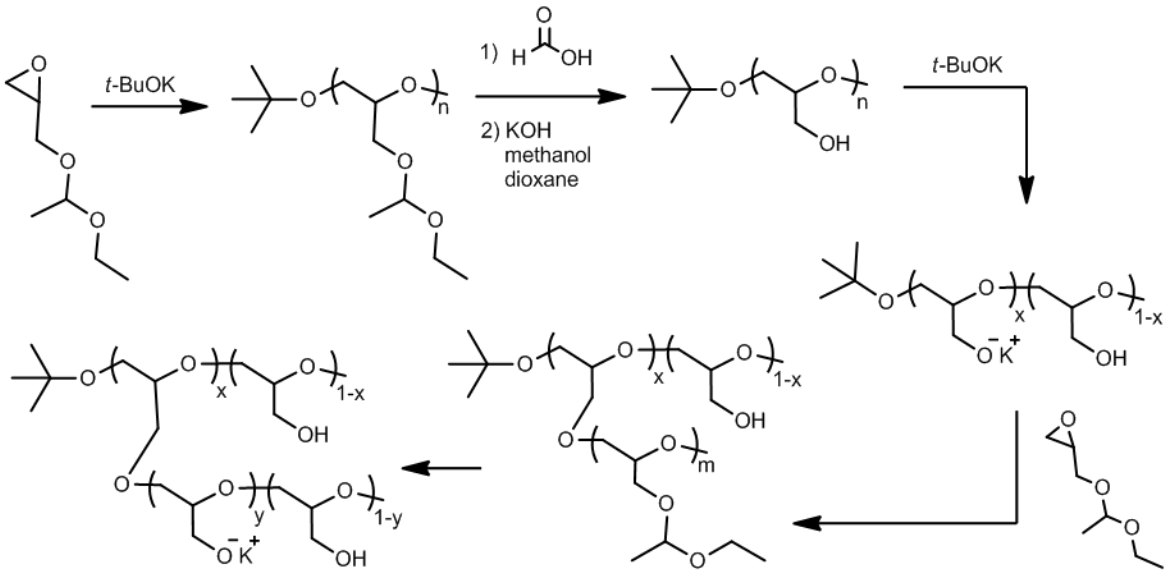

Scheme 2.16 Synthesis of a G0 arborescent polyglycidol molecule.

Relatively low PDI values were obtained in this synthesis (PDI ≈ 1.2 – 1.4), albeit with MWD broadening over successive generations. Substrate activation with *tert*-butoxide targeted a 10 % neutralization level, to provide adequate spacing for the side-chains, but much higher branching densities (reaching 90 %) were observed in practice. This is due to hopping of the potassium counterions among the hydroxyl groups on the macroinitiator substrate, leading to chain growth from most of the deprotected functional groups. Monomer conversion reached 99 % during the first two grafting cycles, but decreased to 27 % for the G2 polyglycidol due to poor solubility of the graft polymer.

An approach similar to the previous divergent *grafting from* method also served to synthesize dendrigraft poly(L-lysine) by ring-opening polymerization,[111] styrene homopolymers and styrene-methacrylate copolymers by a combination of stable free-radical

polymerization and atom transfer radical polymerization (ATRP),[112] and copolymers of 2-hydroxyethyl methacrylate with styrene, or *tert*-butyl methacrylate by ATRP.[113]

Another embodiment of this technique was used for the synthesis of high molecular weight, low PDI arborescent polymers by Yuan and Gauthier in a one-pot synthesis of arborescent polystyrenes.[114] In this case, the anionic copolymerization of styrene (Sty) and 1,3-diisopropenylbenzene (DIB) initiated by *sec*-butyllithium was carried out in a semibatch process. Following complete monomer conversion, the chains were terminated and the isopropenyl moieties of the DIB units were activated with *sec*-butyllithium to produce a polyfunctional anionic macroinitiator without additional workup. Further styrene-DIB monomer mixture additions yielded a comb-branched (G0) copolymer, and subsequently G1 arborescent polystyrene molecules after activation and styrene addition. An illustration of this synthetic technique is provided in Scheme 2.17.

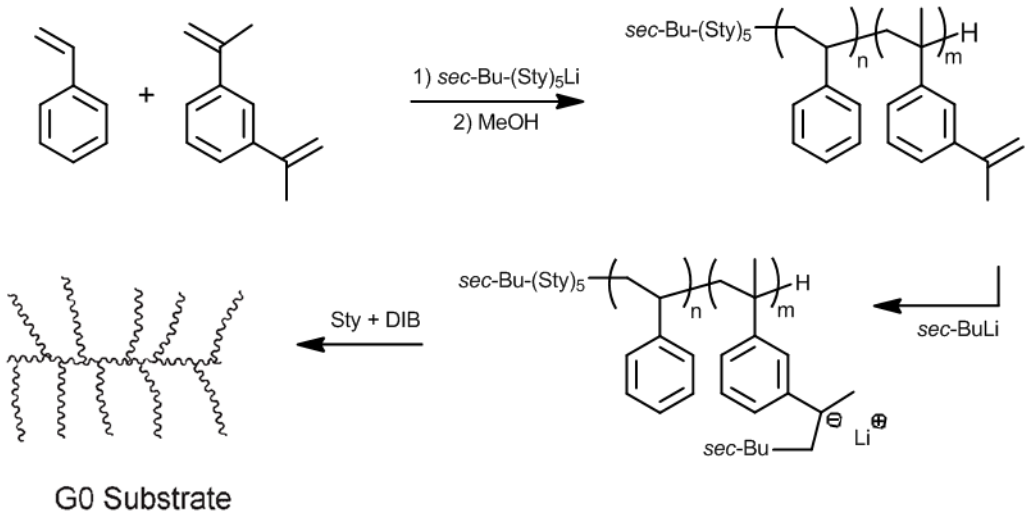

Scheme 2.17 One-pot synthesis of arborescent polystyrene by a semibatch process with mixed monomer additions.[114]

Control over the side-chain molecular weight was achieved through the amount of monomer added to the activated substrates. The PDI values obtained ranged from 1.1 – 1.3 for molecular weights (M_w) reaching 7×10^6 g/mol. The same technique was also used to synthesize arborescent copolymers, by adding other monomers in the last side-chain growth cycle, namely arborescent polystyrene-*g*-poly(*tert*-butyl methacrylate) and polystyrene-*g*-[polystyrene-*b*-poly(2-vinylpyridine)] copolymers.[115]

Hybrid techniques combining *grafting onto* and *grafting from* methodologies have also been investigated for arborescent polymer molecules, by introducing functional groups at the chain ends of an arborescent polymer and activating them to grow a corona of polymer segments with a different chemical composition.[116]

2.4.2.3 Convergent *Grafting Through* Strategy

The convergent grafting through method is the least time- and resource-intensive approach for the synthesis of dendrigraft polymers. This self-branching system, carried in a one-pot-reaction, makes use of bifunctional monomers carrying a vinyl group and a second functional group capable of coupling *in situ* with the living chains. The bifunctional monomer can be added slowly at different stages of the reaction to induce the formation of branching points, while maintaining relatively low polydispersity indices typical for dendrigraft polymers.

This technique was first developed by Knauss et al. for the convergent anionic synthesis of polystyrene. Upon addition of a bifunctional monomer such as 4-(chlorodimethylsilyl)styrene[117] or vinylbenzyl chloride[118] to living polystyryllithium, a portion of the living chains undergo nucleophilic substitution at their chloromethyl or chlorosilyl site, while propagation may take place via the vinyl group. The branched

macromonomers generated in the coupling reaction quickly become sterically crowded, which limits the attainable molecular weight, but this growth mechanism is also believed to be at the origin of the relatively narrow MWD observed in some cases (PDI ≈ 1.1 – 1.8). To facilitate the attainment of higher molecular weights and branching functionalities, styrene monomer can be added along with the bifunctional monomer to introduce polystyrene segment spacers between the branching points, thus reducing the influence of steric crowding on the branching process. In the absence of polystyrene spacers, the branched structures obtained are closer to star-branched polymers than to dendrigraft polymers. A polymerization process with styrene addition to produce spacers between the branching points is depicted in Scheme 2.18.

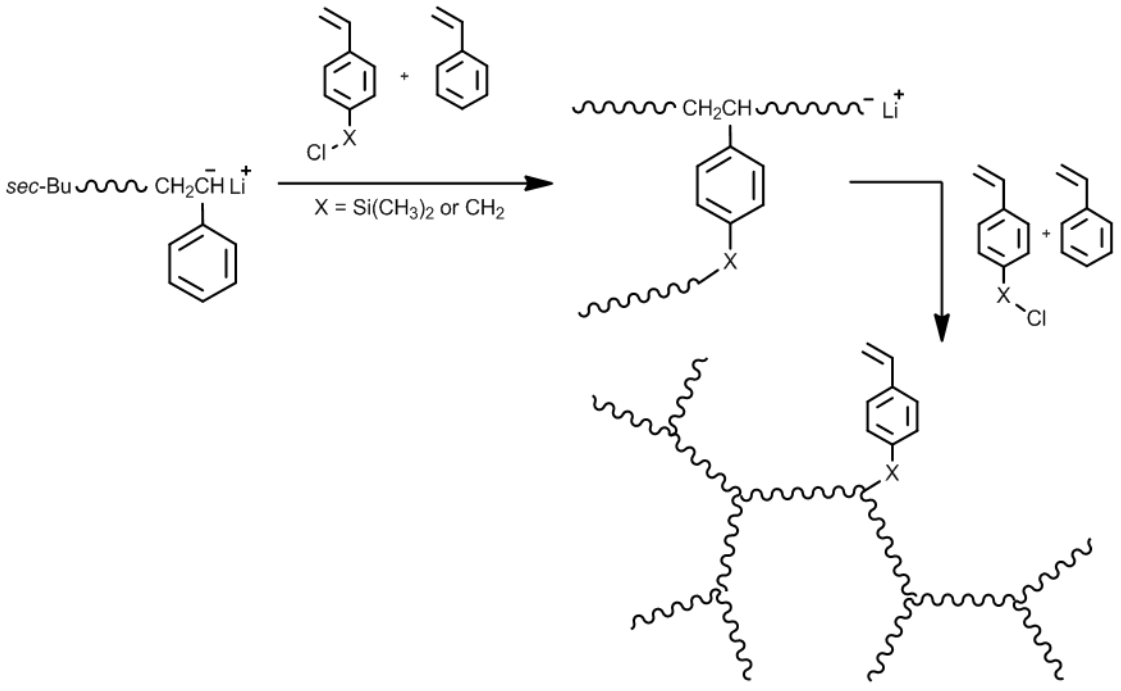

Scheme 2.18 One-pot *grafting through* method to for the convergent synthesis of dendrigraft polystyrene.

The branched structure of dendrigraft polymers obtained by the convergent *grafting through* method can be described in terms of an average generation number (G) determined from Equation 2.13, where M_G and M_0 correspond to the M_n for the graft polymer and the primary chains (before addition of the coupling agent), respectively, and M_B is the molecular weight of the structural unit derived from the coupling agent.

$$G = \log(M_G) - \log(M_0 + M_B) \tag{2.13}$$

The bifunctional monomer approach, with continuous addition of the monomer and the branching agent, is analogous to hyperbranched polymer syntheses using the inimer technology, but the MWD obtained are significantly narrower: The PDI values reported vary from 1.2 – 2.0, albeit the molecular weight is also limited to ca. 10^5 g/mol.[117,118]

A similar approach was used to construct a unique triblock copolymer having dendritic termini connected by linear segment. The synthesis of the dendritic-*block*-linear-*block*-dendritic polystyrene, referred to as "pom-pom" structure due to its dumbbell-like shape, results from a convergent anionic polymerization procedure using dichlorodimethylsilane as a coupling agent.[119]

2.4.3 Applications and Recent Trends

Considering the versatility of dendrigraft polymer syntheses, it is relatively easy to introduce features in the molecules of interest for specific applications. Since the chain segments of dendrigraft polymers are covalently bonded, copolymers with amphiphilic character behave like unimolecular micelles that provide an interesting basis for comparison with regular micelles. The self-assembly of block copolymers into micelles under selective solvency conditions is indeed concentration-dependent, requiring a minimum concentration (the

critical micelle concentration, CMC) which is non-existent for unimolecular micelles. Thus depending on the specific application targeted, the dynamic character of block copolymer assemblies and their sensitivity to solvency conditions may be problematic, for example when trying to load host molecules within their core.

The core-shell morphology of amphiphilic dendrigraft polymers, and the ability to control their characteristics (hydrophobic core size, hydrophilic corona thickness) independently, provides a wider range of structures than can be achieved for block copolymer micelles. A good example of this is arborescent amphiphiles incorporating a hydrophobic arborescent polystyrene core and a corona of polar P2VP segments.[98,99] These copolymers are interesting in terms of their solubilization properties[99] and their ability to host and slowly release hydrophobic compounds.[120] *In vitro* loading and release studies of indomethacin and lidocaine from PS-*g*-P2VP arborescent copolymers of different generations showed that the release profiles for the model drugs displayed an initial burst release, followed by more gradual release over extended time periods. The release profiles obtained for indomethacin and lidocaine from different host PS-*g*-P2VP copolymers are compared in Figure 2.10 as an example.

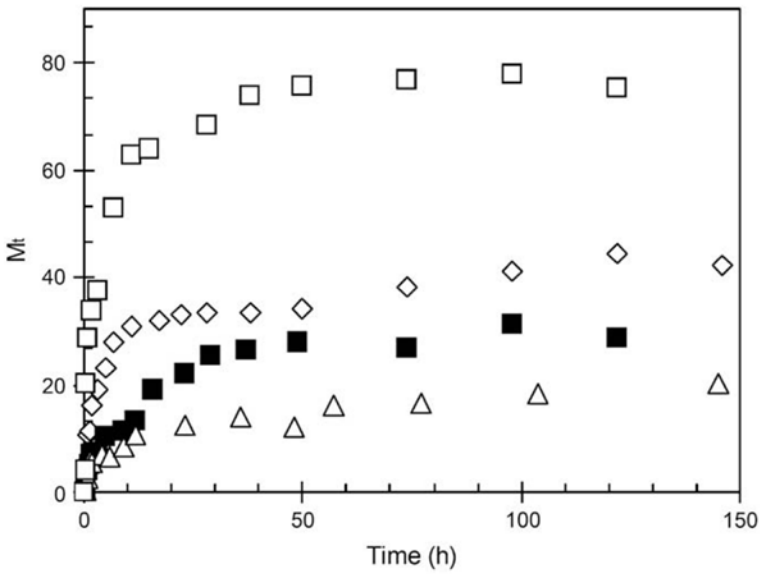

Figure 2.10 Percent mass fraction of lidocaine released from an arborescent PS-*g*-P2VP G1 (□) copolymer and of indomethacin released from G1 (◇), G2 (■), and G3 (△) copolymers.[120]

It is clear from Figure 2.10 that the release from upper generation copolymers is more gradual, which can be attributed to the increased branching functionality of the molecules. It should also be noted that ionic interactions are present between the carboxylic acid group of the drug and the nitrogen atom of the pyridine pendants, which explains the much slower overall release rate for indomethacin as compared to lidocaine.

The usefulness of analogous arborescent copolymers characterized by a layered architecture, with an inner shell of P2VP segments, has been recently demonstrated as unimolecular templates for the preparation of metallic nanoparticles in non-polar solvents.[102] Metallic nanoparticles are being intensively investigated for applications including imaging agents, microelectronics, separation science, catalysis, and biological uses such as targeted labeling and delivery systems or cell therapy. Arborescent copolymers with reverse micelle

characteristics are obtained by grafting living PS-*b*-P2VP block copolymers onto arborescent PS substrates according to the methods described previously.[12,97] A schematic representation of the synthesis of a template molecule, its loading with a metallic salt, and the reduction of the salt to metallic nanoparticles is provided in Figure 2.11. Since the living end of the block copolymer serving as side-chains is located at the end of the P2VP segment, a core-shell-corona copolymer architecture is obtained, with a corona of polystyrene chains providing compatibility with non-polar organic solvents, an inner shell of P2VP, and a PS core. The P2VP shell enables the loading of polar compounds, for example through coordination with transition metals or, for charged species, through ionic interactions. This templating approach to the preparation of metallic nanoparticles has so far been explored using $HAuCl_4$.

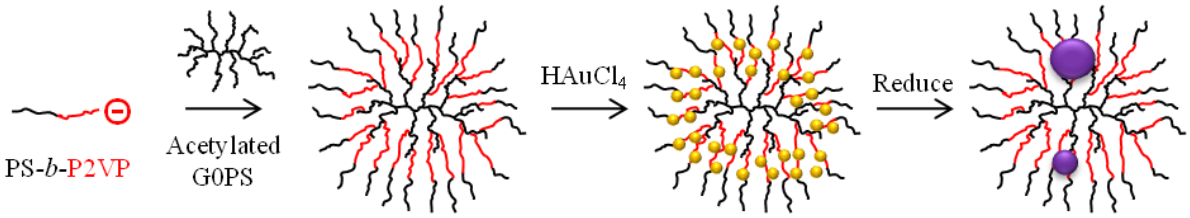

Figure 2.11 Synthesis of an arborescent copolymer, G0PS-*g*-(P2VP-*b*-PS), its application to templating $HAuCl_4$ deposition, and reduction to gold nanoparticles.

The metals loaded in the arborescent templates may be easily viewed by transmission electron microscopy (TEM) as shown in Figure 2.12. The generation number of the PS-*g*-(P2VP-*b*-PS) templates governs the distribution of the metallic species within the molecules: The G0 templates (Figure 2.12a), having an ill-defined core comprised of a single linear PS chain, provide a uniform distribution of gold, while the G2 species (Figure 2.12b),

incorporating a larger non-coordinating G1PS core, display a metal-depleted region at the center of the nanoparticles.

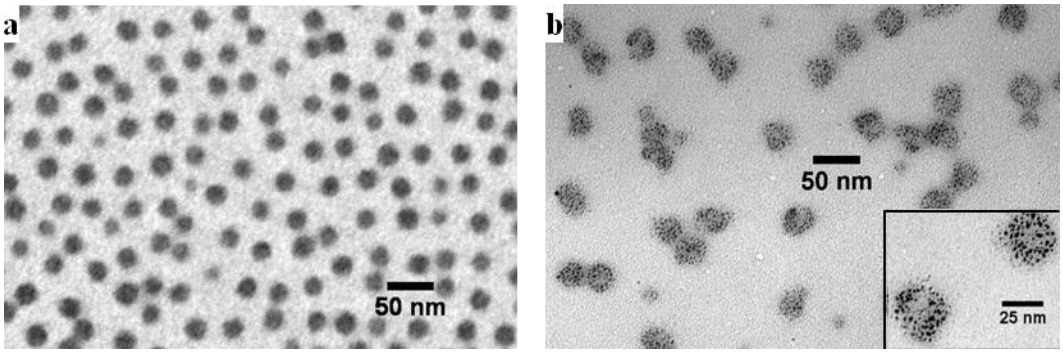

Figure 2.12 TEM micrographs for (a) PS-*g*-(P2VP-*b*-PS) and (b) G1PS-*g*-(P2VP-*b*-PS) loaded with $HAuCl_4$.[102]

The high molecular weight, compact structure, and spherical topology of arborescent polymers confers them a low viscosity as compared to their linear counterparts. These characteristics are also attractive for their potential application as polymer processing additives. It has indeed been demonstrated that branched polymers with a high degree of symmetry have a greater tendency to diffuse to the surface of polymer blends,[121] so they can interact more efficiently with the die wall surface and modify the processing characteristics of the host polymer. Linear fluoroelastomers have been instated as polymer processing additives for many years due to their ability to induce slippage at the walls of processing equipment, which leads to reduced melt defects and energy consumption. For that reason fluorine-containing arborescent polystyrene-*g*-polyisoprene copolymers, combining the inherent properties of branched polymers with the surface energy reduction of fluorinated polymers, have been investigated as processing aids.[121] Arborescent copolymers with a PS

core and polyisoprene (PIP) side-chains were synthesized by a divergent *grafting onto* method,[122] and hydrosilylated with a fluorohydrosilane as depicted in Scheme 2.19.

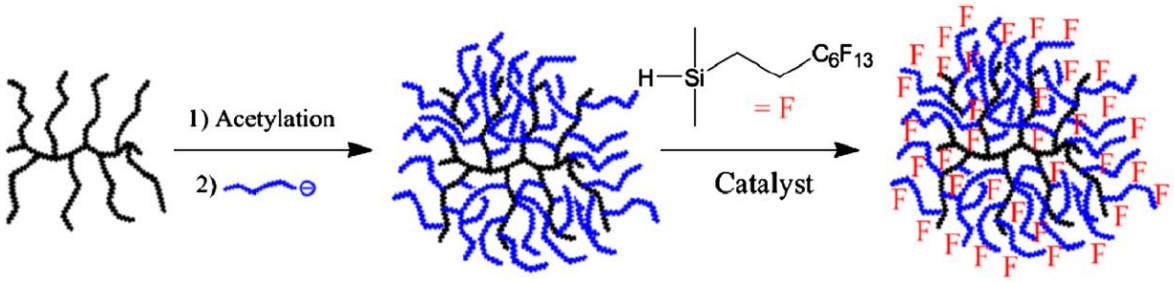

Scheme 2.19 Synthesis of G0PS-*g*-PIP copolymer followed by hydrosilylation with a fluorohydrosilane for use as a processing aid.[121]

Capillary rheometer extrusion tests were performed by monitoring the applied pressure and the extrudate appearance as a function of the deformation (shear) rate, for blends of the arborescent copolymers at 0.5 % w/w with a commercial linear low density polyethylene (LLDPE) resin. In all cases the backpressure was reduced for the blends as compared to virgin LLDPE; however, the performance of the arborescent additives was inferior to a commercial additive used for comparison.

2.5 Concluding Remarks

The dendritic polymer literature reviewed herein provides compelling evidence that these materials are a unique and versatile class of branched polymers. The synthesis of dendritic macromolecules can be accomplished by numerous methods allowing for specific tailoring of the characteristics of the polymer, to yield desired properties or functionality. While some of the procedures reported are quite intricate, requiring multiple cycles of synthetic steps and work-up, one-pot syntheses have also been developed for hyperbranched and dendrigraft polymers, making these materials more viable for (large scale) commercial production and industrial applications.

The low viscosity[123] of dendritic polymers is interesting in terms of their potential applications as rheological (or viscosity) modifiers and/or as polymer processing aids. Further, the multiple chemical functionalities available for these materials offers a wide range of applications in different areas including stabilized catalysts, biological markers, sensors, and micelle mimics.

Dendritic polymers have been the focus of a great deal of application-oriented research in recent years. The number of United States patents related to dendritic polymers issued between 1990 and 1999 totaled 62, and only 3 patents were issued prior to 1990. From year 2000 until July 2010, approximately 240 additional dendrimer-related patents were issued, that is almost four times the number issued in the previous decade.[124] The number of patent applications relating to dendritic species over the same period totaled approximately 430, demonstrating that this field is receiving even more attention than the number of already issued patents suggests. Recent emphasis on more exotic applications within the fields of nanotechnology, pharmaceuticals, and biotechnology has resulted in rapid growth in the

number of filings. Further investigation into these fields as well as the new synthetic approaches and hybrid methodologies being developed will certainly broaden the scope of dendritic polymer applications in the future.

Chapter 3

Literature Review:
Polymeric Nanoparticle Templates

3.1 Introduction

A significant amount of attention has focused on metallic nanoparticle research over the last two decades due to the unique properties displayed by these nano-sized species. Many methods and procedures have been developed to construct metallic nanoparticles, one of the most versatile methods being the templating approach. This Chapter will focus on methods reported in the literature for the preparation of metallic nanoparticles using polymeric templates and the nanoparticles that result.

The templating of metallic nanoparticles with polymers offers benefits as compared to bare nanoparticles typically prepared by a colloidal approach.[1,2] While the polymeric scaffold can be removed following nanoparticle construction,[3] sacrificing the polymer may not be a desired nor a necessary step. Indeed, polymer-templated nanoparticles can be tuned for compatibility with their environment (e.g. colloidal stability) and to control the surface chemistry (e.g. accessibility) of the nanoparticles, which is of utmost importance for catalytic applications.[4] Also important for nanoparticle catalysts is recovery. The removal of contaminants such as inorganic components and the reuse of such catalysts is often improved for polymer-stabilized systems.[5]

The essential attribute that any template must possess is the ability to preferentially accommodate the loading of species within a defined region of the scaffold. This feature can be selected or targeted during template synthesis and/or template formation, for example through the selection of suitable solvency conditions to form a micellar structure. Nanoparticle templating with polymers can be divided into two categories: unimolecular and intermolecular templates. The unimolecular template is a self-contained micellar entity with intramolecular amphiphilic characteristics. As such, the unimolecular template is a covalently

bound structure which does not rely on association or interactions with other species to form a nanodomain over which guest species can be housed or coordinated. Conversely, intermolecular templates are multi-molecular entities which rely on the association of species to form an organized superstructure containing a defined loadable region or phase. The difference between multi-molecular and unimolecular micelle species is illustrated in Figure 3.1.

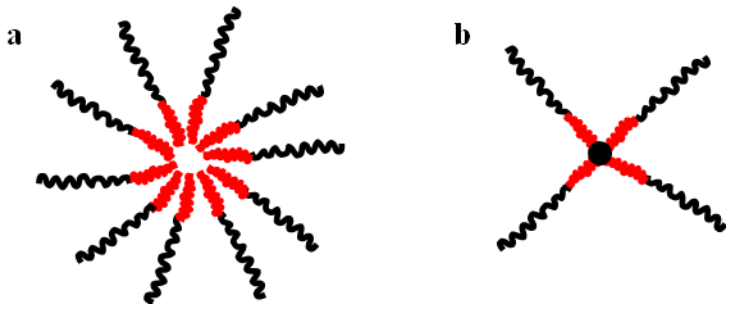

Figure 3.1 Graphical representation of (a) a multi- or inter-molecular micelle and (b) a unimolecular micelle.

As seen in Figure 3.1, the multi-molecular micelle is formed from separate entities while the unimolecular micelle is its own covalently bound species. In some cases, there is cross-over between these categories, as unimolecular species can be created by crosslinking or coupling polymer chains that have self-assembled; imparting covalent stabilization to the intermolecular template essentially makes it unimolecular. The intermolecular micelle approach to templating metallic nanoparticles has been thoroughly investigated over the past 15 years. It relies upon the properties of amphiphilic species forming micelles under selective solvency conditions to form a coordinating domain within the superstructure. This has been accomplished for small molecule amphiphiles,[6] copolypeptides,[7] and block copolymers.[8,9]

Above a certain concentration known as the critical micelle concentration (CMC), regular micelles can form from these compounds in polar solvents, while reverse micelles form in non-polar environments. An important criterion for micelle formation is the preferential solvation of one of the components of the amphiphile. In regular micelles, the hydrophilic segments are more soluble and thus form the corona, while reverse micelles are formed in non-polar environments whereby the hydrophilic segments are hidden within the core.

The well-organized structure that results from micelle formation provides a loadable region within the micelle core. Reverse micelles can house polar species such as metallic salts within their core, given the availability of appropriate binding or coordination sites. Systems such as this have been successfully used for the assembly of many metallic nanostructures, some of which will be reported herein. Amphiphilic diblock copolymers have received particular attention for this application.

Amphiphilic block copolymers have the ability to assemble into different topologies such as spheres, cylinders, or lamellae, and can display long range order with body centered cubic or hexagonal packing in the solid state under the right conditions. The morphologies formed depend on the overall polymer chain length, the respective length of each block, the chemical nature of the segments, and the solvency conditions. Tailoring the polymer and the environment thus provides control over the micellar structure and the location and distribution of nanoparticles within the template.

Much of the initial research in this area focused on micelles containing polyvinylpyridine segments, due of their ability to coordinate with polar compounds through interaction with the nitrogen atom located within the pyridine group.[10] Regular micelles can

thus be formed in polar solvents from block copolymers containing P4VP and PS[9] or PEO segments,[11] but also from copolymers of PS and poly(acrylic acid)[12] or poly(methacrylic acid).[13] A wide range of other polymers can form micelles and may be suitable for nanoparticle templating, either within intermolecular (micellar) templates or unimolecular templates.[14]

Unimolecular templates must also have amphiphilic properties or selective complexation abilities to enable loading, and are therefore commonly referred to as unimolecular micelles. While one region of the template participates in complexation, the other serves to stabilize the entity in the surrounding environment. This can be achieved through monomer selection, the order of monomer addition during polymerization, and/or selection of the proper type of polymerization technique. The trait distinguishing unimolecular micelle templates from their intermolecular analogue is the covalent attachment of copolymer building blocks, which creates a predefined loading region within each macromolecule.

One of the most original forms of unimolecular templates is created through the formation of micelles from linear amphiphilic chains, followed by crosslinking to afford covalently bound micelles. The crosslinking step can be performed *in situ* during polymerization by the addition of a multi-functional coupling agent.[15] Dendritic polymers are another type of unimolecular template providing branched structures with spherical core-shell (CS) or core-shell-corona (CSC) morphologies. Their synthesis can be tailored to place hydrophilic segments on the periphery[16] or within the core[17] of the structure to create regular or reverse unimolecular micelles, respectively. Dendrimers, hyperbranched species, arborescent polymers and, on a larger scale, networks of amphiphilic polymers[18] have all

been successfully applied as unimolecular nanoparticle scaffolds, some of which will be reviewed in this Chapter.

One distinct advantage of unimolecular templates is that their covalent architecture eliminates problems related to concentration. Micellar systems rely on an onset concentration (the CMC) for chain association and superstructure formation. A drop in concentration below the critical level can thus jeopardize the structural integrity of the template and its loading capability due to instability in dilute conditions. Additionally, changes in solvent quality, specifically selectivity to one of the polymer segments, can drastically change micellar arrangement or even dissolve the entire micelle.

The body of work described in the subsequent chapters of this Thesis is focused on the synthesis and the characterization of unimolecular micelles used to prepare metallic nanoparticles. As such, this review chapter will provide a summary of reported methods and strategies for polymeric templating of metallic nanoparticles. More specifically, the use of unimolecular and intermolecular polymeric structures for metallic nanoparticle construction will be discussed. Included will be details on the synthetic procedures employed and the resultant characteristics of the polymer scaffolds and metallic nanoparticles. Particular attention will be paid to unimolecular systems with branched architectures and using nitrogen-containing block copolymers to serve as sites for metal coordination.

3.2 Block Copolymer Micelle Templates

It has been long been established that species containing both hydrophobic and hydrophilic segments can associate under selective solvency conditions at certain concentrations. The two segments can be comprised of a single ionic group attached to a nonpolar chain (e.g. aliphatic, as in the case of surfactants), or two long polymer chains joined together as in block copolymers. In either case, regular or reverse micelles can be formed in polar or non-polar solvents, respectively. This process is driven by the preferential solvation of one of the segments.

Even if preferential solvency is achieved, a minimum concentration of amphiphiles must be present (CMC) below which the amphiphiles exist as non-interacting species. Even above the CMC, non-associated species are present and a dynamic equilibrium exists between these molecules and the ones within the micelles. The formation of micelles from block copolymers is illustrated in Figure 3.2, for an environment leading to preferential solvation of the polymer segment represented by the solid line. Also shown in Figure 3.2 is a depiction of the concentration dependence of polymer amphiphiles either in solution or in the associated (micelle) state.

As shown in Figure 3.2, spherical micelles are formed with the insoluble segment creating a compact core, while the soluble segments form the surrounding corona allowing the aggregated structure to remain soluble. For a regular micelle, the polar segments form the corona and the hydrophobic segments aggregate within the core of the micelle, while in non-polar solvents, the opposite occurs and leads to the formation of a reverse micelle.

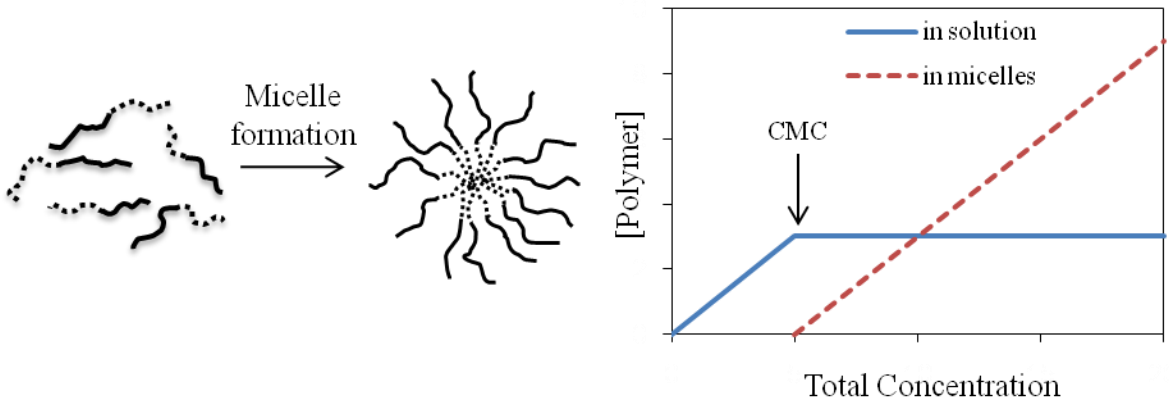

Figure 3.2 Micelle formation from diblock copolymers (left) and concentration dependence of the self-assembly in a selective solvent (right).

The self-assembly process can produce a number of other interesting superstructures including cylinders, vesicles, or large compound micelles. The topology of the superstructures can be investigated in solution by dynamic light scattering measurements[19] or with microscopic techniques, as will be shown in this Chapter. These structures can also form larger scale hierarchical assemblies in the solid state. For example, spherical micelles can organize into arrays with cubic packing (face- or body-centered), cylinders can pack hexagonally, or the block copolymers can arrange into bicontinuous gyroid or lamellar structures.[20] Some of these structures are illustrated in Figure 3.3.

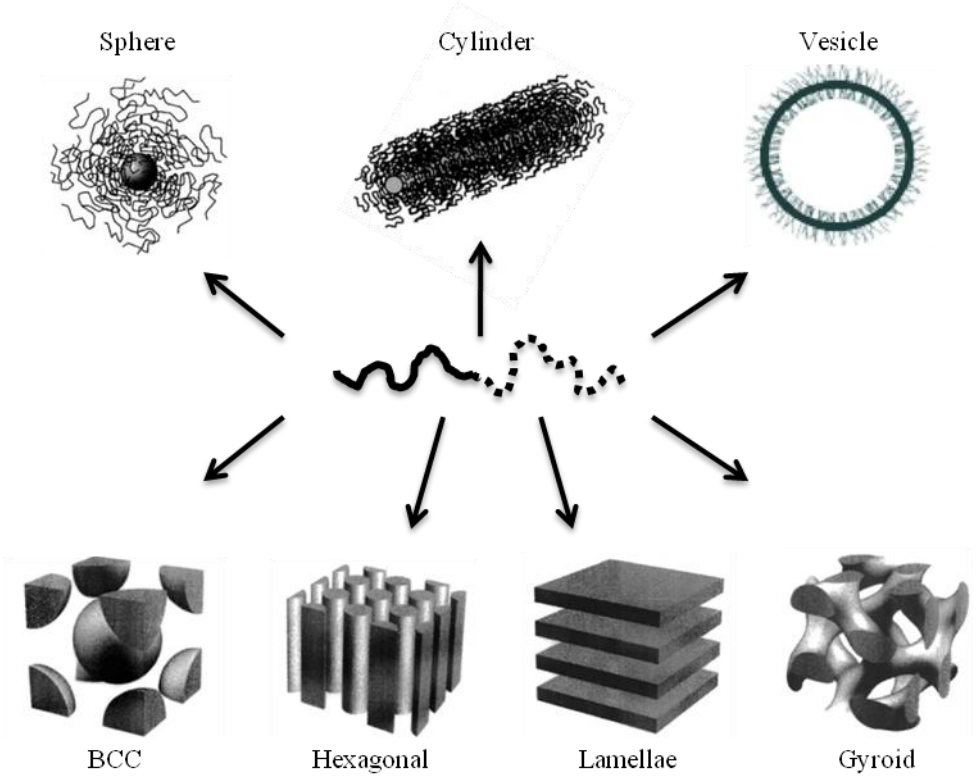

Figure 3.3 Common morphologies for phase-separated diblock copolymers.[20]

The self-assembly of amphiphilic block copolymers is for the most part governed by the chemical make-up of the segments, the respective lengths of each block, and segmental incompatibility.[21] For charged systems (incorporating a polyelectrolyte segment), the ionic strength is also an important factor.[21] Segmental incompatibility, or the degree of immiscibility, is influenced by solvent quality and is characterized by the Flory-Huggins interaction parameter (χ). The interactions of each block with the solvent as well as between each block must be considered. This concept is not limited to diblock copolymers, as similar morphologies have also been observed for triblock terpolymers.[22–24] Further, with increased variability in the make-up of triblock terpolymer systems, more complex and intricate

structures have been discovered.[25] This is due to a greater number of interaction parameters resulting in a larger variety of morphologies being formed.

Since the morphology type can be controlled, along with the size of the domains, block copolymer micelles are an attractive method for nanoparticle construction. Some of the original research and interesting structures observed from metallic nanoparticle templating with block copolymers will be reviewed in this section. Due to the large body of work that has been published in this area, the templating of gold nanoparticles with vinylpyridine-based polymers will be the focus of the review.

3.2.1 Block Copolymers Containing Pyridine Moieties

Polyvinylpyridines are versatile building blocks as their synthesis is well-controlled, they have the ability to form complexes with metallic compounds, and their hydrophilicity can be tailored. Micelles formed from diblock copolymers of polystyrene (PS) with poly(2-vinylpyridine), P2VP, or poly(4-vinylpyridine), P4VP, were first investigated as metallic nanoparticle templates beginning in the mid-1990s by various researchers. The amphiphilic properties of the PS and polyvinylpyridine blocks allow for micelle formation, both regular and reverse, depending on the solvency conditions and the degree of pyridine quaternization used. The pyridine moiety has a strong metal-chelating ability at its nitrogen atom and is able to complex many metallic salts or acids.

The synthesis of block copolymers containing PS and polyvinylpyridine segments is typically carried out by anionic polymerization to produce narrowly dispersed polymers with easily controlled segment lengths. PS-*b*-P2VP and PS-*b*-P4VP are commonly synthesized at –78 °C using *sec*-butyllithium (*sec*-BuLi) as initiator. Lithium chloride[3] or DPE[17] addition

prior to 2VP is used to attenuate the reactivity of the polystyryl anion and prevent side reactions. PS-*b*-P4VP has also been synthesized in tetrahydropyran by gas phase addition of the monomers.[26]

While the properties of PS-*b*-P2VP and PS-*b*-P4VP are very similar, the 4VP analogue has been said to have stronger interactions with metallic compounds due to the *para* position of the nitrogen atom relative to the polymer backbone making it less hindered than in 2VP.[11] However some preference has been given to P2VP, as its anionic polymerization can be performed in more convenient organic solvents (e.g. tetrahydrofuran) and yields narrower molecular weight distributions.

The groups of Möller[10] and Antonietti[27] were among the first to successfully demonstrate the use of PS-*b*-P2VP and PS-*b*-P4VP, respectively, as reverse micelle nanoparticle templates. Möller showed that PS-*b*-P2VP micelles with comparable block lengths, after loading with tetrachloroauric acid ($HAuCl_4$) in toluene, exhibited a spherical micelle morphology that was maintained even with changes in concentration. This contrasted with the neutral unloaded micelles, which displayed a transition from spheres to cylinders as the concentration was increased beyond 0.2 % (2 mg/mL).[10] For an asymmetric diblock copolymer (M_n^{PS} = 7900 g/mol, M_n^{P2VP} = 34,900 g/mol) spherical domains also formed, but only at certain $HAuCl_4$ loading levels: Spherical topologies were obtained at ionization levels of 70 %, while cylindrical micelles were observed at 30 % ionization.[28]

Antonietti observed similar spherical topologies after loading $HAuCl_4$ in PS-*b*-P4VP.[27] Of further interest is the fact that Antonietti investigated the loading of these block copolymers in THF, which is a non-selective solvent; it was found that micellization was

induced in THF after the metal salt uptake. Conversion of the metallic salt to elemental gold with strong (fast) homogeneous reducing agents such as $NaBH_4$ yielded multiple small gold nanoparticles within each micelle core. Slower heterogeneous reduction with hydrazine led to nucleation of the nanoparticles within the micelles to form larger species. Similar morphologies were observed for the loading of $Pd(OAc)_2$ into PS-*b*-P4VP.[2] Möller came to similar conclusions for the PS-*b*-P2VP system.[10] Figure 3.4 shows transmission electron microscope (TEM) micrographs for $HAuCl_4$ loaded within PS-*b*-P2VP micelles (Figure 3.4a) as well as the nanoparticles resulting from solution reduction with a strong ($NaBH_4$) and a weak (hydrazine) reducing agent. The results observed by TEM analysis were identical for both PS-*b*-P2VP and PS-*b*-P4VP micelle systems.

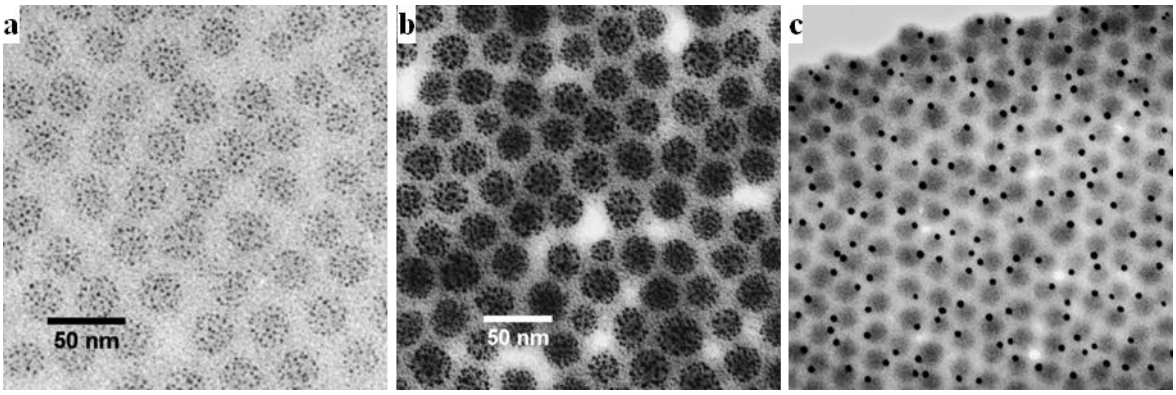

Figure 3.4 TEM micrographs for (a) $HAuCl_4$ loaded in PS-*b*-P2VP micelles,[8] (b) after reduction with $NaBH_4$,[20] and (c) after reduction with hydrazine.[20]

The reverse micelles actually become labile when subjected to polar solvents such as methanol or ethanol, which are selective for the metal-coordinated polyvinylpyridine segments. It has been shown that films of metal-loaded reverse micelles can undergo phase inversion to regular micelles when submerged in an alcohol solution. Both PS-*b*-P2VP

loaded with $HAuCl_4$[29] and PS-*b*-P4VP loaded with silver acetate[30] were reported to have switching nanopatterns as shown in Figure 3.5 and Figure 3.6, respectively.

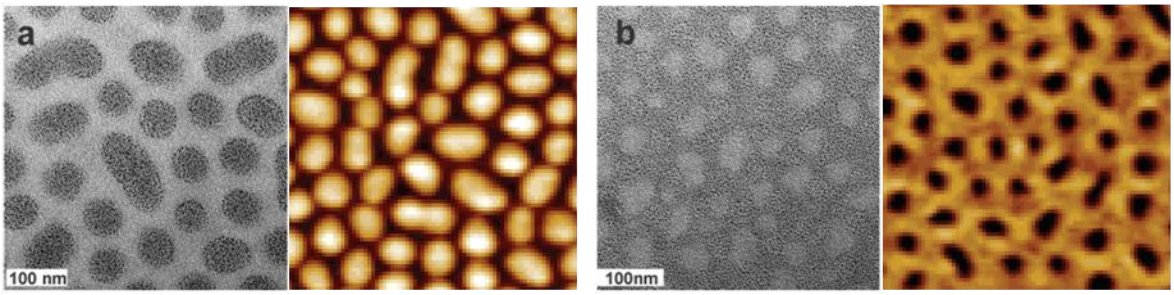

Figure 3.5 TEM and AFM images for PS-*b*-P2VP film-loaded with $HAuCl_4$: (a) cast from toluene and (b) following film treatment with methanol.[29]

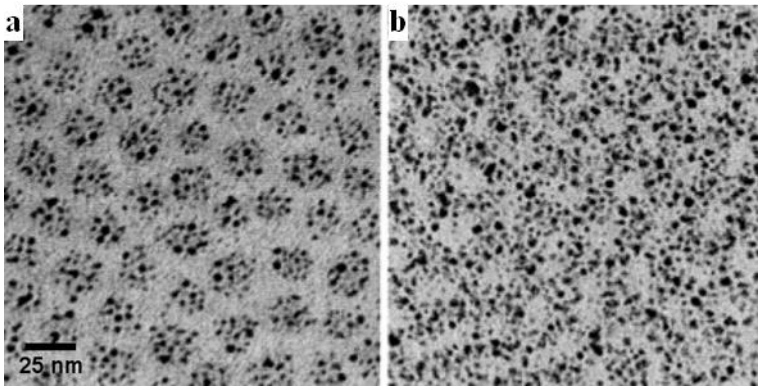

Figure 3.6 Inversion of silver acetate-loaded PS-*b*-P4VP from (a) reverse micelles to (b) regular micelle nanopattern after ethanol treatment.[30]

More recently, Fahmi found a transition from micellar spheres to rods and rings with the addition of water to a reverse micelle system.[31] The transition is apparently initiated by water incorporation in the micellar core inducing swelling. The ratio of PS and P4VP block lengths was near equivalent in this study, with degrees of polymerization (DP) for PS and

P4VP of 206 and 197, respectively. The micelles were loaded at a 1:1 Au:4VP ratio at 0.5 % w/v concentration in toluene or in a binary solvent with varying water contents. Figure 3.7 illustrates the different morphologies resulting from $HAuCl_4$ loading in toluene or water-toluene as solvents. It should be noted that the metal distribution was stable to reduction, in analogy to the previously described systems.

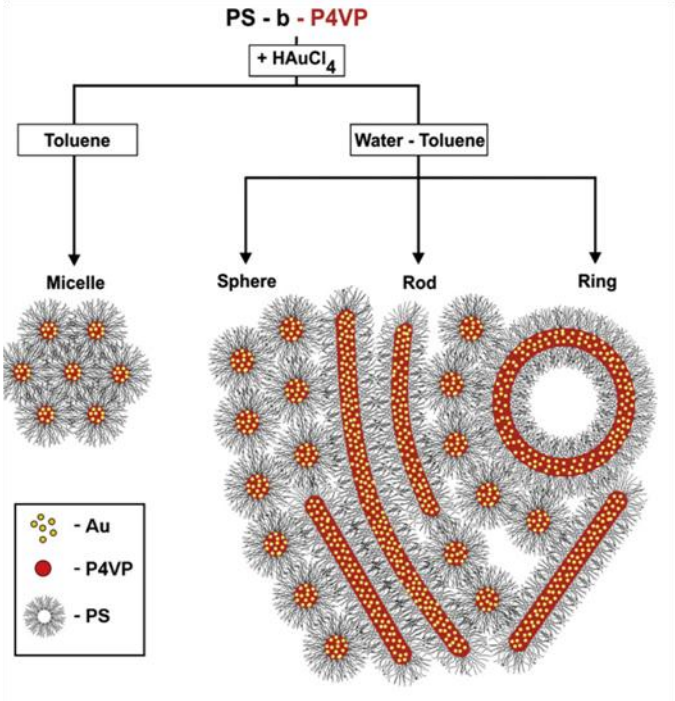

Figure 3.7 Schematic representation of morphologies formed by $HAuCl_4$ loading of PS-*b*-P4VP micelles under different solvency conditions.[31]

Figure 3.8 provides TEM images corresponding to the morphologies depicted in Figure 3.7. Spheres are formed by loading PS-*b*-P4VP with $HAuCl_4$ in toluene (Figure 3.8a). The transition that occurs by the addition of water above a threshold level to form rods,

cylinders and rings/vesicles is shown in Figure 3.8b, while solution reduction with borane-dimethylamine preserves the self-assembled patterns (Figure 3.8c).

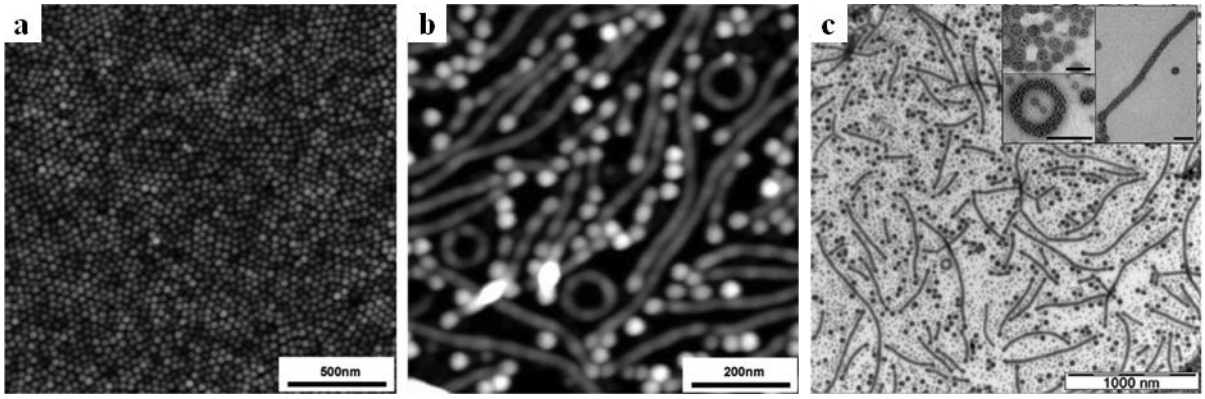

Figure 3.8 TEM micrographs for PS-*b*-P4VP reverse micelles loaded with $HAuCl_4$ (a) in toluene, (b) in water-toluene, and (c) after reducing the nanoparticles loaded in water-toluene.[31]

The solvent composition is paramount to the type and ratio of structures formed; at water contents below 0.5 equiv relative to 4VP, no transition was observed. Dominant rod-like structures were obtained at water levels exceeding 10 equiv vs. 4VP residues, and ring or vesicle structures became predominant when the water concentration exceeded 100 times that of 4VP. These morphological transitions are in agreement with those reported by Discher and Eisenberg for micelles of PS-*b*-PEO and PS-*b*-PAA in binary solvent systems.[32]

Polyvinylpyridine also forms the core of reverse micelles in aqueous environments when incorporated in a block copolymer with poly(ethylene oxide) (PEO) segments. Once ionized by treatment with a metallic acid such as $HAuCl_4$, the structure becomes double hydrophilic, also referred to as bihydrophilic. Thus the copolymer PEO45-*b*-P4VP28 (the numerical values represent the DP of each segment) was loaded with $HAuCl_4$ under aqueous

conditions to form a bihydrophilic species.[11] The addition of the gold acid led to the commonly observed spherical micelles at 8:1 or 4:1 loading ratios (4VP:Au). Upon reduction with hydrazine a sphere-to-rod transition was observed; however, this happened to a much greater extent at higher loading levels. Alternatively, the block copolymer was loaded with $NaAuCl_4$ to observe its micellar behavior under "neutral" (non-protonated) loading conditions. The sodium salt does not protonate the pyridine group, inducing a lower amount of cylinder or rod formation, even after reduction. The majority of the micelles maintained a spherical geometry in this case. It was also demonstrated that similar structures were formed in non-polar environments such as toluene with PS-*b*-PEO diblock copolymers.[33] Micelles with a PEO core can also be loaded with metallic salts such as $LiAuCl_4$: The lithium ions complex with the oxygen atoms within the PEO chains, while the tetrachloroaurate anion forms an ion pair with lithium.

Triblock copolymers have the ability to form many interesting morphologies that can also serve as scaffolds for the preparation of metallic nanoparticles.[23,34] Due to the presence of three distinct polymer segments, many factors affect the morphology of triblock copolymers. In aqueous solutions, Jérôme and colleagues reported the formation of three-layer micelles with spherical or cylindrical topologies.[23,34] The core-shell-corona (CSC) layering of the three phases of PS-*b*-P2VP-*b*-PEO micelles was postulated to result from selective solvation: PS forms the core of the micelle, which is surrounded by a shell of P2VP, and a corona of water-soluble PEO. This morphology is also known as an onion micelle.[35] Due to the presence of P2VP segments, the micelles are pH-responsive. Upon decreasing the pH the P2VP phase swells significantly, but the spherical topology is maintained. This phenomenon is also observed when the CSC micelles are loaded with $HAuCl_4$ and reduced.

Uniformly distributed gold nanoparticles result from $NaBH_4$ reduction, in analogy to diblock copolymer micelles. TEM images for these morphologies are shown in Figure 3.9a.

By modifying the solvency conditions for the PS-*b*-P2VP-*b*-PEO triblock copolymer, a morphological transition could be induced. Preparing the micelles in DMF/toluene mixtures, a selective solvent for PS, adding water, acidifying the micelles, and removing the organic solvent by dialysis thus led to a transition to cylindrical micelles.[34] While some spherical structures persisted, the cylindrical topology was maintained even upon loading with $HAuCl_4$ and reduction with hydrazine. In this case, hydrazine reduction produced results similar to diblock copolymers of PS and P2VP, with partial nucleation of the gold nanoparticles leading to a distribution in sizes.[17] TEM micrographs for the loaded polymers after reduction are shown in Figure 3.9b and Figure 3.9c.

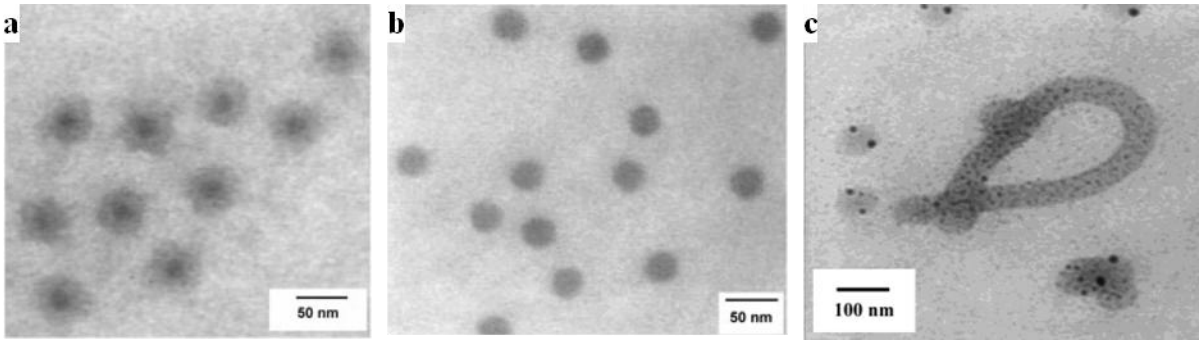

Figure 3.9 CSC triblock copolymer micelles of PS-*b*-P2VP-*b*-PEO prepared from (a) aqueous solution and stained with RuO_4,[23] (b) loaded with $HAuCl_4$ and reduced with $NaBH_4$,[23] and (c) loaded with $HAuCl_4$ from DMF/toluene solution and then reduced.[34]

Triblock terpolymers have also been shown to assemble into multiple nanodomains within multi-molecular micelles.[36] These systems, referred to as multicompartment micelles,

arise from micelle core subdivision to produce structures and have potential applications in drug delivery or biological system simulation. One example of such a terpolymer is polybutadiene-*b*-P2VP-*b*-poly(*tert*-butyl methacrylate), PB-*b*-P2VP-*b*-P*t*BMA, which forms multicompartment micelles with a raspberry-like morphology in acetone. The terpolymer was synthesized by sequential anionic polymerization in THF at low temperature, starting with butadiene initiated with *sec*-BuLi, followed by growth of the P2VP segment. Prior to the *tert*-butyl methacrylate addition, the living P2VP end was capped with DPE to prevent side reactions during monomer crossover.[37]

The raspberry, or sphere-on-sphere, morphology of the micelle is comprised of a polybutadiene core encased by P2VP spheres, and a corona of poly(*tert*-butyl methacrylate) chains. The polybutadiene segments within the core allowed stabilization by crosslinking with S_2Cl_2 or with pentaerythrol tetraacrylate in the presence of UV light. It was determined that crosslinking did not significantly change the sphere-on-sphere morphology observed for the non-covalently bound multicompartment micelles. A schematic representation of this unique morphology is provided in Figure 3.10a, while the TEM images of Figure 3.10b and Figure 3.10c highlight the P2VP segments (at different magnifications) after selective staining with iodine followed by S_2Cl_2 crosslinking, revealing the nanostructured P2VP domains within the micelle.

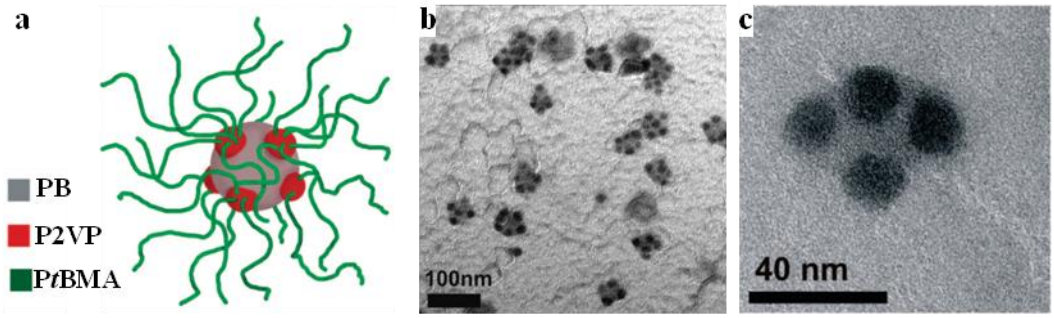

Figure 3.10 Multicompartment micelle formed from PB-*b*-P2VP-*b*-P*t*BMA in acetone: (a) Schematic representation, TEM images after (b) selective staining of P2VP with iodine after crosslinking, and (c) high magnification TEM image.[36]

The same group also illustrated the versatility of this triblock terpolymer by loading the micelles with cesium in an aqueous environment.[38] This was accomplished by hydrolyzing the butyl methacrylate groups within the PB-*b*-P2VP-*b*-P*t*BMA copolymer with HCl, to produce the methacrylic acid (MAA) moieties, and dialyzing against a pH 10 solution of CsCl to produce PB-*b*-P2VP-*b*-PMAA-Cs. This rendered the corona of the micelles compatible with aqueous environments. An alternate modification was performed through quaternization (q) of the pyridine groups with MeI, resulting in polybutadiene-*b*-poly(N-methyl-2-vinyl pyridinium)-*b*-poly(*tert*-butyl methacrylate), PB-*b*-P2VPq-*b*-P*t*BMA, which was then hydrolyzed and dialyzed against a CsCl solution to create the PB-*b*-P2VPq-*b*-PMAA-Cs triblock copolymer. The quaternized triblock copolymer analogue was found to have pH- and salinity-responsive multicompartment micelle properties. The interactions between the two charged segments (P2VPq and PMAA) led to interesting raspberry and core-shell morphologies that could serve as metallic nanoparticle templates. These structures are commonly referred to as interpolyelectrolyte complexes (IPECs) or block ionomer complexes (BICs).

The complexation of charged block copolymers such as P2VPq-*b*-PEO into the IPEC micelles formed by PB-*b*-P2VPq-*b*-PMAA was also demonstrated.[39] The morphologies obtained by complexation of the triblock IPEC and P2VPq-*b*-PEO are shown in Figure 3.11. These structures are also compatible with metallic loading using acids such as $HAuCl_4$. This compound has reduced selectivity, however, because it can bind to both methacrylic acid and vinylpyridine moieties. As a result, the structures formed are not as intricate as those shown for the iodine-stained samples in Figure 3.10.

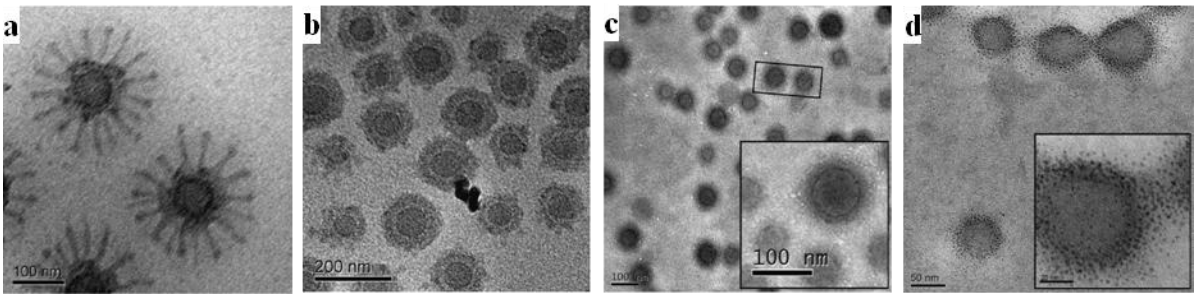

Figure 3.11 TEM images for PB-*b*-P2VPq-*b*-PMAA / P2VPq-*b*-PEO IPEC (a) at high pH after 1 h mixing, (b) after 10 days mixing and staining with iodine, (c) loaded with $HAuCl_4$, and (d) PB-*b*-P2VPq-*b*-PMAA IPEC loaded with $HAuCl_4$.[39]

3.3 Star-branched Architectures

Star-branched polymers can be divided into two main categories, namely the $(AB)_n$ and A_nB_n architectures shown in Figure 3.12.

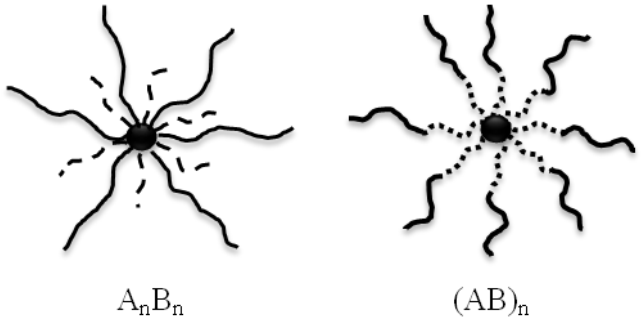

Figure 3.12 Schematic representation of A_nB_n- and $(AB)_n$-type star copolymer architectures.

An (A_nB_n)-type star polymer is formed by an arms-first and microgelation approach. A polymer chain (A_n) is first grown and a divinyl monomer is added which couples, or crosslinks, the chains together but does not terminate the living centers. The remaining active sites are located at the junctions near the core of the branched structure thus obtained. Further monomer addition therefore results in chain growth (B_n) propagating radially outwards from the crosslinked core.

$(AB)_n$-type star polymers contain only one type of block copolymer chains linked to the core, rather than two distinct chains grown separately as in the previous case. This architecture can be created either through divergent arm-growth or arms-first microgelation schemes. The divergent arms-growth approach relies on a multi-functional initiator that dictates the number of arms in the star polymer, with chains growing outward from the active

sites on the initiator. Block copolymers can be obtained by the addition of a second monomer to the living arms. The arms-first microgelation approach can also be applied whereby a block copolymer is grown, a divinyl monomer is added to couple the chains, and the reaction is then terminated, resulting in the $(AB)_n$ branched structure seen in Figure 3.12.

3.3.1 A_nB_n Star-block Copolymers

3.3.1.1 Polystyrene / Poly(2-vinylpyridine)

Gorodyska et al. successfully loaded A_nB_n-type heteroarm star copolymers of PS and P2VP with palladium(II) acetate ($Pd(OAc)_2$).[40] The synthesis was not specifically referenced by the group, but two of the contributors (Tsitsilianis and Voulgari) previously investigated a similar system and provided a description of the synthesis.[41,42] Styrene was polymerized anionically with *sec*-BuLi in THF at –40 °C in the presence of LiCl, and divinylbenzene (DVB) was added to induce crosslinking and provide a PS star-branched polymer with living centers at the core. These were capped with 1,1-diphenylethylene prior to the addition of 2VP, to reduce the reactivity of the anionic propagating centers and prevent potential side reactions during cross-propagation. Termination with degassed methanol yielded the desired heteroarm star-branched copolymer.

Gorodyska investigated a star-branched copolymer with seven PS arms and seven P2VP arms (PS7-P2VP7), where the P2VP chains had a higher molecular weight as compared to PS (M_w^{PS} = 20,000 g/mol, M_n^{P2VP} = 56,500 g/mol) to provide a star structure with a core-shell morphology containing a mixed core of PS and P2VP segments, and a corona of P2VP chains extending further from the core (Figure 3.13).

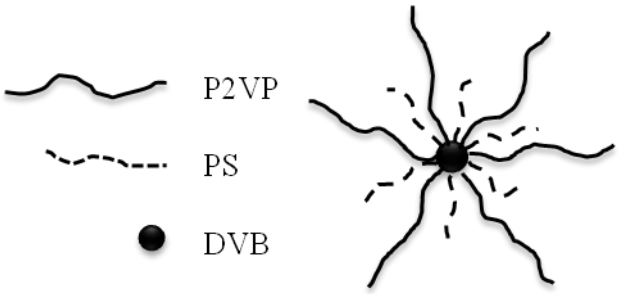

Figure 3.13 A_nB_n-type star copolymer with PS and P2VP segments.

The ability of the chains to reorganize in selective solvents leads to enhanced phase segregation and a distinct core-shell morphology for these systems: The incompatible segments collapse, while the solvated chains extend and swell into the dispersion medium. In non-selective solvents such as THF, however, the template molecules are uniformly solvated and do not display clearly defined phase separation, as confirmed by atomic force microscopy (AFM) imaging.

The P2VP segments give the star-branched copolymers the ability to accommodate salts and polar compounds, thus making them good candidates as templates for the preparation of metallic nanoparticles. Metal inclusion was thus achieved through ion exchange between the protonated 2VP units, $(P2VPH^+)Cl^-$, and a palladium salt. In an acidic environment, $Pd(OAc)_2$ reacts with HCl to form $(2H^+)PdCl_4^-$. The loading procedure was concluded by reduction of the palladium salt with dimethylamine borane, producing metallic nanoclusters visible as nodes along the extended P2VP arms of the star copolymer (Figure 3.14).

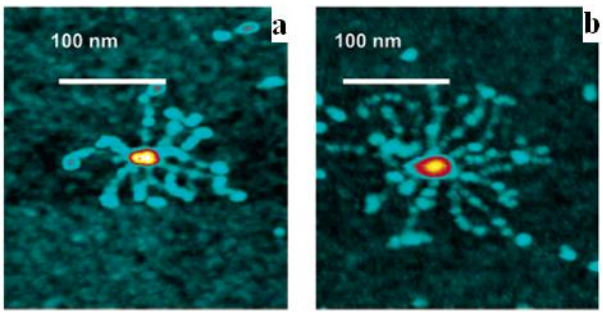

Figure 3.14 AFM images for palladium-metalized PS7-P2VP7 in acidic solution with (a) 7 P2VP arms and (b) 10 P2VP arms.[40]

3.3.1.2 Polystyrene Stars with Carboxylic Acid-functionalized Cores

Du and Chen developed an interesting multi-step method for the synthesis of star-branched polystyrenes containing carboxylic acid functionalities within their core. The preparation of the A_nB_n-type star relies upon a sacrificial polymer, poly(ε-caprolactone), to create the carboxyl functional groups.[43] The synthesis of the nanoparticle template began with the ring-opening polymerization (ROP) of ε-caprolactone using tin(II) 2-ethylhexanoate and benzyl alcohol at 110 °C for 20 h before termination with methanol.[44] The resulting hydroxyl-terminated poly(ε-caprolactone) (PCL) was converted to an atom transfer radical polymerization (ATRP) macroinitiator by modifying the hydroxyl groups to bromoisobutyryl moieties through treatment with 2-bromoisobutyryl bromide. The ATRP of DVB was initiated with this macroinitiator at 110 °C in the presence of CuBr and *N,N,N',N'',N''*-pentamethyldiethylenetriamine (PMDETA) as shown in Scheme 3.1, adapted from the work of Baek et al.[45]

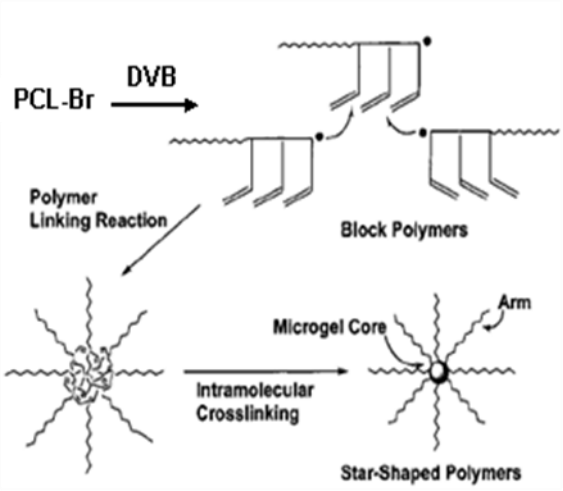

Scheme 3.1 Star-branched PCL synthesis from PCL-Br macroinitiator.[45]

The resulting PCL star-branched polymer thus obtained still contained functional sites within the core that could be used for further ATRP reactions. Polystyrene was thus grown by ATRP from the functional sites within the DVB core using CuCl and PMDETA. In order to introduce carboxyl groups within the core of the star copolymer, the PCL phase was modified by hydrolysis or alcoholysis of the ester functionalities within the PCL backbone. Cleavage of the PCL ester groups removed the PCL chains from the star-block copolymer, leaving one carboxyl group within the DVB core for every PCL chain cleaved. The entire synthetic process including sacrificing of the PCL chains to afford carboxyl functionalities is shown in Scheme 3.2.

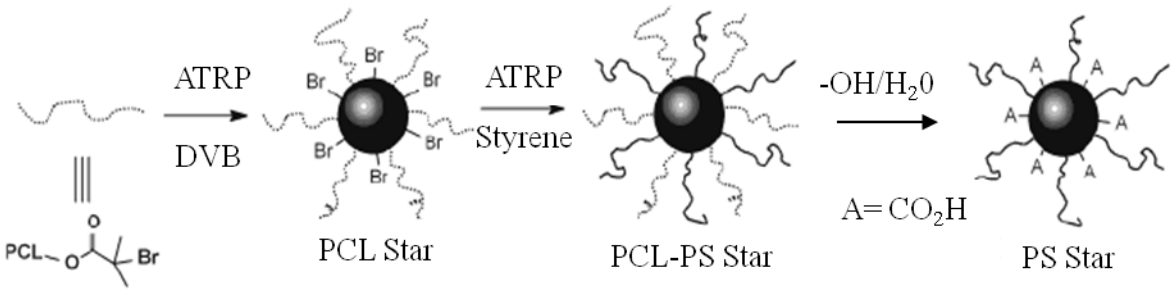

Scheme 3.2 ATRP synthesis of a PS star containing carboxylic acid groups in the core.[43]

Several other reports exist on the synthesis of star-branched polymers with similar architectures and functionalized cores;[45–47] these were not applied to the templating of metallic nanoparticles, however. Lead sulfide (PbS) nanoparticles were assembled within the carboxylate-functionalized PS stars by metal-ion exchange with lead(II) acetate and treatment with H_2S. TEM analysis confirmed the incorporation of PbS into the functionalized core of the PS star, as shown in Figure 3.15. The spherical morphology of the star-polymer template, specifically the core, imparts a spherical topology to the PbS nanoparticles.

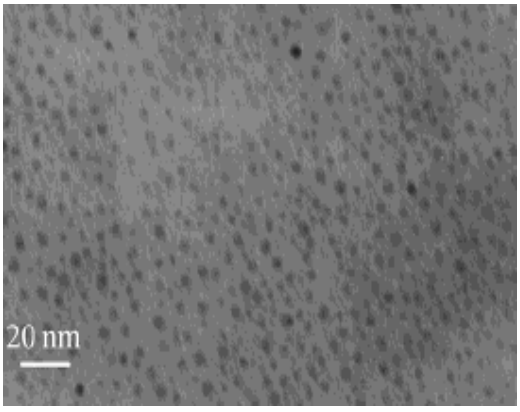

Figure 3.15 TEM micrograph for PbS-loaded PS stars with a carboxyl-functionalized core.[43]

3.3.2 $(AB)_n$ Star-block Copolymers

3.3.2.1 Poly(ethylene glycol) / Poly(ε-caprolactone)

Researchers from Belgium and The Netherlands developed a procedure for the preparation of gold nanoparticles using $(AB)_n$ star-block copolymers.[48] The 5-arm star-block copolymer template synthesized incorporated a core of poly(ethylene glycol) (PEG) surrounded by a shell of PCL. The synthesis began with a 5-arm PEG star macroinitiator having M_n = 2150 g/mol for each arm, which was used for the ROP of ε–caprolactone. This yielded a PCL block extending from each of the five PEG arms. The synthesis was accomplished with a synthetic robot (ASW200)[49] further described by Meier et al.[50] The structure of the PEG-PCL star-block copolymer is shown in Figure 3.16.

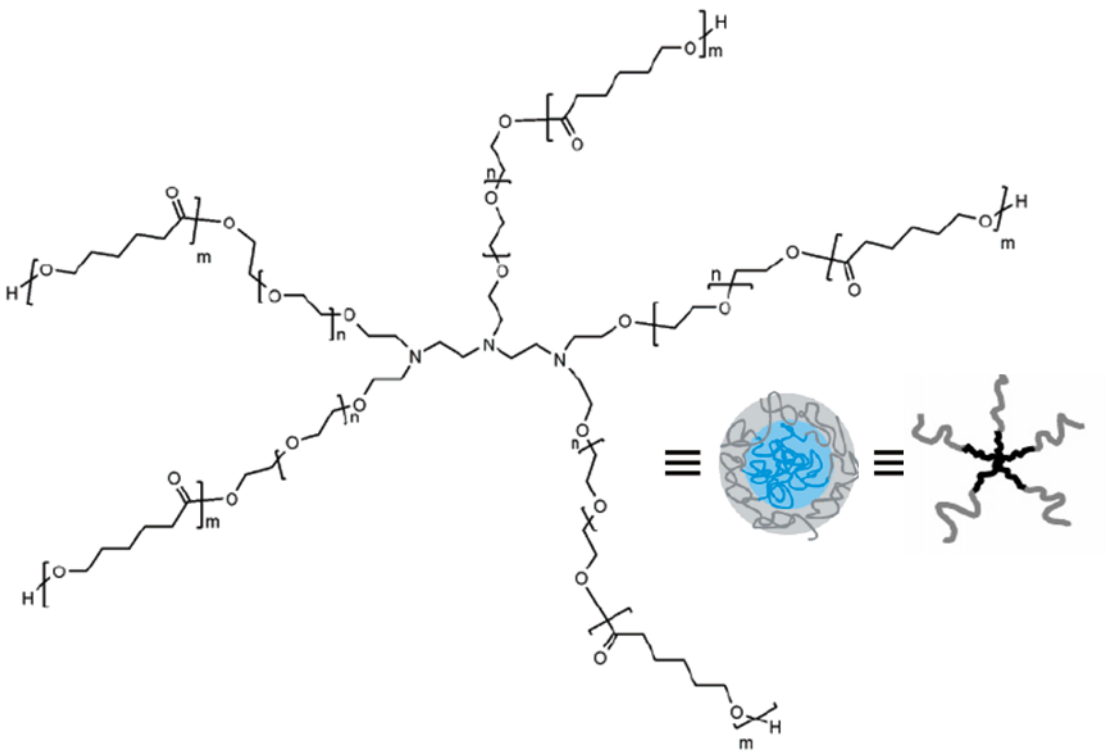

Figure 3.16 $(AB)_n$-type star-block copolymer with PEG-*b*-PCL.[50]

Various templates were synthesized from the same macroinitiator with a range of PCL arm lengths (DP = 3 – 18) and relatively low polydispersities (PDI = $M_w/M_n \approx 1.4$). The resulting star-block copolymers had a CS morphology, the PEG core being able to house metallic acids or salts.

The PEG-PCL template was dissolved in *N*,*N*-dimethylformamide (DMF) at 1 g/L (0.1 %), followed by the addition of potassium tetrachloroaurate ($KAuCl_4$) from a 1 % DMF solution to achieve the desired loading ratio. Molar loading ratios ($KAuCl_4$/EO) from 1/1 to 1/10 were examined. Subsequent reduction of the gold salt was performed with sodium borohydride ($NaBH_4$) at various molar ratios. Optimal results were obtained for a $KAuCl_4$/EO ratio of 1/4 and a $KAuCl_4/NaBH_4$ ratio of 1/2. Films were cast from reduced solutions and examined with TEM to reveal one distinct single gold nanoparticle per template molecule. Template loading and reduction, as well as a TEM micrograph for the nanoparticles, are illustrated in Figure 3.17.

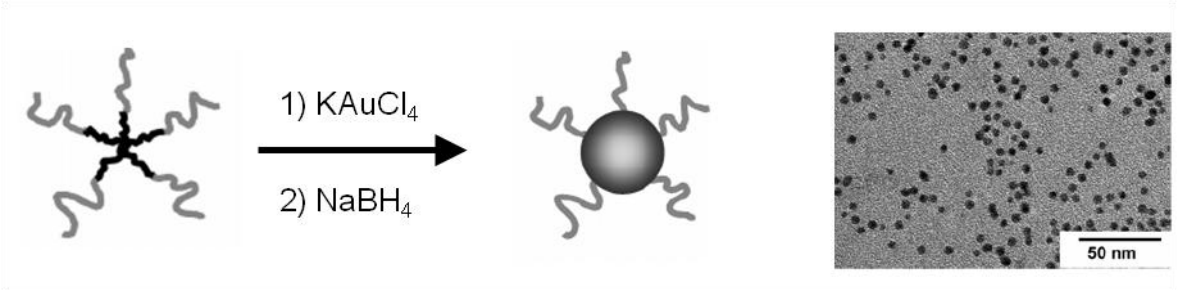

Figure 3.17 $KAuCl_4$ loading and reduction of a 5-arm PEG-PCL template (left) and TEM micrograph for the resulting gold nanoparticles after reduction (right).[48]

It was shown that the stability of the metal-loaded templates could be tuned by altering the length of the PCL corona: Molecules with shorter PCL chains (DP = 3) had the

tendency to aggregate into clusters, whereas templates with longer PCL chains (DP = 18) existed mainly as isolated entities. Longer coronal chains have enhanced ability to shield the charged core of the templates from their surrounding environment, including other charged species, thus limiting their aggregation.

Further to this research, Fustin et al. investigated tuning the hydrophobicity of their gold-loaded star-branched structures by coupling the gold surface with trithiocarbonate-functionalized poly(acrylic acid), to enable the formation of aqueous dispersions.[51] They also successfully constructed stabilized palladium nanoparticles for use in Heck cross-coupling reactions with these templates.[52]

3.3.2.2 Poly(acrylic acid) / Polystyrene

Well-defined amphiphilic star-block copolymers with a carboxylated core have also been prepared by Zhang et al.[53] In this case, the synthesis of $(AB)_n$-type star-branched copolymers was accomplished by a three-step ATRP procedure: A star-branched homopolymer core was first synthesized, followed by a second polymerization step yielding the star-block copolymer, and hydrolysis of the star-branched core yielded the desired functionality.

The first step generated a 6-arm poly(*tert*-butyl acrylate) star-branched polymer from a hexafunctional bromide initiator (Br_6) in the presence of PMDETA, CuBr, and *tert*-butyl acrylate (BA). Following termination and removal of the CuBr catalyst, the star-branched homopolymer, $(Pt\text{BA})_6$, was converted to a star-block copolymer via ATRP by the addition of styrene, PMDETA, and CuCl at 100 °C. Following termination, the BA units of $(Pt\text{BA-}b\text{-PS})_6$ were converted to acrylic acid (AA) moieties by cleavage with trifluoroacetic acid. The pathway for the synthesis of $(\text{PAA-}b\text{-PS})_6$ is illustrated in Scheme 3.3.

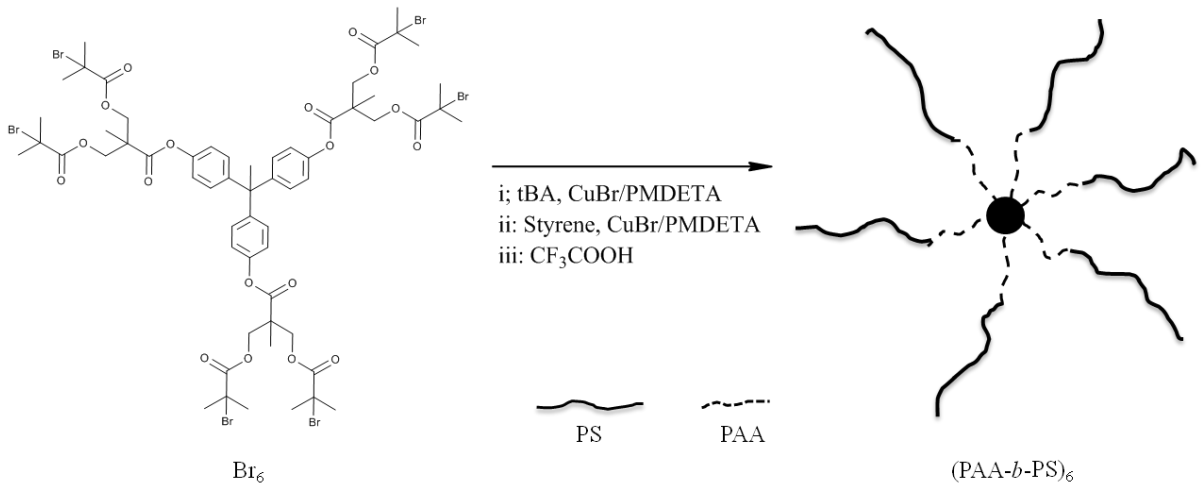

Scheme 3.3 Synthesis of (PAA-*b*-PS)$_6$ star-block copolymer by ATRP.

The resulting (PAA-*b*-PS)$_6$ template was loaded with $PtCl_4$ following ionization of the PAA core by pH adjustment with NaOH. After complexing the template core with $PtCl_4$, the Pt salt was reduced with $NaBH_4$ and analyzed by TEM to characterize the Pt nanoparticle morphology. It was confirmed that one Pt nanoparticle formed within each branched template, as shown in the TEM micrograph shown in Figure 3.18. The nanoparticles depicted, measuring 1.9 ± 0.8 nm in diameter, resulted from a low loading ratio (one Pt for every 40 AA units).

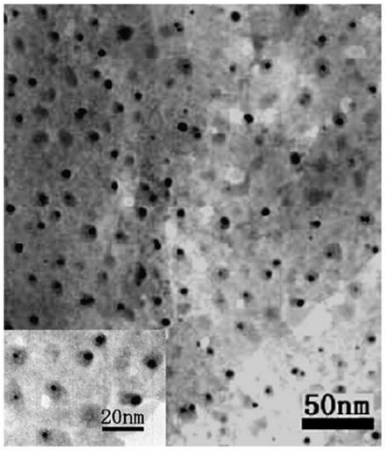

Figure 3.18 TEM micrograph of Pt-loaded (PAA-*b*-PS)$_6$.[53]

Loading ratios of 1:10 and 1:20 (Pt:AA) were also examined and it was determined that the size of the resulting nanoparticles was proportional to the loading ratio and the nanoparticles were of relatively uniform size, 4.2 ± 1.3 nm and 2.9 ± 0.9 nm, respectively.

3.3.2.3 Polystyrene / Poly(2-vinylpyridine)

Youk and co-workers developed a microgelation technique to couple block copolymer chains of PS and P2VP, yielding $(AB)_n$-type star polymers that could be loaded with gold.[15] This arm-first method relied on the synthesis of block copolymer chains as a first step, which were then joined by a microgelation reaction using a divinyl compound.

The block copolymer was synthesized by anionic polymerization using *n*-BuLi initiation in THF at –78 °C and sequential additions of styrene and 2VP monomers by distillation. The divinyl coupling agent, ethylene glycol dimethacrylate (EGDMA), was added to the living block copolymer solution to form the star-block copolymer. The copolymer had a unimolecular reverse micelle structure allowing the solubilization of salts and polar compounds into the P2VP core in non-polar solvents. A schematic representation

of the star-block copolymer formation by living PS-*b*-P2VP chain coupling is shown in Scheme 3.4. It should be noted that the representation of the star copolymer shown is oversimplified, since crosslinking occurs through coupling of multiple EGDMA species.

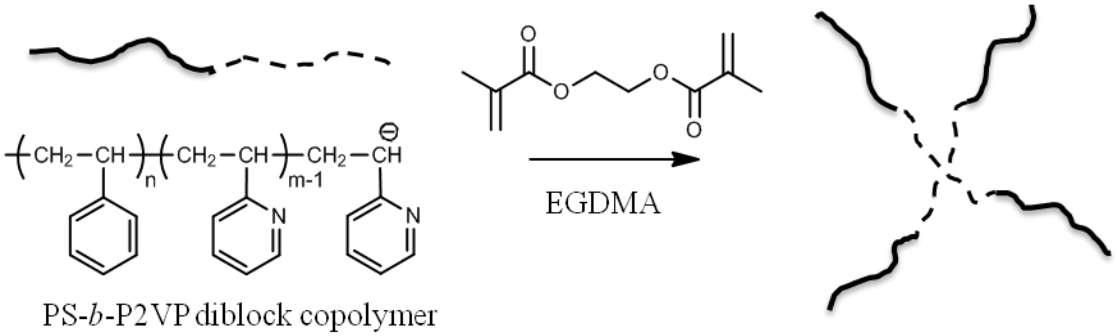

Scheme 3.4 Addition of EGDMA to living PS-*b*-P2VP to form a star copolymer with a P2VP core and a PS corona.

After work-up, the star block copolymer templates were loaded with varying amounts (from 0.1 to 0.5 equivalents of $HAuCl_4$ relative to 2VP units) of $HAuCl_4$ as 0.5 % w/v (5 mg/mL) solutions in dry toluene. Tetrachloroauric acid is insoluble in toluene; however, it is gradually solubilized by the hydrophilic P2VP core of the template as it protonates the pyridine ring, as described in Section 3.2.1 for block copolymer templates. The gold was then reduced with a 0.05 % v/v solution of hydrazine in toluene, resulting in the formation of one gold nanoparticle per template molecule as seen in Figure 3.19.

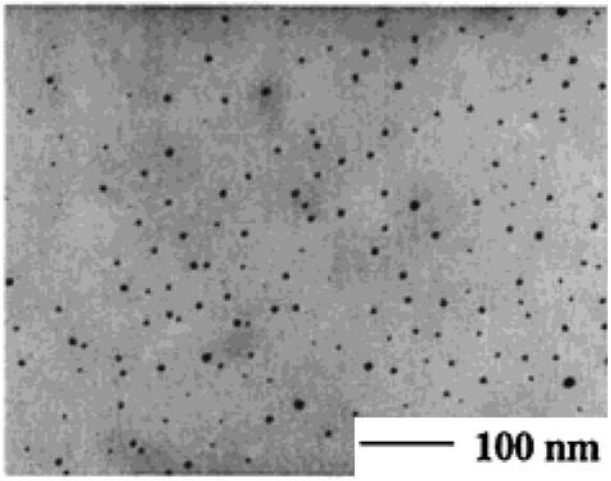

Figure 3.19 TEM micrograph for gold-loaded PS-P2VP star-block copolymer.[15]

3.4 Dendritic Architectures

Unimolecular templates with a dendritic architecture have been the topic of interesting research in recent years, as this class of polymer offers a unique architecture and distinct advantages over intermolecular micellar scaffolds. Unimolecular micelles are covalently bound structures that do not exhibit a critical concentration for formation nor a dynamic equilibrium with linear components. The loading region within the branched scaffold can be controlled through synthesis and can result in nanoparticle property tailoring.

Dendritic polymers fall into three classes: dendrimers, hyperbranched, and arborescent polymers (also referred to as dendrigraft polymers). The architecture of each family of dendritic species is depicted in Figure 3.20. The synthesis and the characteristics of each of these were discussed at length in Chapter 2.

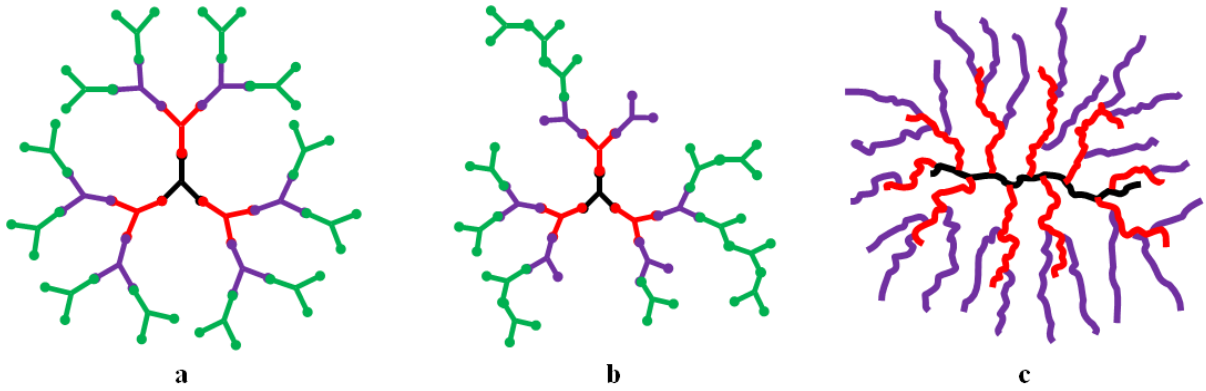

Figure 3.20 Structure of the three classes of dendritic polymers: (a) Dendrimer, (b) hyperbranched polymer, and (c) dendrigraft polymer.

3.4.1 Dendrimer Templates

Polyamidoamine (PAMAM) dendrimers were among the first dendritic macromolecules synthesized and are likely the most widely used dendritic molecules to this day.[54,55] PAMAM dendrimers offer ample opportunities for chemical functionalization given the reactivity of the amine-based building blocks used in their synthesis. Illustrated in Figure 3.21 is the branched architecture of a generation (G1) PAMAM dendrimer containing various amine and oxygen functionalities available for the coordination of various metals. Loading of PAMAM molecules with metals has been accomplished by various researchers, some of which will be described herein. This includes PAMAM dendrimers functionalized with different functional groups, or coupled with polymer segments to create larger templates.

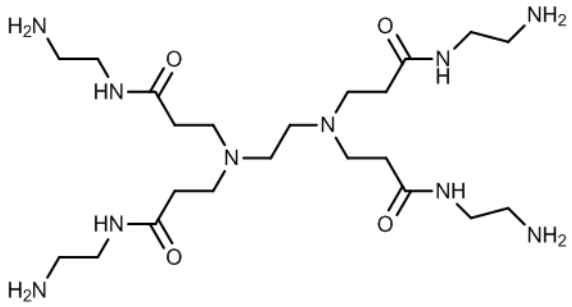

Figure 3.21 Illustration of G1 PAMAM architecture and sites available for metal coordination.

Crooks[56] and Tomalia[57] both investigated the loading and reduction of copper salts within PAMAM dendrimer scaffolds. Crooks loaded both amine- and hydroxyl-terminated G4 PAMAM dendrimers (G4-NH_2 and G4-OH respectively) with Cu^{2+} using $CuSO_4$, and reduced the salt to Cu^0 with $NaBH_4$. It was observed that aqueous solutions of Cu-loaded G4-

OH were stable in the absence of oxygen, showing no agglomeration or precipitation. The size of the Cu nanoparticles was dependent on the template characteristics. As binding only occurred within the dendrimer core,[58] the copper nanoclusters were well shielded from each other and from the aqueous environment, resulting in soluble unimolecular micelles. TEM analysis and UV-Vis spectroscopy both revealed ultra-fine copper particles less than 2 nm in diameter. Intradendrimer copper clusters larger than 5 nm should exhibit a Mie plasmon resonance peak around 590 nm in UV-Vis analysis,[59] but this was not observed for the G4-OH Cu^0 system. For the loaded G4-NH_2 template, in contrast, a plasmon peak was evident after Cu^{2+} reduction. This was attributed to copper complexation with the NH_2-functionalized corona of the dendrimers, and Cu^0 agglomeration into larger clusters on the exterior of the dendrimer after reduction.

Tomalia found similar results in his work: Extremely stable copper-loaded PAMAM dendrimers were obtained in both aqueous and methanolic environments. Specifically, Tomalia examined copper(II) acetate loading and its reduction with hydrazine in PAMAM dendrimers capped with TRIS [tris-(2-hydroxymethyl)methyl, $(CH_2OH)_3$], amino (NH_2), or pivalate [$NHCOC(CH_3)_3$] functionalities. Most samples lacked plasmon resonance in the 590 nm region, with the exception of the TRIS-capped dendrimers for which a small increase in plasmon resonance was observed after 21 h.

The PAMAM structure is not limited to copper loading, as many metallic nanoparticles have been successfully templated including Au,[60] Pd,[61] Pt,[62] Ag,[63] Co,[64] and bimetallic particles of Pd-Au,[65] and Pt-Ru.[66] The images shown in Figure 3.22 are typical for the size, shape, and distribution of metal within dendrimer templates. PAMAM dendrimers can be loaded at various levels relative to the number of coordinating amine sites, which

depends on the generation number of the dendrimer used.[67] Thus Figure 3.22 corresponds to a G4 PAMAM dendrimer end-functionalized with hydroxyl groups and loaded with either 40 or 60 atoms per dendrimer (Figure 3.22a and Figure 3.22b, respectively). The diameter of these nanoparticles was reported to be 1.4 ± 0.2 nm and 1.6 ± 0.2 nm, respectively. Figure 3.22c depicts dendrimers loaded with 40 atoms of Pd, having a diameter of 1.3 ± 0.2 nm.

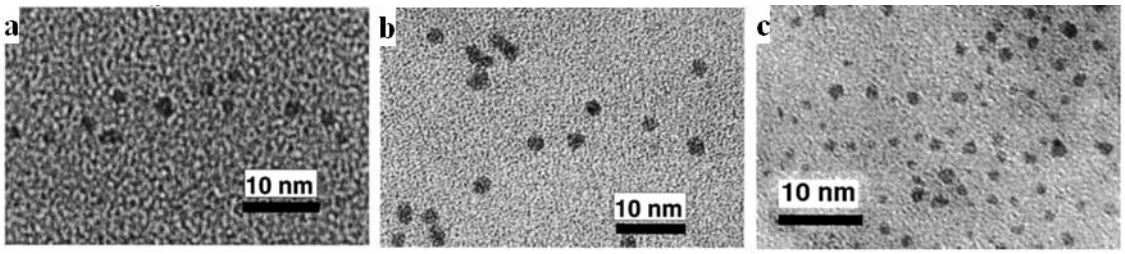

Figure 3.22 TEM images for G4 PAMAM-OH loaded with (a) 40 atoms of Pt, (b) 60 atoms of Pt, and (c) 40 atoms of Pd.[68]

PAMAM dendrimers can also serve as precursors for the synthesis of much larger and higher molecular weight polymers by using the terminal end groups on the periphery of the dendrimers for coupling reactions. For example, vinyl sulfonyl (VS) end-functionalized poly(ethylene glycol), PEG-VS, was coupled with PAMAM dendrimers having amine end groups via Michael addition.[69] The star-branched dendrimer-linear polymer hybrid obtained has a core-shell morphology and the ability to house materials within its core, while the polymer chains in the corona helped to stabilize the molecules in solvents. Metal loading into PAMAM-PEG dendrimer-star polymers was illustrated by the same group.[70] The dendrimer core was thus used to template the deposition of $Cd(NO_2)_3 \cdot 4H_2O$ in methanol before its reaction with $Na_2S \cdot 9H_2O$. Zero-valent gold was also formed within the core of these

dendrimer hybrids by loading $HAuCl_4 \cdot H_2O$ and reduction with $NaBH_4$ in aqueous solution. The synthesis of the hybrid dendrimers and metal loading within their core is shown in Scheme 3.5.

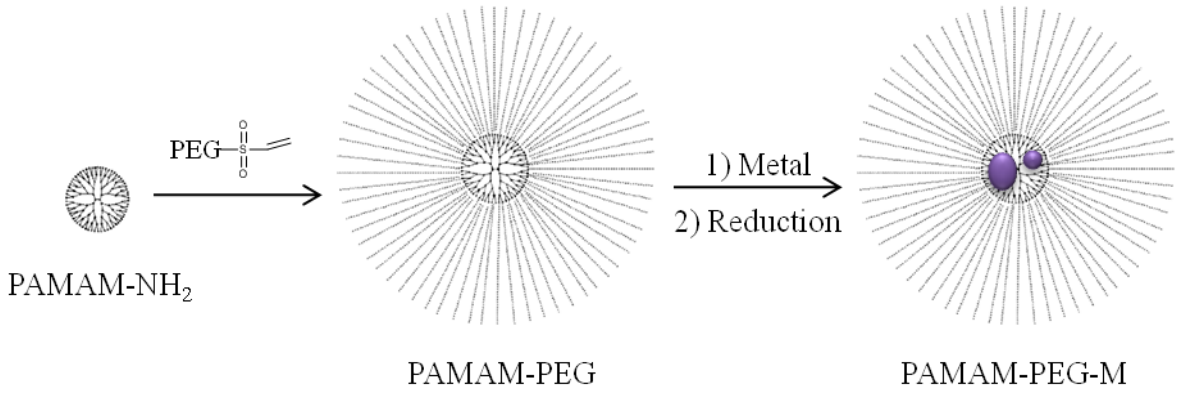

Scheme 3.5 Synthesis and metal loading of PAMAM-PEG dendrimer-star polymer.[70]

Gold and cadmium sulfide (CdS) loading in generation 4, 7, and 10 dendrimers functionalized with 5000 g/mol PEG-VS was examined. In both cases, microscopy and UV analysis suggested that the generation number of the template had a limited influence on the size of the nanoparticles obtained, in analogy to the native PAMAM-NH_2 scaffolds.[22] UV absorbance measurements indicated that the CdS nanoparticle size ranged from 2 to 3 nm, while TEM measurements yielded Au nanoparticles between 1 and 4 nm for a G4 star template, 1 to 6 nm for a G7 PAMAM-PEG template, and between 1 and 3 nm for the G10 star template.

3.4.2 Hyperbranched Polymer Templates

PAMAM-type structures can also be synthesized by a more convenient one-pot method yielding a hyperbranched polymer, referred to as HYPAM.[71] Much like PAMAM dendrimers, HYPAM contains many sites for functionalization with metals as shown in Figure 3.23. Please refer to Chapter 2 for additional information on the HYPAM synthesis.

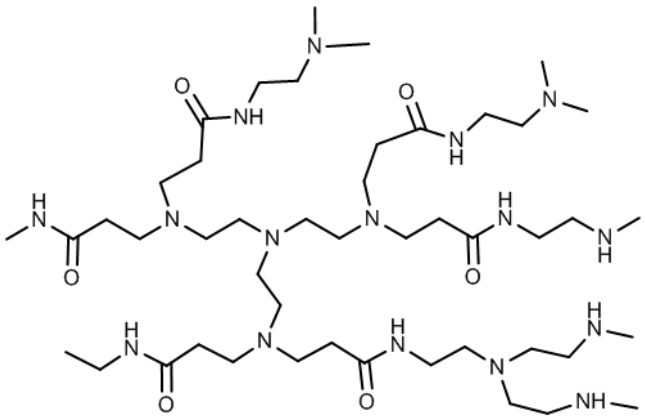

Figure 3.23 Hyperbranched PAMAM (HYPAM) containing metal coordinating sites.

The hyperbranched species otherwise have the same chemical make-up as their dendrimer analogues and thus can serve as nanoparticle templates under similar conditions. A G4 HYPAM sample was thus loaded with $HAuCl_4$ in aqueous solution and reduced with $NaBH_4$.[77] It was found that the polydispersed G4 HYPAM yielded larger diameter gold nanoparticles as compared to the analogous G4 PAMAM dendrimer, namely 4.0 ± 0.9 nm vs. 2.0 ± 0.8 nm, respectively. While the authors did not comment on the source of this discrepancy, the larger diameter nanoparticles derived from HYPAM templating could be either related to the higher PDI (1.4 vs. 1.1) or to the increased number of primary and tertiary amine groups present (20 % more than in PAMAM).

Another nitrogen-rich hyperbranched polymer was synthesized from *N*,*N*'-methylene *bis*-acrylamide (MBA) and *N*-aminoethyl piperazine (AEPZ) in a mixture of methanol and water (70:30) at 50 °C for 6 h and recovered by precipitation in acetone.[72] The reaction sequence involved is shown in Scheme 3.6.

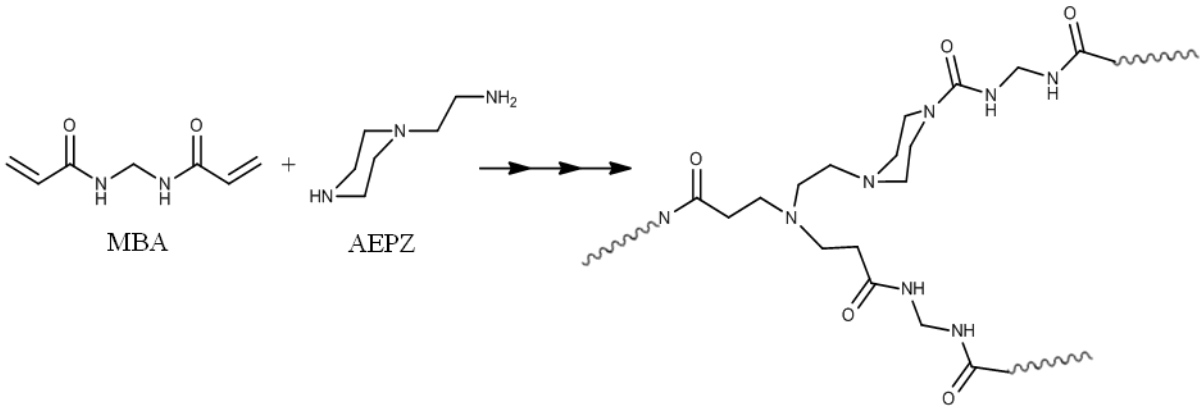

Scheme 3.6 Synthesis of poly(MBA-AEPZ) hyperbranched polymer.

The poly(MBA-AEPZ) structure was used to construct silver nanoparticles in aqueous solution using $AgNO_3$ and reduction with $NaBH_4$. It was discovered that the fashion in which this hyperbranched polymer templated the formation of Ag nanoparticles was different from previously described scaffolds: Rather than forming intrapolymer Ag clusters as shown previously for dendrimers and dendrimer hybrids, the polymer rather encapsulated large Ag colloidal particles. Shown in Figure 3.24 (adapted from Reference 72) is an illustration of the interactions between hyperbranched poly(MBA-AEPZ) and the silver colloidal particles as well as a TEM micrograph for the particles formed.

The size of the Ag colloids formed could be controlled either by the loading ratio (Ag^+ concentration), or through temperature variations. The size distribution was also

affected by these parameters.[72] The influence of the average generation number, controlled through the reaction time, on nanoparticle templating was also investigated.[73] It was reported that generation 1 was formed after 6 h, while generations 3 and 5 resulted after ca. 12 h and 24 h, respectively. It should be noted that the polydispersity of the samples also increased rapidly with the generation, the G5 adduct having a PDI of 3.43. A weak correlation was observed between the generation and the particle size obtained, the G1, G3, and G5 polymers yielding Ag nanoparticles with average diameters of 8.7, 9.6, and 10.2 nm, respectively.

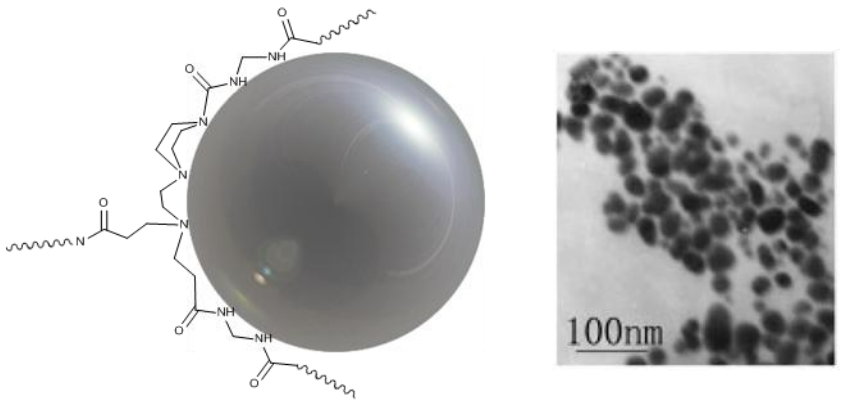

Figure 3.24 Graphical representation of poly(MBA-AEPZ) interactions with Ag (left) and TEM micrograph of the Ag nanoparticles formed (right).[72]

Amphiphilic core-shell hyperbranched polyglycerols have also been synthesized[74] and used to template the formation of gold nanoparticles.[75] The polymer was prepared by 10 % deprotonation of 1,1,1-tris(hydroxymethyl) propane, TMP, by potassium methylate treatment followed by the addition of glycidol. The reaction proceeded for 12 h at 95 °C, the molecular weight being controlled by the amount of glycidol added. The degree of branching was controlled by adjustment of the initiator/monomer ratio. The preparation of amphiphilic

core-shell architectures first involved alkylation of the substrate by treatment with 1-bromo-3-chloropropane in the presence of PEO (acting as phase transfer catalyst) and NaOH. The O-alkylated branched polymer was then again treated with 1-dodecanethiol to generate a hydrophobic corona surrounding the hyperbranched polyglycerol. A simplified reaction scheme showing only a few monomer additions to a TMP core (adapted from Reference 75) is shown in Scheme 3.7.

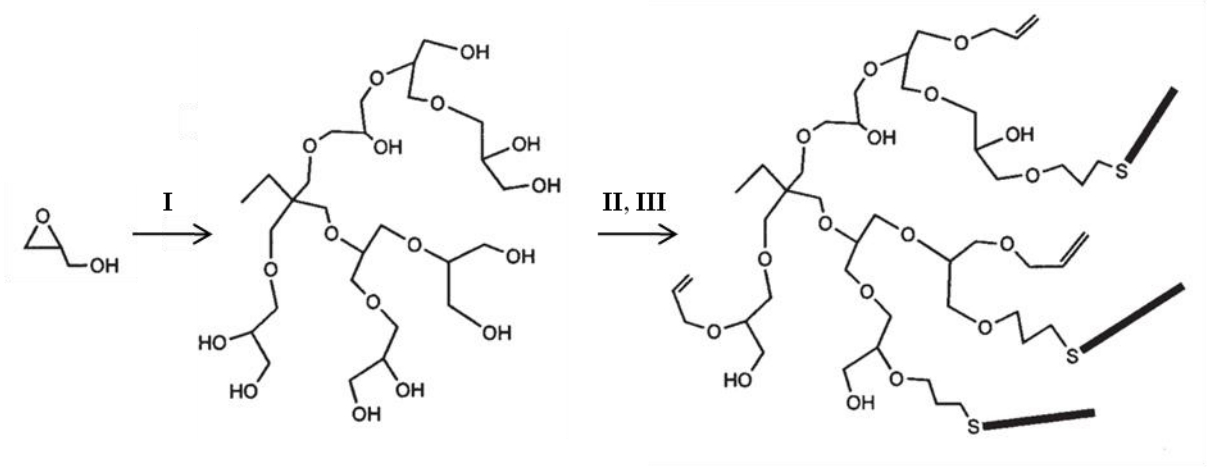

Scheme 3.7 Synthesis of a template from hyperbranched polyglycerol: Glycidol addition to TMP core (I), treatment with 1-bromo-3-chloropropane (II), and dodecanethiol (III).[75]

The thioether groups thus introduced can coordinate with metallic compounds such as $HAuCl_4$. Once loaded by a method developed by Brust,[76] zero-valent gold was formed by reduction with $NaBH_4$. Surface plasmon analysis by UV-Vis spectroscopy and size analysis with TEM both showed a correlation between the polymer molecular weight and the nanoparticle size. While the molecular weights of the final products were not explicitly provided, the thiol-functionalized hyperbranched polyglycerol core with M_n = 2000 g/mol

yielded nanoparticles with a diameter of 3.0 ± 1.6 nm while the higher molecular weight, and larger, template (polyglycerol core M_n = 8000 g/mol) produced larger nanoparticles measuring 5.1 ± 2.4 nm diameter. The larger and higher molecular weight templates had a higher sulfur content, enabling the coordination of more gold and resulting in larger particles, as shown in Figure 3.25.

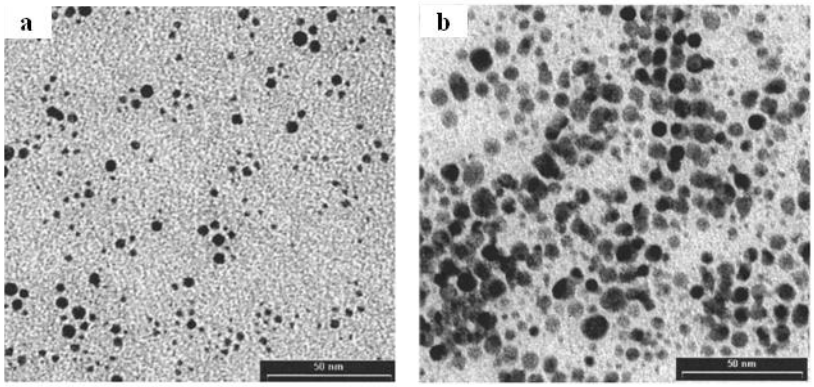

Figure 3.25 Gold nanoparticles templated by hydrophobically modified (a) low and (b) high molecular weight hyperbranched polyglycerols.[75]

3.4.3 Arborescent Polymer Templates

The application of arborescent polymer species as scaffolds for the preparation of metallic nanoparticles has been very limited. Recently, Gauthier and Dockendorff demonstrated the use of arborescent core-shell-corona (CSC) copolymers constructed with polystyrene and poly(2-vinylpyridine) segments, of the type investigated in Chapters 5 and 6 of this Thesis, to template gold nanoparticles.[17] The CSC morphology of the PS-*g*-(P2VP-*b*-PS) species is analogous to unimolecular reverse micelles, but also incorporate a hydrophobic core. As previously seen for a number of templates, the P2VP phase is able to coordinate polar species

and many metallic compounds due to its nitrogen content. In this preliminary report, the authors stated that the overall generation number of the arborescent copolymer template did not govern the size and dispersity of the nanoparticles. The polymer structure did influence the distribution of gold ions within the template as shown in Figure 3.26, however.

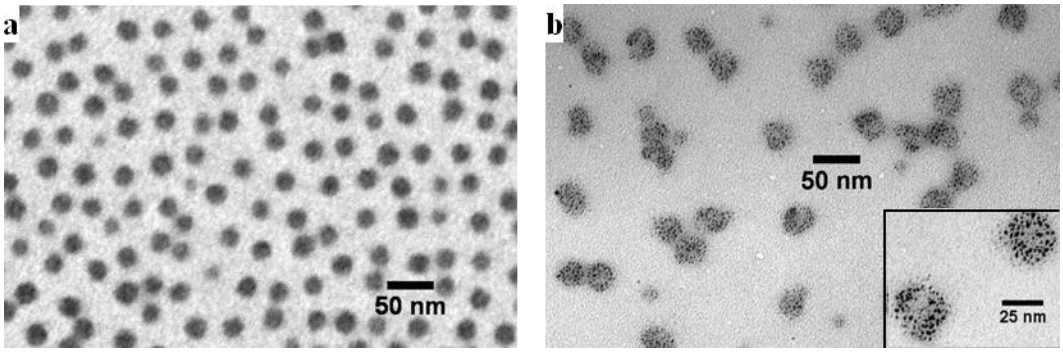

Figure 3.26 TEM micrographs obtained for (a) G0 and (b) G2 templates loaded with $HAuCl_4$.[17]

The synthesis and the application of these unique polymer architectures as metallic nanoparticle templates will be discussed at length in Chapters 5 and 6.

A polymer having a comparable chemical make-up, but a different architecture, is the comb-branched (or brush) polymer structure which has also been applied as nanoparticle template. A brush polymer is analogous to a generation 0 arborescent polymer, and can form rod or cylinder-like structures with high aspect ratios. Schmidt thus investigated a brush polymer incorporating a core of P2VP and a shell of PS chains, synthesized by polymerization of a block copolymer macromonomer.[77] The PS-*b*-P2VP copolymer was synthesized anionically by *sec*-BuLi initiation and sequential additions of styrene and 2VP. Ethylene oxide was added next, followed by methacryloyl chloride to afford the block

copolymer macromonomer. Free radical polymerization of the macromonomer with 2,2'-azobisisobutyronitrile (AIBN) yielded brush-like topologies when the degree of polymerization of the macromonomer was much larger than that of the side-chains, as shown in Scheme 3.8. The resulting cylindrical polymers are shown schematically and by AFM imaging in Figure 3.27.

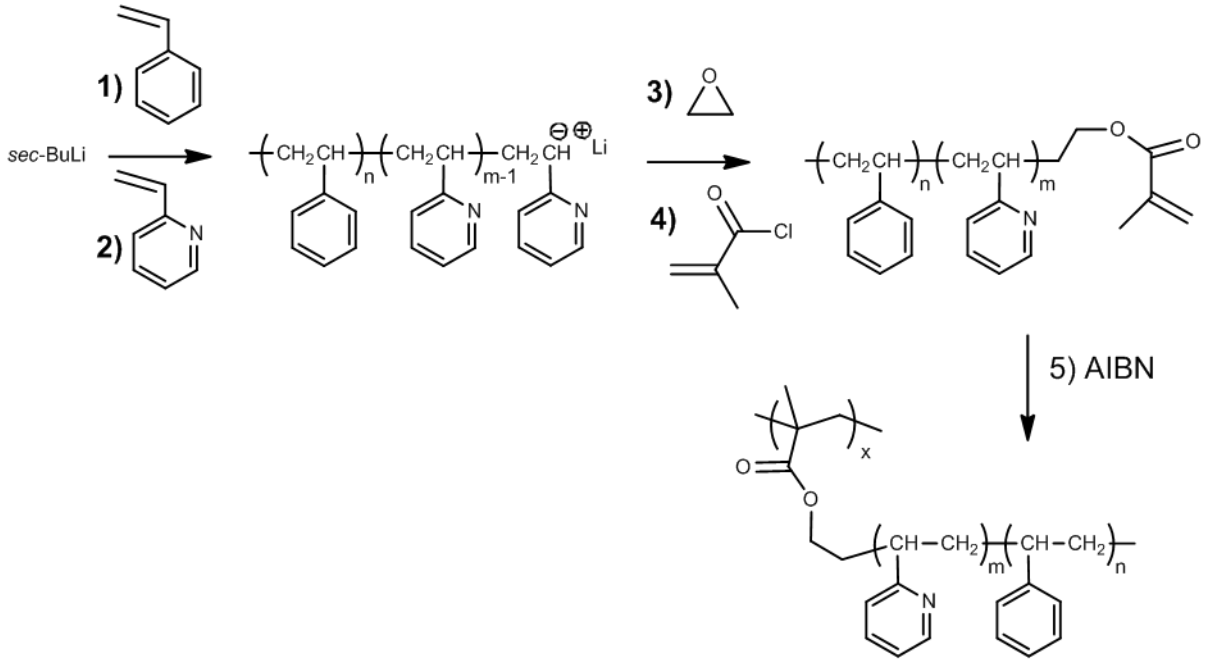

Scheme 3.8 Synthesis of amphipolar PS-P2VP cylindrical brushes.

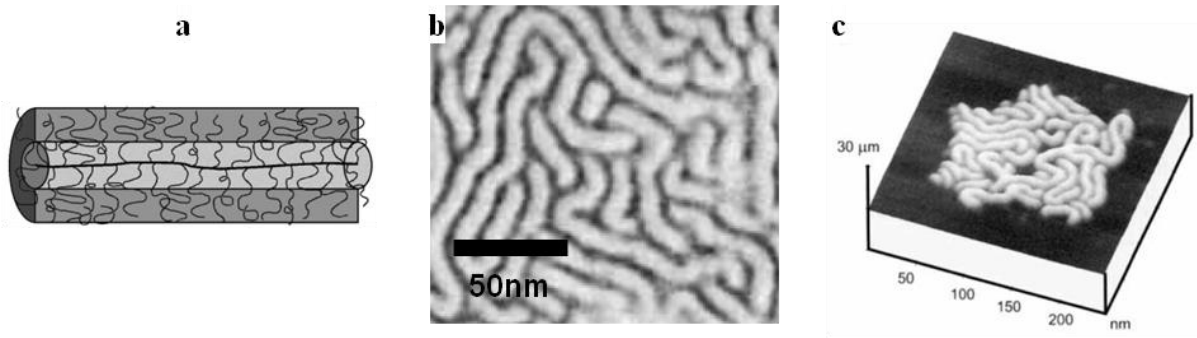

Figure 3.27 Cylindrical brush copolymer: (a) Schematic representation[78] and (b, c) AFM images.[77]

Schmidt loaded these cylinders with $HAuCl_4$ in a similar fashion to other PS-P2VP templates, to form PS-stabilized worm-like structures.[78,79] Interestingly, after loading with the gold compound, end-to-end association of the individual brushes was observed and led to the formation of longer cylinders, as seen in Figure 3.27. Various reduction methods were examined for the loaded brushes including UV light, electron beam irradiation, and hydrazine. TEM micrographs for the bare brush polymer, the gold-loaded brush, and after gold reduction by electron irradiation are compared in Figure 3.28.

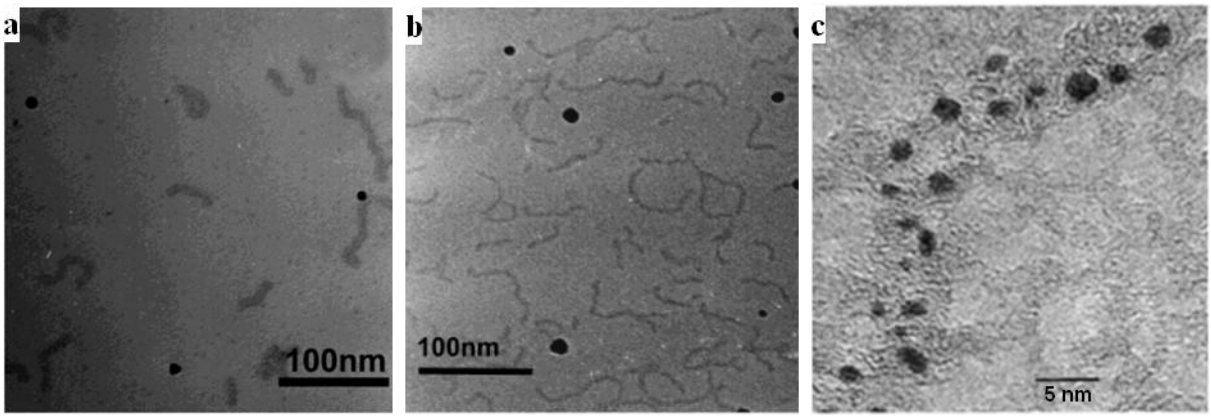

Figure 3.28 TEM for PS-*b*-P2VP brushes (a) stained with ruthenium tetroxide, (b) loaded with $HAuCl_4$, and (c) after reduction with a 150 keV electron beam.[78]

A nearly identical comb-branched polymer having a P2VP core and a poly(α-methylstyrene) (PMS) shell was synthesized by Ishizu.[80] The structure was formed by polymerization of a PMS-*b*-P2VP block copolymer macromonomer synthesized by sequential anionic polymerization, capped with *p*-chloromethylstyrene to yield an unsaturated moiety polymerizable with AIBN. The P2VP core of the resulting "double-cylinder" structure was loaded with Cu^{2+} using a solution of $CuCl_2$ in THF. A second film-loading method was investigated by soaking a film of the double-cylinder structures, adsorbed on a Teflon substrate, in a dioxane/water solution of $CuCl_2$. Films of the polymer-encapsulated Cu^{2+} were used for the polymerization of pyrrole, to create an electrically conducting film.[81]

Zhang and Müller also used ATRP to synthesize core-shell cylindrical brush polymers of identical architecture but with a different chemical make-up, having a poly(acrylic acid) (PAA) core and a poly(*n*-butyl acrylate) corona.[82,83] These structures were used to template the deposition of semiconducting CdS[84] nanowires and superparamagnetic

iron oxide.[85,86] While the architecture of the brushes was similar to that previously described, a different morphology was observed as intramolecular 'pearl-necklace'-like nanodomain formation characterized each cylinder. The domains are believed to be due to ionic crosslinking caused by the multivalent Cd^{2+} or Fe^{3+} ions combined with the monovalent carboxylate groups. The structure formed by metal coordination with the polymer templates can be seen in Figure 3.29. A cross section trace is provided (Figure 3.29c) to illustrate the undulating contour of the phase-segregated cylinders.

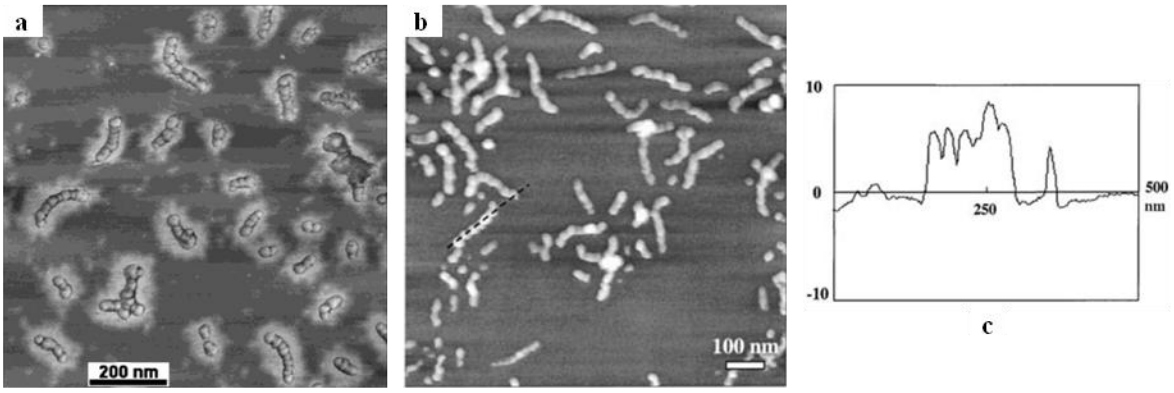

Figure 3.29 AFM images of pearl-necklace domain formation for poly(acrylic acid)-*block*-poly(*n*-butyl acrylate) brush copolymers loaded with (a) Cd^{2+},[84] (b) Fe^{3+},[86] and (c) cross section trace for Fe^{3+} loaded brush.[86]

3.5 Conclusions

Different methods and procedures have been developed to construct metallic nanoparticles, among which polymer templating represents a versatile and elegant approach. The range of chemical functionalities that can be introduced within polymer templates is very broad, allowing coordination with different metals and providing compatibility with a wide range of solvent environments. Both unimolecular and intermolecular templating methods offer interesting approaches to nanoparticle scaffolding. The various polymer architectures that have been reviewed, namely block copolymer micelles, star-branched polymers, and dendritic polymers, have unique morphologies resulting either from tailored synthesis or from self-assembly processes. With expanding interest in the nanotechnology field, interesting new developments are expected for both templating methods, as well as novel nanoparticle properties arising from these scaffolding processes.

Chapter 4

Arborescent Polystyrene-*g*-Poly(2-vinylpyridine) Unimolecular Micelles: Solution Properties and Application as Metallic Nanoparticle Templates

4.1 Overview

Branched copolymers with polystyrene and poly(2-vinylpyridine) segments were investigated for their properties as polyelectrolytes as well as their ability to coordinate metals. The arborescent (dendritic) species incorporate a hydrophobic polystyrene core, either with a linear or a branched architecture, synthesized by anionic polymerization and grafting. After functionalization with acetyl groups, the polystyrene substrates are coupled with living poly(2-vinylpyridine) having M_n = 5000 g/mol or 30,000 g/mol to produce a corona of hydrophilic chains. Due to their core-shell morphology, these copolymers behave like micelles in aqueous environments when the shell segments are protonated. Copolymer molecules derived from a linear polystyrene substrate aggregate when dissolved in aqueous HCl solutions; however, the copolymers with a G0, G1, or G2 arborescent polystyrene cores yield unimolecular micellar species under the same conditions. The 2-vinylpyridine residues within the corona can coordinate with metallic compounds such as $HAuCl_4$ or $Pd(OAc)_2$ and serve as templates for metallic nanoparticle construction. Solubility is reduced upon metal coordination, but distinct metal-loaded species resembling the host polymer molecules are still observed and can be characterized by microscopic techniques.

4.2 Introduction

Amphiphilic block copolymers, containing both hydrophilic and hydrophobic polymer segments, are typically synthesized by living polymerization techniques through sequential monomer additions. These copolymers have the ability to self-assemble into organized macromolecular structures in selective solvents at concentrations above their critical micelle concentration (CMC). This phenomenon has been extensively documented over the past few decades, as discussed in a recent review article by Gohy.[1] In aqueous environments, the incompatible hydrophobic segments associate to reduce their interactions with the polar phase, while the hydrophilic segments act as compatibilizer surrounding the hydrophobic assembly and allow it to remain dispersed. Micelle formation involves a dynamic equilibrium between free chains and the micellar structures: Chains diffuse in and out of the assembly, while a constant average concentration of free chains is maintained within the dispersion medium, as discussed in Chapter 3.

Self-assembly is not limited to diblock copolymers and can lead to a variety of superstructures including spheres, cylinders, vesicles, large compound micelles, or hierarchical assemblies with different packing modes in the solid state (e.g. face- or body-centered packing, hexagonal cylindrical packing, gyroid structures, and lamellae).[2] The morphologies created by the self-assembly of amphiphilic block copolymers depend upon factors such as the chemical nature of the segments, the respective length of each block, their degree of incompatibility, and the ionic strength in the case of charged systems.[3]

A relatively new class of macromolecules, the dendritic polymers, can provide an interesting comparison to the work done with block copolymer micelles. Dendritic polymers, broadly defined as macromolecules incorporating multiple branching levels, can be divided

into three subclasses depending on the specific characteristics of their branched architecture. Dendrimers and hyperbranched polymers are both obtained by the self-condensation of polyfunctional AB_n monomers but the former have a nearly perfect structure, while many defects are present in hyperbranched structures. Dendrigraft polymers (such as the arborescent polymers) have semi-controlled structures with a degree of structural perfection in-between the other two classes. Much of the pioneering work in the area of dendritic polymers began in the 1980s and early 1990s.[4–6]

Arborescent polymers, developed concurrently by Gauthier and Möller[5] and by Tomalia et al.[6] in 1991, are characterized by a tree-like architecture and a narrow molecular weight distribution arising from successive grafting reactions of well-defined polymer segments. Interestingly, the characteristics of arborescent polymers can be tailored to yield covalently bonded (unimolecular) micellar structures, enabling a unique comparison to micelles formed through the dynamic association of block copolymer micelles, referred to as multi-molecular or intermolecular micelles. The experiments described herein involve core-shell (CS) amphiphilic arborescent copolymers comprised of a polystyrene (PS) core and a poly(2-vinylpyridine) (P2VP) corona. The synthesis of these branched polymers was accomplished according to a method reported by Gauthier et al.,[7] described as a divergent 'grafting onto' scheme using anionic polymerization and grafting.

The procedure begins with a linear PS substrate randomly functionalized with acetyl groups on 20 – 30 % of the structural units. 'Living' anionic polymerization is used to synthesize side-chains to be grafted onto the linear substrate, yielding a narrowly dispersed (PDI = $M_w/M_n \leq 1.1$) comb-branched polymer, also called a generation zero (G0) arborescent polystyrene. Additional acetylation and grafting cycles lead to upper generation PS substrates

(G1, G2, and so on). A schematic representation of the step-wise grafting procedure used for the synthesis of arborescent polymers is provided in Figure 4.1.

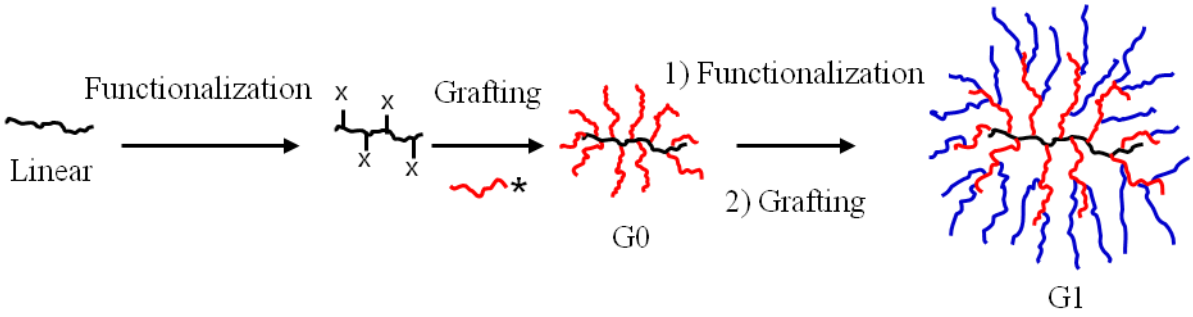

Figure 4.1 Schematic representation of the generation-based synthesis of arborescent polymers.

At any step of the synthetic procedure, the PS substrates can be coupled with living P2VP chains in place of PS to give branched structures with amphiphilic properties, useful as unimolecular micelles. This synthesis of a G1 amphiphilic CS architecture is shown in Figure 4.2 as an example.

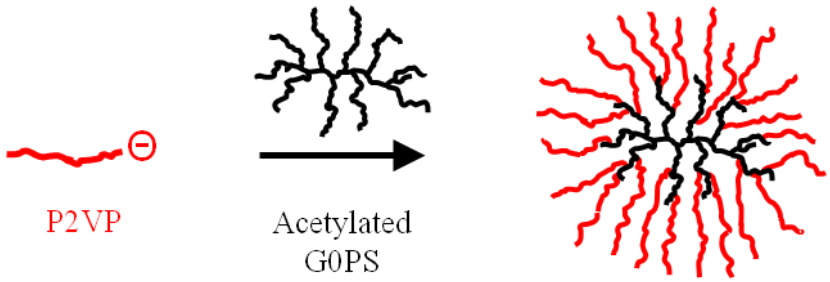

Figure 4.2 Synthesis of an amphiphilic G0PS-*g*-P2VP copolymer.

This micellar structure provides a basis for comparison to intermolecular micelles of diblock copolymers, particularly those obtained through the self-assembly PS-*b*-P2VP copolymers. A key feature of arborescent unimolecular micelles is their static, covalently bonded structure, and therefore the absence of a CMC. Consequently, concentration has no influence on the ability of these molecules to display micellar properties, and structural integrity is preserved even under non-selective solvency conditions. Given the covalently bonded structure of the unimolecular micelles, chain mobility is also presumably decreased as compared to their block copolymer (intermolecular) micelle analogues, since the PS core has a branched architecture. The non-polar core of arborescent species can still act as a holding compartment for hydrophobic compounds (such as drugs) which can be released over time, as shown in a previous study.[8] The first portion of current investigation focuses on the solution properties of these copolymers, particularly in their ionized state, leading to the formation of unimolecular micelles in aqueous environments.[7]

Another key feature specific to the chemical make-up of arborescent PS-*g*-P2VP copolymers is their ability to coordinate with metallic compounds, leading to their use as a template for the formation of metallic nanoparticles. As discussed in Chapter 3, much research has been completed on metallic nanoparticle templating within the core of reverse intermolecular micelles,[9-11] but less work has focused on the regular micelle approach in aqueous environments.[12] The arborescent PS-*g*-P2VP copolymers are compatible with aqueous environments when their P2VP shell is partly ionized, while the 2-vinylpyridine units can serve as metal binding sites either through coordination or ion exchange. Gold has been the focus of many studies since the inception of micellar templating.[2,9,10,13,14] This is particularly true for tetrachloroauric acid ($HAuCl_4$), as it is easy to handle and has been well-

documented in different systems. A schematic representation of P2VP ionization (for aqueous solubility) and metal coordination in a G0PS-*g*-P2VP arborescent copolymer can be seen in Figure 4.3, where the peripheral P2VP chains are shown in red and the branched PS core is shown in black.

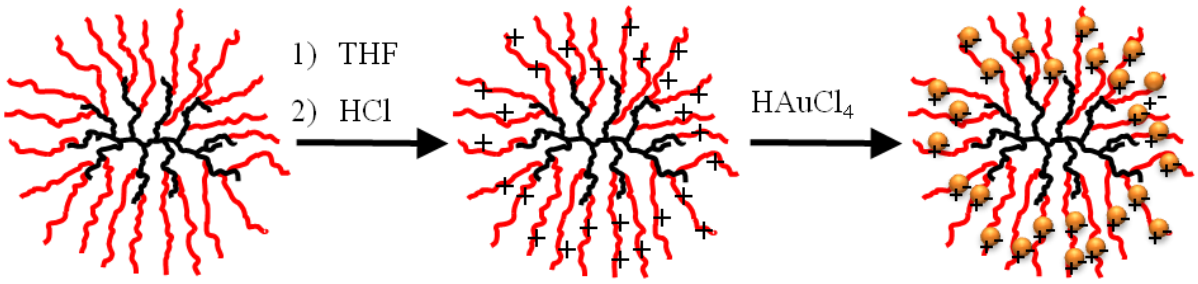

Figure 4.3 G0PS-*g*-P2VP arborescent copolymer ionization and metal loading.

Gold nanoparticles compatible with aqueous environments are attractive for their potential biological applications including bio-sensors and markers.[15] Consequently, metal loading in these branched copolymers has been investigated in conjunction with their solubility. These amphiphilic core-shell molecules can be viewed as potentially serving a dual purpose: Their hydrophobic core can be loaded with hydrophobic compounds for sustained release, while they can act as sensors or markers when their shell is coordinated with a metal. The copolymer compositions used in the current investigation are not biocompatible, but they can still provide a better understanding of how highly branched species respond to solvency in the presence of metal coordination. The information gathered can thus be useful in developing biocompatible analogues for practical applications.

4.3 Experimental Procedures

4.3.1 Synthesis

The arborescent copolymers used in this investigation were synthesized by Li et al.[7] as well as by Munam and Gauthier more recently.[16] Specifically, the solution ionization studies were completed with the copolymers synthesized by Li while the other samples, available in larger amounts, were used for the metal templating investigations. The main features of the synthetic protocols used for the two copolymer series are briefly described subsequently.

4.3.1.1 PS-*g*-P2VP Arborescent Copolymers for the Solution Ionization Studies

The arborescent copolymers used contained linear or branched polystyrene cores derived from M_n = 5000 g/mol PS segments and grafted with M_n = 5000 g/mol or 30,000 g/mol P2VP chains. The linear PS substrate was synthesized by anionic polymerization using *sec*-BuLi as initiator. The linear PS substrate was randomly functionalized with acetyl groups on ca. 30 % of the styrene units by Friedel-Crafts acetylation with $AlCl_3$ and acetyl chloride. To produce a G0PS substrate, living PS side-chains (M_n = 5000 g/mol) were synthesized and capped with 3 – 5 units of 2VP before titration with the acetylated PS substrate. The acetylation and grafting procedure was repeated to obtain a G1PS substrate. The arborescent copolymers were produced by addition of the acetylated PS substrate to a solution of living P2VP chains (M_n = 5000 g/mol or 30,000 g/mol), obtained by initiation with 1,1-diphenyl-3-methylpentyllithium. A detailed description of the synthesis of the PS substrates and the copolymers can be found in References 17 and 7, respectively.

4.3.1.2 PS-*g*-P2VP Arborescent Copolymers for Metallic Nanoparticle Templating

The arborescent copolymers used as metallic nanoparticle templates also contained a linear or a branched polystyrene core grafted with 5000 g/mol or 30,000 g/mol P2VP chains. The procedure serving in the synthesis of these copolymers was essentially identical with the one described previously, except that the reaction was carried out on a large scale (100-g scale, as opposed to 10-g in the first case). The only significant difference for the large-scale synthesis is the inclusion of 1,1-diphenylethylene before adding 3 – 6 equivalents of 2-vinylpyridine per living end to cap the living PS chains prior to grafting.[18]

4.3.2 Characterization and Sample Preparation

4.3.2.1 Polyelectrolyte Solutions

Two dissolution protocols were examined to ionize the PS-*g*-P2VP arborescent copolymers. In the first case the copolymers (in their powdered form) were directly dissolved in 0.1 N aqueous HCl (prepared from a 12.0 N reagent grade solution, Fisher, in Milli-Q water). In the second protocol, the arborescent copolymer was first dissolved in tetrahydrofuran (THF), and the solution was diluted with 10 volumes of 0.1 N aqueous HCl while maintained in a sonication bath (Bransonic ultrasonic cleaner, 2210R-MTH). The organic component (THF) volume fraction was therefore 9.1 %, and the copolymer concentration of the solutions ranged from 0.02 to 0.5 % w/v, the most dilute conditions being used for the characterization of the higher generation polymers.

4.3.2.2 Viscosity Measurements

Knowledge of the viscosity of the polymer solutions was required for the hydrodynamic radius calculations. The viscosity was measured with a Kimax 300 Ostwald viscometer

immersed in a 25 °C controlled temperature bath. The solutions were filtered with a 5 μm PTFE membrane filter before measurement. Each flow time measurement for the solutions and the pure solvent was performed five times. The viscosity of the polyelectrolyte solutions was calculated from the relative flow times and the absolute viscosity of water (η = 0.89 cP).[19]

4.3.2.3 Metal Loading in Arborescent Copolymers

Solution Loading of $HAuCl_4$. The arborescent copolymers were dissolved in THF (10 mg/mL or 1.0 % w/v) from the powdered state and 9 volumes of aqueous HCl were slowly added with vigorous stirring or with sonication to provide a solution with 10 % THF content. The amount of HCl added to the polymer solution was 0.75 equiv with respect to 2VP residues (HCl:2VP units ratio = 0.75). For each sample the amount of HCl required was calculated and diluted with water to maintain the 1:9 THF:H_2O ratio after addition to the THF copolymer solution. $HAuCl_4$ (Alfa Aesar, 99.9 %) was added slowly as a 1.0 % solution in Milli-Q water (ca. 90 μL per mL of copolymer solution) with vigorous mixing to load the polymer with 0.25 equiv $HAuCl_4$ per 2VP unit. The mole fraction of 2VP residues in the copolymers, used to determine the exact amounts of HCl and $HAuCl_4$ added to the micellar solutions, was determined by ^{1}H NMR analysis (Appendix 4.1). The solutions were stirred for at least 24 h before analysis. As a specific example, 2.5 mg of PS-*g*-P2VP30 (98 % 2VP content) were dissolved in 0.25 mL of THF, and to this solution 2.0 mL of 0.009 N HCl was added, followed by 0.23 mL of 10 mg/mL $HAuCl_4$ in Milli-Q water.

Film Loading of $HAuCl_4$. In the film loading technique, an ionized copolymer solution was deposited on a substrate before exposing the dry film to a $HAuCl_4$ solution. The ionization

procedure was identical to that described in the previous section, but 1 equiv of HCl was added with respect to the 2VP residues (HCl:2VP units ratio = 1.0) for improved adhesion to the substrate. The solutions were cast onto TEM grids or AFM substrates as described in Sections 4.3.2.9 and 4.3.2.10, respectively. Once the polymer film was prepared, it was exposed to a 1.0 % w/v $HAuCl_4$ solution in Milli-Q water by placing a single drop on the TEM grid, or multiple drops on the AFM (1 cm^2) film with a syringe and a 22-gauge needle. The solution was left in contact with the surface for 1 min for the TEM films and 5 min for the AFM films. The solution was then wicked away with filter paper and the film was rinsed by gently dropping Milli-Q water onto the surface with a syringe. Remaining water droplets were wicked away with filter paper and the film was blow-dried with a gentle stream of filtered air. The films were left to dry overnight before analysis.

Solution Loading of $Pd(OAc)_2$. Arborescent copolymers were dissolved in THF at a concentration of 0.1 % w/v (1 mg/mL). In a separate vial, palladium(II) acetate ($Pd(OAc)_2$; Strem Chemicals, min. 98 %) was dissolved in THF at a concentration of 1.0 % w/v. The amount of $Pd(OAc)_2$ solution required to reach the desired loading level (0.25 equiv or 0.5 equiv relatively to 2VP units) was slowly added to the polymer solution with vigorous stirring. Stirring was continued for at least 24 h before analysis.

4.3.2.4 Solution Reduction

Reduction of the gold salt-loaded copolymers was performed in solution with two separate reagents. Each reagent was added directly to the copolymer solution with vigorous stirring. Hydrazine monohydrate (Sigma-Aldrich, 98 %) was used as a 1 % v/v (10 μL/mL) solution in THF. A sodium borohydride ($NaBH_4$; Sigma-Aldrich, 98 %) solution in methanol (0.5 %

w/v, 5 mg/mL) was prepared immediately before addition. Each reducing reagent was added in a 10:1 ratio relatively to the metal content of the copolymers.

4.3.2.5 Nuclear Magnetic Resonance (NMR) Spectroscopy

^{1}H NMR spectroscopy was performed on a Bruker AM-250 instrument to determine the P2VP content of the arborescent copolymers and allow for targeting of the desired metallic loading level. Solutions in $CDCl_3$ (1.5 % w/v) were used for the analysis. See Appendix 4.1 for the peak integration algorithms used and the P2VP content calculations.

4.3.2.6 Size Exclusion Chromatography (SEC) Analysis

Analytical SEC was used for the characterization of the polystyrene substrates, the P2VP copolymers, the crude reaction products, and the fractionated copolymers. The SEC system consisted of a Waters 510 HPLC pump, a Waters 410 DRI detector, and a Wyatt Dawn DSP-F SEC-MALLS (multi-angle laser light scattering) detector operating at 632.8 nm, to allow the determination of the absolute molecular weight of the samples using the ASTRA v4.70 software package. Jordi DVB Mixed-bed Linear columns (500 mm × 10 mm, molecular weight range $10^2 – 10^7$ g/mol) were used for the separation. The system was operated at a flow rate of 1 mL/min at room temperature (25 °C), with THF as the mobile phase.

4.3.2.7 Refractive Index Increment

The refractive index increment (dn/dc) of all the copolymers was measured at 25 °C using a Brice-Phoenix differential refractometer at both 510 and 632 nm. The instrument was calibrated with five different NaCl solutions ranging in concentration from 0.2 to 2.0 % w/v. The refractive index of the copolymer solutions was measured at five different concentrations

from 0.2 and 1.0 % w/v for the G0 – G2 samples, while the G3 samples were measured from 0.1 to 0.5 % w/v.

4.3.2.8 Dynamic Light Scattering Measurements

Batch-wise dynamic light scattering measurements were carried out on a Brookhaven BI-200 SM light scattering goniometer equipped with a BI-2030AT 201-channel correlator and a 2-W argon ion laser operating at 514.5 nm. All the samples were measured at 25 °C and at a scattering angle of 90°, after at least 3 filtrations with a 0.45 μm PTFE membrane filter. The correlator was operated in the exponential sampling mode and hydrodynamic radii were calculated from the z-average translational diffusion coefficients obtained from first- and second-order cumulant analysis of the correlation function, to better account for polydispersity effects. Solutions were prepared at concentrations ranging from 0.02 to 0.25 % w/v, depending on the molecular weight (generation number) of the sample. Detailed theoretical background on this technique can be found in the Appendix 4.2.

4.3.2.9 Transmission Electron Microscopy (TEM)

Film Casting. Thin films were cast onto 300-mesh copper TEM grids coated with carbon and Formvar® (Electron Microscopy Sciences, FCF300-CU). For the film loading procedure, silicon monoxide-coated copper grids were used (Electron Microscopy Sciences, SF400-CU). The films were obtained by placing a drop of the solution (0.1 to 0.5 % w/v) onto the grid atop a piece of filter paper. The filter paper acted as a wicking agent to remove excess fluid and allow the formation of a thin film. The grid was then immediately transferred onto a fresh piece of filter paper and placed in a Petri dish for drying overnight under ambient conditions.

Instrumentation and Analysis Methods. The metal-loaded films were imaged with a Philips CM10 TEM instrument operating at 60 kV. The images were recorded with an Advance Microscopy Techniques 11 megapixel digital camera and the accompanying Image Capture Software Engine version 5.42.558. Feature size analysis was performed with the ImageJ processing software[20] by setting the scale for each digital image (pixels/nm) on the basis of the magnification and the image resolution used. Feature size measurement was carried out manually using the circle area function: Each feature was delimited manually by drawing a circle around the area of metal content, and the effective radius was calculated from the area. In some cases, a high pass filter was applied to the images with photo editing software to correct for uneven exposure. A minimum of 20 measurements were taken for each sample to provide adequate size distribution information.

4.3.2.10 Atomic Force Microscopy (AFM)

Substrate Preparation and Film Casting. Muscovite mica sheets cut into 1 cm^2 pieces were adhered onto a steel substrate of approximately the same size using double-sided tape, to allow securing of the sample to the magnetic spin coater and the magnetic scanner head of the AFM instrument. Immediately prior to film casting, the mica was cleaved with a strip of Scotch™ Magic™ brand tape to expose a fresh (hydrophilic) surface.

Silicon substrates were also used after cleaning and activation immediately prior to film casting. A silicon wafer was cleaved into 1 cm^2 pieces with a diamond knife, cleaned in an ultrasonic bath with 2-propanol for 3 min, and then blown dry with filtered nitrogen. The wafers were then exposed to UV light (UV Technik Speciallampen GmbH) and ozone for 12 min with an oxygen flow of 500 mL/min. When the UV/ozone apparatus was unavailable,

acidic etching served to clean and activate the silicon surface by submersion in a solution of sulfuric acid and hydrogen peroxide (30 %) 3:1, followed by water, acetone, methanol, and 2-propanol rinses. The substrates were dried with a stream of filtered nitrogen and fixed to a metal substrate using double-sided tape.

After mounting the substrate on the magnetic spin coater, enough solution (0.1 to 0.5 % w/v) was placed on the surface with a pipette to completely cover it and the substrate was spun for at least 15 s at 3000 rpm.

Instrumentation and Analysis Methods. AFM micrographs were recorded in the tapping mode with a Nanoscope III (Digital Instruments, model MMAFM-2, scan stage J) SFM instrument housed in a NanoCube acoustic isolation cabinet/enclosure mounted on a Halcyonics Micro 40 vibration isolation table. The measurements were performed under ambient conditions using Si probes (VistaProbes, T300) having a spring constant of 40 N/m, a resonance frequency of 300 kHz, and the following characteristics: length 125 μm, width 40 μm, tip height 14 μm, and tip radius < 10 nm. The images were analyzed using the Nanoscope v5.30r3.sr4 software.

4.4 Results and Discussion

4.4.1 Solution Properties

The characteristics of arborescent copolymers can be tailored through variations in the synthetic procedure. Thus composition can be varied by adjusting the length of the grafted side-chains, the grafting density through the functionalization level of the substrate, and the overall branching functionality and dimensions by using acetylated PS substrates of different generations. In the current investigation the P2VP side-chain length and the PS substrate generation were varied, while the functionalization level was maintained constant at an average level of 24 % and the PS core building blocks used had a M_n of ca. 5000 g/mol in all cases. The target M_n of the P2VP side-chains grafted to form the corona was either 5000 g/mol or 30,000 g/mol. Full characterization data for the PS substrates and the copolymers used in the solution property investigations are provided in Table 4.1 and Table 4.2, respectively. These were synthesized previously.[7,17]

Table 4.1 Characteristics of polystyrene substrates used for P2VP grafting

	Side-chains			Substrate		
Polymer	M_w[a]	M_w/M_n[a]	F[b]	M_w[a]	M_w/M_n[a]	M_w[c]
PS (linear)	–	–	25	5.1×10^3	1.07	–
G0PS	4400	1.09	22	5.3×10^4	1.08	3.3×10^4
G1PS	4500	1.07	27	4.3×10^5	1.08	1.3×10^5
G2PS	5000	1.08	20	3.9×10^6	1.09	4.5×10^5

[a] Absolute values from SEC-MALLS measurements before acetylation; [b] Acetylation level (mole %) from ^{1}H NMR analysis; [c] Apparent values from SEC analysis using a linear PS standards calibration curve

Table 4.2 Arborescent copolymers used in the solution properties investigation[a]

	P2VP Side-chains			Graft Copolymer			
Copolymer[a]	M_w[b]	M_w/M_n	dn/dc (mL/g)	M_w[b]	M_w/M_n	f_w[c]	% 2VP[d]
PS-*g*-P2VP5	5600	1.07	0.167	7.2×10^4	1.06	12	92
G0PS-*g*-P2VP5	5400	1.06	0.155	5.3×10^5	1.08	88	88
G1PS-*g*-P2VP5	5900	1.08	0.149	4.3×10^6	1.07	650	87
G2PS-*g*-P2VP5	5300	1.07	0.166[e]	2.4×10^7	–[f]	3790	82
PS-*g*-P2VP30	34900	1.06	0.168	3.9×10^5	1.06	11	> 97
G0PS-*g*-P2VP30	35200	1.07	0.158	2.5×10^6	1.07	70	97
G1PS-*g*-P2VP30	35700	1.07	0.148	1.3×10^7	1.08	350	96
G2PS-*g*-P2VP30	32500	1.06	0.140[e]	6.1×10^7	–[f]	1760	91

[a] All grafting reactions done at 0 °C with 5 equiv LiCl added; [b] Absolute values from SEC-MALLS or laser light scattering measurements; [c] Branching functionality: number of branches added in the last grafting cycle; [d] P2VP content from ^{1}H NMR analysis, mol %; [e] dn/dc at 510 nm, all other values determined at 632 nm; [f] G3 molecules did not elute

The arborescent copolymer sample nomenclature, seen in Table 4.2 and throughout this Chapter, provides $M_n \times 10^{-3}$ of the P2VP side-chains. Arborescent copolymers with short P2VP segments can be viewed as branched block copolymers with radial symmetry, having a relatively thin corona in comparison to the core dimensions. These arborescent copolymers are therefore analogous to crew-cut micelles[21] (Figure 4.4a). When long P2VP segments are used in the final grafting step the corona layer is thick relatively to the substrate, yielding a structure closer to a star-branched polymer (Figure 4.4b). The P2VP segments can be protonated by acids, making the molecules freely soluble in aqueous solutions and giving them their unimolecular micelle characteristics.

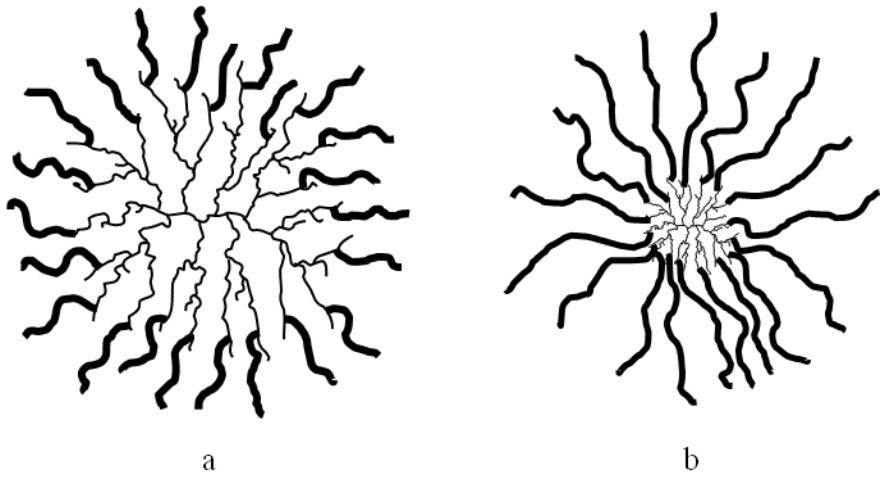

Figure 4.4 Comparison of the structures obtained when a G1 polystyrene substrate is grafted with (a) short and (b) long P2VP side-chains.

The extent of solubilization of the branched polyelectrolyte molecules was investigated with dynamic light scattering (DLS) measurements. Two different dissolution protocols were applied to compare their influence on the hydrodynamic size and size distribution of the dissolved species. In the first case the copolymers were dissolved directly in 0.1 N aqueous HCl. In the second protocol, aiming to minimize aggregate formation, the copolymers were first dissolved in THF and then diluted with 10 volumes of 0.1 N aqueous HCl to induce a more gradual increase in the ionization level. First- and second-order analysis of the correlation function, $|g_1(\tau)|$, provides information on the size dispersity of the system. The first- and second-order hydrodynamic radii (r_{h1} and r_{h2}, respectively) obtained are compared for the two dissolution protocols in Table 4.3. The uncertainties reported are either the standard deviation for a series of 10 measurements or 1 nm, whichever is larger. The results for the first- and second-order analyses are expected to be identical for a monodispersed (uniform) size distribution, since the correlation function can be represented

by a single exponential decay under these conditions.[22] The discrepancy between the two results therefore increases as the size distribution broadens.

Table 4.3 Hydrodynamic radii of P2VP copolymers in 0.1 N HCl

	HCl[a]		THF/HCl[b]	
Sample	r_{h1}[c]	r_{h2}[d]	r_{h1}[c]	r_{h2}[d]
PS-*g*-P2VP5	47 ± 26	21 ± 10	13 ± 7	8 ± 1
G0PS-*g*-P2VP5	15 ± 1	13 ± 1	14 ± 1	14 ± 1
G1PS-*g*-P2VP5	23 ± 1	21 ± 1	26 ± 1	26 ± 1
G2PS-*g*-P2VP5	59 ± 1	56 ± 1	51 ± 1	49 ± 1
PS-*g*-P2VP30	32 ± 3	20 ± 2	14 ± 1	10 ± 1
G0PS-*g*-P2VP30	42 ± 1	40 ± 1	39 ± 1	37 ± 1
G1PS-*g*-P2VP30	59 ± 1	57 ± 1	65 ± 4	57 ± 1
G2PS-*g*-P2VP30	80 ± 1	77 ± 1	68 ± 1	67 ± 1

[a] Direct dissolution into 0.1 N aqueous HCl; [b] Dissolution in THF and addition of 10 volumes of 0.1 N aqueous HCl; [c] Hydrodynamic radius from first-order analysis of the correlation function (nm); [d] Hydrodynamic radius from second-order analysis of the correlation function (nm)

For copolymers of overall generation G1 and above the first- and second-order analyses are in good agreement, confirming that the branched polyelectrolytes exist as isolated (monomolecular) species in solution. This phenomenon is observed even for direct aqueous 0.1 N HCl dissolution of the solid (powdered) samples. This contrasts with the G0 copolymer polyelectrolytes, derived from the linear polystyrene substrates (PS-*g*-P2VP5 and PS-*g*-P2VP30), which exist as aggregates in solution irrespective of the dissolution protocol used. There is a slight decrease in average size when the samples are first dissolved in THF prior to being protonated with the acidic solution, however.

Analysis of the correlation function with the CONTIN algorithm is often used to generate size distributions. CONTIN is a complex data analysis procedure developed by Provencher in the early 1980s,[23] based on the Laplace transform of the correlation function. The procedure acquired its name from "determining CONTINuous distributions in molecular weight (polydispersity) through photon correlation". The method can also be used to determine the distribution of other parameters such as relaxation times, electron densities, and diffusion coefficients. CONTIN analysis is useful to compare, on a semi-quantitative basis, the aggregation behavior of arborescent copolymers in solution. The size distributions in Figure 4.5 show the influence of the two dissolution protocols and the generation number on molecular aggregation for copolymers with 5000 g/mol P2VP side-chains in the corona. Even for the low-generation copolymers, the majority of the polyelectrolyte molecules remain isolated (non-aggregated) in solution (intensity maximum at r = 6 nm), but some molecules also associate and form aggregates seen as a larger size population with a radius of ca. 110 – 160 nm (Figure 4.5a). When the copolymer is first dissolved in THF prior to addition of the acid, there is a reduction in the relative amount of the large aggregated species (Figure 4.5b). The discrepancy between the first- and second-order correlation function analysis results can therefore be attributed unambiguously to aggregation of the molecules. It is also interesting to note that sample G1PS-*g*-P2VP5, with a higher branching functionality (and therefore a lower interpenetrability) than sample PS-*g*-P2VP5,[24] yields unimolecular micellar solutions without any notable aggregation irrespective of the preparation method used (Figure 4.5c, d). Narrowing of the size distribution is nonetheless observed when the polymer is protonated from a THF solution, in analogy to the decreased aggregation observed

for sample PS-*g*-P2VP5 under these conditions. Similar results were obtained for all copolymers based on G0 – G2 substrates.

The core-shell morphology of the copolymers obtained by grafting short hydrophilic P2VP chains on the hydrophobic polystyrene core is interesting not only to prevent aggregation, but also in terms of the solubilization and sustained release of hydrophobic compounds. The uptake and release of hydrophobic compounds from arborescent PS-*g*-P2VP5 copolymers has also been the topic of an investigation.[8]

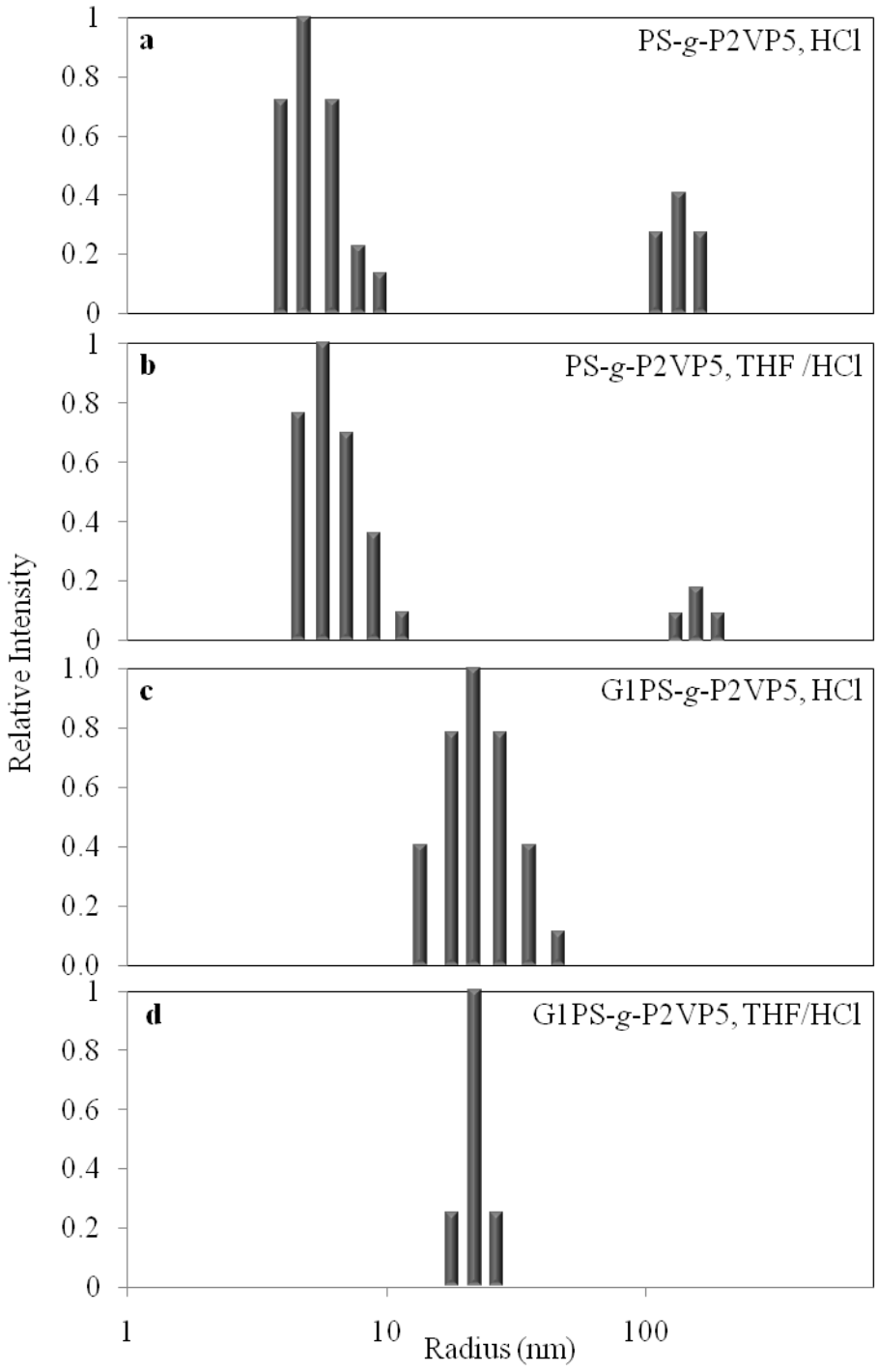

Figure 4.5 Hydrodynamic radius distributions obtained by CONTIN analysis of the correlation functions: PS-*g*-P2VP5 with (a) direct dissolution in HCl, (b) dissolution in THF prior to HCl dilution and G1PS-*g*-P2VP5 with (c) direct dissolution in HCl, (d) dissolution in THF prior to HCl dilution.

4.4.2 Metallic Loading of PS-*g*-P2VP Unimolecular Micelles

4.4.2.1 Loading with $HAuCl_4$

There are numerous reports on the use of polymers as scaffolds for the preparation of metallic nanoparticles, as discussed in Chapter 3. Two of the major template families investigated are block copolymer micelles (specifically multi-molecular / intermolecular micelles) and networks of amphiphilic polymers.[11] Dendrimers and hyperbranched polymers, structurally more closely related to this work, have also received attention as unimolecular scaffolds.[25]

The majority of polymeric nanoparticle templates are reverse micelle systems, allowing the loading of metallic compounds into their polar core, while the compatibilizing shell ensures solvency in non-polar organic solvents. Since arborescent PS-*g*-P2VP copolymers have an architecture corresponding to regular unimolecular micelles and are non-associating in aqueous solutions,[7] they may also function as metallic nanoparticle templates in aqueous environments. The P2VP segments allow the loading of polar species within the corona of the copolymers either through the coordination of transition metals with the pyridine moieties, or through protonation by metallic acids such as $HAuCl_4$. In the latter case, the metal acts as a counterion ($AuCl_4^-$) for the protonated species. The arborescent scaffold is interesting to investigate in terms of the loading distribution, the size, and the shape of the resulting nanoparticles, but metal templating also opens the path to the use of these copolymers as hydrophobic carriers. With the understanding that arborescent PS-*g*-P2VP can solubilize and release hydrophobic drugs,[8] metal coordination can also provide marker or sensor characteristics to these molecules allowing their monitoring by microscopic

or spectroscopic techniques. The ability of these unimolecular micelles to coordinate metals will be the focus of the present investigation.

The PS substrates[18] and the copolymers[16] used for the metallic loading studies were synthesized by Munam and Gauthier and are analogous to those investigated for the polyelectrolyte solution study previously discussed. Complete characterization data for the substrates and copolymers are provided in Table 4.4 and Table 4.5, respectively.

Table 4.4 Characteristics of polystyrene substrates used for the synthesis of the copolymer templates

	Side-chains			Substrate		
Polymer	M_n[a]	M_w/M_n[a]	F[b]	M_n[c]	M_w/M_n[c]	M_n[d]
PS (linear)	–	–	30	5.2×10^3	1.06	–
G0PS	5500	1.06	24	9.7×10^4	1.03	5.0×10^4
G1PS	4900	1.07	21	1.1×10^6	1.03	1.8×10^5
G2PS	5000	1.09	31	8.1×10^6	1.04	5.7×10^5

[a] Absolute values from SEC analysis using a linear PS standards calibration; [b] Acetylation level (mole %), determined by ^{1}H NMR analysis; [c] Absolute values from SEC-MALLS analysis; [d] Apparent values from SEC analysis using a linear PS standards calibration

Table 4.5 Characteristics of arborescent copolymers used as metallic nanoparticle templates

	P2VP Side-chains			Graft Copolymer				
Copolymer[a]	M_n[b]	M_w/M_n[b]	G_y[c]	M_n[b]	M_w/M_n[b]	f_w[d]	%2VP[e]	C_e[f]
PS-*g*-P2VP5	5100	1.15	96	7.4×10^4	1.08	13	93	90
G0PS-*g*-P2VP5	5500	1.15	90	1.1×10^6	1.08	182	91	82
G1PS-*g*-P2VP5	6200	1.10	70	8.4×10^6	1.09	1177	87	53
G2PS-*g*-P2VP5	4100	1.14	42	3.3×10^7	1.10	6073	87	25
PS-*g*-P2VP30	31500	1.08	80	2.6×10^5	1.08	8	98	54
G0PS-*g*-P2VP30	27700	1.08	71	2.4×10^6	1.10	83	96	37
G1PS-*g*-P2VP30	32700	1.07	25	1.1×10^7	1.08	303	90	14
G2PS-*g*-P2VP30	25600	1.10	5	2.5×10^7	1.08	660	80	3

[a] All grafting reactions done at 0 °C with 5 equiv LiCl added; [b] Absolute values from SEC-MALLS or laser light scattering measurements; [c] Grafting yield: fraction of side-chains attached to the substrate; [d] Branching functionality: number of branches added in the last grafting cycle; [e] P2VP content from by ^{1}H NMR analysis, mol %; [f] Coupling efficiency: percentage of available coupling sites on the substrate consumed

Loading experiments with $HAuCl_4$ were initially attempted in pure and mixed solvents systems including toluene, chloroform, THF, methanol, and a 1:1 mixture of THF and methanol. The copolymers, when reacted with $HAuCl_4$ in these solvents, precipitated immediately upon addition of the metallic acid. The addition of the gold compound either in the solid salt form or as a solution in the same solvent produced similar results, although the solution addition protocol was preferred due to its ease of control over the amount of metal added. Direct addition of the solid (powdered) copolymers to an aqueous $HAuCl_4$ solution was also attempted; however, no copolymer solvation was observed in this case even after mixing for several days. Due to the difficulties encountered, these loading protocols were not investigated further.

The addition of a salt (NaCl) to increase the ionic strength of the solutions was also investigated, in an attempt to provide intermolecular charge shielding and prevent aggregation of the copolymer molecules. This approach led to no visible solubility improvement, but rather appeared to enhance aggregation and complicate microscopic (TEM) analysis. A TEM micrograph for $HAuCl_4$-loaded G0PS-*g*-P2VP5 (0.25 equiv per 2VP unit) in the presence of 1 % NaCl, provided in Figure 4.6, only displays irregular aggregates and crystalline salt residues. This result can be compared with Figure 4.8b, prepared without salt and under different conditions to be discussed later in this Chapter.

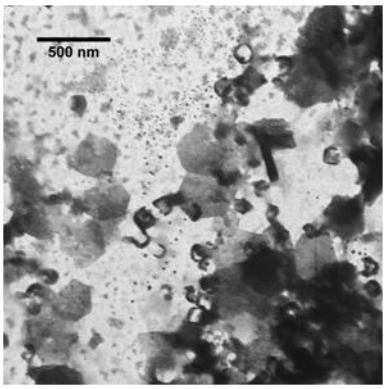

Figure 4.6 TEM micrograph for $HAuCl_4$-loaded G0PS-*g*-P2VP5 in the presence of NaCl.

The poor results obtained for the complexation of $HAuCl_4$ in organic solvents led to the development of the standard procedure described in Section 4.3.2.1, derived from the method developed for arborescent copolymer protonation in Reference 7. The arborescent copolymers were first dissolved in THF (1.0 % w/v) and gradually protonated by the addition of an aqueous HCl solution at a level of 3:4 HCl:2VP, effectively targeting 75 % protonation of the 2VP residues. The calculated pH of the solution used for protonation was determined

to be 2.2, which has been reported to protonate P2VP to a level of at least 70 %.[26] Aqueous $HAuCl_4$ (1.0 % w/v) was then added corresponding to the desired loading level (0.25 equiv per 2VP residue). The final solutions contained 10 % THF (v/v) in all cases. The mole fraction of 2VP residues in the copolymers, required to target that loading level, was determined by ^1H NMR analysis as shown in Appendix 4.1. This relatively low loading level (0.25 equiv per 2VP unit) was selected to allow the majority of free (uncoordinated) 2VP units in the copolymer to become protonated and ensure solubility in the aqueous environment. It was also thought that this would be particularly important when $HAuCl_4$ is reduced to elemental gold (Au^0) and thus no longer contributes to solubility in the polar environment.

The results discussed previously on the solubility of the arborescent P2VP copolymers showed that while all the samples were soluble, the copolymers of overall generations G1 – G3, in particular, were devoid of aggregation. A similar qualitative solubility trend was observed for the copolymers loaded with $HAuCl_4$ in the THF/HCl mixture, even though stability was dependent on the degree of loading and on solution aging. At a loading level of 0.25 equiv (1:4 Au:2VP), all templates formed transparent solutions regardless of the generation number or the length of the P2VP side-chains. After one week of storage in a sealed vial without stirring, G2 and G3 copolymer solutions remained clear and devoid of any colloidal precipitate, while the G0 and G1 copolymers displayed increased cloudiness and sedimentation. Quantification of the degree of colloid or precipitate formation was not attempted. TEM analysis reflects these qualitative observations, as can be seen in Figure 4.7 and Figure 4.8 for the samples with 5000 g/mol and 30,000 g/mol P2VP side-chains, respectively.

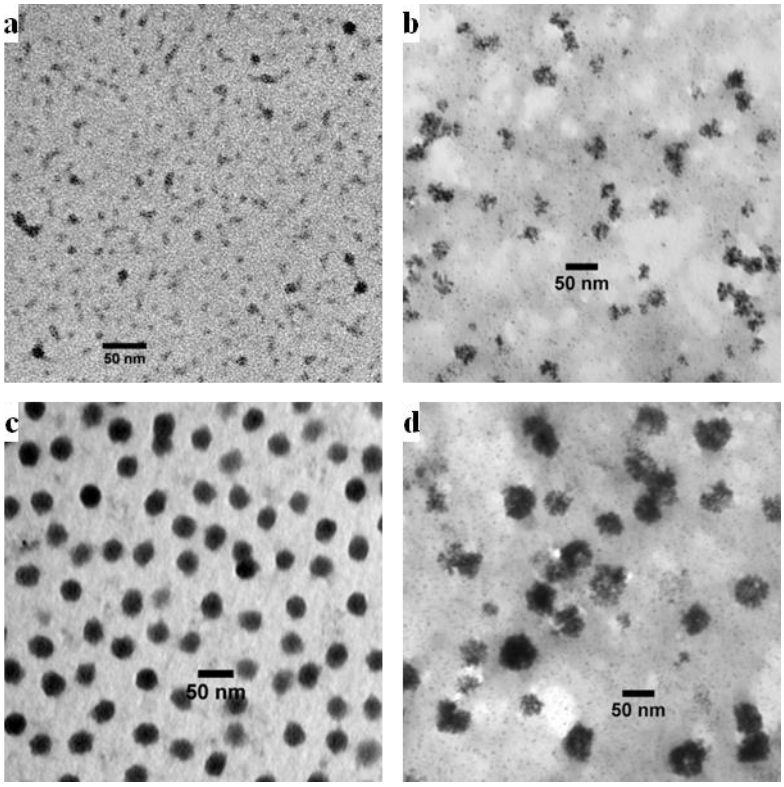

Figure 4.7 TEM micrographs for arborescent copolymers with 5000 g/mol P2VP side-chains loaded with 0.25 equiv $HAuCl_4$/2VP units: (a) PS-*g*-P2VP5, (b) G0PS-*g*-P2VP5, (c) G1PS-*g*-P2VP5, and (d) G2PS-*g*-P2VP5.

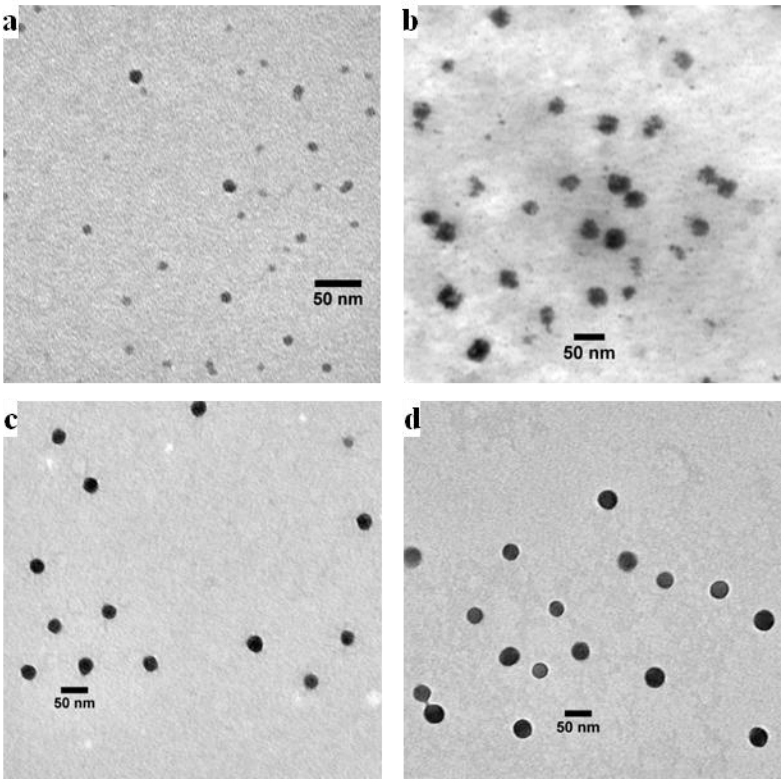

Figure 4.8 TEM micrographs for arborescent copolymers with 30,000 g/mol P2VP side-chains loaded with 0.25 equiv $HAuCl_4$/2VP units: (a) PS-*g*-P2VP30, (b) G0PS-*g*-P2VP30, (c) G1PS-*g*-P2VP30, and (d) G2PS-*g*-P2VP30.

It is interesting to note that the gold salt appears to be uniformly distributed within the G2PS-*g*-P2VP30 copolymer (Figure 4.8d), as shown by its smooth and uniform spherical features. Copolymer G2PS-*g*-P2VP5 has a different appearance, however, with feathered edges (Figure 4.7d). This difference is attributed to the length for the P2VP chains relative to the core. The long P2VP chains extend well beyond the PS chains within the core, such that it has little or no influence on the distribution of the metal. For short P2VP segments, in contrast, interpenetration of the PS chains in the core and the P2VP chains in the corona appears to affect the distribution of the gold in template G2PS-*g*-P2VP5.

The solutions of gold-loaded templates were stable for up to 48 h, at which point PS-*g*-P2VP and G0PS-*g*-P2VP samples formed a colloidal precipitate, seen as a transition from a clear to a cloudy or opaque solution. The G1PS-*g*-P2VP and G2PS-*g*-P2VP templates were stable without signs of colloidal precipitate formation for over one week. The stability of these metal-loaded copolymers was not investigated further, although future work with dynamic light scattering would provide useful quantitative data in that respect.

At increased loading levels (0.50 equiv or 1:2 Au:2VP), colloidal precipitate formation was immediately evident for samples PS-*g*-P2VP5, G1PS-*g*-P2VP30, and G2PS-*g*-P2VP30. All the template samples formed colloidal precipitates that sedimented within seven days in the absence of stirring. At a loading level of 0.75 equiv, all the samples precipitated immediately.

Microscopic analysis of the samples forming colloidal precipitates was for the most part unsuccessful, the large flocculated particles being wicked away during film casting on the TEM grid. For example, only small dense nanoparticles (1.5 ± 0.5 nm radius) were visible for PS-*g*-P2VP5 loaded with 0.50 equiv of Au. These features are significantly smaller than the bare template dimensions and are thus attributed to unbound residual $HAuCl_4$ clusters. Subsequent treatment of the film with iodine vapors, to selectively stain the P2VP phase,[27] led to no change in feature characteristics, which supports the conclusion that no copolymer molecules were left on the grid. Furthermore, reports exist for $HAuCl_4$-loaded P2VP copolymers showing a diffuse loading pattern in TEM analysis (as a light grey or sometimes speckled appearance within each P2VP-loaded region),[28] which was not observed in the current case. A speckled gold distribution is evident for the 0.25 equiv $HAuCl_4$-loaded samples seen in Figure 4.7 and Figure 4.8, however.

Even for template solutions displaying good optical clarity, larger colloidal aggregates were found in TEM analysis. This was true also for the upper generation samples, which remained clear after extended storage: Multi-molecular species were visible amongst the unimolecular metal-loaded domains, as shown in a representative TEM micrograph in Figure 4.9.

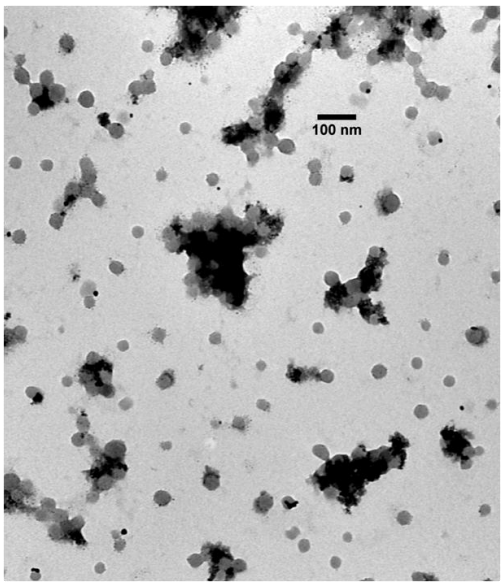

Figure 4.9 TEM micrograph for intermolecular aggregates formed by $HAuCl_4$-loaded G2PS-*g*-P2VP30.

The radius of the isolated Au-loaded templates, measured from the TEM micrographs of Figure 4.7 and Figure 4.8, are listed in Table 4.6. The multi-molecular (aggregated) species were not accounted for in the measurements, and the bulk polymer radii (calculated for collapsed spheres) are also provided for comparison.

Table 4.6 $HAuCl_4$ domain radii by TEM analysis and theoretical bulk polymer radii

	Radius (nm)		
Copolymer	TEM[a]	Bulk[b]	Au-Poly[c]
PS-*g*-P2VP5	5 ± 1	3	3
G0PS-*g*-P2VP5	14 ± 2	7	8
G1PS-*g*-P2VP5	17 ± 1	15	15
G2PS-*g*-P2VP5	19 ± 2	23	24
PS-*g*-P2VP30	6 ± 1	5	5
G0PS-*g*-P2VP30	16 ± 2	10	10
G1PS-*g*-P2VP30	17 ± 1	16	17
G2PS-*g*-P2VP30	20 ± 2	21	22

[a] Manually measured from features on micrograph; [b] Theoretical, copolymer only; [c] Theoretical, copolymer loaded with 0.25 equiv $HAuCl_4$

The theoretical bulk copolymer and Au-polymer complex radii (r_{bulk}) were calculated from Equation 4.1, where N_A represents Avogadro's number (6.022×10^{23} mol^{-1}), ρ is the density, and M_n is the corresponding number-average molecular weight of the template (Table 4.5), or the effective M_n of the Au-copolymer complex. The average density was calculated for each specific copolymer given its composition and the following densities of each component (ρ^{PS} = 1.01 g/mL, ρ^{P2VP} = 1.09 g/mL, ρ^{Au} = 3.9 g/mL).

$$r_{bulk} = \left(\frac{M_n}{N_A \rho} \Big/ \frac{4}{3}\pi \right)^{\frac{1}{3}} \tag{4.1}$$

The radius increases with the generation number of the template as expected, albeit the uncertainties, represented by the standard deviation of measurement across at least 20

features, are large enough for the error domains to overlap in some cases. When compared with the hydrodynamic radii of the templates before loading (Table 4.3), the TEM radii are significantly smaller. This decrease is attributed to the partial collapse of the molecules upon coordination of P2VP with $HAuCl_4$, reducing the compatibility of the solvent with the P2VP phase, as evidenced by sample precipitation for increased loading levels and residence time. It should also be considered that the TEM measurements were performed on dry polymer films, more closely resembling the bulk material than the hydrodynamic measurements where the molecules are swollen by the solvent.

When compared to the bulk radii calculated for the copolymers using Equation 4.1, the TEM radii are larger in most cases due to flattening of the polymer templates by adsorption onto the TEM grid substrate. Collapse of the polymer scaffold would be expected to counteract this size increase due to flattening. There is indeed a decreasing trend in the percentage difference between the TEM radius and the calculated bulk radius from G0PS-*g*-P2VP to G2PS-*g*-P2VP polymers. For the 5000 g/mol P2VP samples, the discrepancies between the TEM and bulk radii for G0PS-*g*-P2VP5, G1PS-*g*-P2VP5, and G2PS-*g*-P2VP5 amount to 47, 14, and –21 %, respectively, and are well outside the uncertainties on the TEM measurements, and suggest that the trend is real. For the 30,000 g/mol analogues, the differences are 40, 6, and –5 % for G0PS-*g*-P2VP30, G1PS-*g*-P2VP30, and G2PS-*g*-P2VP30 templates, respectively. This trend is thought to result from the greater structural rigidity of increasing generation numbers;[24] upper generation copolymers display less flattening upon film formation and thus the measured (TEM) dimensions more closely resemble the calculated theoretical dimensions. The side-chains on the P2VP30 copolymers being longer

and more flexible than those on the P2VP5 copolymers, may also be able to rearrange more easily.

Visualization of the metal-loaded arborescent copolymers by AFM analysis proved to be challenging in some cases due to strong tip interactions with the charged polymers.[29] Height and phase images for metal-loaded G2PS-*g*-P2VP copolymers with short and long side-chains are compared in Figure 4.10 and Figure 4.11, respectively.

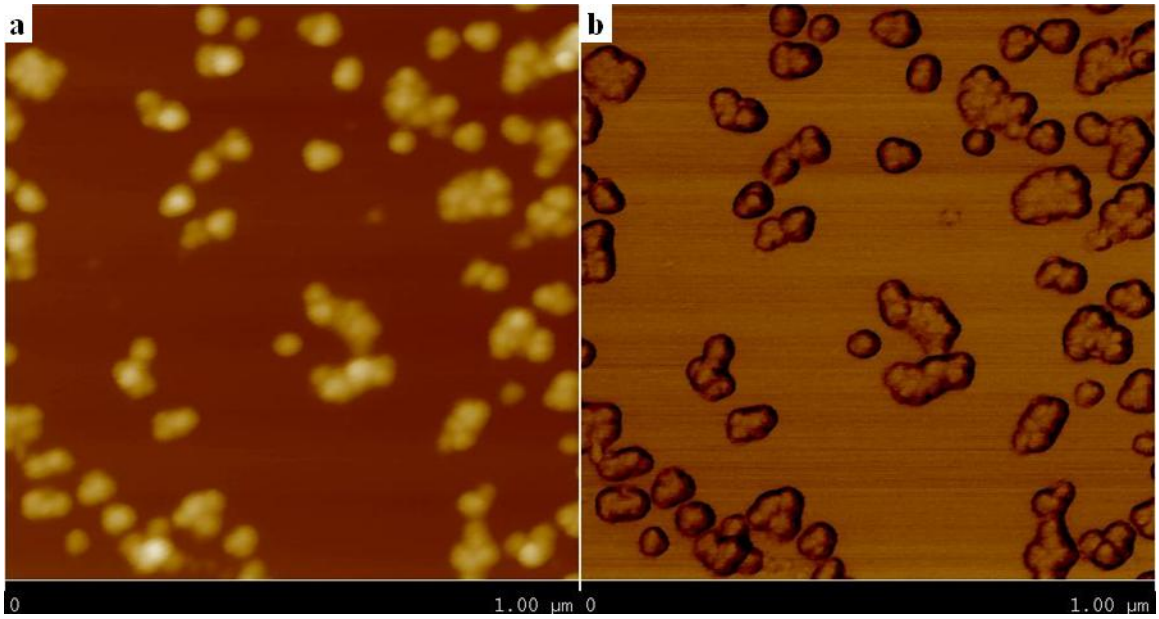

Figure 4.10 AFM images for $HAuCl_4$-loaded G2PS-*g*-P2VP5: (a) height and (b) phase scans.

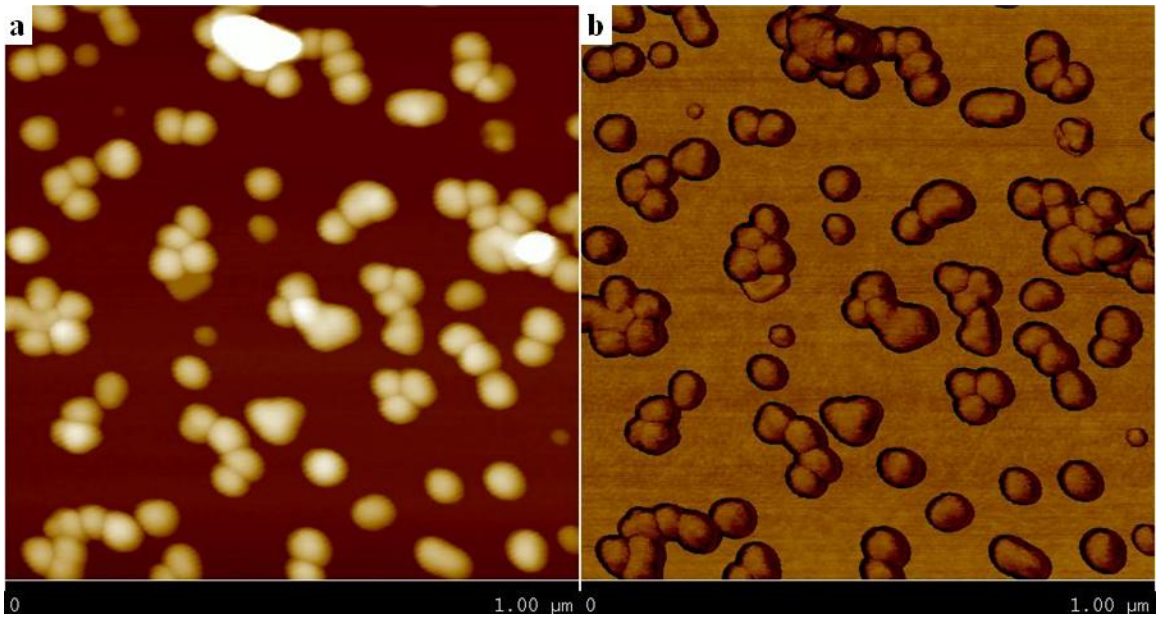

Figure 4.11 AFM images for $HAuCl_4$-loaded G2PS-*g*-P2VP30: (a) height and (b) phase scans.

Interesting parallels can be drawn between the AFM images and the TEM images of Figure 4.7 and Figure 4.8. The gold appears to be uniformly distributed in the TEM image obtained for the G2PS-*g*-P2VP30 copolymer (Figure 4.8d), and it displays a comparable uniformity in the AFM images: Both the height and phase images show well-defined spherical species with a smooth surface, as seen in Figure 4.11. Sample G2PS-*g*-P2VP5, which has a more jagged appearance in TEM analysis (Figure 4.7d), also appears to have a rougher surface in AFM imaging as compared to its P2VP30 analogue; however this could not be confirmed by cross section analysis due to resolution limitations of the instrument. The spherical structure and topography of the $HAuCl_4$-loaded structures is comparable to that observed for the native arborescent polymers.[30,31]

4.4.2.2 Solution Reduction

Two solution reduction regimes were examined for comparison to reported reduction conditions.[28,32] Anhydrous hydrazine is commonly used in organic solvents, but since loading was performed in aqueous solution there was little sense in using the anhydrous form.[33] We rather used hydrazine monohydrate (1 % v/v in THF) and sodium borohydride ($NaBH_4$, 0.5 % w/v in methanol). These reducers were added at a 10:1 ratio relative to gold in an attempt to 'freeze' the gold in its location within the copolymer and prevent Ostwald ripening.[34,35]

The yellow $HAuCl_4$-loaded copolymer solution turned purple immediately upon addition of either reducing agent. $NaBH_4$ is known to be a stronger reducing agent than hydrazine, and this was apparent as the solution turned purple faster. The reducing agent was added all at once with vigorous stirring of the copolymer solution. Immediate precipitation was observed in all cases once the entire aliquot was added, a clear solvent supernatant being obtained with adherence of a purple residue on the sidewalls of the vial. This complicated microscopic sample analysis, as many of the particles did not adhere to the TEM grid and were wicked away during film casting and yielded featureless samples. In most cases very large (0.5 μm) agglomerates of gold-rich material and clusters of nanoparticles carrying no resemblance to the polymer templates from which they were derived (Figure 4.7 and Figure 4.8) were observed. In cases where nanoparticles could be visualized, $NaBH_4$ led to smaller nanoparticles than hydrazine. Examples of nanoparticle agglomerates and isolated nanoparticles obtained by the two reduction methods are shown in Figure 4.12. Subsequent treatment of the hydrazine-reduced film with iodine vapor, to selectively stain the P2VP domains,[27] resulted in increased contrast for the large agglomerates and revealed spherical species believed to be the arborescent copolymers. This demonstrates that the polymeric

templates remain within the large agglomerates; however, the template molecules did not appear to be coordinated with any metal, as they only became visible following I_2 staining, demonstrating that the system is characterized by inter-template gold migration as observed previously for multi-molecular micelles.[2,10]

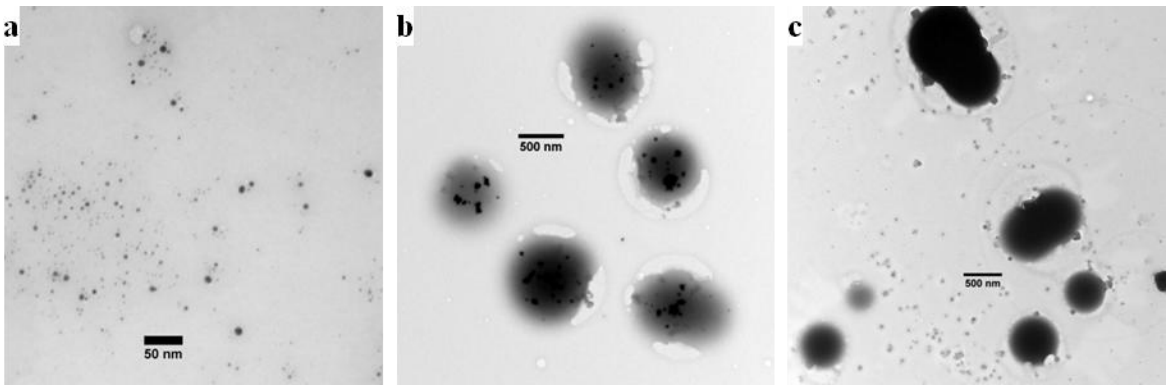

Figure 4.12 Gold nanoparticles obtained by $HAuCl_4$-loaded PS-*g*-P2VP5 and solution reduction using (a) $NaBH_4$, (b) hydrazine, and (c) hydrazine reduction followed by iodine vapor treatment to reveal P2VP phases.

The G1PS-*g*-P2VP copolymers allowed the best comparison of the two reduction methods as they yielded distinct measureable features (Figure 4.13). Large agglomerates were also present in these samples, as seen in Figure 4.13d, although these were not taken into consideration for size analysis. A low magnification TEM micrograph illustrating the larger gold agglomerates scattered amongst the nanoparticles is provided in Appendix 4.3.

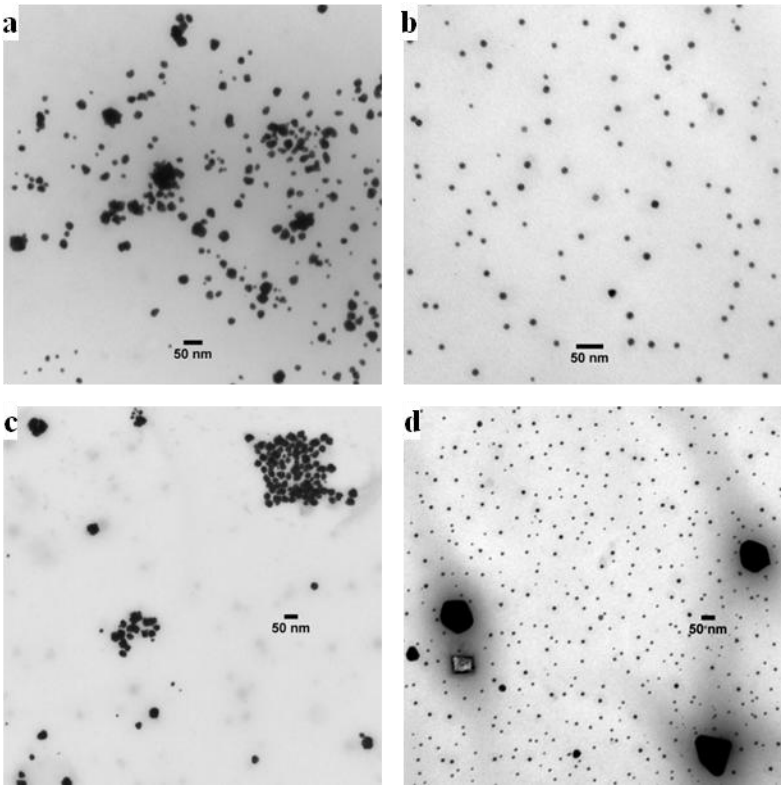

Figure 4.13 Gold nanoparticles obtained from $HAuCl_4$-loaded G1PS-*g*-P2VP5 reduced with (a) hydrazine and (b) $NaBH_4$, and $HAuCl_4$-loaded G1PS-*g*-P2VP30 reduced with (c) hydrazine and (d) $NaBH_4$.

It is quite clear that $NaBH_4$ reduction produced smaller and more uniform nanoparticles. The size of the nanoparticles was essentially identical for $NaBH_4$ reduction of the two G1PS-*g*-P2VP copolymer templates, yielding radii of 6 ± 1 nm for G1PS-*g*-P2VP5 and 6 ± 2 nm for G1PS-*g*-P2VP30. In comparison, the same templates produced nanoparticles with radii of 9 ± 4 nm and 13 ± 7 nm, respectively, with hydrazine reduction.

While the $HAuCl_4$-loaded G2PS-*g*-P2VP copolymers were apparently most stable in solution, and distinct loading regions could be identified by TEM and AFM analysis,

individual nanoparticles could not be identified in the films following reduction but rather large agglomerates as shown in Figure 4.14 for the $NaBH_4$ reduction.

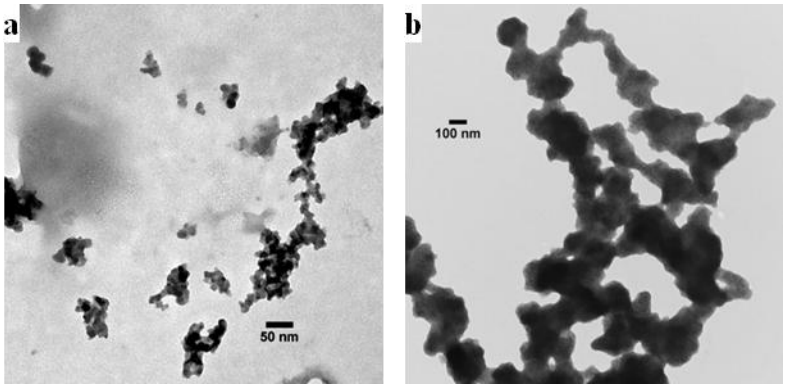

Figure 4.14 TEM image for $HAuCl_4$-loaded (a) G2PS-*g*-P2VP5 and (b) G2PS-*g*-P2VP30 reduced with $NaBH_4$.

Given the insolubility of the reduced metal-copolymer complexes, some samples did not yield any features, or produced large agglomerates of species not worthy of measurement due to their irregular shape (Figure 4.12b, Figure 4.14). Listed in Table 4.7 are the gold nanoparticle radii measurements from TEM analysis results for the various copolymers.

It should be noted that attempts to characterize the nanoparticles obtained with both reducing agents by UV-Vis absorbance measurements were unsuccessful due to extensive precipitation of the gold-polymer complexes.

Table 4.7 Gold nanoparticle radii by $NaBH_4$ and hydrazine reduction

	Radius (nm)	
Copolymer	$NaBH_4$	Hydrazine
PS-*g*-P2VP5	2 ± 1	21 ± 8[a]
G0PS-*g*-P2VP5	–[b]	–[b]
G1PS-*g*-P2VP5	6 ± 1	9 ± 4
G2PS-*g*-P2VP5	–[c]	–[b]
PS-*g*-P2VP30	–[b]	–[b]
G0PS-*g*-P2VP30	–[b]	–[b]
G1PS-*g*-P2VP30	6 ± 2	13 ± 7
G2PS-*g*-P2VP30	–[c]	–[b]

[a] Particles within large agglomerates (as seen in Figure 4.12b); [b] No features observed; [c] Large agglomerates (as seen in Figure 4.14)

4.4.2.3 Investigation on Alternate Loading Procedures and Media

Film Loading. Since the solution-loaded templates were difficult to characterize due to their limited solubility, preliminary work was completed using film loading. This approach was also investigated to gain further insight into potential morphology changes occurring upon coordination with $HAuCl_4$. The polymers were pre-ionized in acidic solution as previously reported in Section 4.3.2.3 prior to film casting, but at equivalent amounts of HCl relatively to 2VP (1:1 HCl:2VP).

TEM images were acquired for selected samples after deposition of the films and loading. While there appeared to be partial debonding of the films, interesting features were visible. The ionized P2VP side-chains of the copolymer, once adhered to the substrate, appear to expose the PS core that is not able to coordinate $HAuCl_4$. Consequently, the PS core appears as a white circle in the TEM micrographs and is surrounded by a dark region

corresponding to the gold-loaded P2VP side-chains. This is shown for the PS-*g*-P2VP30 and G0PS-*g*-P2VP5 templates in Figure 4.15a and b, respectively.

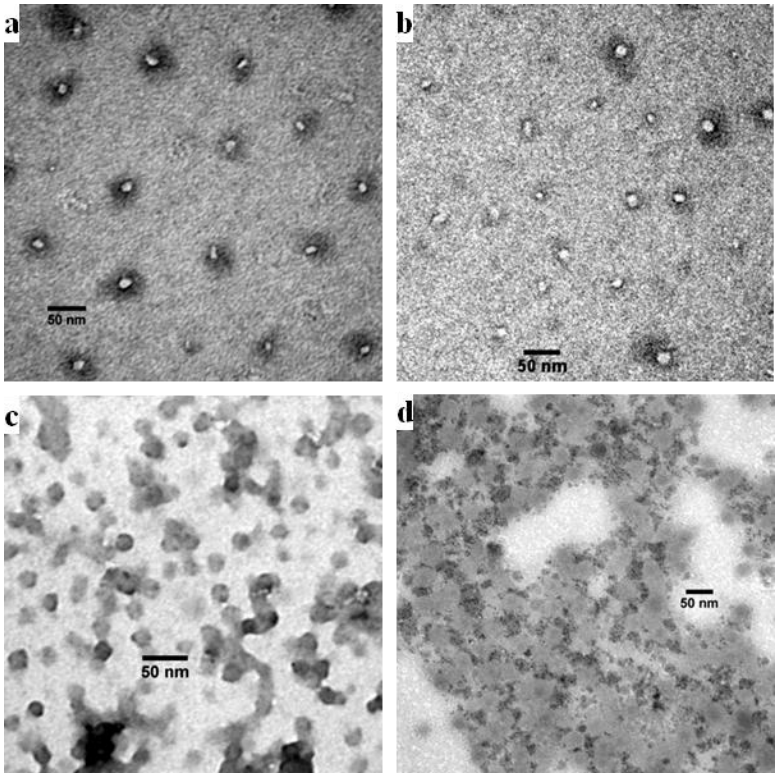

Figure 4.15 TEM micrographs for films loaded with $HAuCl_4$: (a) PS-*g*-P2VP30, (b) G0PS-*g*-P2VP5, (c) G1PS-*g*-P2VP30, and (d) G2PS-*g*-P2VP30.

The size of the core increased according to the generation, yielding radii of 6 ± 1 nm and 9 ± 1 nm for the linear and the G0 cores, respectively. The shell thickness for PS-*g*-P2VP30 was 15 ± 2 nm, while it was difficult to measure for G0PS-*g*-P2VP5 as it was visibly much thinner and more diffuse due to the short 5000 g/mol P2VP side-chains resulting in poor contrast with the background.

Samples G1PS-*g*-P2VP30 and G2PS-*g*-P2VP30 do not display a bare core, which can be explained by their higher side-chain content; there are significantly more P2VP side-chains in the copolymers above G1 (see branching functionality, f_w, in Table 4.5). The G0 and G1 copolymers with a visible core have f_w of 8 (30,000 g/mol P2VP) and 182 (5000 g/mol P2VP), respectively, while the G2 and G3 copolymers have f_w of 303 (30,000 g/mol P2VP) and 660 (30,000 g/mol P2VP), respectively. The spherical species with no detectable core, as seen in Figure 4.15c and Figure 4.15d, have average radii of 12 ± 1 nm and 18 ± 1 nm for G1PS-*g*-P2VP30 and G2PS-*g*-P2VP30, respectively. These values are nearly identical to those for the solution-loaded templates (Table 4.6). Despite using the same concentration to prepare both samples, G2PS-*g*-P2VP30 had a tendency to form large island-like aggregates, presumably through association of the P2VP side-chains. The areas between the aggregates display enhanced contrast, possibly due to increased metal content resulting from the P2VP chain entanglements. The association of P2VP side-chains creates a somewhat continuous distribution of gold (P2VP) phase and isolated PS cores. The aggregation of the ionized PS-*g*-P2VP copolymers is analogous to observations reported for Langmuir/Blodgett films of neutral amphiphilic PS-*g*-PEO polymers formed at the air/water interface.[30]

Metallic Ion Coordination. The effect of loading by coordination with an ionic salt was investigated using $Pd(OAc)_2$. This salt has also been loaded into different block copolymer reverse micelles including PS-*b*-P2VP on many occasions,[36] as palladium is attractive due to its catalytic applications, particularly on polymer supports.[37] Complexation of the copolymer with $Pd(OAc)_2$ occurs by a different mechanism from $HAuCl_4$ loading and thus provides an

interesting comparison: Complexation of $Pd(OAc)_2$ occurs through the lone pair electrons on two separate nitrogen atoms while $AuCl_4^-$ forms an ion pair with the protonated nitrogen.

As the native arborescent polymers and $Pd(OAc)_2$ are insoluble in aqueous environments, loading was investigated in THF. The results obtained upon complexation of $Pd(OAc)_2$ by the copolymers were somewhat different than for $HAuCl_4$ loading. At loading levels of 0.25 equiv (1:4 Pd:2VP), all the copolymers formed a colloidal suspension within a few minutes of the palladium addition, with the exception of G0PS-*b*-P2VP30 for no obvious reason. Even at an increased loading level of 0.50 equiv Pd, the G0PS-*b*-P2VP30 template remained soluble without visible changes in solution clarity for up to 48 h. After this time the G0PS-*b*-P2VP30 sample also yielded a colloidal suspension. Within one week of sample preparation, sedimentation was observed for all the samples.

Despite the colloidal dispersions formed by the solutions, some distinct features resembling the host polymer were seen in microscopic analysis, as shown in Figure 4.16: Pearl necklace-like ribbons of lightly aggregated, well-defined spheres were obtained for G1PS-*g*-P2VP, while the G0PS-*g*-P2VP templates yield much less defined patterns.

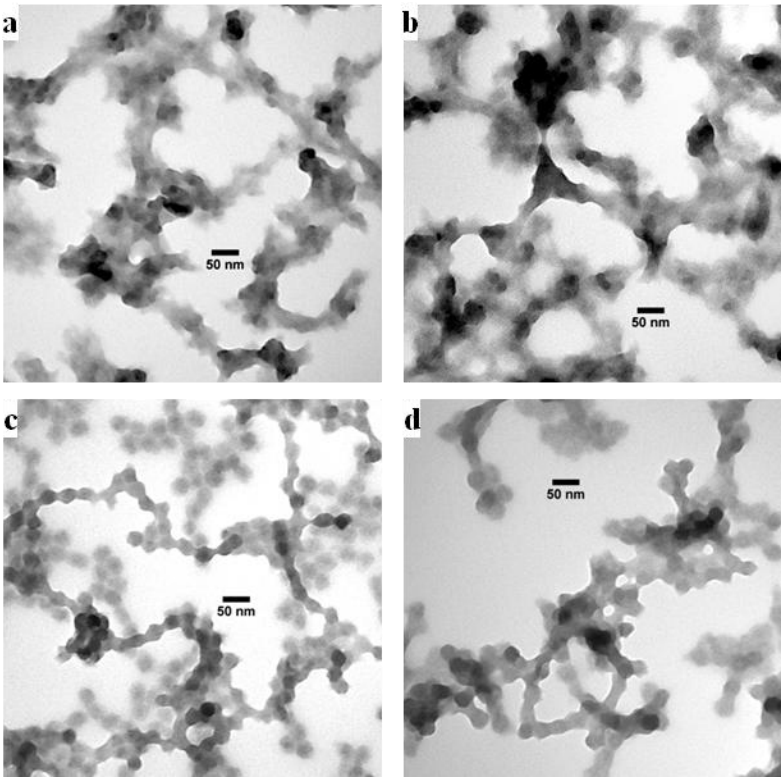

Figure 4.16 Palladium(II) acetate loading of (a) G0PS-*g*-P2VP5, (b) G0PS-*g*-P2VP30, (c) G1PS-*g*-P2VP5, and (d) G1PS-*g*-P2VP30.

The TEM micrographs for the Pd-loaded G0PS-*g*-P2VP copolymers clearly show spherical species within the network. The greater tendency for the Pd system to form a network, as compared to the gold-loaded analogue, may be due to the absence of excess counterions: In the $HAuCl_4$ system, the ionic strength is higher due to Cl^- provided by the pre-ionization of the templates with HCl, which can more effectively shield the charged polymer scaffold.

The spheres observed for the G1PS-*g*-P2VP5 copolymer have an average radius of 17 ± 1 nm (Figure 4.16c), and the radius for G1PS-*g*-P2VP30 was 20 ± 2 nm (Figure 4.16d). While there are no distinct spherical species present in the G0PS-*g*-P2VP samples, some of

the shading patterns suggest that spherical species are present. The width of the narrow portions of the network for the G0PS-*g*-P2VP5 and G0PS-*g*-P2VP30 templates was 31 ± 4 nm and 37 ± 7 nm, respectively. Since the narrow ribbons linking larger aggregated areas likely consist of single arborescent molecules loaded with $Pd(OAc)_2$, their width was compared to the molecular dimensions measured for the $HAuCl_4$-loaded system. The diameter of the $HAuCl_4$-loaded G0PS-*g*-P2VP5 and G0PS-*g*-P2VP30 templates was very similar, measuring 28 nm and 32 nm respectively (Table 4.6), in support of the hypothesis that the narrow regions are one molecule wide.

4.5 Conclusions

Arborescent copolymers derived from linear or branched PS substrates, having a corona of M_n = 5000 g/mol or 30,000 g/mol P2VP side-chains, are freely soluble in dilute aqueous HCl solutions. The G0 copolymers (PS-*g*-P2VP) exhibit partial aggregation in DLS analysis; however, the higher generation copolymers are present as unimolecular species in solution, independently of the molecular weight of the P2VP side-chains. Two dissolution protocols were investigated and yielded similar results, albeit dissolution in THF prior to protonation with an aqueous HCl solution led to a somewhat narrower size distribution.

The PS-*g*-P2VP unimolecular regular micelles have been shown to coordinate metallic compounds in polar environments. After equilibration with an aqueous solution of $HAuCl_4$, coronal metal-loading of the polymers was observed. The solubility was reduced but the polymers with a low level of Au coordination (1:4 Au:2VP) remained soluble when they were protonated prior to loading. Distinct loaded species were observed by TEM and AFM analysis, the dimensions and topology of the spherical species being clearly related to the characteristics of the arborescent copolymer templates. Reduction of the gold-copolymer complex by $NaBH_4$ and hydrazine hydrate did not result in stable nanoparticle dispersions, precipitation and large agglomerated species being observed.

Non-ionized solution loading with $Pd(OAc)_2$ in an organic solvent (THF) resulted in colloidal precipitate formation, but distinct spherical species were nonetheless observed within long chain aggregates resembling a pearl necklace.

4.6 Appendices

Appendix 4.1 Determination of 2VP content in PS-*g*-P2VP arborescent copolymer using ^{1}H NMR analysis

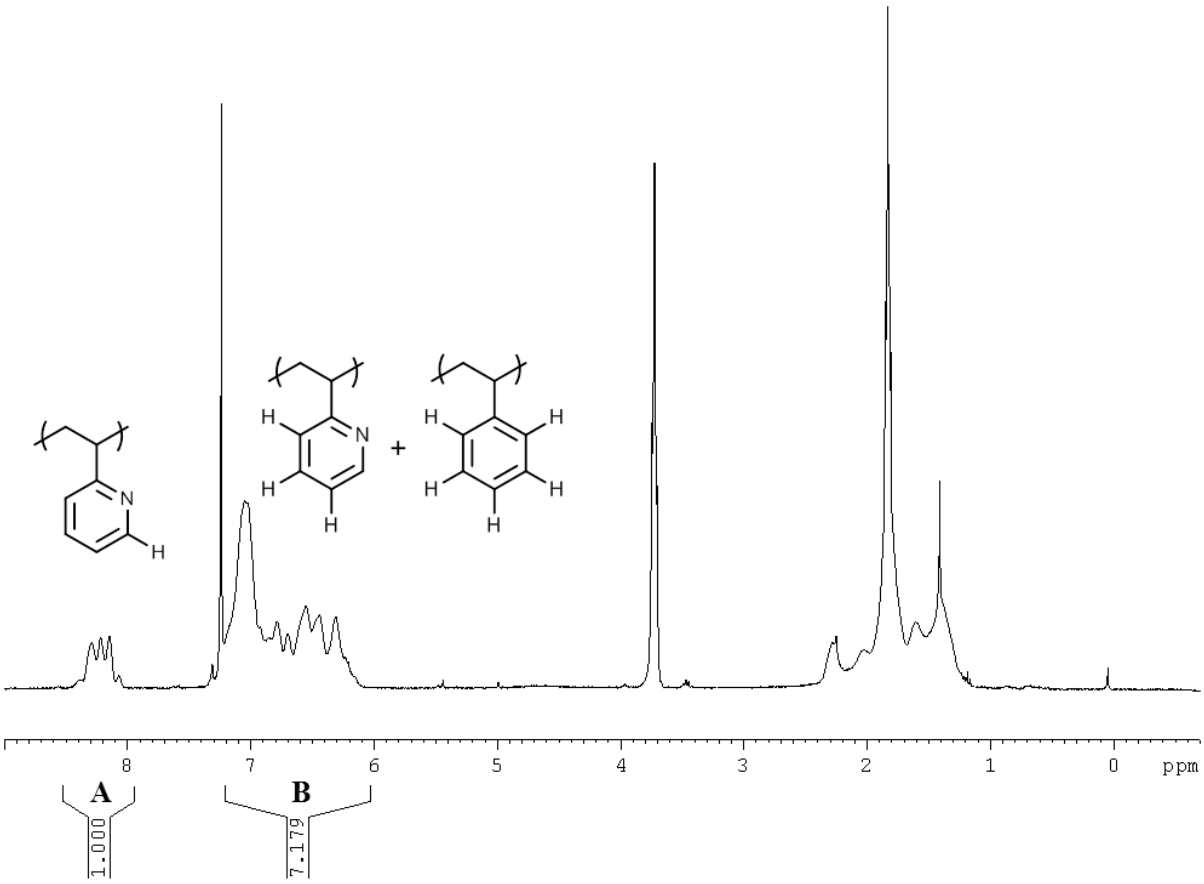

2VP = A = 1

(3 × 2VP) + (5 × Sty) = B = 7.179
Sty = 0.836

mol % 2VP = 2VP / (2VP + Sty) = 0.545 (54.5 %)

Appendix 4.2 Dynamic Light Scattering

Dynamic light scattering (DLS) provides information on the hydrodynamic radius, the size distribution, and the diffusion coefficient of polymers in solution.

As a polymer moves through an incident light beam, the dipole moments of the molecule interact and oscillate with the electric field of the light wave. The relaxation of the oscillating dipoles leads to light scattering. The light is thus reemitted at essentially the same wavelength as the incident light. The intensity of the scattered light resulting from the interaction of monochromatic light with the sample is measured with a photosensitive device such as a photomultiplier tube. In the specific case of DLS, the time-dependent (instantaneous) scattering intensity is measured and analyzed. The fluctuations in scattering intensity are due to molecular diffusion (Brownian motions) through the sample volume probed by the light beam. Figure A4.1 depicts the fluctuations in scattered light intensity over time as polymer molecules or particles move in and out of the beam. The scattering intensity fluctuates around the average scattering intensity $\langle A \rangle$, and the intensity values measured at different time intervals (A) are indicated by subscripts on the Figure. Typical time scales for the whole measurement interval range from 1 μs to 1 ms, and the acquisition intervals are either distributed linearly or exponentially over the experiment.

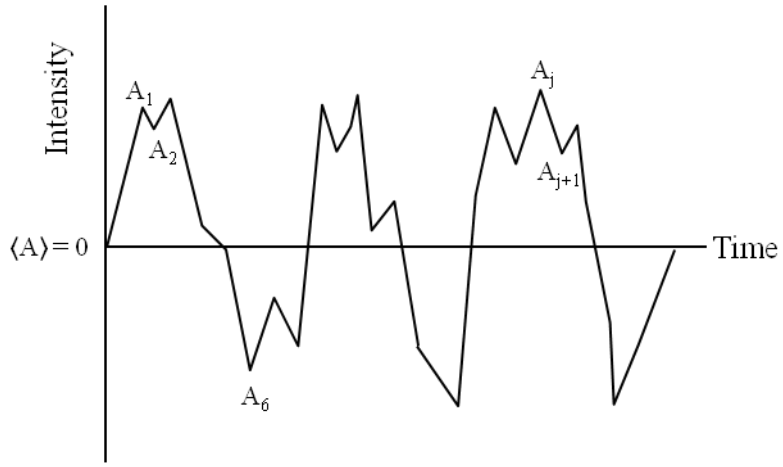

Figure A4.1 Variations in the scattered light intensity over time.

The fluctuations in scattered light intensity can be described by an autocorrelation function, generated by correlating the scattered light intensities at different times. For example, intensity A_1 in Figure A4.1 is highly correlated to A_2, but is much less correlated to A_6. It is evident that as the time interval between two measurements increases, the signals become less correlated. It should be noted that the labeled peaks in Figure A4.1 (A_1, A_2, etc.) are for illustration purposes only; the autocorrelation function compares all the measured scattering intensities, not just peak values. If the scattering data fluctuations are centered on the average value, $\langle A \rangle = 0$, the correlation function can be generated by analysis of the different channels (time intervals). The autocorrelation function can then be expressed by Equations A4.1 and A4.2 in their summation and integral forms, respectively, where N represents the total number of channels used, n is the channel number, t is the time, τ represents a small time increment, and the total measurement time (T) is equal to $N\Delta t$.

$$\langle A(0)A(\tau)\rangle = \lim_{N\to\infty} \frac{1}{N}\sum_{j=1}^{N} A_j\, A_{j+n} \tag{A4.1}$$

$$\langle A(0)A(\tau)\rangle = \lim_{T\to\infty} \frac{1}{T}\int_0^T A(t)\, A(t+\tau) \tag{A4.2}$$

The value of the correlation function for the first channel (or channel 0) is highest, since it equals the sum of the squares of the intensity values.

$$\langle A(0)A(\tau)\rangle = \sum A_j A_j = \sum A_j^2 = \langle A^2\rangle \tag{A4.3}$$

For all other channels (1, 2, 3, … n), the value of the correlation function will be lower, because a portion of the intensity value products are negative. The autocorrelation function thus decays from $\langle A^2\rangle$ to a completely uncorrelated value of $\langle A\rangle^2$ which is defined as the baseline. Figure A4.2 depicts a typical autocorrelation function decay.

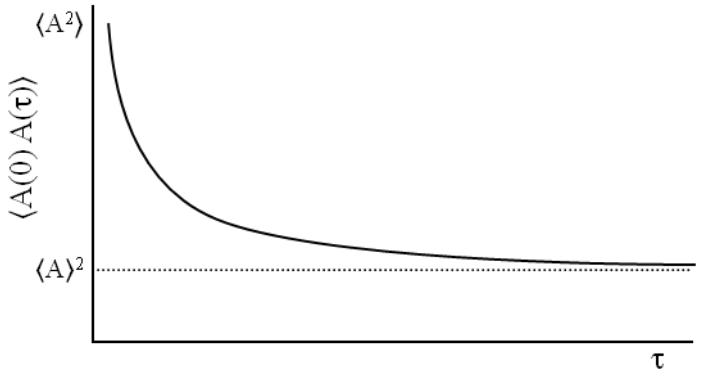

Figure A4.2 Autocorrelation function decay.

The autocorrelation function for monodispersed (single-sized) species decays in a monoexponential fashion. Under these conditions, the first-order correlation function can be

expressed by Equation A4.4 where Γ represents the rate of decay of the correlation function, which is related to the mutual diffusion coefficient (D, Equation A4.6).[1–3] It is the mutual diffusion coefficient which is related to the hydrodynamic radius via the Stokes-Einstein relationship (Equation A4.6).

$$|g_1(\tau)| = \langle A(0)A(\tau)\rangle = \exp(-\Gamma\tau) \tag{A4.4}$$

$$\Gamma = Dq^2 \tag{A4.5}$$

$$\text{where } D = \frac{k_B T}{6\pi\eta_o r_h} \tag{A4.6}$$

$$\text{and } q = \left(\frac{4\pi n}{\lambda}\right)\sin\frac{\theta}{2} \tag{A4.7}$$

Γ = Correlation function decay constant
η_o = Viscosity of the dispersion medium (cP, $N\cdot m^{-2}$, $Kg\cdot m^{-1}\cdot s^{-1}$)
λ = Wavelength of scattered light (m)
θ = Observation angle
D = Diffusion coefficient ($m^2\cdot s^{-1}$)
k_B = Boltzmann's constant (1.38×10^{-23} $m^2\cdot Kg\cdot s^{-2}\cdot K^{-1}$)
n = Refractive index of the sample
q = Scattering vector (m^{-1})
r_h = Hydrodynamic radius (m)
T = Temperature (K)

A plot of the natural logarithm of the correlation function $|g_1(\tau)|$ versus time yields a straight line for uniformly sized (monodispersed) spherical species. The hydrodynamic radius (r_h) can then be calculated from the slope of the line, equal to $-Dq^2$ (D is inversely proportional to r_h). For species of uniform size, the second-order correlation function $|G_2(\tau)|$ (Equation A4.8) has the same monoexponential decay as the first-order function, where A is the baseline of the autocorrelation function and β is an optical (instrument-specific) factor.

$$|G_2(\tau)| = A[1 + \beta\exp(-2\Gamma\tau)] = A[1 + \beta|g_1(\tau)|^2] \quad \text{(A4.8)}$$

For a polydispersed sample, each size population can be characterized by a different exponential decay. DLS can offer insight into the polydispersity of a sample by comparing the first- and second-order analysis results of the correlation function. If the autocorrelation function exhibits a monoexponential decay due to a uniform size distribution, the first- and second-order analyses will yield identical hydrodynamic radii ($r_{h1} = r_{h2}$). Conversely, if the sample is highly polydispersed or bimodal (for example because of polymer chain association), the two analyses will yield very different radii ($r_{h1} \neq r_{h2}$). Analysis according to first- and second-order fits of the correlation function is also referred to as the method of moments.[4] In moments analysis, the decay moment (μ_k) is expressed by Equation A4.9.

$$\mu_k = \int_0^\infty t^k D(t) dt \quad \text{(A4.9)}$$

For DLS, D(t) represents the autocorrelation function for a monoexponentially decaying system, $D(t) = \exp(-Dq^2t)$, and k represents the k^{th} moment. A first moment analysis examines the ratio μ_1/μ_0, which is expanded below.

$$\mu_0 = \int_0^\infty t^0 \exp(-Dq^2t)\, dt = (Dq^2)^{-1} \quad \text{(A4.10)}$$

$$\mu_1 = \int_0^\infty t^1 \exp(-Dq^2t)\, dt = (Dq^2)^{-2} \quad \text{(A4.11)}$$

$$\frac{\mu_1}{\mu_0} = (Dq^2)^{-1} \quad \text{(A4.12)}$$

Second moment analysis examines the solution to Equation A4.13. When these two analyses are computed for a monoexponentially decaying system, the solutions are identical.

$$\left[\frac{\mu_2}{\mu_0} - \left(\frac{\mu_1}{\mu_0}\right)^2\right]^{0.5} \quad \text{(A4.13)}$$

Thus an essentially monodispersed and non-aggregated system will yield similar hydrodynamic radii from first- and second-moment analysis of the correlation function. Additionally, reproducible radii results in a series of measurements are indicative of a well-defined system with a narrow size dispersity. It is also possible to derive the size distribution from the autocorrelation function using CONTIN analysis. A review of this complex analysis method, based on the Laplace transform of the correlation function, will not be described herein. Specific details on the CONTIN algorithm, developed by Provencher in the early 1980s, can be found in Reference 5.

Appendix 4.3 Low magnification TEM micrograph depicting Au nanoparticles and larger aggregates after $NaBH_4$ reduction of $HAuCl_4$-loaded G1PS-*g*-P2VP5

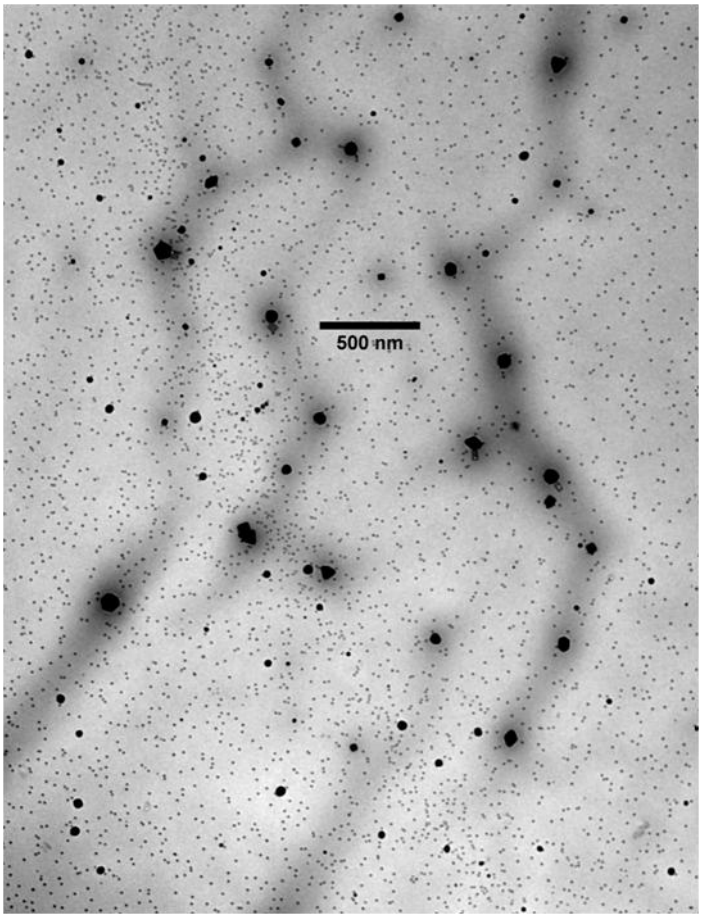

Chapter 5

Synthesis of Arborescent Polystyrene-*g*-[Poly(2-vinylpyridine)-*b*-Polystyrene]

5.1 Overview

Arborescent polymers with a core-shell-corona (CSC) architecture, incorporating a core of polystyrene (PS), an inner shell of poly(2-vinylpyridine), P2VP, and a corona of PS chains, were obtained by anionic polymerization and grafting. The main motivation for the synthesis of these dendritic molecules is their application as templates for the preparation of metallic nanoparticles in non-polar solvents. Polystyryllithium was synthesized by anionic polymerization in THF and capped with 1,1-diphenylethylene before adding 2-vinylpyridine to generate a living block copolymer PS-*b*-P2VPLi. A substrate of linear or arborescent polystyrene of generation G0 – G3, randomly functionalized with acetyl or chloromethyl coupling sites, was then added to the PS-*b*-P2VPLi solution for the grafting reaction. Purification of the crude grafting products was problematic due to the amphipolar character of the graft copolymers and the block copolymer side-chain contaminant. A fractionation method by cloud-point centrifugation was developed for polymers of generations G1 and above. The grafting yield and the coupling efficiency observed in the synthesis of arborescent PS-*g*-(P2VP-*b*-PS) copolymers were much lower than for analogous coupling reactions to synthesize arborescent PS homopolymers and PS-*g*-P2VP copolymers from the same types of coupling sites and side-chains with comparable lengths. It was determined from static and dynamic light scattering analysis that solutions of PS-*b*-P2VP formed aggregates in THF, the solvent used for the synthesis. This presumably hindered coupling of the macroanions with the substrate and explains the low grafting yield and coupling efficiency observed in these reactions.

5.2 Introduction

5.2.1 Arborescent Polymers

The cascade-branched (dendritic) structure of arborescent polymers, resulting from successive grafting reactions of linear polymer segments, is unique in terms of architecture and properties. Using ionic polymerization, the characteristics (side-chain molecular weight and uniformity) of these branched polymers are easily controlled. The introduction of polymer chains with a different composition in the last grafting cycle allows the generation of copolymers;[1–3] alternately copolymers can be generated by grafting (growing) side-chains from the chain termini of the branched substrates.[4,5]

The technique reported herein for the synthesis of dendritic graft polymers utilizes a 'grafting onto' method, whereby a substrate functionalized with coupling sites is added to a solution of 'living' polymer chains. This divergent method was first reported for the synthesis of dendritic graft polymers in 1991 by Tomalia et al.[6] and by Gauthier and Möller.[7] The scheme developed by Tomalia et al. used the cationic polymerization of 2-ethyl-2-oxazoline and deacylation to generate secondary amine coupling sites along the chains, while Gauthier and Möller relied on the anionic polymerization of styrene and chloromethylation for the introduction of coupling sites. The anionic method was subsequently extended to the synthesis of arborescent copolymers from chloromethylated and acetylated substrates.[1–3]

The synthesis of arborescent PS substrates typically starts from linear chains with a number-average molecular weight (M_n) = 5000 g/mol and a low polydispersity (PDI = M_w/M_n ≤ 1.1), randomly functionalized with 20 – 30 mol % of chloromethyl or acetyl groups.[7,8] Coupling of polystyryllithium with the functionalized linear polystyrene substrate yields a

comb-branched or generation zero (G0) polystyrene. Further functionalization and grafting cycles lead to upper generation (G1, G2, etc.) arborescent polystyrenes with increasing branching functionalities. A schematic representation of the step-wise grafting procedure used for the synthesis of arborescent polymers is shown in Figure 5.1.

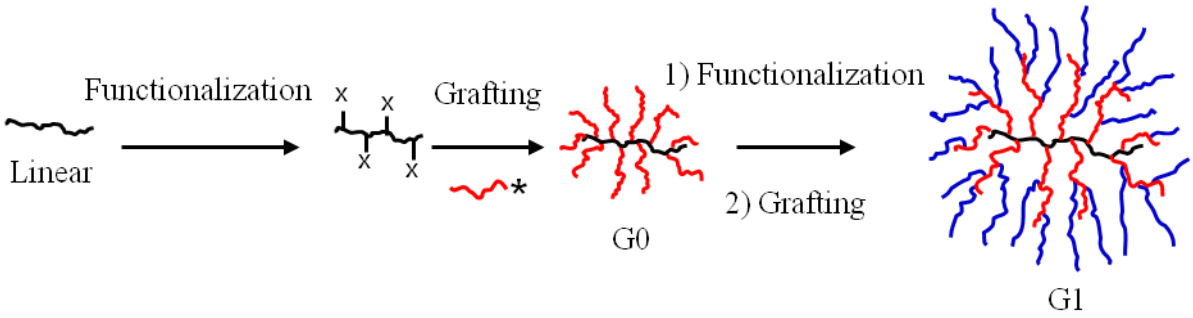

Figure 5.1 Generation-based synthesis of arborescent polymers.

Because arborescent polymers are constructed from linear polymer building blocks and a large number of coupling sites are introduced on the substrates, the molecular weight of the branched species increases very rapidly over successive generations. For the specific case where the number of coupling sites per side-chain (*f*) and the molecular weight of the side-chains (or branch molecular weight, M_{br}) remain constant for each cycle, geometric growth in the molecular weight (M) is expected as described by Equation 5.1, where x is the grafting cycle number and G is the final generation of the arborescent polymer.

$$M = M_{br} + M_{br}f + M_{br}f^2 + M_{br}f^3 + \ldots = \sum_{x=0}^{G+1} M_{br}f^x \qquad (5.1)$$

Arborescent copolymers of PS substrates grafted with P2VP segments, having a core-shell morphology, have also been synthesized.[2,3] The incorporation of the P2VP shell

provides amphipolar character to the molecules, which behave like unimolecular micelles in acidic aqueous solutions, since the covalently bonded structures exist as non-aggregated species.[3] Grafting of a living block copolymer (PS-*b*-P2VP) onto a PS substrate should yield a unique core-shell-corona (CSC) architecture with an inner P2VP layer, since the living end resides on the P2VP end of the block copolymer.[9] The procedure now reported for the synthesis of this new CSC amphipolar architecture is directly derived from the methods previously developed for the preparation of arborescent PS homopolymer and arborescent PS-*g*-P2VP core-shell copolymers, although the yield of the grafting procedure is lower. The CSC architecture allows the dissolution or binding of polar species within the P2VP shell, while the PS corona makes the molecules freely soluble in non-polar environments. The ability of these molecules to solubilize polar components (including metallic salts) in apolar media and the possibility of tailoring their characteristics (size of each block and number of side-chains) is the main motivation for the synthesis of such polymer architectures. The CSC architecture is thus analogous to reverse micelles but it possesses a covalently bonded structure, incorporates a hydrophobic core, and its characteristics can be varied over a broad size and composition range.

The synthesis of these CSC copolymers was carried out similarly to established protocols, but was nonetheless challenging: Isolation of the graft polymer from the linear side-chain contaminant was difficult, and unusually low graft yields were observed. The detailed synthetic procedure used for preparation of these unique arborescent copolymers is presented herein, as well as a purification method developed to purify the crude products. The low yield of the grafting reaction is rationalized on the basis of light scattering analysis results.

5.3 Experimental Procedures

5.3.1 Reaction Apparatuses

The reaction vessels, manifolds, and ampoules used in the syntheses were thoroughly cleaned, dried, and flamed prior to their use due to the sensitivity of anionic polymerization reactions to impurities. The reactions and final purification steps were performed on a high-vacuum (HV, $< 10^{-5}$ mm Hg) line and under inert atmosphere (purified N_2). The ampoules for reagent purification were equipped with polytetrafluoroethylene (PTFE) stopcocks and ground glass joints, to enable mounting on the purification manifolds and the polymerization reactor. Purified solvents were transferred from the stills to the manifolds through PTFE tubing.

5.3.2 Solvent and Reagent Purification

Toluene (Caledon, HPLC grade) was purified by distillation from oligostyryllithium under N_2. Tetrahydrofuran (THF; EMD, HPLC grade) was distilled from sodium benzophenone ketyl under N_2. LiCl (Aldrich, 99.99+ %) was first dried in a vacuum oven at 110 °C overnight, and further dried by heating (flaming) in the reaction vessel under HV. Acetyl chloride (Aldrich, 99 %) was distilled under N_2, and nitrobenzene (Aldrich, 99%) was purified by reduced pressure distillation. *n*-Butyllithium (*n*-BuLi; Aldrich, 2.5 M in hexanes), *sec*-butyllithium (*sec*-BuLi; Aldrich, 1.4 M in cyclohexane), *tert*-butyllithium (*tert*-BuLi; Aldrich, 1.7 M in pentane), and $AlCl_3$ (Aldrich, anhydrous, 99.99 %) were used as received. The exact *sec*-BuLi concentration was determined by the method of Burchat et al.[10]

Styrene (Aldrich, 99 %) was first distilled from CaH_2 after stirring for 12 h and further purified with phenylmagnesium chloride (Sigma-Aldrich, 2.0 M in THF, 1 mL per 10

mL styrene) immediately before polymerization. 2-Vinylpyridine (2VP; Aldrich, 97 %) was distilled under reduced pressure from CaH_2 after stirring overnight. A second purification with CaH_2 was performed immediately before polymerization. *N*,*N*,*N'*,*N'*-Tetramethylethylenediamine (TMEDA; Aldrich, 99 %) was purified on a HV line by titration with *tert*-BuLi until a persistent yellow color was observed, degassing with three freeze-pump-thaw cycles, and condensation to an ampoule. 1,1-Diphenylethylene (DPE; Aldrich, 97 %) was titrated with *n*-BuLi until a deep red color was observed and distilled under reduced pressure. A final DPE purification step was accomplished by azeotropic distillation with dry THF. The monomer and TMEDA ampoules were filled with N_2 and stored at –20 °C until used (24 h at most).

5.3.3 Polystyrene Substrates Synthesis

Polystyrene substrates with linear and branched architectures served for the synthesis of the copolymers. The preparation of a generation zero (G0, or comb-branched) polystyrene substrate will be described as an example in the following sections.

5.3.3.1 Polystyrene Synthesis

Previously distilled styrene (30 mL) was further purified on a HV line by three freeze-pump-thaw cycles in the presence of phenylmagnesium chloride. The monomer was then slowly recondensed to the ampoule. The monomer ampoule containing styrene (28.5 mL, 0.248 mol), and the purified toluene and THF lines were mounted on a round-bottomed glass reactor containing a magnetic stirring bar. After evacuation, flaming, and filling with N_2, 200 mL of toluene was added followed by three drops of styrene, and the solution was titrated with *sec*-BuLi until a persistent yellow color was observed. The amount of *sec*-BuLi required

for the target M_n = 5000 g/mol (5.2 mmol, 3.7 mL) was then added, followed by the drop-wise addition of styrene causing the solution to turn orange. After 10 min the reactor was cooled to –78 °C with a dry ice/acetone bath and 150 mL of dry THF was added to increase the polymerization rate. After 15 min the polymerization was terminated with a few drops of degassed acidified methanol. The product was isolated by precipitation in methanol.

5.3.3.2 Acetylation of Polystyrene

Linear polystyrene (10.0 g, 92 mmol styrene units) in a 250 mL round-bottomed flask was dried under HV overnight, the flask was filled with N_2, and the polymer was dissolved in 100 mL of nitrobenzene. For a 30 mol % target functionalization level, a catalyst solution was prepared in a separate vessel by dissolving 5.12 g (38 mmol) of $AlCl_3$ in 20 mL of nitrobenzene and adding 2.73 mL of acetyl chloride (38 mmol). The catalyst solution was added drop-wise to the polymer solution, inducing a color change to red-brown. After 30 min the acetylated polymer was recovered by precipitation in methanol/HCl (10 %) and further purified according to Reference 8.

5.3.3.3 Grafting Reaction

The method for coupling polystyryl anions with the functionalized polystyrene substrate is not generation-specific. The synthesis of a G0 arborescent polystyrene from a linear acetylated substrate is described here as an example.

The acetylated linear PS substrate (1.0 g, 26 % acetylation, 2.25 meq acetyl groups) was dissolved in 25 mL of THF and transferred to an ampoule on a HV line. The substrate was purified by five cycles of azeotropic distillation with 50 mL portions of dry THF and dissolved in 20 mL of dry THF. Ampoules containing purified styrene (6.42 g, 61 mmol) and

2VP (0.41 g, 3.9 mmol, dissolved in 10 mL of dry THF), and the acetylated PS substrate, were mounted on the reaction vessel containing 0.27 g (6.4 mmol) of LiCl. The polymerization of styrene proceeded as reported in Section 5.3.3.1 (0.92 mL, 1.28 mmol *sec*-BuLi, for a target M_n = 5000 g/mol), using a proportionate solvent volume, and 2VP was added as a reactivity modifier causing a color change from orange to dark red. The reaction was warmed to 0 °C after 30 min and the 2VP-capped macroanions were slowly titrated for 30 min with the acetylated substrate until a faint red color persisted. The remaining macroanions were terminated with degassed methanol after approximately 60 min. The graft polymer was recovered by precipitation in methanol and precipitation fractionation using toluene and methanol. Other polystyrene substrates were prepared by colleagues in the Gauthier laboratory.[11]

5.3.4 Arborescent Copolymer Synthesis

Linear and arborescent polystyrene substrates were functionalized with acetyl coupling sites,[8] with the exception of one sample subjected to chloromethylation.[7] The characteristics of the grafting substrates are summarized in Table 5.1. A detailed procedure is provided for grafting a block copolymer of PS (M_n = 11,000 g/mol) and P2VP (M_n = 12,500 g/mol) onto an acetylated G0PS substrate, to yield a G0PS-*g*-(P2VP-*b*-PS) arborescent copolymer, is described as an example.

A round-bottomed 2-L glass reactor equipped with a vacuum-tight mechanical stirrer was fitted with a THF line from the drying still, a rubber septum, and ampoules containing styrene (5.04 g, 48.4 mmol), 2-vinylpyridine (5.72 g, 54.4 mmol), DPE (0.12 mL, 0.69 mmol in 5 mL of THF), and acetylated G0 polystyrene (0.385 g, 27.5 % acetylation, 0.91 meq acetyl groups, dissolved in 50 mL of THF). LiCl (97.0 mg, 2.3 mmol) was added to the

reactor before it was evacuated, flamed, and filled with N_2. After cooling, the reactor was charged with 200 mL of THF. It should be noted that when low molecular weight side-chains were generated ($M_n \leq 5000$ g/mol), the reaction was initiated in toluene as described in Section 5.3.3.1. After cooling to –78 °C, 3 – 5 drops of styrene were added and titrated with *sec*-BuLi until a persistent yellow color was observed. The calculated amount of *sec*-BuLi (0.35 mL, 0.46 mmol, for a target M_n = 11,000 g/mol) was added, followed by styrene drop-wise, yielding an orange color. After 10 min a small sample was removed from the reactor and terminated with degassed acidified methanol. DPE was then added, causing the solution to turn deep red; the 2VP was added 10 min later. A sample of the PS-*b*-P2VP side-chains was removed after 15 min and terminated with degassed methanol. The reactor was warmed to 0 °C with an ice-water bath and the acetylated polystyrene substrate solution was slowly added, resulting in gradual fading of the color. The titration was stopped after a faint red color was obtained and the reactor was warmed to room temperature, leading to further color fading. Residual living chains were terminated with degassed methanol and the crude product was recovered by precipitation in hexane.

5.3.5 Instrumentation

5.3.5.1 Nuclear Magnetic Resonance (NMR) Spectroscopy

^{1}H NMR spectroscopy was performed on a Bruker AM-250 instrument to determine the functionalization level of the PS substrates (Table 5.1) and the 2VP content of the arborescent (Table 5.3) and block copolymers (Table 5.4). Determination of the functionalization level of acetylated PS substrates and the 2VP copolymer content by ^{1}H NMR spectroscopy is illustrated in Appendix 5.1 and Appendix 5.2, respectively. Polymer solutions in $CDCl_3$ (1.5% w/v) were used for the analysis (16 scans).

5.3.5.2 Size Exclusion Chromatography (SEC)

Analytical SEC was used routinely for the characterization of the polystyrene substrates, the PS-*b*-P2VP block copolymers, the crude reaction products, and the fractionated arborescent copolymers. Two different mobile phases were used for characterization: THF and *N*,*N*-dimethylacetamide (DMA) with 0.1 % LiCl. Each solvent was selected on the basis of the response and the peak resolution achieved for the different polymers. The SEC system, operated at a flow rate of 1 mL/min at room temperature, consisted of a Waters 510 HPLC pump, a Waters 410 DRI detector (operated at 35 °C), and a Wyatt Dawn DSP-F SEC-MALLS (multi-angle laser light scattering) detector operating at 632.8 nm, to allow the determination of the absolute molecular weight of the samples using the ASTRA v4.70 software package. Jordi DVB Mixed-bed Linear columns (500 mm × 10 mm, molecular weight range $10^2 – 10^7$ g/mol) were used in THF for the characterization of the linear side-chains and the G0 and G1 arborescent copolymers. Samples of generations G2 and above were characterized in DMA using two Polymer Laboratories ultra high molecular weight PLgel 20 μm Mixed-A DVB columns (300 mm × 7.5 mm, molecular weight range $2 \times 10^3 – 4 \times 10^7$ g/mol) connected in series. The absolute M_n and PDI of the linear PS samples were determined from the DRI signal and a linear PS standards calibration curve. The absolute M_n of the PS-*b*-P2VP block copolymers was calculated from the absolute M_n of the PS block from SEC analysis along with ^{1}H NMR providing the copolymer composition. The absolute M_n and PDI of the graft copolymers were determined by SEC-MALLS analysis.

Preparative SEC, used in some cases for the fractionation of crude products, was performed on a separate system equipped with a Waters M-45 solvent delivery system, a

Waters R401 DRI detector, a 250 mm × 22 mm Jordi DVB Mixed-bed preparative column, and either THF or DMA as eluent at room temperature and a flow rate of 3 mL/min.

5.3.5.3 Light Scattering

Instrumentation. Detailed information on the theory behind light scattering, both dynamic and static, can be found in Appendix 4.2 and Appendix 5.3, respectively. Batch-wise light scattering measurements were carried out on a Brookhaven BI-200 SM light scattering goniometer equipped with a BI-2030AT 201-channel correlator and a Claire Lasers CLAS2-660-140C (120 mW) laser operating at 660 nm. All the samples were measured at 25 °C after at least 3 filtrations with a 0.45 μm PTFE membrane filter.

Dynamic Light Scattering. For dynamic light scattering (DLS) measurements, the correlator was operated in the exponential sampling mode. The hydrodynamic radii were calculated from the z-average translational diffusion coefficients obtained from first- and second-order cumulant analysis of the correlation function (to better account for polydispersity effects) at a scattering angle of 90°. The uncertainties reported for the first- and second-order radii are the standard deviation for a series of at least 10 measurements. Diffusion coefficient measurements were recorded at angles ranging from 35° to 140°. The solutions for the DLS measurements were prepared at concentrations ranging from 0.05 to 2.5 %, depending on the molecular weight of the sample. Detailed theoretical background on this technique can be found in Appendix 4.2.

Static Light Scattering. Static light scattering (SLS) data was acquired to determine the second virial coefficient (A_2), the z-average radius of gyration (r_g), and the weight-average molecular weight (M_w) of selected samples by the Zimm extrapolation technique to zero angle and concentration. Measurements on at least five solutions ranging in concentration

from 0.4 to 2.0 % (w/v) and angles between 35° and 140° were used for that purpose. Detailed theoretical background on this technique can be found in Appendix 5.3.

5.3.5.4 Arborescent Copolymer Purification

Instrumentation. The crude polymer samples were purified with a Beckman Coulter Avanti J-30I centrifuge equipped with a Beckman Coulter JA-30.50Ti rotor. The Polyallomer™ centrifuge tubes (50 mL) used were also provided by Beckman Coulter.

Procedure. The crude product was dissolved in THF (2.5 % w/v), methanol was added until an opalescent cloud-point was observed, and the solution was transferred to the centrifuge tubes. The solution was subjected to centrifugal fields ranging from 25,000 – 50,000 × *g* for 30 min before the clear supernatant was decanted. The sediment was analyzed by SEC to verify the absence of side-chain contaminant, and subjected to further purification cycles if necessary until no linear contaminant was detected. The number of purification cycles required varied and some materials also required a final purification step by preparative SEC as described in Section 5.3.5.2. Detailed information on the specific purification protocol used for each polymer can be found in Table 5.5. After the removal of all linear contaminant, the pure graft copolymers were precipitated in hexane and freeze-dried from benzene to give a powered product.

5.3.5.5 Atomic Force Microscopy (AFM)

Instrumentation. AFM micrographs were recorded in the tapping mode with a Nanoscope III (Digital Instruments, model MMAFM-2, scan stage J) SFM instrument housed in a NanoCube acoustic isolation cabinet/enclosure mounted on a Halcyonics Micro 40 vibration isolation table. The measurements were performed under ambient conditions using Si probes

(VistaProbes, T300) with a spring constant of 40 N/m, a resonance frequency of 300 kHz, and the following characteristics: length 125 μm, width 40 μm, tip height 14 μm, and tip radius < 10 nm. The images were analyzed using the Nanoscope v5.30r3.sr4 software.

Substrate Preparation and Film Casting. Muscovite mica sheets cut into 1 cm^2 pieces were adhered to a steel substrate of approximately the same size using double-sided tape, to allow securing of the sample to the magnetic spin coater and the magnetic scanner head of the AFM instrument. Immediately prior to film casting, the mica was cleaved with a strip of tape (Scotch™ Magic™ brand) to expose a fresh (hydrophilic) surface. After mounting on the magnetic spin coater, solution droplets were placed onto the surface with a pipette to completely cover it, and the substrate was spun for at least 15 s at 3000 rpm.

5.4 Results and Discussion

5.4.1 Substrate Synthesis and Functionalization

The PS chains synthesized for the arborescent copolymer substrates had a $M_n \approx 5000$ g/mol in all cases, affording a roughly geometric increase in molecular weight over successive generations. Characterization data for all the functionalized PS substrates prepared are listed in Table 5.1.

The functionalization (acetylation) level of the PS substrates (F) was determined by ^{1}H NMR analysis as shown in Appendix 5.1. A target acetylation level of 20 – 30 mol % was used to minimize steric crowding of the chains during the grafting reaction. This corresponds to ca. 10 – 15 coupling sites per polystyrene side-chain with M_n = 5000 g/mol. The formation of branched PS substrates in high yield requires end-capping of the polystyryl anions with 2VP prior to grafting, to attenuate living end reactivity, thereby reducing the likelihood of side reactions. This grafting reaction, investigated in detail by Li and Gauthier,[8] will be discussed further in Section 5.4.2.

It should be noted that another functionalization method previously developed for polystyrene involved chloromethylation. However only one of the substrates used in the current investigation (synthesized previously[4]) was chloromethylated. The chloromethylation procedure is not described herein but was discussed in a paper by Gauthier and Möller.[7] A scheme describing the chloromethylation reaction and the corresponding grafting reaction can also be found in Appendix 5.4.

Table 5.1 Polystyrene substrates characterization

Substrate	F[a]	M_w/M_n	M_n[b]	f_w[c]
Linear	0.26	1.06	5775	13
G0PS	0.28	1.09	1.0×10^5	238
G1PS-1	0.30	1.11	8.3×10^5	2145
G1PS-2[d]	0.30	1.07	8.7×10^5	2235
G2PS	0.22	1.09	1.1×10^7	21002
G3PS	0.26	1.08	2.0×10^7	46023

[a] Functionalization (mole %) from ^{1}H NMR analysis; [b] Absolute values from SEC-MALLS or laser light scattering measurements before functionalization; [c] Branching functionality: number of branches added in the last grafting cycle; [d] Functionalized with chloromethyl groups, all other substrates contained acetyl functional groups

5.4.2 Arborescent CSC Copolymer Synthesis

The synthesis of the CSC arborescent copolymers proceeded in similar fashion to the branched PS samples previously described; however, in this case block copolymers of PS and P2VP were coupled with the functionalized substrate. In order to prepare arborescent copolymers with the desired CSC architecture, the living end of the PS-*b*-P2VP copolymer must lie on the P2VP end to give an internal layer of P2VP and a peripheral shell of PS after grafting. A graphical representation of the branched CSC copolymer architecture formed by grafting onto a G0PS substrate is shown in Figure 5.2.

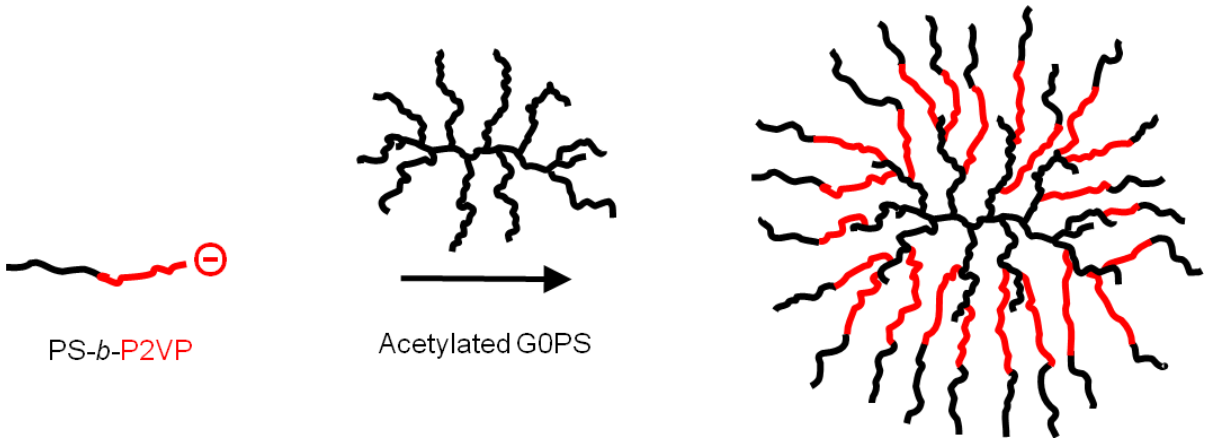

Figure 5.2 Graphical representation of the synthesis of G0PS-*g*-(P2VP-*b*-PS).

After *sec*-BuLi initiation and growth of the PS segment, reactivity attenuation of the living PSLi macroanions is required to avoid side reactions during crossover to the second monomer (2VP) and yield a well-defined P2VP block. Side reactions which can result from uncapped PSLi include chain dimerization and branching as illustrated in Appendix 5.5. DPE was shown to be useful as a capping agent to reduce the reactivity of anionic centers.[12] To that end, 1.5 equivalents of DPE relative to the living chain ends was added to PSLi, to ensure the reaction of all chain ends and controlled crossover to the P2VP block after the 2VP addition. The complete reaction sequence involved in the synthesis of a G0PS-*g*-(P2VP-*b*-PS) arborescent copolymer is shown in Scheme 5.1.

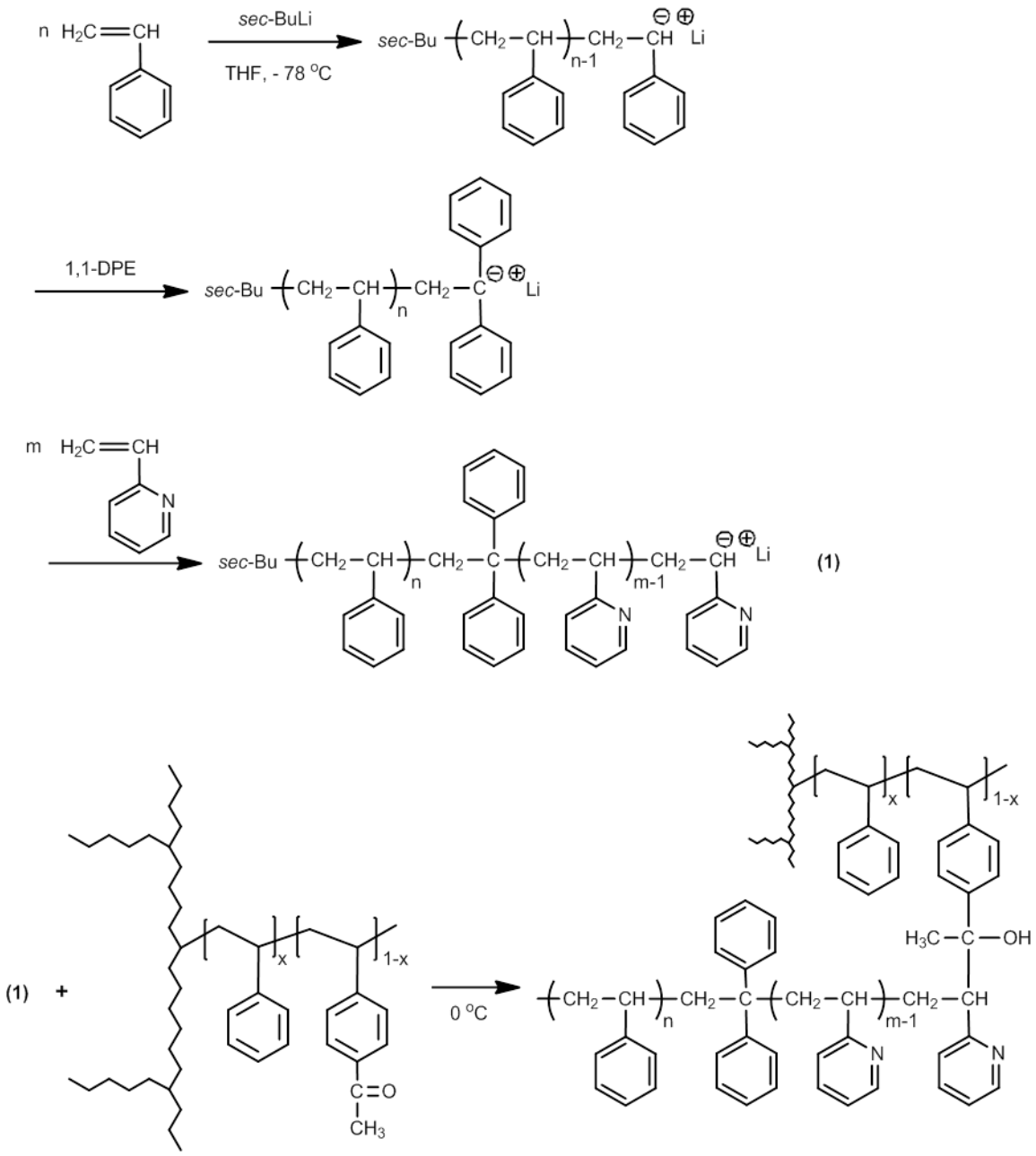

Scheme 5.1 Synthesis of G0PS-*g*-(P2VP-*b*-PS) arborescent copolymer.

The reaction conditions for grafting polystyryllithium (PSLi) and poly(2-vinylpyridinyl)lithium (P2VPLi) onto both acetylated and chloromethylated PS substrates have been optimized previously.[13] The influence of reactivity modifiers (capping agents such as DPE and 2VP or additives such as LiCl and TMEDA) as well as the temperature on the

grafting reaction was clarified. In the current case, the living end of the PS-*b*-P2VP side-chains was located on the 2VP terminus of the chains (PS-*b*-P2VPLi). Consequently, the conditions optimized to graft P2VPLi onto PS substrates were applied to the synthesis of the CSC arborescent copolymers. This involved the addition of 5 equiv of LiCl as a common ion salt, to stabilize the reactive centers by shifting the dissociation equilibrium in favor of the less reactive ion pairs, and a grafting temperature of 0 °C.[3]

A chloromethylated G1PS substrate was used in the synthesis of two G2 CSC copolymers, G1PS-*g*-(P2VP-*b*-PS), in the presence of TMEDA to enhance the reactivity of the living ends.[2,14] Following the growth of the P2VP block at −78 °C the reactor was warmed to −40 °C, found to be optimal by Kee and Gauthier,[2] for the grafting reaction. Table 5.2 provides the specific additives and grafting reaction conditions used for each of the arborescent copolymer syntheses. The additives were added at 5 equiv relatively to the living chain ends in all cases.

Characterization data for the resulting arborescent CSC copolymers are listed in Table 5.3, while the characteristics of the PS-*b*-P2VP block copolymers used in the syntheses are provided in Table 5.4. The sample nomenclature used for the side-chains provides the $M_n \times 10^{-3}$ of the respective blocks (P2VP or PS).

Table 5.2 Reaction conditions for the CSC arborescent copolymer syntheses

Graft Copolymer	Solvent	Graft Temp. (°C)	[PS-*b*-P2VPLi] (mM)	Additives (meq)	
				LiCl	TMEDA
PS-*g*-(P2VP14-*b*-PS11)	THF	–40	1.2	–	5
G0PS-*g*-(P2VP8-*b*-PS8)	THF	0	2.2	5	–
G1PS-*g*-(P2VP5-*b*-PS6)	Tol/THF	0	3.0	5	–
G1PS-*g*-(P2VP11-*b*-PS11)	THF	–40	2.5	–	5
G1PS-*g*-(P2VP25-*b*-PS20)	THF	–40	1.7	–	5
G2PS-*g*-(P2VP8-*b*-PS11)	THF	0	2.2	5	–
G2PS-*g*-(P2VP15-*b*-PS11)	THF	0	1.8	5	–
G2PS-*g*-(P2VP13-*b*-PS20)	THF	0	1.6	5	–
G3PS-*g*-(P2VP14-*b*-PS11)	THF	0	2.2	5	–

Table 5.3 Characteristics of arborescent CSC copolymers synthesized

Description	Graft Copolymer						
	M_n[a]	M_w/M_n	G_y[b]	f_w[c]	C_e[d]	% 2VP[e]	r_{h2}[f]
PS-*g*-(P2VP14-*b*-PS11)	3.2×10^5	1.06	0.22	13	0.99	52	11
G0PS-*g*-(P2VP8-*b*-PS8)	2.8×10^6	1.10	0.40	173	0.73	73	23
G1PS-*g*-(P2VP5-*b*-PS6)[g]	8.0×10^6	1.03	0.49	590	0.28	33	25
G1PS-*g*-(P2VP11-*b*-PS11)[h]	1.9×10^7	1.03	0.30	785	0.36	75	26
G1PS-*g*-(P2VP25-*b*-PS20)[h]	1.6×10^7	1.05	0.15	343	0.16	62	34
G2PS-*g*-(P2VP15-*b*-PS11)	3.8×10^7	1.02	0.02	1053	0.05	65	51
G2PS-*g*-(P2VP8-*b*-PS11)	3.1×10^7	1.03	0.06	1007	0.05	46	48
G2PS-*g*-(P2VP13-*b*-PS20)	3.7×10^7	1.01	0.06	806	0.04	55	63
G3PS-*g*-(P2VP14-*b*-PS11)	6.7×10^7	1.03	0.03	1857	0.04	70	75

[a] Absolute values determined from SEC-MALLS or laser light scattering measurements; [b] Grafting yield: fraction of side-chains becoming attached to the substrate; [c] Branching functionality: number of branches added in the last grafting cycle; [d] Coupling efficiency: fraction of available coupling sites consumed on the substrate; [e] mol %, determined by ^{1}H NMR analysis; [f] Hydrodynamic radius (nm) determined by second-order analysis of the correlation function; [g] From substrate G1PS-1; [h] From substrate G1PS-2

Table 5.4 Block copolymer side-chain characterization

	Block Copolymer Side-chain					
	PS		P2VP	Copolymer		
Graft Copolymer	M_n[a]	M_w/M_n	M_n[b]	M_n[c]	% 2VP[d]	M_w/M_n
PS-*g*-(P2VP14-*b*-PS11)	11200	1.04	13500	24700	55	1.11
G0PS-*g*-(P2VP8-*b*-PS8)	7900	1.04	7800	15700	50	1.19
G1PS-*g*-(P2VP5-*b*-PS6)	6600	1.06	5600	12200	46	1.14
G1PS-*g*-(P2VP11-*b*-PS11)	11000	1.02	11800	22800	52	1.14
G1PS-*g*-(P2VP25-*b*-PS20)	20000	1.02	24500	44500	55	1.13
G2PS-*g*-(P2VP8-*b*-PS11)	11500	1.17	8100	19600	41	1.02
G2PS-*g*-(P2VP15-*b*-PS11)	11000	1.06	14800	25800	57	1.01
G2PS-*g*-(P2VP13-*b*-PS20)	19900	1.12	12700	32600	39	1.05
G3PS-*g*-(P2VP14-*b*-PS11)	11400	1.03	13700	25100	55	1.01

[a] Absolute values from SEC analysis with DRI detector and PS calibration; [b] Determined from difference between PS and copolymer M_n; [c] Absolute values from ^{1}H NMR analysis; [d] From ^{1}H NMR analysis (mol %)

5.4.3 Purification of Arborescent Copolymers

The crude grafting products were always contaminated with linear side-chain material deactivated during the grafting reaction. Removal of the linear contaminant proved to be quite difficult because of its amphipolar properties and its relatively high molecular weight. Simple precipitation (batch) fractionation by addition of a non-solvent was unsuccessful, possibly due to the self-assembly of the block copolymer into micelle-like aggregates with size and solubility characteristics similar to the graft material. Consequently, both the linear and the graft copolymer settled out of solution simultaneously. Association of the linear copolymer with the graft copolymer was also evident from SEC analysis, which also complicated the purification of the graft polymer. Even after purification of the graft copolymer by preparative SEC under conditions where the graft copolymer peak was fully

resolved from the side-chains, characterization of the 'purified' graft material by analytical SEC revealed the presence of residual side-chains.

A method referred to as cloud-point centrifugation was developed to facilitate the purification process. To that end, the crude product was dissolved in THF (2.5 % w/v) and methanol was added until the solution became opalescent (cloud-point). The solution was then subjected to centrifugation at forces ranging from 25,000 – 50,000 × *g*, followed by decantation of the supernatant. A flow-chart outlining the cloud-point centrifugation purification protocol for a G2 arborescent copolymer is provided in Appendix 5.6 as an example. The collected sediment was tested by SEC analysis to verify the absence of side-chain contaminant. This process was repeated as necessary (1 – 3 times) until all linear contaminant was removed (undetected in analytical SEC).

While cloud-point centrifugation worked well for copolymers of generations G2 and above, the G0 and G1 copolymers could not be purified satisfactorily by that method. They were either too similar in mass to the micelles formed by the self-assembly of the side-chains, and thus sedimented along with the linear material, or were not large enough to sediment at all on the centrifugation equipment available. In this case fractionation was accomplished by preparative SEC. This sometimes required multiple injections of the collected graft copolymer fraction, as the linear contaminant had the tendency to associate with the graft copolymer (as discussed above). In some cases cloud-point centrifugation and preparative SEC were combined to expedite the purification process. The specific purification protocol used for each arborescent copolymer is outlined in Table 5.5.

Table 5.5 Purification protocol for arborescent copolymers

Description	Purification Method Cycles		
	Batch Fractionation	Preparatory SEC	Cloud-point Centrifugation
PS-*g*-(P2VP14-*b*-PS11)	–	3	–
G0PS-*g*-(P2VP8-*b*-PS8)	–	2	1
G1PS-*g*-(P2VP5-*b*-PS6)	3	–	–
G1PS-*g*-(P2VP11-*b*-PS11)	–	–	2
G1PS-*g*-(P2VP25-*b*-PS20)	–	–	3
G2PS-*g*-(P2VP8-*b*-PS11)	–	–	2
G2PS-*g*-(P2VP15-*b*-PS11)	–	–	2
G2PS-*g*-(P2VP13-*b*-PS20)	–	–	3
G3PS-*g*-(P2VP14-*b*-PS11)	–	–	2

Atomic force microscopy (AFM) analysis was found to be sensitive to the presence of linear contaminant in the graft copolymer samples. The AFM images of Figure 5.3 clearly show the difference between a properly purified sample and a crude sample containing approximately 50 % by weight of linear side-chain material. Light circular features corresponding to the graft copolymer molecules are clearly visible amongst the linear contaminant in Figure 5.3a, while these are the only features present in the purified sample (Figure 5.3b). Both samples were cast at the same concentration (10 mg/mL or 1 %).

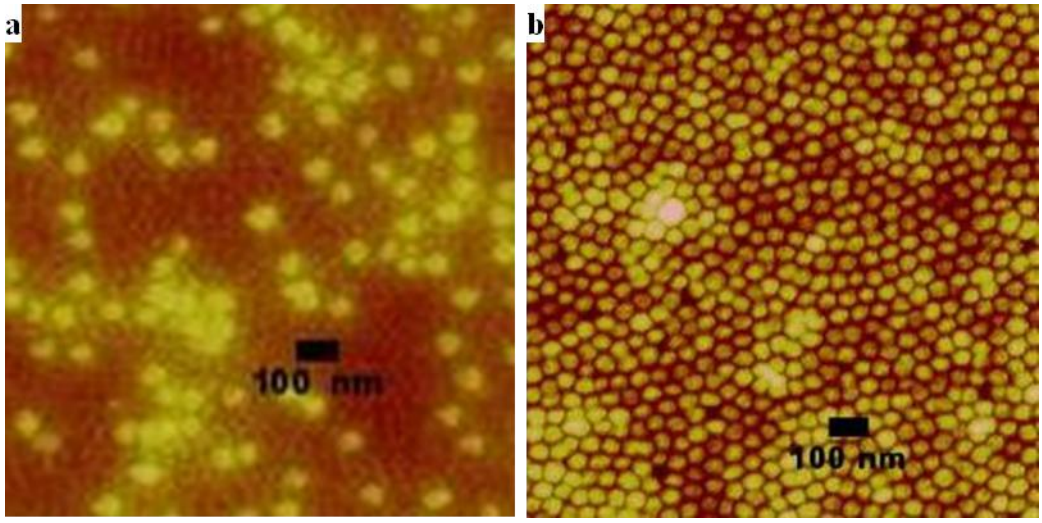

Figure 5.3 AFM image of G1PS-*g*-(P2VP5-*b*-PS6) graft copolymer sample (a) containing side-chains and (b) purified graft material.

The purification of selected samples was monitored by mass recovery for comparison to the grafting yield obtained by SEC analysis. The mass recovered by centrifugation was for the most part comparable to the SEC grafting yields, as seen in Table 5.6.

Table 5.6 Comparison of centrifugation recovery to the grafting yield from SEC

	Yield	
Description	Mass[a]	Graft[b]
G1PS-*g*-(P2VP11-*b*-PS11)	0.32	0.30
G1PS-*g*-(P2VP25-*b*-PS20)	0.23	0.15
G2PS-*g*-(P2VP8-*b*-PS11)	0.10	0.06
G2PS-*g*-(P2VP13-*b*-PS20)	0.14	0.06

[a] Final weight of pure product divided by initial weight of crude material; [b] Grafting yield: fraction of side-chains attached to the substrate, calculated by SEC

The synthesis and the purification of the CSC copolymer samples could be monitored by SEC analysis, as shown by the DRI detector traces provided in Figure 5.4 for sample G1PS-*g*-(P2VP11-*b*-PS11), by comparing elution curves for the side-chains, the substrate, the crude product, and the purified copolymer.

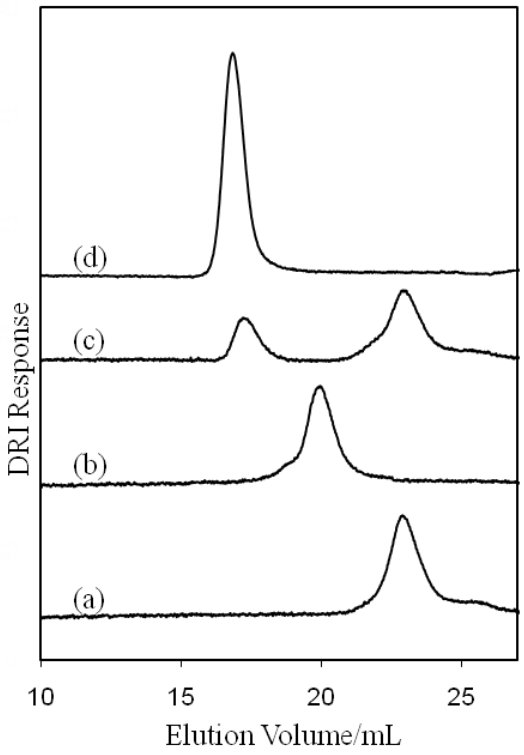

Figure 5.4 Synthesis of G1PS-*g*-(P2VP11-*b*-PS11): SEC traces for (a) PS-*b*-P2VP side-chains, (b) G1PS substrate, (c) crude product, and (d) fractionated G2 copolymer.

5.4.4 Grafting Reaction Yield

While procedures for the anionic synthesis of arborescent polymers have been established for some time, the preparation of the copolymers with a core-shell-corona (CSC) architecture proved to be quite challenging in comparison with arborescent styrene homopolymers[7,8] and core-shell (CS) arborescent copolymers incorporating a PS core and a P2VP corona.[2,3] It has

been reported that the length of the side-chains and the generation number of the substrate are major factors determining the success of the grafting reaction. Two parameters characterizing the grafting reaction are the grafting yield, also known as the grafting efficiency,[7] and the coupling efficiency.[2] The grafting yield (G_y) is defined as the fraction of side-chains generated in the reaction that becomes attached to the substrate, as expressed by Equation 5.2. This value can be determined by SEC analysis from the peak integrations for the graft polymer and the side-chains.

$$\text{Grafting Yield } (G_y) = \frac{\text{Graft Polymer Peak Area}}{\text{Graft Polymer Peak Area} + \text{Side-chain Peak Area}} \tag{5.2}$$

The coupling efficiency (C_e), corresponding to the fraction of coupling sites becoming coupled to a side-chain, is defined as the ratio of the number of chains added in a grafting reaction, also defined as the branching functionality (f_w), to the number of coupling or grafting sites (f) available on the substrate, as shown by Equation 5.3.

$$\text{Coupling Efficiency } (C_e) = \frac{f_w}{f} \tag{5.3}$$

The branching functionality of a polymer of generation G is defined in terms of its overall molecular weight $M_n(G)$, that of the preceding generation $M_n(G-1)$, and the molecular weight of the side-chains or branches (M_n^{br}), as expressed in Equation 5.4.

$$\text{Branching Functionality } (f_w) = \frac{M_n(G) - M_n(G-1)}{M_n^{br}} \tag{5.4}$$

The number of coupling sites (f) on a substrate can be calculated from its molecular weight, the average molecular weight of the structural units (MW_{avg}), and its functionalization level (F), as defined in Equation 5.5.

$$\text{Grafting Sites } (f) = \frac{M_\text{n}}{\text{MW}_\text{avg}}\ \text{F} \tag{5.5}$$

The functionalization level of the substrates was determined by ^{1}H NMR analysis as shown in Appendix 5.1, while the average molecular weight of the structural units was calculated from Equation 5.6, where M_m and M_fm represent the molecular weight of a styrene unit (104.16 g/mol) and the molecular weight of an acetylated styrene unit (146.19 g/mol), respectively.

$$\text{MW}_\text{avg} = \text{F}M_\text{fm} + (1 - \text{F})M_\text{m} \tag{5.6}$$

The coupling efficiency provides a more accurate picture of the success of the grafting reaction, as it does not take premature termination of the side-chains nor over-titration (the addition of a larger amount of substrate than necessary on a stoichiometry basis) into consideration, both of which can influence the grafting yield.

The grafting yield and the coupling efficiency are nonetheless both inversely related to the side-chain length: Fewer side-chains can be attached to the substrate when grafting longer chains. This effect has been explained on the basis of steric crowding limiting the accessibility of the coupling sites to the living ends of the unreacted chains.[1–3,7,8,15,16] Similar steric arguments can be invoked to explain the decrease in grafting yield and coupling efficiency observed for larger (upper generation) substrates: The diffusion of longer living chains to the interior of the substrate, where a fraction of the coupling sites are located, is more difficult. Further to steric congestion and diffusion limitations, upper generation substrates bring additional synthetic challenges: The substrates are purified by azeotropic distillation, but it may be more difficult to remove impurities (protic or other) buried within these densely branched polymers. These impurities can terminate the living chains before

they are able to couple with the substrate, thus reducing the grafting yield. This should not affect the coupling efficiency however, provided that enough substrate is available to titrate the living polymer and that sufficient time is allowed in the titration process (keeping in mind that the chains will eventually be terminated by the THF used as solvent, but also promoting the grafting reaction). The trends seen for the grafting yield and the coupling efficiency among the series of CSC samples prepared are consistent with the observations reported for arborescent styrene homopolymers and P2VP copolymers: Both generally decrease as the generation number of the substrate increases and for longer side-chains (Table 5.3). While the trends are similar, the synthesis of CSC arborescent copolymers is marred by surprisingly low grafting yields for all generations as compared to arborescent styrene homopolymer and PS-*g*-P2VP copolymer syntheses with comparable characteristics (substrate generation and side-chain M_n). The grafting yield and the coupling efficiency of each type of reaction are compared in Table 5.7 for selected samples (those having side-chains with an overall $M_n \approx$ 30,000 g/mol).

Table 5.7 Comparison of grafting yield and coupling efficiency when grafting PS, P2VP, and P2VP-*b*-PS side-chains with $M_n \approx$ 30,000 g/mol onto PS substrates

	Grafting Yield (%)			Coupling Efficiency (%)		
Generation	PS	P2VP	PS-*b*-P2VP	PS	P2VP	PS-*b*-P2VP
0	87	86	22	92	92	99
1	75	78	40	71	70	73
2	55	56[a]	30[a]	39	58[a]	36[a]
3	43	26	2	30	27	5
4	–	–	3	–	–	4

[a] Grafting onto chloromethylated substrate; all other values are for acetylated substrates

5.4.5 Origin of Low Grafting Yield

The unexpectedly low grafting yields and coupling efficiencies observed in the reactions prompted an investigation into the mechanism limiting the grafting reaction. Block copolymers such as PS-*b*-P2VP are known to form reverse micelles under selective solvency conditions, for example in non-polar solvents such as toluene, selective for the PS segment.[17] However, to the best of our knowledge, the micellization of PS-*b*-P2VP in THF (the solvent selected for the arborescent copolymer syntheses) has not been reported. It was nevertheless postulated that PS-*b*-P2VPLi could aggregate (in analogy to many living polymers) or otherwise self-assemble in solution, thus making the living centers less accessible for the coupling reaction. Indeed, aggregation (or self-assembly into larger micelle-like superstructures) should hinder the reaction of the living chains with the coupling sites on the substrate, or impose further restrictions to the diffusion of the living ends to the coupling sites. This situation is analogous to grafting long side-chains, known to lower the grafting yield.

To investigate this hypothesis, static and dynamic light scattering measurements were undertaken to determine the M_w, the second virial coefficient (A_2), the radius of gyration (r_g), the hydrodynamic radius (r_h), and the diffusion coefficient (D) for PS, P2VP, and PS/P2VP mixtures, as well as for PS-*b*-P2VP copolymers. Detailed background information on these analysis techniques can be found in Appendix 4.2 and Appendix 5.3.

5.4.5.1 Dynamic Light Scattering Analysis

Dynamic light scattering (DLS) measurements served to probe polymer chain aggregation under conditions similar to those used in the synthesis, apart from using terminated (non-living) polymer chains. It is understood that any association effects detected for the non-

living polymers would likely be further enhanced by the presence of the ionic chain ends. In DLS analysis, the time-dependent autocorrelation function for the scattered light intensity corresponds to a monoexponential decay curve for monodispersed species, the rate of decay (slope) being related to the diffusion coefficient. Through the Stokes-Einstein relationship (Equation 5.8), the hydrodynamic radius can be extracted from the correlation function $|g_1(\tau)|$ as shown in Equation 5.7.

$$|g_1(\tau)| = \exp(-Dq^2\tau) \tag{5.7}$$

$$\text{where } D = \frac{k_B T}{6\pi\eta_o r_h} \tag{5.8}$$

$$\text{and } q = \left(\frac{4\pi n}{\lambda}\right) sin\frac{\theta}{2} \tag{5.9}$$

The diffusion coefficient (D, Equation 5.8) is defined in terms of Boltzmann's constant ($k_B = 1.38 \times 10^{-23}$ $m^2 \cdot Kg \cdot s^{-2} \cdot K^{-1}$), the temperature T (in Kelvin), the viscosity of the dispersion medium (η_o in $Kg \cdot m^{-1} \cdot s^{-1}$), and the hydrodynamic radius (r_h in m), whereas in the expression for the scattering vector (q, Equation 5.9), n represents the refractive index of the sample, λ is the wavelength of the scattered light, and θ is the observation angle.

When performing first- and second-order cumulant analyses of an autocorrelation function corresponding to a truly monoexponential decay, due to a uniform size distribution, the two analyses yield identical hydrodynamic radii ($r_{h1} = r_{h2}$). Conversely, if the sample is highly polydispersed or bimodal (for example because of open association), the two analyses yield very different radii ($r_{h1} \neq r_{h2}$). Furthermore, narrowly dispersed species with one size population typically yield very reproducible results with a small standard deviation among

multiple measurements. More detailed information on this analysis technique can be found in Appendix 4.2.

Since the polymer concentrations used in the arborescent CSC copolymer syntheses ranged from 2 – 7 % w/v, the DLS experiments were performed within the same concentration range. The linear polymers tested had a molecular weight similar to the side-chains in the CSC copolymer syntheses. This included homopolymers of styrene (M_n = 47,000 g/mol, PDI = 1.05; M_n = 17,000 g/mol, PDI = 1.05) and 2VP (M_n = 30,000 g/mol, PDI = 1.08) which were first characterized to determine their r_h and were subjected to CONTIN distribution analysis[18] in known good solvents (THF for PS and methanol for P2VP). As expected, first- and second-order analyses of the correlation function of these low PDI samples yielded very similar hydrodynamic radii (indicative of monodispersed species) and CONTIN analysis revealed a single, narrowly dispersed size population. Since the CSC copolymer syntheses were performed in THF, different P2VP and PS-*b*-P2VP samples were also analyzed in that solvent. The results obtained are summarized in Table 5.8 (the sample nomenclature used corresponds to the $M_n \times 10^{-3}$ of the chain segments). P2VP30 was characterized at different concentrations on its own, as a 1:1 mixture with PS (PS17 + P2VP30), or as a component of block copolymers with different ratios and lengths of the PS and P2VP segments. The number of populations detected and the breadth of each population is also specified as narrowly (N) or broadly (B) distributed in each case.

Table 5.8 Size and distribution analysis for P2VP homopolymer, PS + P2VP mixture, and PS-*b*-P2VP copolymer solutions

			Radii (nm)		CONTIN	
Sample	Conc. (%)	Solvent	r_{h1}[a]	r_{h2}[b]	Populations[c]	Breadth[d]
PS47	2.5	THF	4.5 ± 0.1	4.0 ± 0.2	1	N
P2VP30	2.0	MeOH	4.7 ± 0.1	4.3 ± 0.1	1	N
P2VP30	2.0	THF	11 ± 3	6 ± 1	2	N, N
PS17 + P2VP30	2.5	THF	33 ± 11	16 ± 6	2	B, B
PS6-*b*-P2VP5	0.5	THF	78 ± 2	63 ± 2	2	N, B
PS11-*b*-P2VP14	0.5	THF	47 ± 3	29 ± 2	2	N, B
PS50-*b*-P2VP20	0.5	THF	27 ± 3	17 ± 2	2	B, B
PS25-*b*-P2VP25	5.0	THF	152 ± 3	103 ± 2	2	B, B
PS25-*b*-P2VP25	2.0	THF	45 ± 1	29 ± 1	2	N, N
PS25-*b*-P2VP25	0.5	THF	23 ± 2	13 ± 1	2	B, N
PS25-*b*-P2VP25	0.05	THF	39 ± 8	19 ± 2	1	B

[a] Hydrodynamic radius from first-order analysis of the correlation function; [b] Hydrodynamic radius from second-order analysis of the correlation function; [c] Number of distinct size populations observed in CONTIN analysis; [d] Breadth of size distribution observed in CONTIN analysis: broad (B) or narrow (N)

Selected examples of size distributions obtained by CONTIN analysis are provided in Figure 5.5.

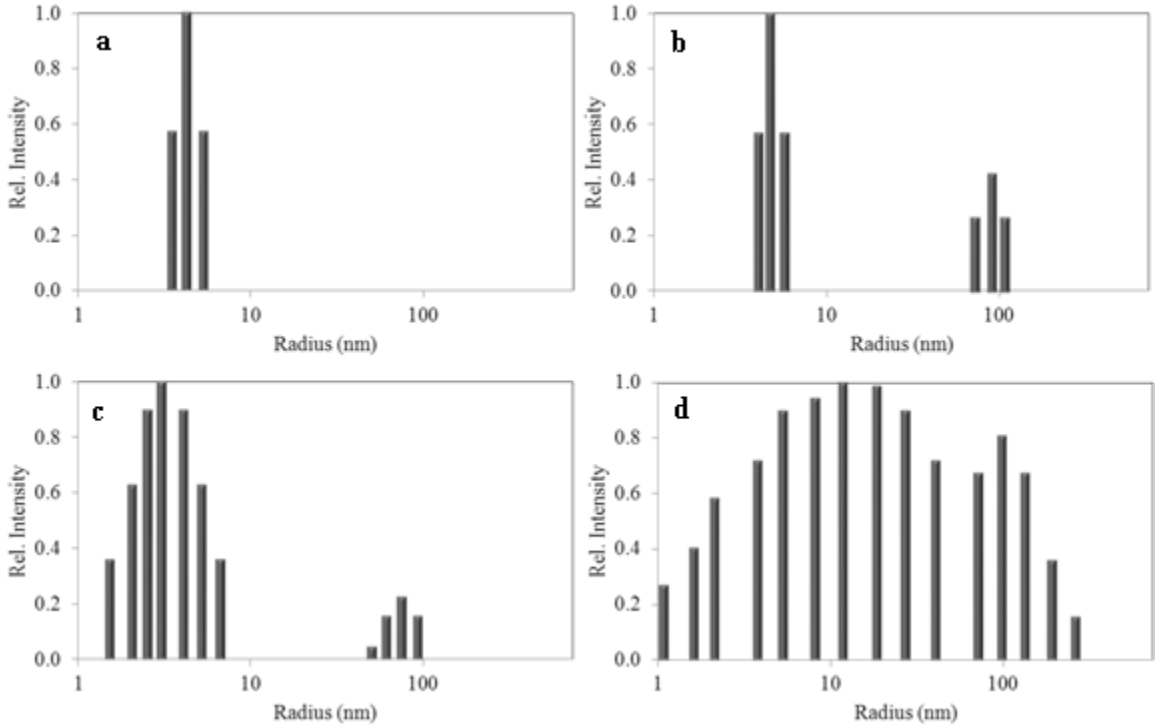

Figure 5.5 Representative size distributions from CONTIN analysis: (a) single narrow population (P2VP in methanol), (b) bimodal narrow populations (P2VP in THF), (c) bimodal broad populations (PS and P2VP in THF), and (d) single broad population (PS-*b*-P2VP in THF).

In analogy to PS in THF and P2VP in methanol, narrowly dispersed species should yield comparable radii from first- and second-order analyses of the correlation function (r_{h1} and r_{h2}, respectively), good reproducibility (small statistical errors) within a series of measurements, as well as a single narrow population in CONTIN analysis. This was not observed for any of the THF solutions containing homo- and copolymers of 2VP. Aggregation was evident in these systems on the basis of the poor agreement between r_{h1} and r_{h2}, large variations in size among successive runs (large standard deviations), and either broad or multiple populations in CONTIN analysis as shown in Table 5.8. The analysis software used only provided the size distributions shown in Figure 5.5, weighted in terms of

relative scattering intensity (proportional to both the mass and the concentration of the scattering species), and skewed towards larger particles. However it is acknowledged that size distributions on a number (or ideally weight) basis could reveal different trends. Size distributions on a weight basis, in particular, should reflect the relative amounts (mass) of reactive chains in the free vs. aggregated state in the reaction, and therefore relate more directly to the grafting yields observed.

Concerning the influence of concentration, also examined in Table 5.8, PS25-*b*-P2VP25 formed larger and more polydispersed aggregates at higher concentrations, but aggregation was still evident even at a concentration two orders of magnitude lower than that typical for the grafting reaction (0.05 %). The solutions containing the PS-*b*-P2VP copolymer had larger aggregates and broader size distributions than the 2VP homopolymer in THF.

The influence of additives was also investigated, for the PS25-*b*-P2VP25 block copolymer (5.0 % w/v in THF), as the CSC copolymer syntheses relied upon reactivity modifiers such as LiCl. Methanol (5 % v/v) was also added, with and without LiCl (0.05 % w/v) in some cases, to probe its influence on aggregation in a good solvent for P2VP. The results obtained for the additives studied are summarized in Table 5.9. It is clear that the additives had no significant influence on aggregation. The effect of solution aging in THF was also monitored. Increasing radii and broader size distributions were observed after longer time intervals, indicating that these polymers have a tendency to aggregate further with time. These results are shown in Appendix 5.7.

Table 5.9 Effect of additives on radii and size distribution for PS25-*b*-P2VP25 in THF

Polymer Conc. (%)	Additive	Additive Conc. (%)	r_{h1}[a]	r_{h2}[b]	Populations[c]
5.0	–	0	152 ± 3	103 ± 2	2
5.0	LiCl	0.05	143 ± 3	95 ± 2	2
5.0	MeOH	5.0	121 ± 2	77 ± 2	2
5.0	LiCl/MeOH	0.05/5.0	137 ± 5	89 ± 5	2

[a] Hydrodynamic radius from first-order analysis of the correlation function (nm); [b] Hydrodynamic radius from second-order analysis of the correlation function (nm); [c] Number of distinct size populations observed in CONTIN analysis

DLS can also confirm the occurrence of aggregation by the appearance of slower diffusion modes in the correlation function due to the contributions from larger particles. Larger, aggregated, species show enhanced scattering effects at low observation angles and thus the dependence of the diffusion coefficient can be monitored as a function of the observation angle. The diffusion coefficient characterizes the rate at which a molecule diffuses through a medium as defined by Equation 5.8. If a substance is monodispersed, all species diffuse at the same rate and there is no angular dependence of the diffusion coefficient. Furthermore, larger species are characterized by a smaller diffusion coefficient.

Since the scattering intensity varies strongly with the observation angle for large particles,[19] an aggregated sample should display a stronger angular dependence as compared to a unimolecular analogue. Larger particles are detected more easily at low angles, since the intensity of scattered light is greatest under these conditions.[20] In such a situation, the diffusion coefficient also displays a decreasing trend for decreasing observation angles. The angular dependence of the diffusion coefficient observed for non-aggregated (small) and aggregated (large) species is compared in Figure 5.6 as a function of the scattering vector (q, Equation 5.9) for three samples: P2VP (M_n = 30,000 g/mol) in methanol, P2VP (M_n = 30,000

g/mol) in THF, and PS-*b*-P2VP (M_n^{PS} = 25,000 g/mol, M_n^{P2VP} = 25,000 g/mol) in THF, all at a concentration of 2 % w/v.

Aggregation is evident in THF for both P2VP and PS-*b*-P2VP, as the diffusion coefficient decreases at low scattering vector values (low angles). These results are in agreement with the observations of Nordmeier and Lechner for a model system containing two different sizes of latex particles:[21] A decrease in the apparent diffusion coefficient (reduced first cumulant) at low observation angles was observed for a dispersion containing 91 nm (80 %) and 176 nm (20 %) diameter latex particles.

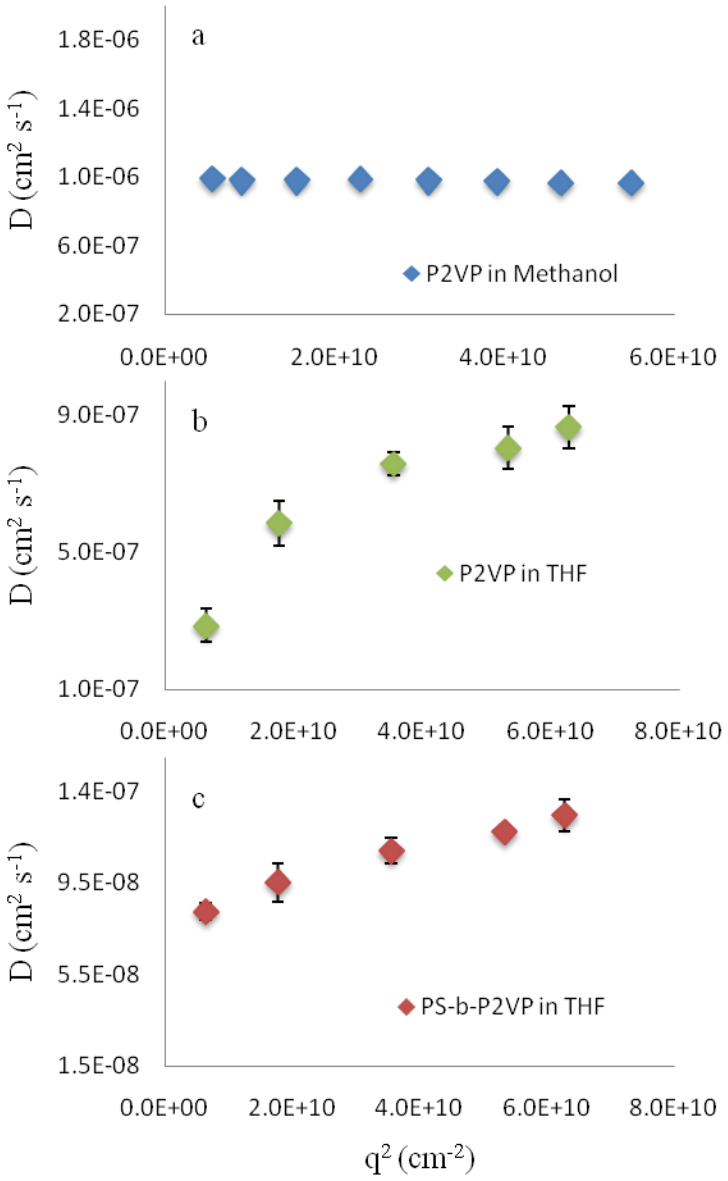

Figure 5.6 Angular dependence of the diffusion coefficient for P2VP homo- and copolymers: (a) P2VP in methanol, (b) P2VP in THF, and (c) PS-*b*-P2VP in THF.

5.4.5.2 Static Light Scattering Analysis

Static light scattering (SLS) also provides evidence for aggregate formation through the comparison of trends in Zimm plots[22] (curvature) and the polymer characteristics determined from the analysis, namely the molecular weight, the radius of gyration (r_g), and the solvent

quality (characterized by the second virial coefficient, A_2). A Zimm plot represents KC/R_θ vs. $q^2 + kC$ where K is an optical constant, C is the polymer concentration, R_θ represents the Rayleigh ratio, q is the scattering vector, and k is an arbitrary plotting constant. Background information on SLS can be found in Appendix 5.3.

When comparing Zimm plots obtained for P2VP in a good solvent (methanol) and in the solvent used for the grafting reaction (THF), it is evident that large (aggregated) species are present in THF: KC/R_θ drops at low angles, especially for the higher concentration samples, in analogy to the diffusion coefficients at low scattering angles (Figure 5.6). This downward trend is clear in the Zimm plot of Figure 5.7b, for which zero concentration and angle extrapolation was not attempted, and is due to the presence of larger species causing more intense scattering at low angles. This contrasts with the Zimm plot for P2VP in methanol (Figure 5.7a), where all the data points lie along parallel lines over the entire concentration and angle range, confirming that the polymer is well-solvated (non-associated). The curvature of the lines in the Zimm plot for PS25-*b*-P2VP25 in THF (Figure 5.7c) is more subtle, but still indicates a distribution of sizes in the sample. A single trend line was added to the data set representing the maximum concentration (C = 2.0 % w/v), and only for data points at angles above 90°, to better illustrate the drop in the KC/R_θ values.

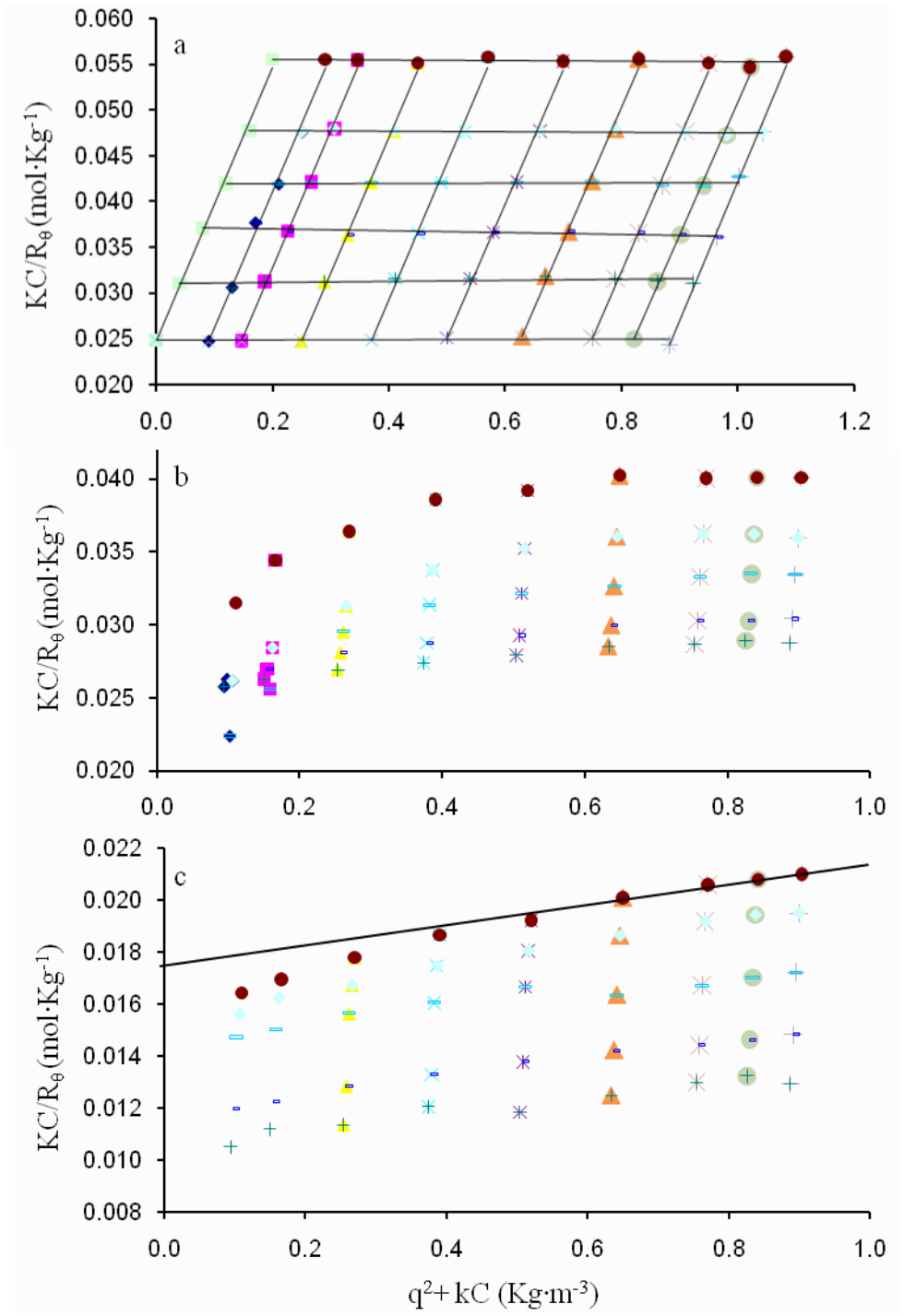

Figure 5.7 Zimm plot for P2VP (a) in methanol, (b) in THF, and (c) PS-*b*-P2VP in THF.

Table 5.10 provides the M_w, r_g, and A_2 ($cm^3 \cdot mol \cdot g^{-2}$) values determined from the Zimm plots.

Table 5.10 SLS analysis of P2VP samples

Sample	Solvent	M_w	A_2 ($\times 10^4$)	r_g
P2VP30	Methanol	40,000	7.18	6.0
P2VP30	THF	44,000	1.99	24.4
P2VP30[a]	THF	43,000	2.70	16.0
PS25-*b*-P2VP25	THF	107,000	1.88	29.9

[a] Low KC/Rθ values disregarded

The second virial coefficient characterizes solvent quality, larger values corresponding to more favorable interactions between the polymer and the solvent molecules (better solvency conditions). Large aggregates are less soluble than their linear components, so A_2 should decrease accordingly. As seen in Table 5.10 for P2VP30, A_2 is smaller in THF than in methanol. Furthermore, the (average) M_w calculated for PS25-*b*-P2VP25 is nearly twice as large as the absolute values determined by SEC analysis (M_w = 62,000 g/mol). Additional support of aggregation is provided by r_g comparison: r_g is drastically larger for P2VP30 in THF compared to in methanol. Lastly, THF is known to be a good solvent for PS, as characterized by large A_2 values (greater than 4.9×10^{-4} $cm^3 \cdot mol \cdot g^{-2}$)[23,24] in comparison to both P2VP and PS-*b*-P2VP in Table 5.10. The lower values observed for the P2VP homopolymer and the block copolymer in THF are attributed to the poor solvent quality for the P2VP segments. This suggests that, in addition to aggregation, preferential solvation for the PS segments of the block copolymers in THF could lead to encapsulation of the P2VP segments carrying the living end, which would further hinder the ability of the living ends to couple with the substrate. This provides another basis for the lower grafting yields observed when grafting PS-*b*-P2VP side-chains, as opposed to P2VP homopolymers, onto arborescent polystyrene substrates. An illustration of the encapsulation of the P2VP living ends by the PS

segments is provided in Figure 5.8 for a simple aggregate of two living block copolymer chains.

Figure 5.8 Illustration of living chain ends hindrance in a PS-*b*-P2VPLi aggregate by encapsulation due to preferential PS segment solvation.

5.5 Conclusions

Arborescent copolymers having unimolecular reverse micelle-like characteristics and a core-shell-corona architecture were synthesized by anionic polymerization and grafting. The tri-layered copolymers, with a PS core, a P2VP inner shell, and a corona of PS chains, were obtained by grafting living PS-*g*-P2VP block copolymers onto functionalized PS substrates. The synthesis of the PS-*g*-(P2VP-*b*-PS) copolymers was demonstrated for different PS substrates and for block copolymer side-chains of varying lengths. Specifically linear, G0, G1, G2, and G3 acetylated PS substrates were grafted with PS-*b*-P2VP having overall M_n values ranging from 12,000 to 45,000 g/mol. It will be demonstrated in the following Chapter that these branched amphipolar copolymers have the ability to house polar species such as metallic salts within their inner P2VP layer, which makes them useful as templates for the preparation of metallic nanoparticles.

The grafting reaction was characterized by lower than expected yields; the origin of this phenomenon was investigated using light scattering analysis. These measurements provided strong evidence for chain aggregation, and thus a potential explanation for the low yields observed for the grafting reaction of PS-*g*-(P2VP-*b*-PS). Aggregation should strongly interfere with the diffusion of the living chain ends to the sterically hindered coupling sites on the substrates. This is particularly true if the living end of PS-*b*-P2VPLi becomes buried within the aggregates. It was also shown that the solvent quality is reduced for the P2VP chain segments as compared to PS in THF. Preferential solvation of the PS segment may further lead to encapsulation of the P2VP segment carrying the reactive center, again reducing the ability of the living block copolymer chain to couple with the substrate.

While the grafting yields and the coupling efficiencies observed when grafting onto linear or G0 substrates are satisfactory, presumably because their coupling sites are relatively accessible, they decrease very rapidly for more congested substrates of generations G1 and above. Decreased coupling efficiency for upper generation substrates and when grafting longer side-chains has been observed in other arborescent polymer syntheses, but the effect was less pronounced than in the current case.

The low grafting yields also complicated product purification, and not only because of the large amounts of side-chain contaminant needing to be removed from the crude product. The amphipolar nature of the graft copolymers and the block copolymer side-chains limited the usefulness of the precipitation (batch) fractionation technique to purify many of the samples. For that reason, a cloud-point centrifugation method was developed to purify the G2, G3, and G4 graft copolymers, while preparatory SEC was necessary to isolate the G0 and G1 products.

5.6 Appendices

Appendix 5.1 Determination of the functionalization level of acetylated polystyrene by ^{1}H NMR analysis

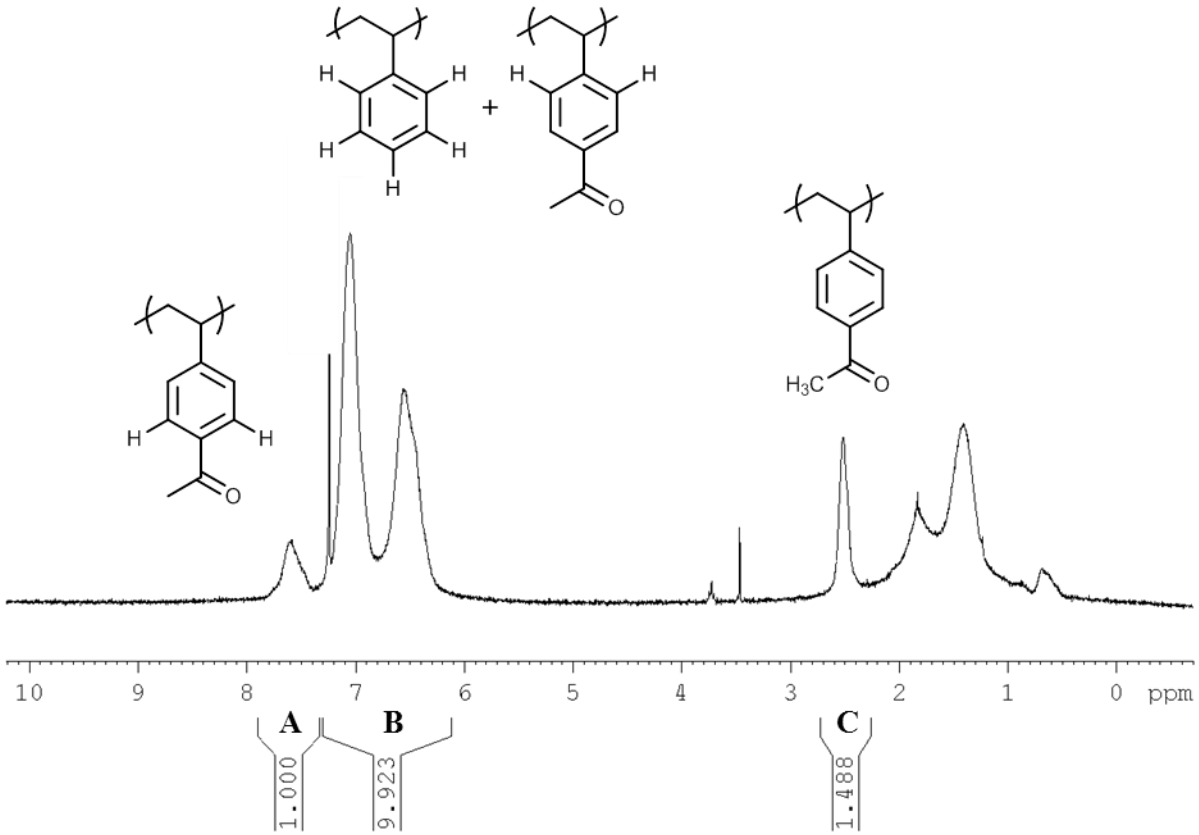

2 × Acetyl = A = 1 or 3 × Acetyl = C = 1.488
Acetyl = 0.50

(2 × Acetyl) + (5 × Sty) = B = 9.923
Sty = 1.7846

Acetylation level (mol%) = Acetyl / (Acetyl + Sty) = 0.219 (21.9 %)

Appendix 5.2 Determination of 2VP content in PS-P2VP copolymer by ^{1}H NMR analysis

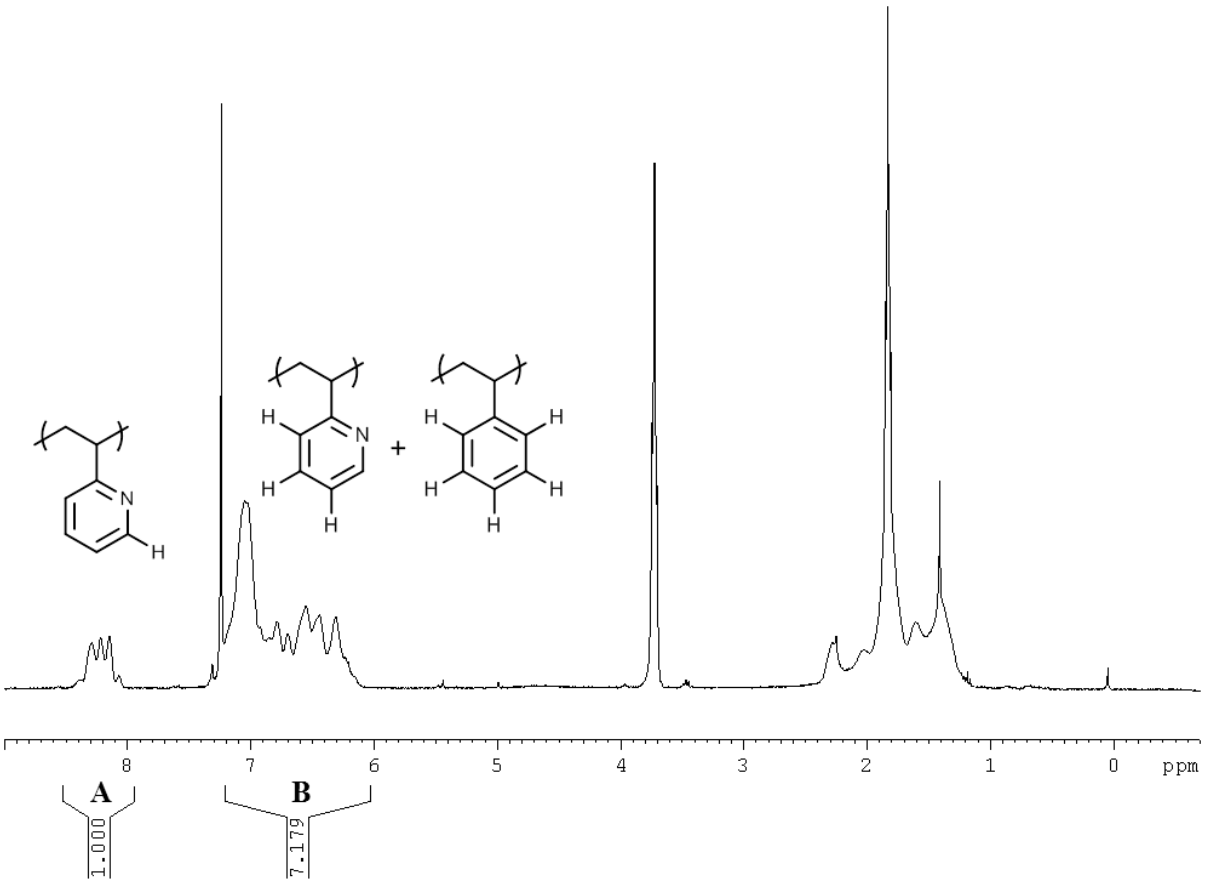

2VP = A = 1

(3 × 2VP) + (5 × Sty) = B = 7.179
Sty = 0.836

mol % 2VP = 2VP / (2VP + Sty) = 0.545 (54.5 %)

Appendix 5.3 Static Light Scattering

Static light scattering (SLS) provides information on the radius of gyration (r_g), the solvent quality (second virial coefficient, A_2), and the weight-average molecular weight (M_w).

The Rayleigh equation describes the intensity of light scattered by small particles, defined as having a size (root mean squared radius of gyration, $[\langle s \rangle_z^2]^{1/2}$) of less than roughly $\lambda / 20$. The intensity of light scattered at an angle (θ) can be represented by Equation A5.1.

$$i_\theta = \frac{I_o 2\pi^2 n_o^2}{N_A \lambda^4 r^2} \left(\frac{dn}{dc}\right)^2 (1 + \cos^2\theta) MC \tag{A5.1}$$

i_θ = Intensity of scattered light at angle θ
θ = Observation angle
I_o = Intensity of incident light
n_o = Refractive index of solvent
N_A = Avogadro's number (6.022×10^{23} mol^{-1})
λ = Wavelength of light (m)
r = Radius (distance) from scattering center (m)
dn/dc = Refractive index increment ($m^3 \cdot Kg^{-1}$)
M = Mass (Kg)
C = Concentration ($Kg \cdot m^{-3}$)

From this, the Rayleigh ratio (R_θ) and the optical constant (K) can be defined.

$$R_\theta = \frac{i_\theta}{I_o} \frac{r^2}{(1 + \cos^2\theta)} \propto i_\theta \tag{A5.2}$$

$$K = \frac{2\pi^2 n_o^2}{N_A \lambda^4} \left(\frac{dn}{dc}\right)^2 \tag{A5.3}$$

Combining Equations A5.2 and A5.3 yields the following.

$$R_\theta = KMC \tag{A5.4}$$

For an ideal polymer solution (dilute and non-interacting molecules), the Rayleigh ratio represents the total scattered intensity from each species, revealing that it is related to the weight-average molecular weight (M_w) of the polymer.

$$R_\theta = K\sum_i M_i C_i \tag{A5.5}$$

$$\frac{KC}{R_\theta} = \frac{\sum_i C_i}{\sum_i C_i M_i} \text{ where } C_i = \frac{N_i M_i}{V} \text{ so } \frac{Kc}{R_\theta} = \frac{\sum_i N_i M_i}{\sum_i N_i M_i^2} = \frac{1}{M_w} \tag{A5.6}$$

To account for interactions within the system between the macromolecules and the solvent, a virial expansion is introduced:

$$\frac{KC}{R_\theta} \approx \frac{1}{M_w} + 2A_2C + 3A_3C + \cdots \approx \frac{1}{M_w} + 2A_2C \tag{A5.7}$$

For large macromolecules with $[\langle s\rangle_z^2]^{1/2} > \lambda / 20$, destructive interferences become significant such that the Mie theory[1] states that a particle scattering function or factor P(θ) must be included. The function P(θ) can be defined as the ratio of the scattering intensity for the non-ideal system being measured and the scattering from a small particle (i_θ^o).

$$P(\theta) = \frac{i_\theta}{i_\theta^o} = \frac{R_\theta}{R_\theta^o} \tag{A5.8}$$

$$\frac{KC}{R_\theta} \approx \frac{1}{M_w P(\theta)} + 2A_2C \tag{A5.9}$$

For large random coils, the particle scattering function has the form

$$P(\theta) = \left(1 + \frac{16\pi^2 n_o^2}{3\lambda^2}\langle s\rangle_z^2 \sin^2\frac{\theta}{2}\right)^{-1} \tag{A5.10}$$

$$\langle s\rangle_z^2 \equiv r_g^2 \text{ (squared z} - \text{average radius of gyration)}$$

Substituting Equation A5.10 into Equation A5.9 we arrive at the following

$$\frac{KC}{R_\theta} = \frac{1}{M_w} + \frac{16\pi^2 n_o^2}{3\lambda^2 M_w}\langle s\rangle_z^2 \sin^2\frac{\theta}{2} + 2A_2C \tag{A5.11}$$

By substituting in the scattering vector (q, Equation 5.9), the equation becomes

$$\frac{KC}{R_\theta} = \frac{1}{M_w} + \frac{1}{3M_w}\langle s\rangle_z^2 q^2 + 2A_2C \tag{A5.12}$$

The angular dependence of the scattered light intensity for small and large species is compared in Figure A5.1. Rayleigh scattering by small particles (Equation A5.1) is shown on the left, while Mie scattering for large particles (Equation A5.9) is shown on the right. Notice that for large particles the scattering envelope becomes asymmetrical, as more intense scattering occurs at low angles.

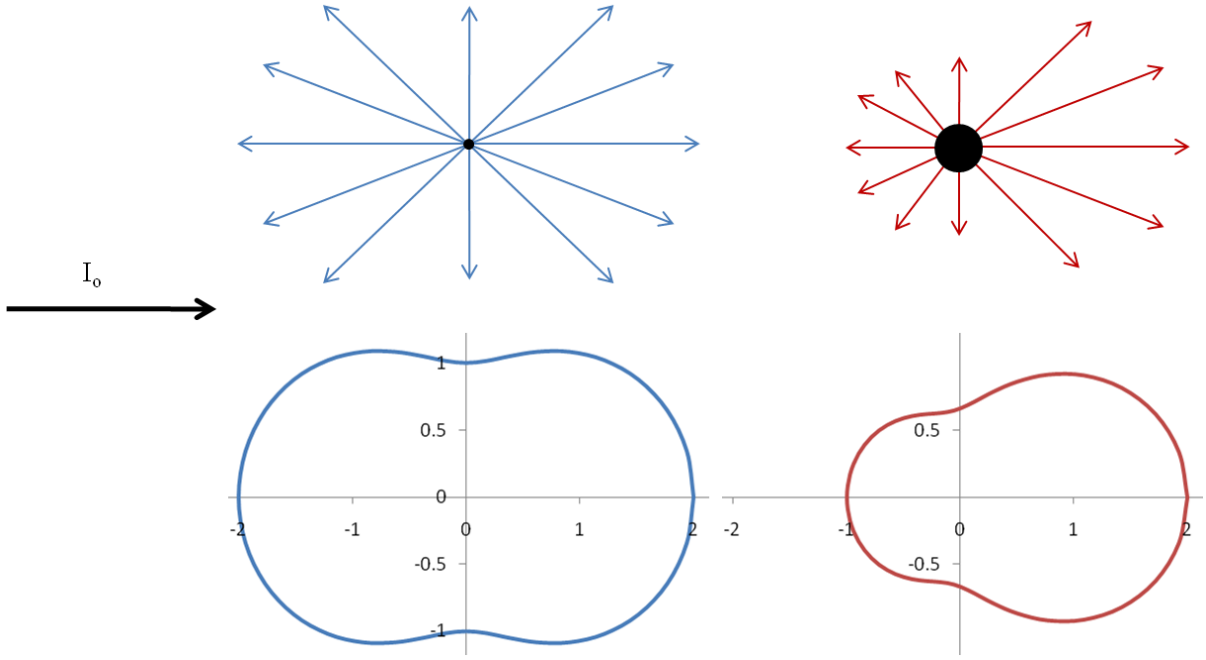

Figure A5.1 Illustration of the angular dependence of scattered light intensity for small (left) and large particles (right).

By measuring R_θ at different angles for various concentrations, the data collected can be represented in a Zimm plot (Equation A5.13),[2] where k is an arbitrary plotting constant. An example of a Zimm plot is provided in Figure A5.2.

$$\frac{KC}{R_\theta} \text{ vs. } q^2 + kC \qquad \text{(A5.13)}$$

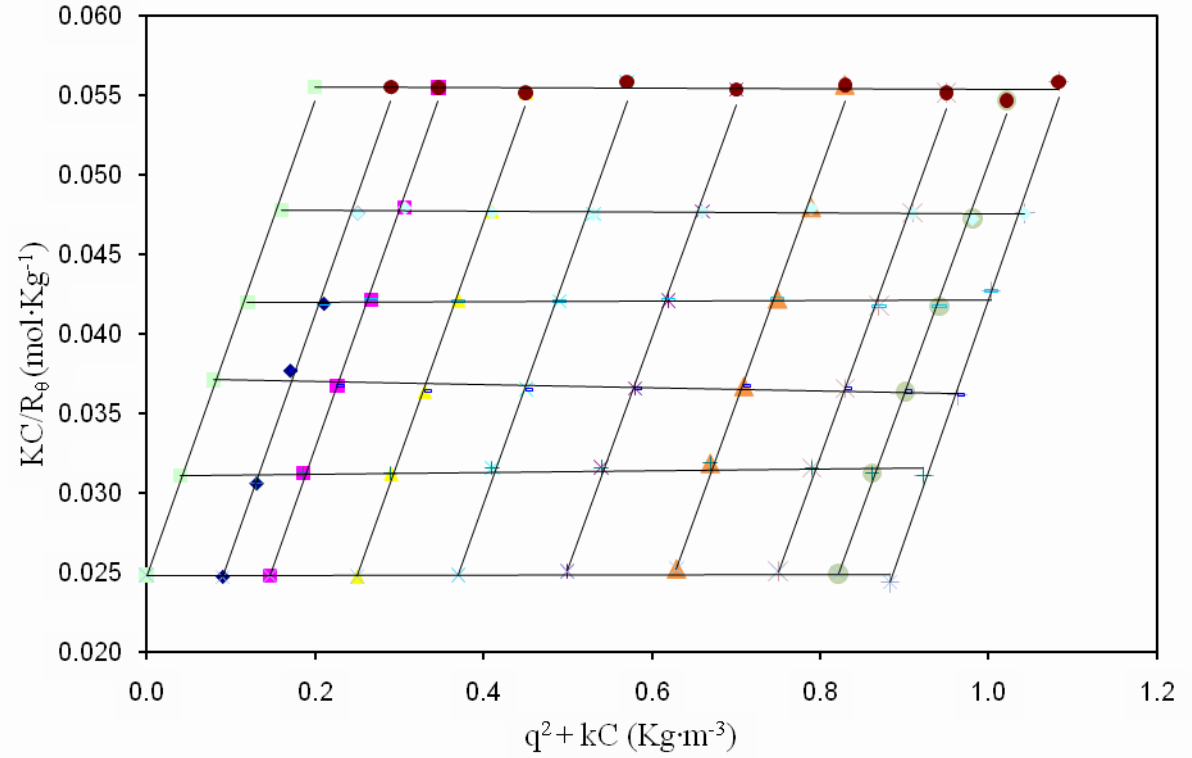

Figure A5.2 Zimm plot with trend lines.

Two limiting cases can be determined by extrapolation from the Zimm plot, corresponding to zero angle and zero concentration. By extrapolating to zero angle ($\theta = 0$) M_w is obtained from the intercept, and A_2 is extracted from the slope of the line.

$$\frac{KC}{R_\theta} = \frac{1}{M_w} + 2A_2C \tag{A5.14}$$

By extrapolating to zero concentration ($C = 0$), M_w is also determined from the intercept and the radius of gyration (r_g, $[\langle s \rangle_z^2]^{1/2}$) is derived from the slope.

$$\frac{KC}{R_\theta} = \frac{1}{M_w} + \langle s \rangle_z^2 \frac{1}{3M_w} q^2 \tag{A5.15}$$

Appendix 5.4 Chloromethylation of polystyrene and 'grafting onto' chloromethylated substrates

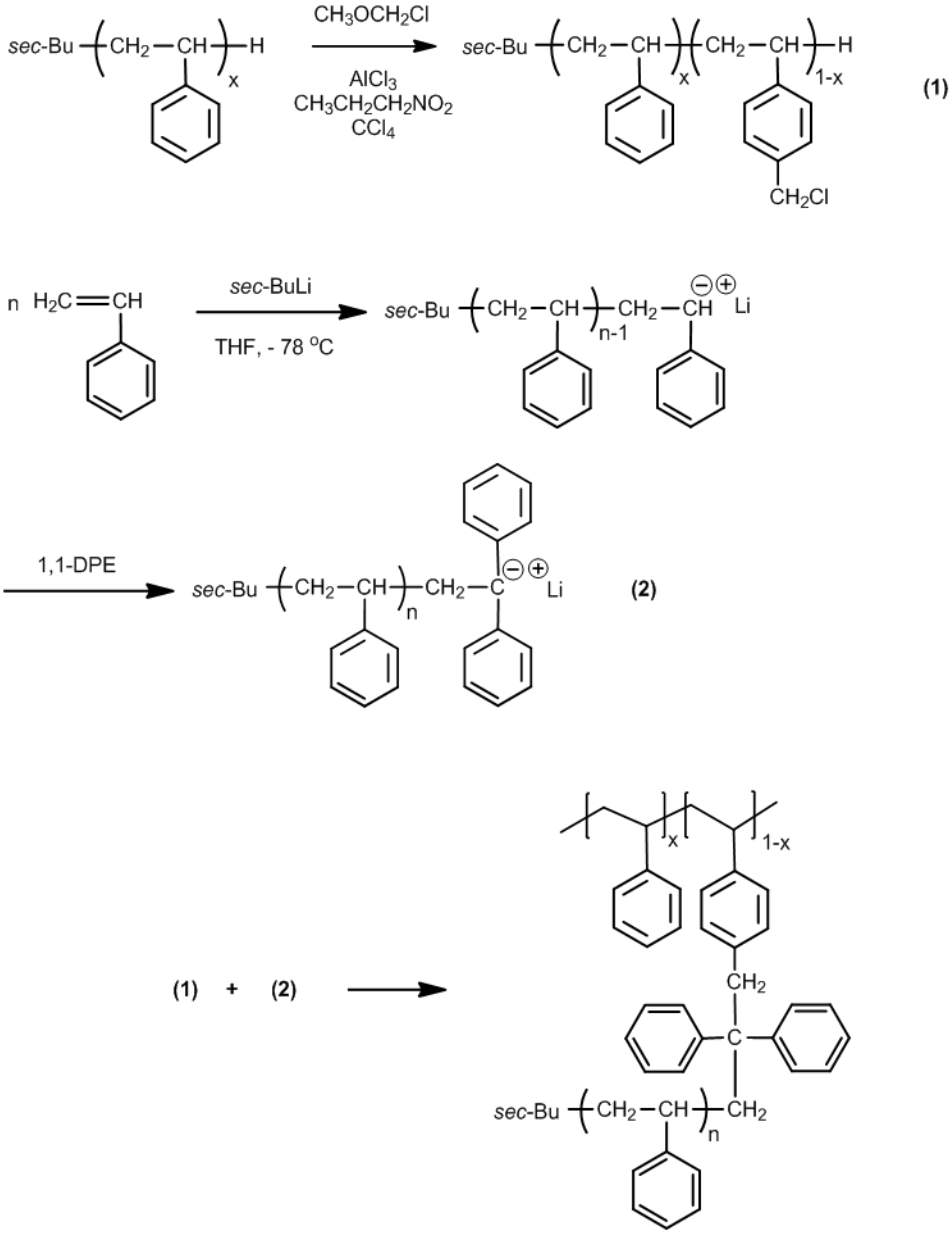

Appendix 5.5 Side reaction resulting from uncapped PSLi during 2VP addition

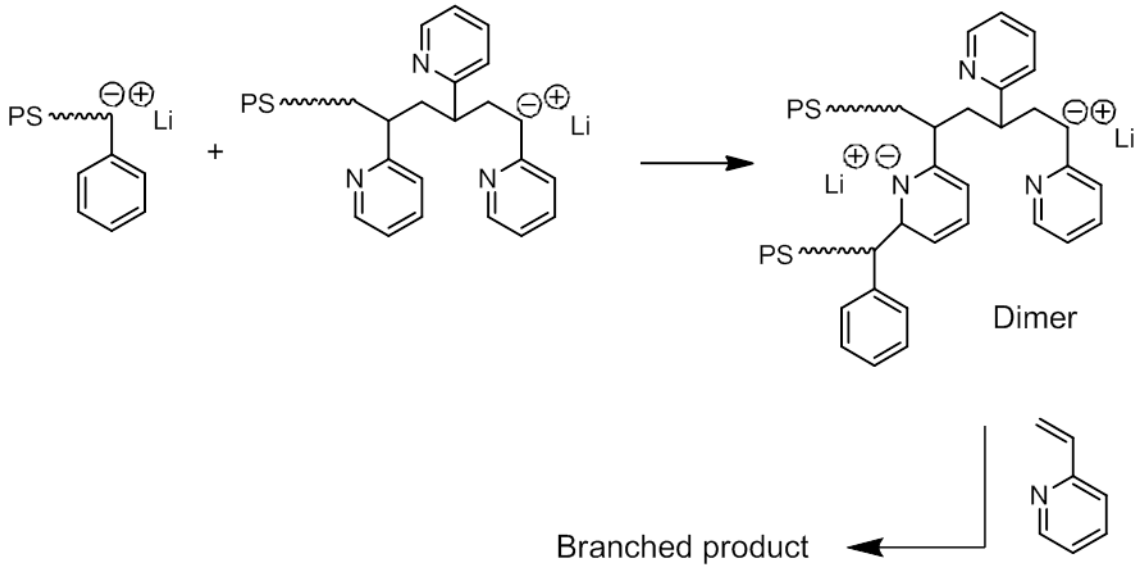

Appendix 5.6 Cloud-point centrifugation purification of G2 arborescent CSC copolymer

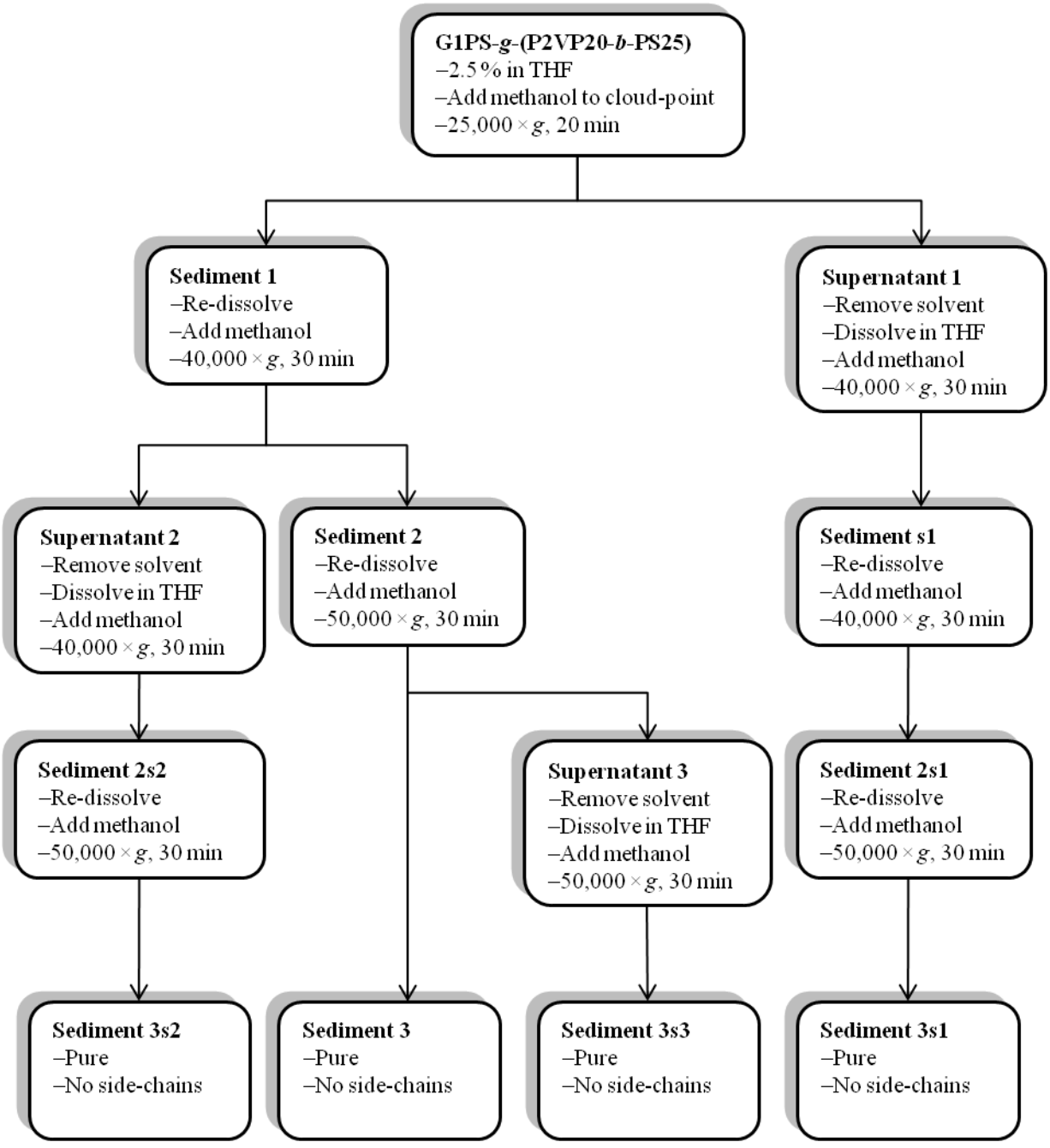

Appendix 5.7 Effect of aging on size and distribution for solutions of P2VP homo- and copolymers in THF

Sample	Polymer Conc. (%)	Additive	Additive Conc. (%)	Aging (days)	r_{h1} [a]	r_{h2} [b]
P2VP30	2	–	0	–	11 ± 3	6 ± 1
P2VP30	2	–	0	3	28 ± 3	14 ± 2
PS17 + P2VP30	2.5	–	0	–	33 ± 11	16 ± 6
PS17 + P2VP30	2.5	–	0	3	82 ± 1	58 ± 1
PS11-*b*-P2VP14	5	TMEDA	0.5	–	45 ± 2	29 ± 1
PS11-*b*-P2VP14	5	TMEDA	0.5	3	134 ± 16	92 ± 5
PS25-*b*-P2VP25	5	LiCl/MeOH	0.05/5.0	–	137 ± 5	89 ± 5
PS25-*b*-P2VP25	5	LiCl/MeOH	0.05/5.0	3	158 ± 3	104 ± 3

[a] Hydrodynamic radius from first-order analysis of the correlation function (nm); [b] Hydrodynamic radius from second-order analysis of the correlation function (nm)

Chapter 6

Amphipolar Arborescent Copolymers with a Core-Shell-Corona Architecture: Metal Coordination and Phase Segregation

6.1 Overview

Dendritic graft (arborescent) copolymers with a novel core-shell-corona (CSC) architecture have been synthesized and used as templates for the preparation of metallic nanoparticles. The inner poly(2-vinylpyridine) layer of these arborescent polystyrene-*graft*-[poly(2-vinylpyridine)-*block*-polystyrene] molecules can coordinate with metallic salts and acids in non-polar and intermediate polarity solvents. Upon loading with $HAuCl_4$, the characteristics of the polymer templates (mainly their generation number) govern the distribution of the metal within the molecules. Numerous morphologies were observed by microscopic analysis of the G0 – G4 arborescent copolymers investigated, namely spherical, toroidal, raspberry-like, and spherical nano-cage morphologies, as well as a new cylinder-in-sphere morphology. The morphologies obtained result from intramolecular phase segregation induced by the uptake of the charged metallic species. Various reduction methods were examined for the $HAuCl_4$-loaded molecules, the size and dispersity of the resulting nanoparticles being independent of the template polymer characteristics and rather controlled by the amount and the strength of the reducing agent used. Stronger and/or excesses of reducing agents provided smaller, more uniform nanoparticles, while reduction methods also degrading the polymer template such as UV and plasma treatments generated narrowly dispersed but larger nanoparticles. Reduction of $HAuCl_4$-loaded copolymer films with $NaBH_4$ solution resulted in improved morphology retention; the Au^0 nanoparticles remained concentrated within the phase-segregated regions of the template.

6.2 Introduction

Nanoparticle research has received much attention in recent years due to the unique properties and applications that nano-sized species possess. Metallic nanoparticles, in particular, have diverse application areas including imaging agents, nonlinear optics, microelectronics, separation science, diagnosis, targeted biological labeling and delivery systems, cell therapy or destruction, and catalysis.[1] Various methods have been examined for the preparation of metallic nanoparticles using polymeric templates, as discussed in Chapter 3 of this Thesis. Some of these methods include self-assembled block copolymer reverse micelles[2,3] and networks of amphiphilic polymers.[4] The use of dendrimers and hyperbranched polymers as unimolecular scaffolds, closely related to the work described in this Chapter, has also been successfully demonstrated.[5]

We have investigated a new method for the preparation of metallic nanoparticles using a class of amphipolar graft copolymers with a dendritic architecture, the arborescent polymers, as templates. Specifically, arborescent polystyrene-*graft*-[poly(2-vinylpyridine)-*block*-polystyrene] copolymers with a core-shell-corona (CSC) architecture were synthesized and applied to the preparation of gold nanoparticles.[6] The synthesis of the polymeric scaffolds requires the functionalization of linear and branched polystyrene (PS) substrates with acetyl coupling sites and grafting with 'living' polystyrene-*block*-poly(2-vinylpyridine) chains, as illustrated in Figure 6.1. General information on arborescent polymer synthesis, and particularly the *grafting onto* method used herein, can be found in Chapter 2.

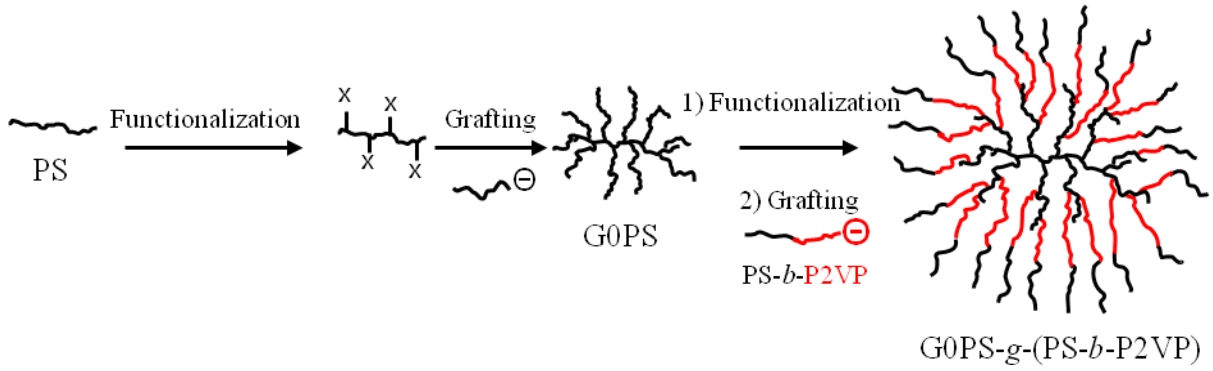

Figure 6.1 Schematic representation of a G0PS-*g*-(P2VP-*b*-PS) arborescent CSC copolymer synthesis.

The layered CSC architecture of the arborescent copolymer (PS core, P2VP shell, and PS corona) is clearly seen in Figure 6.1. Since the grafting reaction used has been reported previously for coupling PS and P2VP homopolymer side-chains with functionalized PS substrates, it was expected that grafting would proceed in a similar fashion for PS-*b*-P2VP copolymer side-chains. While successful, coupling with block copolymer side-chains was characterized by lower grafting yields as compared to their homopolymer analogues. This was attributed to selective solvency conditions for the PS and P2VP segments leading to the formation of aggregates under the grafting reaction conditions used, and/or encapsulation of the propagating centers limiting the ability for the living chain ends to diffuse to the coupling sites on the functionalized substrates. Details on the synthesis of these polymers can be found in Chapter 5.

The resulting amphipolar dendritic species have a covalently bonded, layered architecture with an inner P2VP shell that can be coordinated with metallic salts or acids such as tetrachloroauric acid ($HAuCl_4$). This architecture effectively corresponds to a reverse unimolecular micelle, but also containing a hydrophobic core in this case. The current

research has focused mainly on $HAuCl_4$, as this is a well-documented nanoparticle precursor investigated by numerous templating methods, as discussed in Chapter 3. Additionally, $HAuCl_4$ is easy to work with and has its own important properties and applications in catalysis, biological sensors, and nonlinear optics, due to the surface plasmon resonance effect which the nanoparticles exhibit. There have been numerous reviews on gold nanoparticles discussing their synthesis, characterization, and applications at length.[7] Metal coordination and reduction within a G0PS-*g*-(P2VP-*b*-PS) template are illustrated in Figure 6.2.

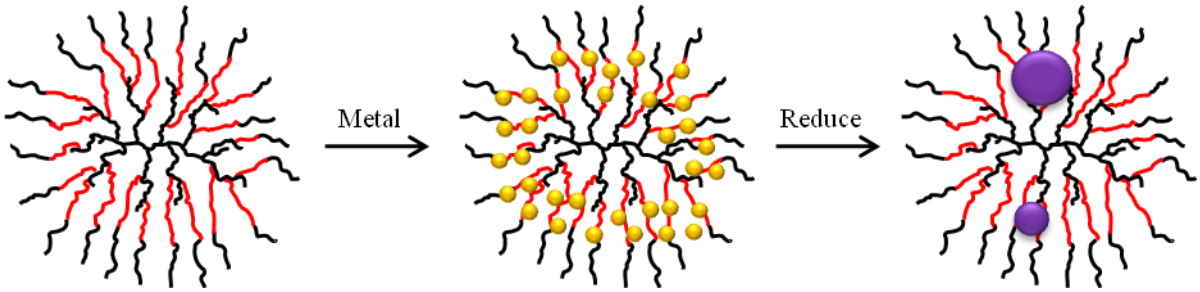

Figure 6.2 Metallic loading of G0PS-*g*-(P2VP-*b*-PS) CSC copolymer and subsequent reduction.

The unimolecular micelle architecture of amphipolar arborescent copolymers is much more stable as a template for loading polar compounds than micelles formed by the self-assembly of linear block copolymers (also known as intermolecular micelles), as it has no critical micelle concentration. The dynamic exchange of chains within the micellar structures with free chains in solution is suppressed in these unimolecular micelles, even under non-selective solvency conditions, while the PS shell provides solubility in low- to medium-polarity solvents.

Aside from their inherent stability, arborescent copolymers offer other important advantages over other templating methods. For example, variations in the degree of polymerization of the side-chain building blocks and the number of grafting cycles (generations) can provide control over the characteristics of the templates (e.g. core size, chain mobility, stabilizing layer thickness) beyond the limits achievable through the self-assembly of block copolymer chains. These characteristics may be important to tailor the activity of these nanospecies in catalytic applications,[8] or their optical properties relevant to biological applications such as cell therapy.[1b,h-j]

The self-assembly of block copolymers has been investigated for many systems and leads to the formation of different nanostructures in the solid state including spheres, cylinders, vesicles, compound micelles, or hierarchical assemblies with different packing modes (e.g. face- or body-centered packing, hexagonal cylindrical packing, gyroid structures, lamellae).[9] Some of these structures, shown in Figure 6.3, are also encountered for both di- and triblock copolymer amphiphiles in solution.[10–15]

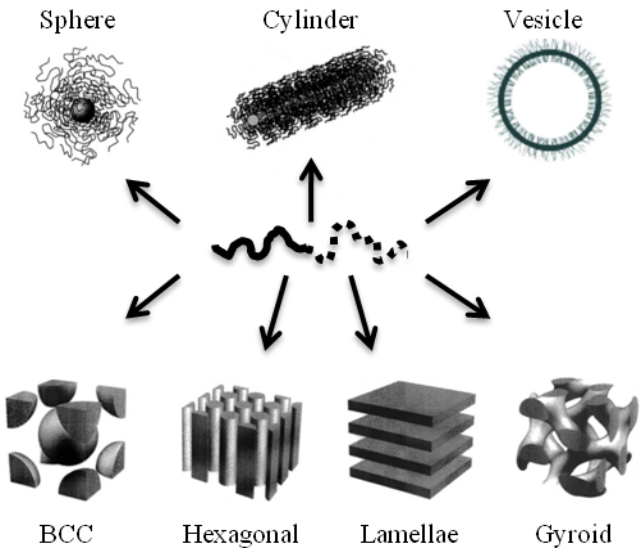

Figure 6.3 Examples of structures formed by block copolymer self-assembly.[9]

The types of morphologies obtained depend on factors such as the chemical nature of the segments, the length of each block, their degree of incompatibility, and in the case of charged systems, the ionic strength.[16] While core-shell morphologies are commonly encountered for block copolymer micelles, so-called multicompartment micelles, which form internal subdivisions or multiple nanodomains, are as also encountered.[17–19] These nanophase-separated micelles have potential applications in areas such as drug delivery, biological system simulation, and catalysis.[20,21] It should be noted that intricate phase-segregated morphologies such as those seen in Figure 6.3 have not been reported for arborescent copolymers so far, with the exception of core-shell morphologies.[22] The amphipolar arborescent copolymers investigated in this Chapter display unique phase segregation upon coordination with metallic salts or acids, including intramolecular nanodomain formation with morphologies resembling their block copolymer analogues, as well as new intricate structures.

Numerous modeling methods have been applied to predict micelle morphologies from phase segregation.[23–29] Unfortunately, there are no reports in the literature relating to the prediction or the existence of morphologies arising from intramolecular phase segregation in truly unimolecular species. Additionally, to the best of our knowledge, there are currently no reports on intramolecular phase segregation to the extent observed for arborescent copolymers with a CSC architecture.

6.3 Experimental Procedures

6.3.1 Synthesis

A comprehensive investigation of the synthesis and the purification of the arborescent CSC copolymers used as metallic nanoparticle templates was provided in Chapter 5 of this Thesis. The characteristics of the grafting substrates used can be found in Table 6.1 and the characteristics of the CSC copolymers used in the templating experiments are provided in Table 6.3.

6.3.2 Metal Loading and Reduction

6.3.2.1 Solution Loading

The solvents used were toluene (EMD, Omnisolv), tetrahydrofuran (THF; EMD, Omnisolv), and chloroform ($CHCl_3$; Sigma-Aldrich, CHROMASOLV®, for HPLC, ≥ 99.8 %, with 0.5 – 1.0 % ethanol as stabilizer). The template polymer was dissolved in the selected solvent at a concentration ranging from 0.1 to 0.5 % w/v. Two different solution loading protocols were investigated: direct addition of the metallic salt or acid in the solid form to the polymer solution, or addition as a 1 % w/v solution in the same solvent. For example when loading was performed in toluene solid $HAuCl_4$ was added, as it is not soluble in toluene, while in experiments using THF the gold was added as a THF solution. The template loading levels ranged from 0.125 to 1.0 equivalent of metal per 2VP unit. The polymer solutions were allowed to equilibrate with magnetic stirring for at least 24 h before analysis, unless time-dependent experiments were performed. The metallic compounds investigated were tetrachloroauric acid ($HAuCl_4$; Alfa Aesar, 99.9 %), palladium(II) acetate ($Pd(OAc)_2$; Strem

Chemicals, min. 98 %), and hexachloroplatinic(IV) acid (H_2PtCl_6; Sigma-Aldrich, ACS reagent).

6.3.2.2 Film Loading

The film loading technique involved the deposition of an ionized copolymer solution and loading of the dry film by exposure to a $HAuCl_4$ solution. The arborescent copolymers were ionized by dissolution in THF (1.0 % w/v, 10 mg/mL) and the addition of 1 equiv of HCl (Fisher brand, reagent grade, 12.0 N) per 2VP unit (HCl:2VP unit ratio = 1.0) with vigorous stirring. The concentration of the HCl solution was varied for each composition of copolymer to maintain a final solution composition of 98 % v/v THF and 2 % v/v water.

Thin films were cast from these solutions onto TEM grids or AFM substrates as described in Sections 6.3.4 and 6.3.6, respectively. Once the polymer film was dry, 1.0 % w/v $HAuCl_4$ solution in Milli-Q water was placed on top of the film with a syringe and a 22-gauge needle (a single drop for the TEM grid, multiple drops for the AFM films due to their much higher surface area; namely 0.8 mm^2 vs. 1 cm^2). The solution was left on the surface for 1 min for the TEM films and 5 min for the AFM films, and then wicked away with filter paper while holding the substrate with fine-tipped forceps. The films were rinsed by gently dropping Milli-Q water onto their surface with a syringe, remaining water droplets being wicked away with filter paper, and blow-dried with a gentle stream of filtered air. The films were left to dry overnight before analysis.

6.3.2.3 Solution Reduction

Anhydrous Hydrazine. That compound was prepared by vacuum thermolysis of hydrazonium cyanurate by a method adapted from Nachbaur and Leiseder.[30] Glass wool was placed

loosely at the bottom of a 4.0 cm diameter glass tube terminated with a ground glass joint. The tube was connected to a finger condenser with a vacuum pump and a nitrogen purging line (See Appendix 6.1 for the reaction scheme and the apparatus used). The apparatus was evacuated and flamed to remove adsorbed moisture, and then purged with nitrogen. The cylindrical glass tube was disassembled while purging with nitrogen and hydrazine cyanurate (Fluka, 99+ %) was loaded within the glass wool fibers. The tube was re-attached to the condenser and placed in a horizontal tube furnace (Lindberg Heavy Duty, type 54032). After evacuation to 0.1 mm Hg, the sample was dried at 110 °C for 1 hour. The temperature was then increased to 220 °C at a rate of approximately 2 °C/min, while the finger condenser was placed in a Dewar flask containing liquid nitrogen. The anhydrous hydrazine collected was transferred to a vial under nitrogen. The sealed vial was stored and used in a dry box. It should be noted that hydrazine is a highly toxic compound and is unstable, especially in the anhydrous form.

Solution reduction with anhydrous hydrazine (0.02 % v/v in dry toluene) was performed in two different regimes, i.e. nearly stoichiometric conditions (1.2:1) and with a large excess (10:1) of N_2H_4:Au. The calculated amounts of hydrazine solution were added to the $HAuCl_4$-loaded templates. Following a loading time of at least 24 h, excess hydrazine was quenched by addition of an equimolar amount of concentrated HCl. The samples were then removed from the glove box for centrifugation (1300 × *g*, 10 min) and films were cast from the supernatant.

Sodium Borohydride. A sodium borohydride ($NaBH_4$; Sigma-Aldrich, 98 %) solution in methanol (0.5 % w/v, 5 mg/mL) was prepared immediately before use and was added in a

10:1 ratio relatively to the metal. The reducing reagent was added directly to the copolymer solution with vigorous stirring.

6.3.2.4 Solid State Reduction

Ultraviolet Light Irradiation. Reduction of the $HAuCl_4$-loaded arborescent copolymers by UV irradiation used low pressure mercury lamps (Rayonet Photochemical Reactor Lamp, No. RPR-2537A) for 12 h at a distance of approximately 5 cm from the sample films cast on AFM or TEM substrates.

Plasma Treatment. $HAuCl_4$-loaded polymer samples were subject to hydrogen plasma to both reduce the metallic salt and remove the polymer template in one step. A PVA TePla 100 Plasma System was used to create a 200-W hydrogen plasma and the samples (thin films cast on AFM or TEM substrates) were exposed for 60 min at 0.879 mbar H_2.

Hydrazine Vapor. $HAuCl_4$-loaded arborescent copolymer films cast on AFM or TEM substrates were placed in a vacuum line manifold also housing a small vial of anhydrous hydrazine. The manifold was purged with nitrogen and then partly evacuated to approximately 5 mm Hg. The system was isolated from the vacuum and the hydrazine vapor was allowed to diffuse and react with the metal-loaded polymer films for 12 h.

Sodium Borohydride Film Reduction. Arborescent copolymers were loaded in solution with $HAuCl_4$ as per Section 6.3.2.1, and then cast onto TEM grids as described in Section 6.3.4. One drop of freshly prepared $NaBH_4$ solution in methanol (1.0 % w/v, 10 mg/mL) was placed on top of the film using a syringe with a 22-gauge needle. The solution was left on the surface for 1 min, wicked away with filter paper, and the surface was gently rinsed with Milli-Q water. The remaining water droplets were wicked away with filter paper and the film

was blow-dried with a gentle stream of filtered air. The films were left to dry overnight before analysis.

6.3.3 Dynamic Light Scattering

Batch-wise light scattering measurements were carried out on a Brookhaven BI-200 SM light scattering goniometer equipped with a BI-2030AT 201-channel correlator and a Claire Lasers CLAS2-660-140C (120 mW) laser operating at 656 nm. All the samples were measured at 25 °C after at least 3 filtrations with a 0.45 μm PTFE membrane filter. The correlator was operated in the exponential sampling mode. The hydrodynamic radii were calculated from the z-average translational diffusion coefficients obtained from first- and second-order cumulant analysis of the correlation function (to better account for polydispersity effects) at a scattering angle of 90°. The solutions were prepared at concentrations ranging from 0.05 % to 2.5 %, depending on the molecular weight of the sample. The uncertainties reported on the radii measurements correspond to the standard deviation for a series of at least 10 measurements. Detailed information on this analysis technique can be found in Appendix 4.2.

6.3.4 Transmission Electron Microscopy (TEM)

Thin Film Preparation. Thin films were cast onto 300-mesh copper TEM grids coated with carbon and Formvar® (Electron Microscopy Sciences, FCF300-CU). When film treatment was required (metal loading, film reduction, UV, plasma), silicon monoxide-coated copper grids were used (Electron Microscopy Sciences, SF400-CU) due to their improved stability. The thin films were obtained by placing a drop of the polymer solution (0.1 to 0.5 % w/v) onto the grid atop a piece of filter paper. The filter paper acted as a wicking agent to remove

excess fluid and allow the formation of a thin film. The grid was then immediately transferred onto a fresh piece of filter paper and placed in a Petri dish for drying overnight under ambient conditions.

Instrumentation and Analysis Methods. The metal-loaded polymer films were imaged with a Philips CM10 TEM instrument operating at 60 kV. The images were recorded with an Advance Microscopy Techniques 11 megapixel digital camera and the accompanying Image Capture Software Engine version 5.42.558. Feature size analysis was performed with the ImageJ processing software[31] by setting the scale for each digital image (pixels/nm) on the basis of the magnification and the resolution used. Feature size measurement was carried out by two methods. Samples not subjected to reduction were measured manually using the circle area function: Each feature was delimited by a manually drawn circle whose area was determined by the software, and the effective radius was calculated from the area. At least 30 measurements were recorded for each sample to provide adequate size distribution information. For the reduced samples the features were well-defined and had high contrast with the background, and thus the automatic analysis tool (Analyze Particles) was used. This tool measures the area of all particles within the limits of a user-defined circular threshold which encompassed the individual metallic regions. This process typically yielded at least 300 area measurements from which the radii and size distribution were calculated.

In some cases, a high pass filter was applied to the TEM micrographs with photo editing software, to correct for uneven exposure and allow for better visualization and more accurate measurement of the features.

6.3.5 Scanning Electron Microscopy

Scanning electron microscopy (SEM) was performed with a Hitachi model S2000N instrument at voltages ranging from 3 to 15 kV and working distances from 5 to 10 mm in the field emission mode (FE-SEM). Samples analyzed by SEM were prepared on silicon substrates as described in Section 6.3.6.

6.3.6 Atomic Force Microscopy (AFM)

Substrate Preparation and Film Casting. Muscovite mica sheets cut into 1 cm^2 pieces were adhered to a steel substrate of approximately the same size using double-sided tape, to allow securing of the sample to the magnetic spin coater and the magnetic scanner head of the AFM instrument. Immediately prior to film casting, the mica was cleaved with a strip of tape (Scotch™ Magic™ brand tape) to expose a fresh (hydrophilic) surface.

Silicon substrates were also used after cleaning and activation immediately prior to film casting. A silicon wafer was cleaved into 1 cm^2 pieces with a diamond knife, cleaned in an ultrasonic bath with 2-propanol for 3 min, and then blown dry with filtered nitrogen. The wafers were then exposed to UV light (5 mW/cm^2, 40 W, UV Technik Speciallampen GmbH, main emission 185 nm) and ozone for 12 min at an oxygen flow of 500 mL/min. Acidic etching was also used to clean and activate the silicon when the UV/ozone apparatus was not available. This was performed by immersion of the substrate in a solution of sulfuric acid and hydrogen peroxide (30 %) 3:1, followed by water, acetone, methanol, and 2-propanol rinses. The substrates were dried with a stream of filtered nitrogen and fixed to a metal substrate using double-sided tape.

After mounting on the magnetic spin coater, drops of solution were placed on the substrate with a pipette to completely cover it and the substrate was spun for at least 15 s at 3000 rpm.

Instrumentation and Analysis Methods. AFM micrographs were recorded in the tapping mode on a Nanoscope III SFM instrument (Digital Instruments, model MMAFM-2, scan stage J) housed in a NanoCube acoustic isolation cabinet/enclosure mounted on a Halcyonics Micro 40 vibration isolation table. The measurements were performed under ambient conditions using Si probes (VistaProbes T300) having a spring constant of 40 N/m, a resonance frequency of 300 kHz and the following characteristics: length 125 μm, width 40 μm, tip height 14 μm, and tip radius < 10 nm. The images were captured and analyzed using the Nanoscope v5.30r3.sr4 software.

Images were recorded at a maximum scan rate of 1 Hz while simultaneously acquiring height and phase information. Set-point amplitudes were sample-dependant, ranging from 0.85 for hard-tapping and 0.50 for light-tapping conditions. Typical feedback control settings were as follows: Integral Gain 0.20, Proportional Gain 2.0, and Scan Angle 0. Feature size was determined by power spectral density (PSD) analysis,[32–34] with uncertainties representing the standard deviation on multiple PSD analyses, or by manual measurement using the software.

6.3.7 Optical Microscopy

The films cast for the AFM studies of film-loaded species were examined for substrate adhesion with a Zeiss Axioplan optical reflection microscope equipped with a differential

interference contrast (DIC) module. The microscope was equipped with a Zeiss Axio Cam MR digital camera for image acquisition.

6.3.8 UV-Vis Spectroscopy

Absorption spectra were acquired on a CARY 100 Bio UV-Vis Spectrophotometer with Cary Varian UV Scan Application (v3.001339). A quartz cell with a 1 cm path length was used to measure the absorption for metal-loaded polymer solutions at concentrations of ca. 0.02 mg/mL.

6.3.9 Ellipsometry

Layer thicknesses for thin polymer films to be analyzed by AFM were determined using a MM-SPEL-VIS ellipsometer from OMT. Each film was prepared by spin-casting at 2500 rpm from a polymer solution concentration of 0.2 % w/v (2 mg/mL).The silicon substrates were examined with a spectral method in the wavelength range from 450 to 900 nm while the azimuthal angle was kept at 15 degrees. Sample position is paramount for consistent measurement of film thickness and can result in systematic errors due to variations in the angle of incidence and the azimuthal angle. Errors were minimized by measuring all the samples in one measurement session to ensure that the geometry of the device and the sample holder position remained the same. Each measurement was recorded over an average area of 3 × 5 mm. A bare, newly cleaned silicon substrate was also measured to correct for the oxide layer thickness. Each sample was measured 3 times in different areas, resulting in film thickness variations of less than 1 nm in all cases.

6.4 Results & Discussion

6.4.1 Characteristics of the Polymer Substrates

The characteristics of the polystyrene substrates, the PS-*b*-P2VP block copolymers used, and the resulting CSC copolymers are summarized in Tables 6.1, 6.2, and 6.3, respectively. The molecular weight ($M_n \times 10^{-3}$) of the P2VP and PS blocks are specified in the sample nomenclature used in Tables 6.2 and 6.3.

Table 6.1 Characteristics of polystyrene substrates used for the synthesis of the CSC copolymers

Substrate	F[a]	M_w/M_n	M_n[b]	f_w[c]
Linear	0.26	1.06	5775	13
G0PS	0.28	1.09	1.0×10^5	238
G1PS-1	0.30	1.11	8.3×10^5	2145
G1PS-2[d]	0.30	1.07	8.7×10^5	2235
G2PS	0.22	1.09	1.1×10^7	21002
G3PS	0.26	1.08	2.0×10^7	46023

[a] Functionalization (mole %) from ^{1}H NMR analysis; [b] Absolute values from SEC-MALLS or laser light scattering measurements before functionalization; [c] Branching functionality: number of branches added in the last grafting cycle; [d] Functionalized with chloromethyl groups, all other substrates contain acetyl functional groups

Table 6.2 Block copolymer side-chain characterization

	Block Copolymer Side-chain					
	PS		P2VP	Copolymer		
Graft Copolymer	M_n[a]	M_w/M_n	M_n[b]	M_n[c]	% 2VP[d]	M_w/M_n
PS-*g*-(P2VP14-*b*-PS11)	11200	1.04	13500	24700	55	1.11
G0PS-*g*-(P2VP8-*b*-PS8)	7900	1.04	7800	15700	50	1.19
G1PS-*g*-(P2VP5-*b*-PS6)	6600	1.06	5600	12200	46	1.14
G1PS-*g*-(P2VP11-*b*-PS11)	11000	1.02	11800	22800	52	1.14
G1PS-*g*-(P2VP25-*b*-PS20)	20000	1.02	24500	44500	55	1.13
G2PS-*g*-(P2VP8-*b*-PS11)	11500	1.17	8100	19600	41	1.02
G2PS-*g*-(P2VP15-*b*-PS11)	11000	1.06	14800	25800	57	1.01
G2PS-*g*-(P2VP13-*b*-PS20)	19900	1.12	12700	32600	39	1.05
G3PS-*g*-(P2VP14-*b*-PS11)	11400	1.03	13700	25100	55	1.01

[a] Absolute values from SEC analysis with DRI detector and PS calibration; [b] Determined from difference between PS and copolymer M_n; [c] Absolute values from ^{1}H NMR analysis; [d] From ^{1}H NMR analysis (mol %)

Table 6.3 Arborescent CSC copolymers characterization

Description	M_n[a]	M_w/M_n	f_w[b]	% 2VP[c]
PS-*g*-(P2VP14-*b*-PS11)	3.2×10^5	1.06	13	52
G0PS-*g*-(P2VP8-*b*-PS8)	2.8×10^6	1.10	173	73
G1PS-*g*-(P2VP5-*b*-PS6)[d]	8.0×10^6	1.03	590	33
G1PS-*g*-(P2VP11-*b*-PS11)[e]	1.9×10^7	1.03	785	75
G1PS-*g*-(P2VP25-*b*-PS20)[e]	1.6×10^7	1.05	343	62
G2PS-*g*-(P2VP8-*b*-PS11)	3.1×10^7	1.03	1007	46
G2PS-*g*-(P2VP15-*b*-PS11)	3.8×10^7	1.02	1053	65
G2PS-*g*-(P2VP13-*b*-PS20)	3.7×10^7	1.01	806	55
G3PS-*g*-(P2VP14-*b*-PS11)	6.7×10^7	1.03	1857	70

[a] Absolute values from SEC-MALLS or laser light scattering measurements; [b] Branching functionality: number of branches added in the last grafting cycle; [c] mol %, from ^{1}H NMR analysis; [d] From substrate G1PS-1; [e] From substrate G1PS-2

It is important to assess the characteristics of the template polymers in solution, as metallic salt deposition may alter their properties significantly. Additionally, it allows their comparison to intermolecular micelles. Even though the unimolecular micelles synthesized have a PS corona, aggregation is possible in non-polar solvents such as toluene due to the P2VP component. The characteristics of the polymer in toluene are also important because the metal loading studies will be carried out in this solvent for comparison to intermolecular micelles of PS-*b*-P2VP. Measurement of the molecular dimensions, namely the hydrodynamic radii by dynamic light scattering, should yield multi-modal distributions (derived from CONTIN analysis[35] of the autocorrelation function) for aggregated species, or alternately significant differences in hydrodynamic radii for first- and second-order analyses providing r_{h1} and r_{h2}, respectively. Irreproducible radii in successive measurements, leading to large standard deviations, are also indicative of poorly-defined aggregates with a broad size distribution.

The first- and second-order hydrodynamic radii determined from the autocorrelation function are summarized in Table 6.4 for both the polystyrene grafting substrates and the CSC copolymers. For comparison purposes, the bulk radius (r_b) calculated from Equation 6.1 is also provided. The average density (ρ) of each copolymer was estimated from its composition determined by ^{1}H NMR spectroscopy (ρ = 1.09 g/cm^3 for P2VP and 1.01 g/cm^3 for PS). As expected, all arborescent copolymers have dimensions (r_h) significantly larger than their respective bulk radii due to swelling of the molecules.

$$r_b = \left(\frac{M_w}{\rho \, N_A \frac{4}{3}\pi} \right)^{\frac{1}{3}} \tag{6.1}$$

Table 6.4 Hydrodynamic radii of PS substrates and arborescent CSC copolymers in toluene

PS Substrate			Graft Copolymer			
r_{h1}[a]	r_{h2}[b]	r_b[c]	Description	r_{h1}[a]	r_{h2}[b]	r_b[c]
1.7 ± 0.3	1.2 ± 0.4	1	PS-*g*-(P2VP14-*b*-PS11)	16 ± 1	11 ± 1	5
8.2 ± 0.1	7.3 ± 0.1	3	G0PS-*g*-(P2VP8-*b*-PS8)	24 ± 1	23 ± 1	10
12.2 ± 0.1	11.9 ± 0.3	7	G1PS-*g*-(P2VP5-*b*-PS6)	25 ± 1	25 ± 1	15
14.1 ± 0.1	13.3 ± 0.1	7	G1PS-*g*-(P2VP11-*b*-PS11)	25 ± 1	24 ± 1	19
14.1 ± 0.1	13.3 ± 0.1	7	G1PS-*g*-(P2VP25-*b*-PS20)	34 ± 1	31 ± 1	18
30 ± 1	28 ± 1	16	G2PS-*g*-(P2VP8-*b*-PS11)	49 ± 1	48 ± 1	23
30 ± 1	28 ± 1	16	G2PS-*g*-(P2VP15-*b*-PS11)	54 ± 1	51 ± 1	24
30 ± 1	28 ± 1	16	G2PS-*g*-(P2VP13-*b*-PS20)	66 ± 1	63 ± 1	24
30 ± 1	29 ± 1	20	G3PS-*g*-(P2VP14-*b*-PS11)	82 ± 1	75 ± 1	29

[a] Hydrodynamic radii (nm) from first-order analysis of the correlation function; [b] Hydrodynamic radii (nm) from second-order analysis of the correlation function; [c] Bulk radii (nm) calculated by Equation 6.1

All template polymers appear to be monodispersed in solution with the exception of the G0 copolymer, PS-*g*-(P2VP14-*b*-PS11). Monodispersity is evident from the excellent agreement between the first- and second-order analyses of the correlation function and the consistent values obtained, as indicated by the small standard deviations. The G0 copolymer, in contrast, has a significant discrepancy between the r_{h1} and r_{h2} values, even though the standard deviations on the measurements are comparable to the other samples.

CONTIN analysis provided results consistent with these findings: Arborescent copolymers of generation 1 and above display a single, narrowly dispersed size population in toluene. Provided in Figure 6.4 are examples of size distributions observed for G0 and G3 arborescent copolymers in toluene and the corresponding G2PS substrate from which the G3

copolymer was derived. Evidence for aggregation was seen for PS-*g*-(P2VP14-*b*-PS11) in CONTIN analysis as a broad distribution (Figure 6.4a) distinct from G2PS and G2PS-*g*-(P2VP15-*b*-PS11), seen in Figure 6.4b and Figure 6.4c, respectively. As expected, the radius for the G2PS substrate is smaller than for the G3 copolymer, and both are larger than the G0 copolymer. Since the PS-*g*-(P2VP14-*b*-PS11) copolymer was derived from linear PS (M_n = 5775 g/mol, Table 6.1), the light scattering intensity was too low to provide accurate distribution information by CONTIN analysis, and is thus not shown in Figure 6.4.

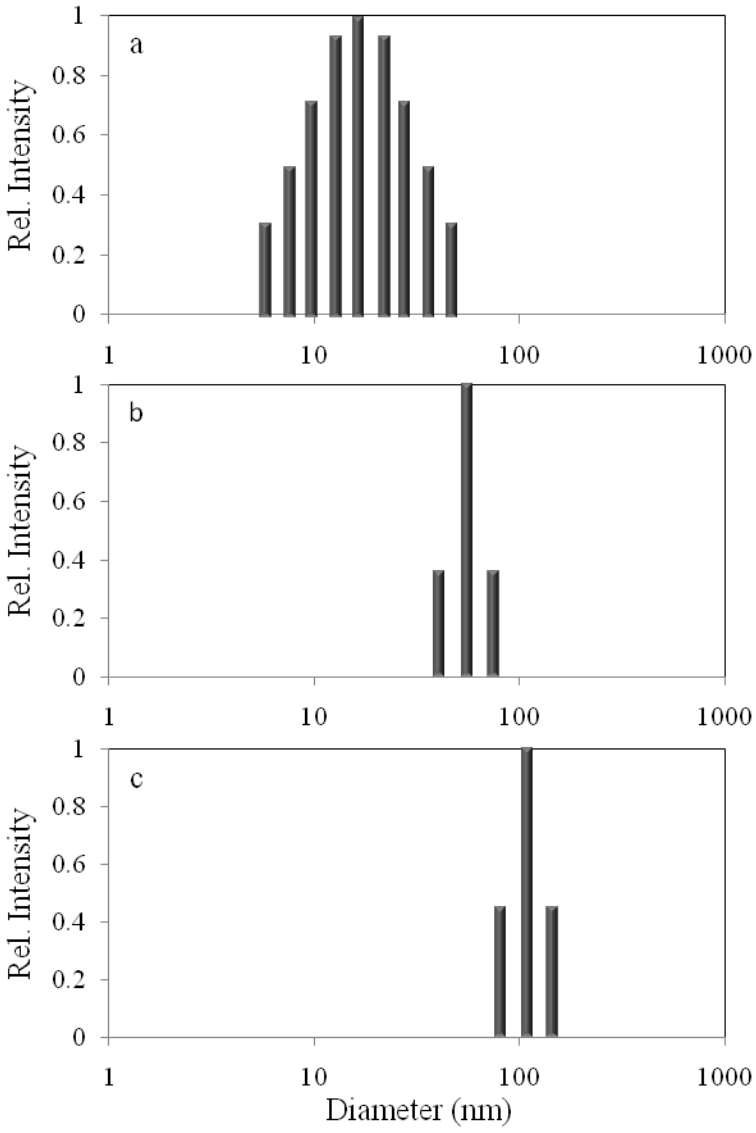

Figure 6.4 Size distribution in toluene by CONTIN analysis of (a) PS-*g*-(P2VP14-*b*-PS11), and the (b) G2PS substrate for (c) G2PS-*g*-(P2VP15-*b*-PS11).

DLS analysis was also performed in THF and in chloroform, which are better solvents for both the PS and P2VP components of the copolymers. The hydrodynamic radii of the arborescent copolymers in all three solvents are compared in Table 6.5.

The hydrodynamic radii were slightly larger in these solvents than in toluene for the majority of the samples. One notable exception to this is sample PS-*g*-(P2VP14-*b*-PS11), for which a decrease is observed in chloroform and THF, as well as better agreement between the first- and the second-order analysis results, due to the suppression of aggregation.

Table 6.5 Hydrodynamic radii of arborescent copolymers in different solvents

Sample	Toluene		THF		$CHCl_3$	
	r_{h1}[a]	r_{h2}[b]	r_{h1}[a]	r_{h2}[b]	r_{h1}[a]	r_{h2}[b]
PS-*g*-(P2VP14-*b*-PS11)	16 ± 1	11 ± 1	10 ± 1	9 ± 1	15 ± 1	14 ± 1
G0PS-*g*-(P2VP8-*b*-PS8)	24 ± 1	23 ± 1	35 ± 1	32 ± 1	23 ± 1	22 ± 1
G1PS-*g*-(P2VP5-*b*-PS6)	25 ± 1	25 ± 1	28 ± 1	28 ± 1	28 ± 1	28 ± 1
G1PS-*g*-(P2VP11-*b*-PS11)	25 ± 1	24 ± 1	28 ± 1	28 ± 1	35 ± 1	34 ± 1
G1PS-*g*-(P2VP25-*b*-PS20)	34 ± 1	31 ± 1	34 ± 1	33 ± 1	42 ± 1	41 ± 1
G2PS-*g*-(P2VP8-*b*-PS11)	49 ± 1	48 ± 1	56 ± 1	55 ± 1	60 ± 1	58 ± 1
G2PS-*g*-(P2VP15-*b*-PS11)	54 ± 1	51 ± 1	60 ± 1	56 ± 1	67 ± 1	65 ± 1
G2PS-*g*-(P2VP13-*b*-PS20)	53 ± 1	52 ± 1	59 ± 1	57 ± 1	66 ± 1	63 ± 1
G3PS-*g*-(P2VP14-*b*-PS11)	82 ± 1	75 ± 1	72 ± 1	67 ± 1	79 ± 1	76 ± 1

[a] Hydrodynamic radii (nm) from first-order analysis of the correlation function; [b] Hydrodynamic radii (nm) from second-order analysis of the correlation function

Molecules with a spherical topology are expected, as the PS substrates for all arborescent copolymers are constructed with 5000 g/mol PS chains and the core dimensions are comparable to the side-chains; this was confirmed by AFM analysis, in analogy to arborescent copolymers with similar architectures but different composition.[36,37] Provided in Figure 6.5 are AFM micrographs (phase images) acquired for the various generations (G0 – G4) of arborescent CSC copolymers cast from toluene solutions.

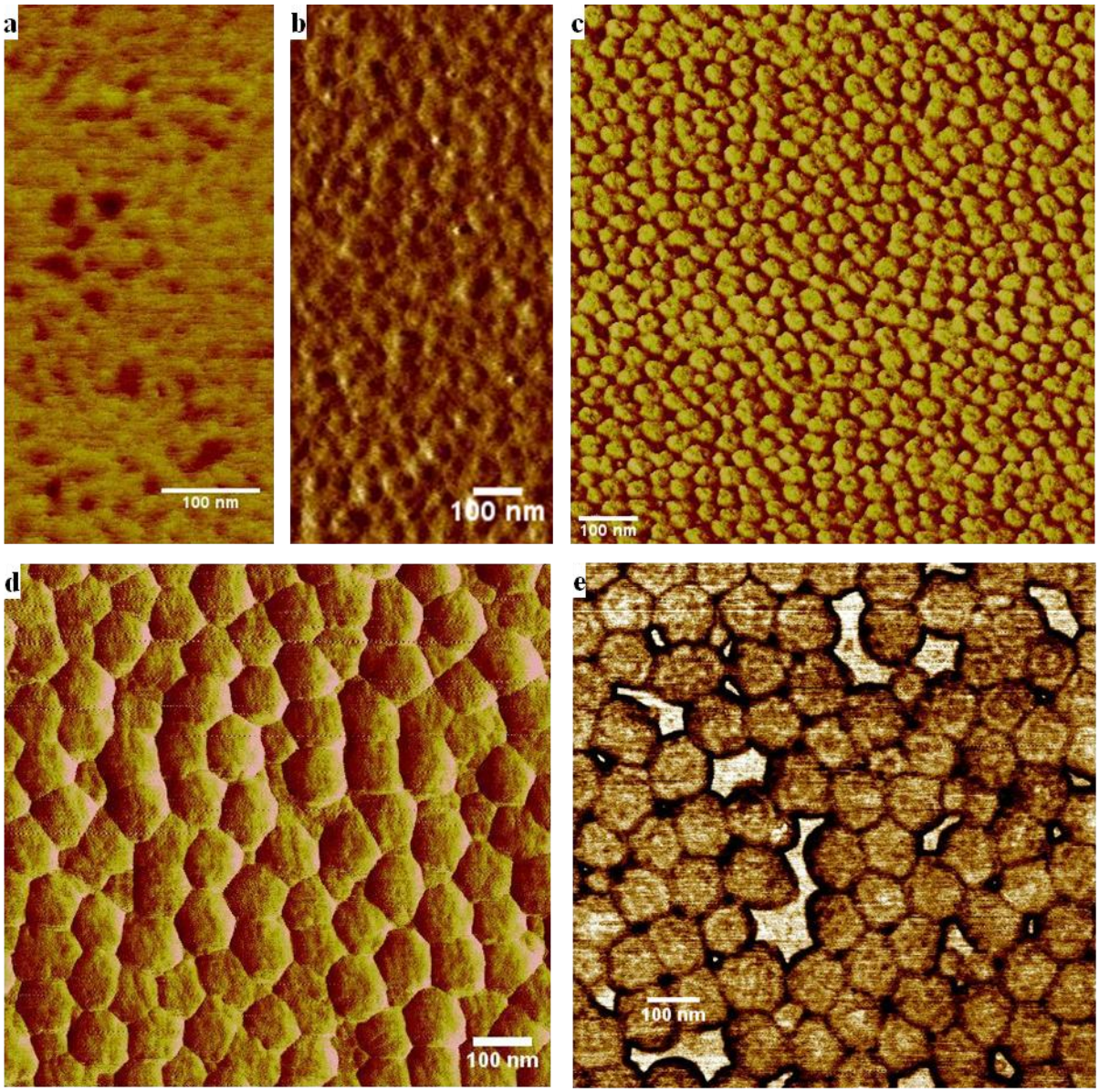

Figure 6.5 AFM phase images for arborescent copolymers: (a) PS-*g*-(P2VP14-*b*-PS11), (b) G0PS-*g*-(P2VP8-*b*-PS8), (c) G1PS-*g*-(P2VP25-*b*-PS20), (d) G2PS-*g*-(P2VP15-*b*-PS11), and (e) G3PS-*g*-(P2VP14-*b*-PS11).

It is evident that as the generation number increases not only does the size increase as expected, but more importantly, better defined spherical structures result. This is attributed to the increased branching density of the side-chains leading to more perfect and less

interpenetrable spherical structures. The spherical topology of arborescent polymers has been evidenced in terms of the scaling behavior (molecular weight dependence) of the second virial coefficient (A_2), the z-average translational diffusion coefficient (D_z), and the radius of gyration (r_g), which are all similar to rigid spheres.[38] More relevant to the compositions being examined in the current case (PS and P2VP), preferential adsorption of the P2VP segments onto the hydrophilic substrate can cause significant flattening of the structures, especially for lower generation (G0 and G1) species which are more flexible, as seen in Figure 6.5a and Figure 6.5b, respectively. Similar results have been reported for arborescent styrene homopolymers.[36] Finer details can be observed for the upper generation structures when examining height scan (topology) AFM images. The structures are not perfectly smooth, and a rippled pattern is evident as observed for the arborescent PS systems. These surface features are referred to as a 'cauliflower' morphology.[36] This surface detail can be seen in the AFM height scans of Figure 6.6a for G2PS-*g*-(P2VP15-*b*-PS11) and Figure 6.5b for G3PS-*g*-(P2VP14-*b*-PS11).

Coordination with metals was performed for the arborescent CSC copolymers displaying a spherical morphology in AFM analysis and existing as unimolecular (non-associating) species in solution, to monitor changes in morphology within the branched copolymer micelles.

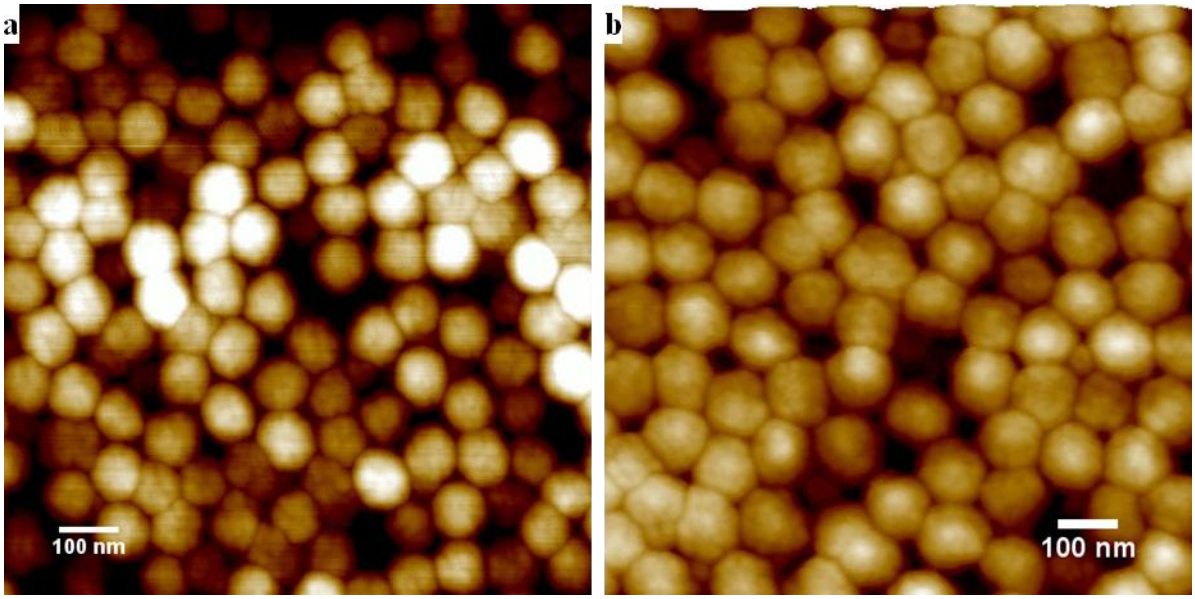

Figure 6.6 AFM height scans for (a) G2PS-*g*-(P2VP15-*b*-PS11) and (b) G3PS-*g*-(P2VP14-*b*-PS11) arborescent CSC copolymers.

6.4.2 $HAuCl_4$ Loading

Since $HAuCl_4$ is a widely investigated metallic nanoparticle precursor, particularly for polymeric templating, it was also selected for the initial templating investigations with the amphipolar arborescent copolymers synthesized (Table 6.3).

Intermolecular PS-*b*-P2VP block copolymer reverse micelles have been investigated as nanoparticle templates for $HAuCl_4$ by coordination with the nitrogen atom in the pyridine moiety.[2] The interaction of the pyridine group with metallic acids in general, and the reduction of the coordinated metal to its elemental state are shown in Scheme 6.1.

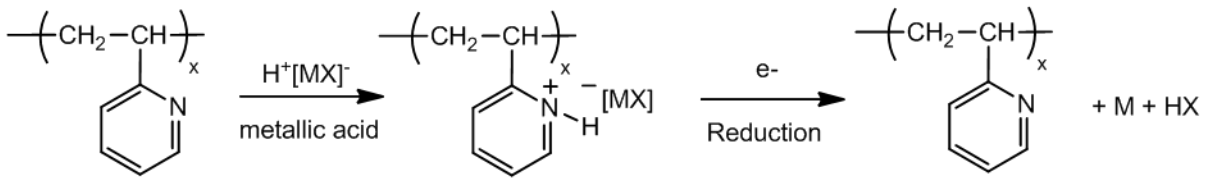

Scheme 6.1 Metallic acid coordination with poly(2-vinylpyridine) and reduction.

As the metal only coordinates with the P2VP phase of the copolymer template, the distribution of the metal should conform to the morphology of the micelles. For example, spherical intermolecular micelles of PS-*b*-P2VP lead to spherical organization of the metal as observed by TEM analysis.[2] Since arborescent copolymers have a composition and a spherical topology similar to their intermolecular micelle analogues, linear PS-*b*-P2VP was first synthesized and loaded with $HAuCl_4$ to substantiate the loading procedure. A PS-*b*-P2VP copolymer (M_n^{PS} = 25,000 g/mol, M_n^{P2VP} = 29,000 g/mol, PDI = 1.17) was dissolved in toluene, a solvent selective for PS, at a concentration of 0.5 % w/v (5 mg/mL), to form spherical micelles with a core of P2VP and a shell of PS. Following the dissolution and a waiting time of 6 h, $HAuCl_4$ crystals were added to the polymer solution which was allowed to equilibrate further for 48 h, to allow the coordination of Au by the 2VP units. The micelles were loaded with 0.5 equiv of $HAuCl_4$ per 2VP unit (1:2, Au:2VP). The analysis of a thin film of $HAuCl_4$-loaded PS-*b*-P2VP copolymers by TEM revealed distinct Au-rich spherical domains, assumed to match P2VP domains of the micelle cores as seen in Figure 6.7.

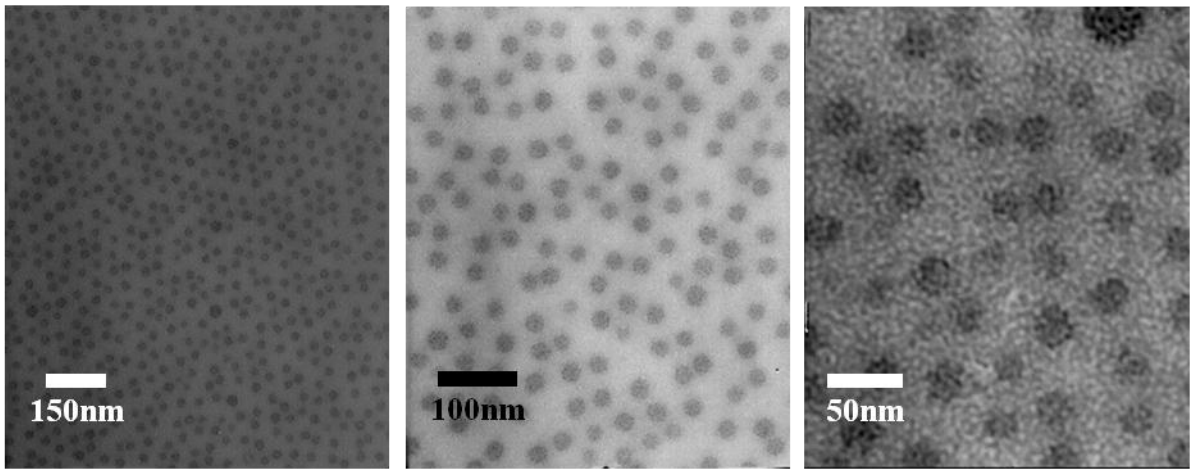

Figure 6.7 TEM micrographs for $HAuCl_4$-loaded PS-*b*-P2VP micelles at three different magnifications.

The spherical organization of $HAuCl_4$ observed within the micellar cores replicates results reported in the literature,[39] thus validating the loading procedure used. The same procedure was therefore applied to the arborescent copolymer systems. After 48 h of equilibration time, 0.5 equiv of $HAuCl_4$ was successfully loaded into the PS-*g*-(P2VP14-*b*-PS11) template, yielding a spherical distribution of gold very similar to the intermolecular micelles, as seen in Figure 6.8a. It will later be demonstrated (Section 6.4.3.4) that the loading/coordination process occurs quite rapidly. The individual arborescent molecules are clearly visible by TEM following metal coordination (0.5 equiv in toluene). Also provided in Figure 6.8 is a TEM micrograph for a G1 template, G0PS-*g*-(P2VP8-*b*-PS8), which affords a similar result. The radii of the Au-loaded regions of the templates were measured to be 9 ± 1 nm and 11 ± 1 nm for PS-*g*-(P2VP14-*b*-PS11) and G0PS-*g*-(P2VP8-*b*-PS8), respectively.

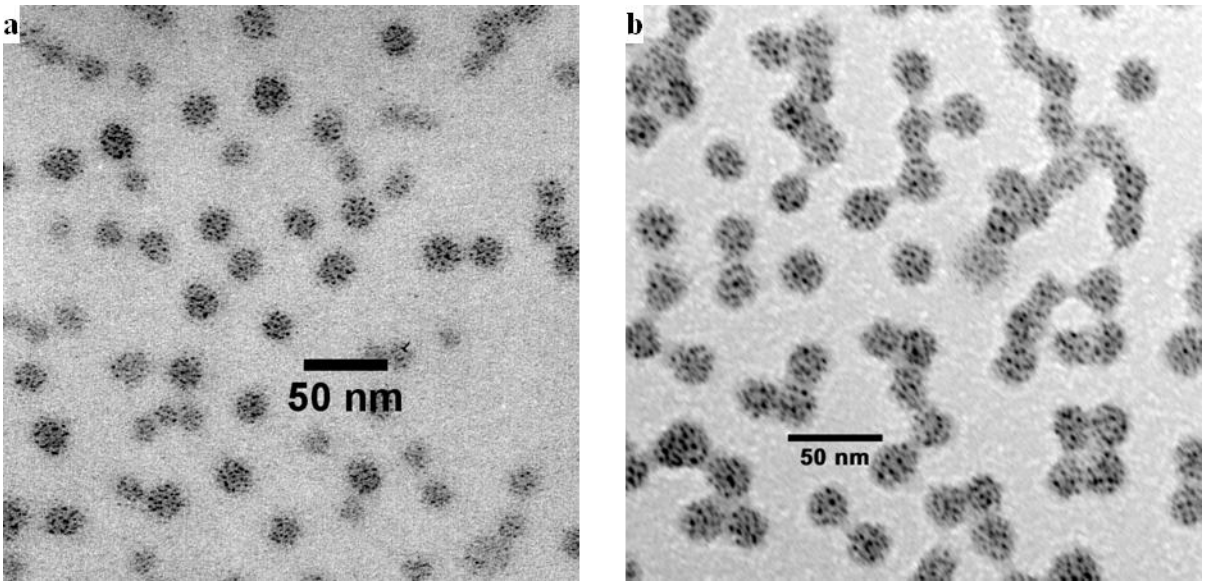

Figure 6.8 TEM micrographs for (a) PS-*g*-(P2VP14-*b*-PS11) and (b) G0PS-*g*-(P2VP8-*b*-PS8) loaded with 0.5 equiv of $HAuCl_4$ in toluene.

It is evident that both the G0 and G1 unimolecular micelles exhibit templating characteristics similar to intermolecular micelles of PS-*b*-P2VP (Figure 6.7). The hydrophobic PS core, which cannot coordinate with metals, seemingly does not affect metal organization within these templates. It should be noted that significant aggregation is observed for G0PS-*g*-(P2VP8-*b*-PS8), both in DLS and microscopic analysis, which is attributed to the short PS chains in the corona (M_n = 7900 g/mol) being unable to shield the charged metal-loaded cores in the non-polar (toluene) environment, and leading to the aggregation of adjacent molecules. Considering the spherical organization of the metal within the templates, AFM analysis was also performed to confirm the spherical morphology of the Au-loaded micelles. AFM height images for $HAuCl_4$-loaded PS-*g*-(P2VP14-*b*-PS11) and G0PS-*g*-(P2VP8-*b*-PS8) had radii of 14 ± 1 nm and 17 ± 1 nm, respectively, as shown in

Figure 6.9. Further analysis results of molecular morphology are provided in Table 6.7 for a larger set of copolymers.

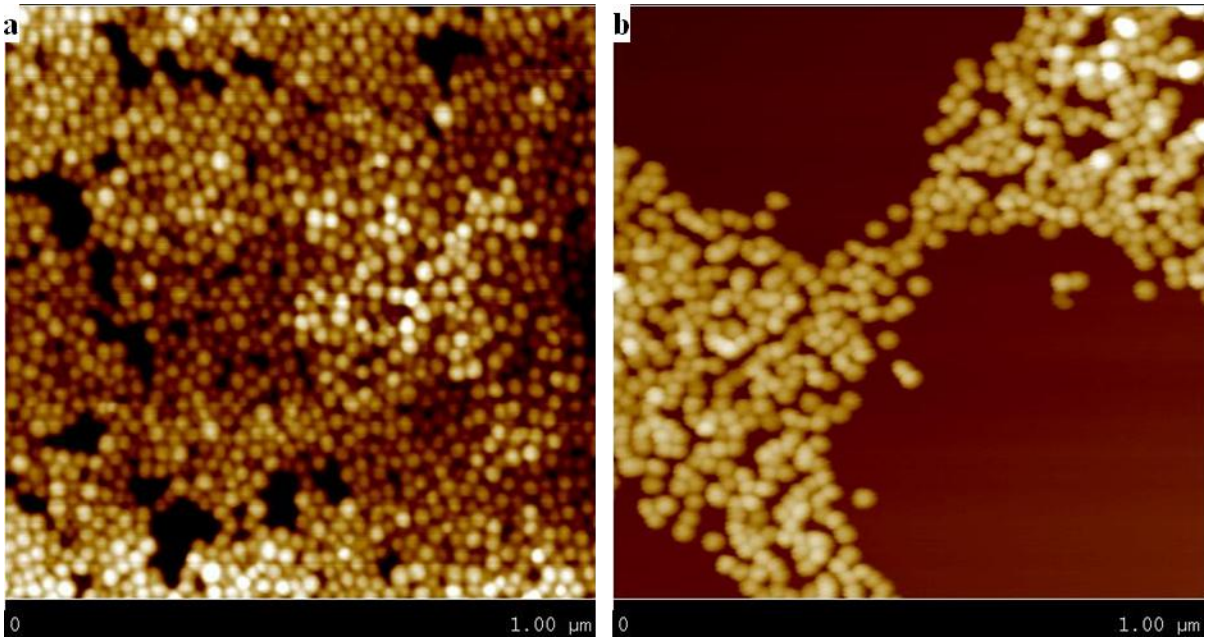

Figure 6.9 AFM height images for $HAuCl_4$-loaded (a) PS-*g*-(P2VP14-*b*-PS11) and (b) G0PS-*g*-(P2VP8-*b*-PS8).

Gold loading in the upper generation templates was performed and upon close examination of sample G1PS-*g*-(P2VP25-*b*-PS20) at a $HAuCl_4$ loading level of 0.5 equiv/2VP unit, it was discovered that nanoscale organization of the metal existed within each template molecule: A non-uniform distribution of gold salt within the G2 templates could be observed, the periphery being more densely loaded than the center. The ring-like nanostructures within the G2 templates, with a radius of 15 ± 2 nm, could be indicative of a layered morphology in the molecules (Figure 6.10). While some of the molecules display distinct radial gradation of the metal, complete ring structures are not observed in all cases.

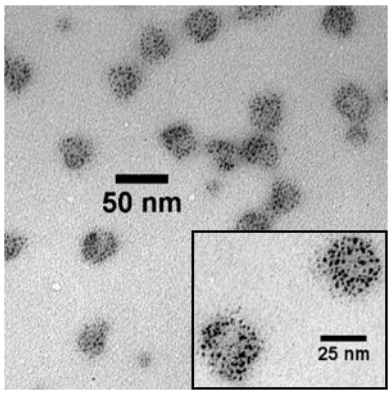

Figure 6.10 Ring-like organization of $HAuCl_4$ within G1PS-*g*-(P2VP25-*b*-PS20) loaded in toluene as seen by TEM.

It was postulated that the ring and partial ring-like organization of the metal within the arborescent templates resulted from flattening of the spherical metal-loaded structures upon transfer to the TEM grid. During film deposition, the long block copolymer chains may collapse in radial fashion, exposing the metal-depleted G1PS core as shown schematically in Figure 6.11. This would lead to greater penetration of the electron beam in the Au-depleted center of each template.

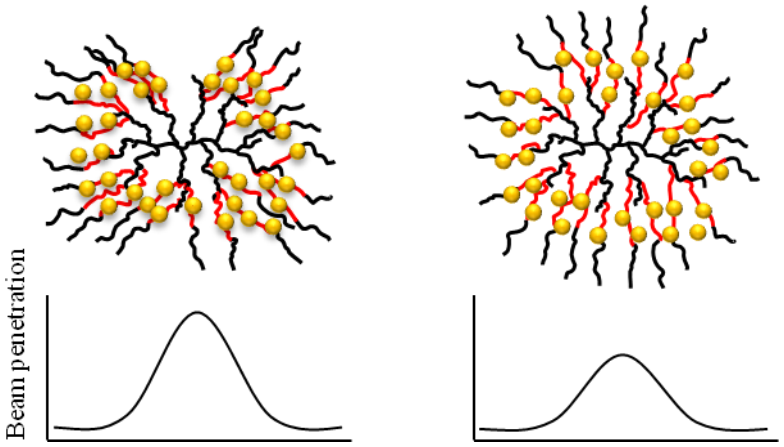

Figure 6.11 Possible origin of ring-like organization of $HAuCl_4$ observed by TEM analysis of G1PS-*g*-(P2VP25-*b*-PS20): Beam penetration differential for (left) core-exposed or (right) spherical polymer templates.

To investigate this phenomenon further, AFM analysis was employed to provide a clearer picture of the ring-like organization of the metal. AFM analysis of a film displaying ring-like organization of the gold nanoparticles (Figure 6.10a) thus revealed similar morphological features (Figure 6.12). It therefore appears that metal uptake into the polymer scaffold by coordination with the 2VP units induces intramolecular phase separation within each polymer molecule. Intramolecular phase separation, also referred to as phase segregation or self-assembly, resulted in the toroidal and partial-toroid polymer morphologies visualized by TEM and AFM analysis. The toroidal nanostructures have a mean radius of 22 ± 2 nm, in agreement with the TEM measurements. Core-shell phase segregation has been reported on a few occasions,[22] and toroidal micelles have been reported previously for charged triblock terpolymers;[40] however, to our knowledge nanostructures resulting from intramolecular phase segregation within unimolecular species has not been

reported previously. The prediction of such structures by modeling triblock copolymer has also been reported,[41,42] although it was stated that this phenomenon was rarely observed.

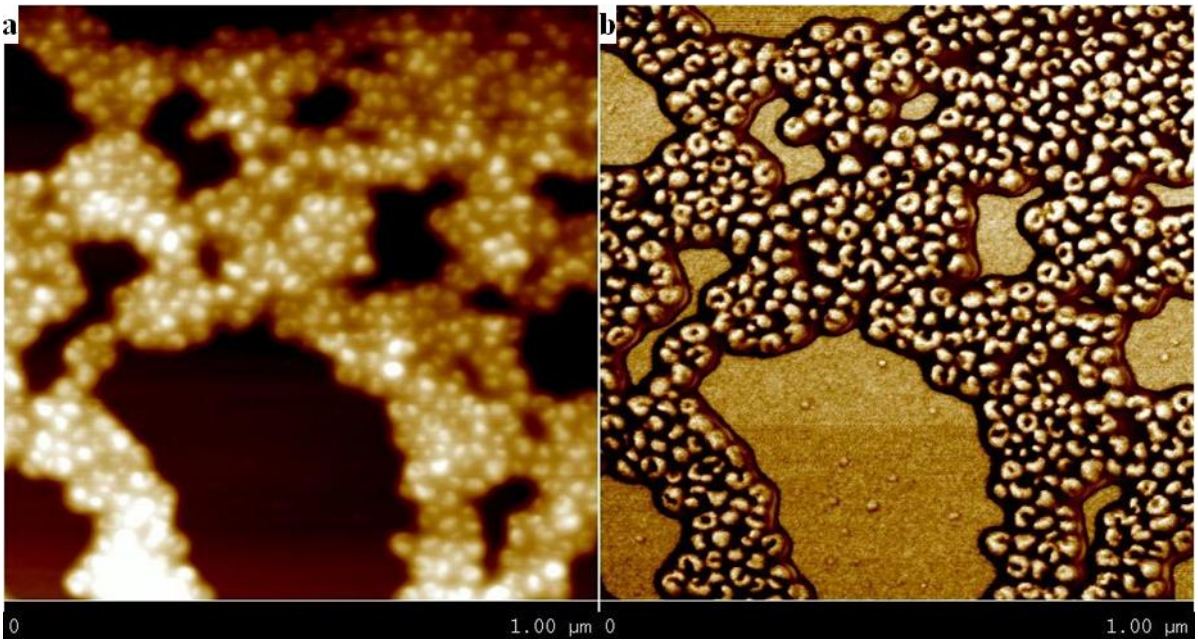

Figure 6.12 AFM micrograph of intramolecular toroidal phase segregation of G1PS-*g*-(P2VP25-*b*-PS20) loaded with 0.5 equiv $HAuCl_4$ in toluene: (a) height and (b) phase scans.

Following the observation of this unique transition from spheres to toroidal structures upon metal uptake, subsequent generations of copolymers were also closely monitored by TEM and AFM imaging for metal organization and polymer morphology.

It was hypothesized that these copolymers would produce similar toroidal morphologies on a larger scale, due to their similar architecture and the presence of larger non-coordinating PS cores. The results obtained were surprisingly different, however. Shown in Figure 6.13 and Figure 6.14 are TEM and AFM images for a G3 copolymer, G2PS-*g*-

(P2VP15-*b*-PS11), and a G4 copolymer, G3PS-*g*-(P2VP14-*b*-PS11), after loading with 0.5 equiv of $HAuCl_4$ in toluene.

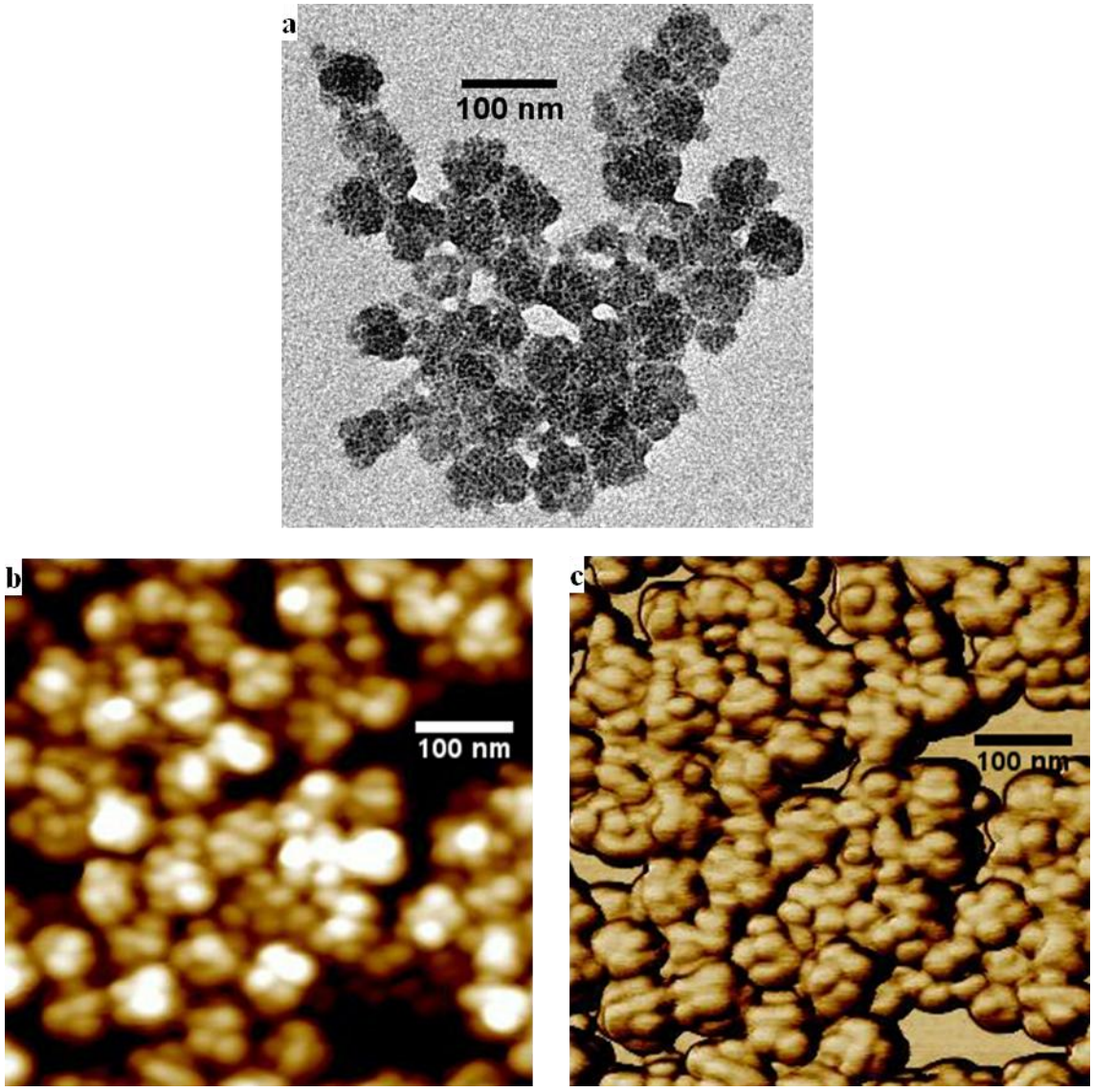

Figure 6.13 Raspberry morphology in G2PS-*g*-(P2VP15-*b*-PS11) loaded with 0.5 equiv of $HAuCl_4$ in toluene: (a) TEM, (b) AFM height, and (c) AFM phase images.

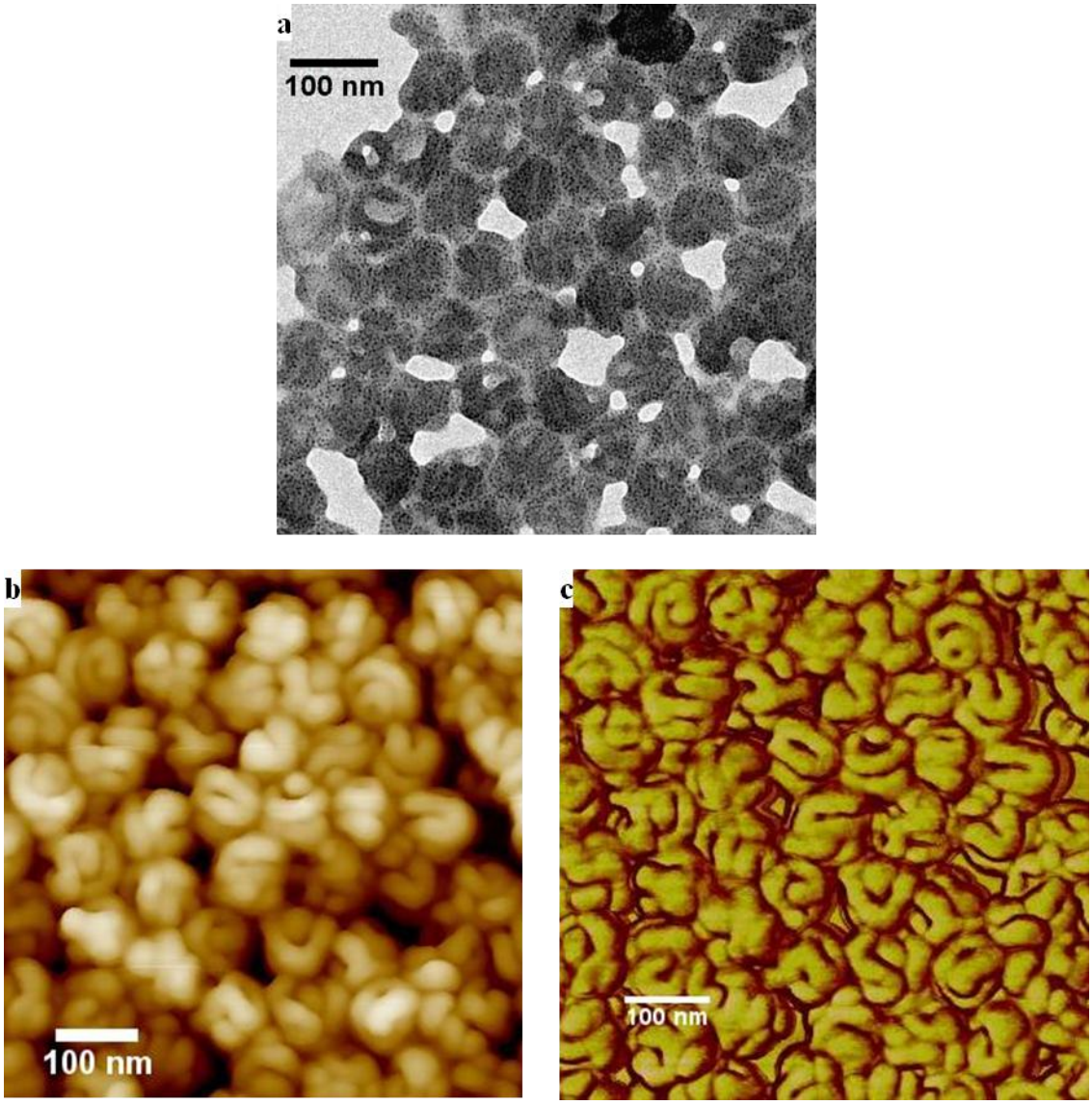

Figure 6.14 Cylinder-in-sphere morphology of G3PS-*g*-(P2VP14-*b*-PS11) loaded with 0.5 equiv of $HAuCl_4$ in toluene: (a) TEM, (b) AFM height, and (c) AFM phase images.

The G3 and G4 templates again displayed distinct morphologies with intramolecular phase segregation and intricate nanodomain formation. In the case of the G3 template, G2PS-*g*-(P2VP15-*b*-PS11), a raspberry or sphere-in-sphere morphology was formed, each polymer segregating into multiple nodules within a spherical boundary giving it a raspberry-like

appearance, as observed in both TEM and AFM images. AFM imaging provides a much clearer picture of the morphology, as it probes the material itself and not only the metal-containing regions as TEM. According to AFM analysis, the nodules have a diameter of 25 ± 4 nm and are bound within a spherical volume with a radius of 34 ± 1 nm. The molecular boundaries defined by gold deposition have a radius of 33 ± 2 nm in the TEM images. Similar morphologies, albeit less defined, have been reported for intermolecular micelles,[13,17,43,44] as well as for cylindrical copolymer brushes, which upon metal loading formed "pearl necklace" structures.[45–47] The polymer brush investigated was a once-grafted branched polymer, which however differs from the spherical G0 arborescent copolymer we investigated, as the substrate chains were much longer than the side-chains in that case. As previously shown in Figure 6.8 and Figure 6.9, the G0 arborescent copolymer PS-*g*-(P2VP14-*b*-PS11) did not display any distinct phase segregation of the types observed for the G2 – G4 templates. Micelles that are able to reorganize into distinct nanodomains such as the G3 and G4 templates are commonly referred to as multicompartment micelles. Most of these are intermolecular micelles resulting from the association of amphiphilic block and miktoarm terpolymers.[17–20,48–51]

The morphology of the gold-loaded G4 template, G3PS-*g*-(P2VP14-*b*-PS11), is a seemingly continuous cylindrical structure coiled within the spherical boundary of each branched template molecule; this topology somewhat resembles a brain or an intestine. While cylindrical morphologies are well-known for block copolymers and terpolymers in the bulk state, the discrete spherical volumes with phase-segregated cylindrical morphologies reported herein are the first of their kind for unimolecular species, and are described as a "cylinder-in-sphere" morphology. Worm- or string-like morphologies have been observed within PS-*b*-

P2VP films,[52] but not within individual polymer molecules as in the current case. Cylinder-in-sphere morphologies have nonetheless been predicted by Pinna et al. when modeling thin block copolymer films wrapped around solid nanoparticles.[53] Indeed, cell dynamics simulations produced so-called "cylinder shell" structures (Figure 6.15) displaying striking similarities to our unimolecular systems such as $HAuCl_4$-loaded G3PS-*g*-(P2VP14-*b*-PS11) as shown in Figure 6.14. The experimental data collected by Pinna et al. did not produce highly resolved cylindrical domains of the type predicted by their simulations, however.

Figure 6.15 Simulation results for a nanoparticle coated with a block copolymer film resulting in a cylinder shell structure.[53]

The spherical volume limiting the cylindrical polymer segments for the arborescent system, shown in Figure 6.14, has a radius of 40 ± 2 nm and 39 ± 2 nm according to TEM and AFM analysis, respectively. The width of the cylinders measured by AFM analysis is 28 ± 3 nm, which is comparable within error limits to the nodule diameter measured for the G3 copolymer (25 ± 4 nm). The similar dimensions observed in both cases is attributed to the length of the PS and P2VP in the block copolymers used to construct the templates, which is similar for both templates.

Considering that the G3 and G4 templates discussed above have nearly identical block copolymer side-chain molecular weights and block length ratios, a relationship can be established between polymer structure and the morphology obtained after coordination with $HAuCl_4$. Since the side-chains are nearly identical, our attention was drawn to the characteristics of the PS cores used as substrates (Table 6.1, Table 6.2, and Table 6.4). While the PS cores differ in generation (G2PS and G3PS for the G3 and G4 copolymers, respectively) and in molecular weight by nearly 10^6 g/mol, their hydrodynamic radii are identical (r_{h1} = 30 nm). This suggests that the G3PS substrate, being denser than G2PS, impacts the location of the grafted side-chains. For a denser substrate, grafting should be favored on the periphery of the substrate, as chain diffusion to coupling sites within the interior is hindered by steric crowding. The peripheral grafting hypothesis is supported by the hydrodynamic dimensions of the copolymers: The G4 copolymer (r_{h2} = 75 ± 1 nm) is significantly larger than its G3 analogue (r_{h2} = 51 ± 1 nm), even though the substrates and the side-chains used had similar characteristics. With enhanced peripheral grafting, phase separation between the PS substrate and the P2VP shell should be favored. A P2VP phase relatively devoid of substrate PS chains presumably has a greater tendency to form a continuous cylindrical phase-separated morphology in the G4 species. The G3 species, having more significant intermixing of the PS chains from the core, due to greater fluctuations in the position of the grafted side-chains, would perturb the continuity of phase separation and produce nodular domains.

6.4.3 Influence of Loading Protocol on Phase Segregation

6.4.3.1 Film Loading

Further investigation into the intramolecular phase segregation process was performed using a film loading procedure, whereby a drop of $HAuCl_4$ solution was placed on a thin film of the template polymer. Film stability was a concern in this procedure, as subjecting the film to a solvent could result in debonding from the substrate. Consequently, film quality was monitored by optical microscopy to ensure that adhesion to the substrate was maintained.

In a control experiment, a film prepared from G1PS-*g*-(P2VP11-*b*-PS11) in its neutral state was observed to debond from a silicon AFM substrate upon loading (Figure 6.15a). Ionization of the copolymer before film casting provided stronger binding to the substrate and prevented debonding, presumably due to stronger interactions with the oxide layer present on the surface. The gold-loaded portion of the pre-ionized polymer film is clearly seen in Figure 6.16b, with no indication of debonding from the surface.

Film loading for PS-*g*-(P2VP14-*b*-PS11), G1PS-*g*-(P2VP25-*b*-PS20), G2PS-*g*-(P2VP15-*b*-PS11), and G3PS-*g*-(P2VP14-*b*-PS11) produced similar results when viewed by optical microscopy: The previously ionized polymer films did not debond from the substrate during film loading. Consequently, all the polymers were ionized prior to film casting and metal loading in these experiments. Film loading with aqueous $HAuCl_4$ solution also resulted in interesting phase segregation in the template molecules, even when the polymer was bound to the substrate. Contact of the AFM polymer films with the aqueous $HAuCl_4$ solution for up to 5 min, or 1 min for the TEM samples, provided enough chain mobility for the partly protonated P2VP chain segments to lead to phase segregation. While spherical or toroidal

phase segregation are not very evident for the G2 species by AFM imaging (Figure 6.17a), the morphology is very different from the ionized species without metal, which displayed no phase segregation. This point will be discussed further later in this Chapter. TEM analysis nevertheless shows signs of ring-like metal organization, albeit not very well-defined.

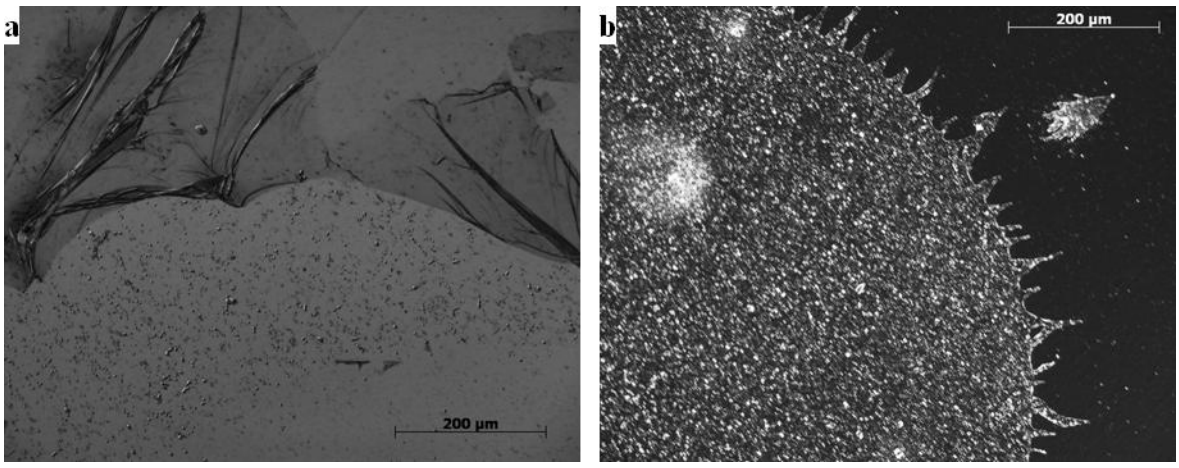

Figure 6.16 Optical microscopy images of film adherence to AFM silicon substrates following $HAuCl_4$ film loading of (a) neutral and (b) ionized arborescent copolymer films of G1PS-*g*-(P2VP11-*b*-PS11).

The G3 and G4 copolymers (Figure 6.17b, Figure 6.17c) also exhibit significant morphological transitions $HAuCl_4$ film loading as compared to the neutral and the ionized metal-free polymer samples. Distinct phase segregation confined by a circular boundary is visible in both cases. While the phase segregation observed by AFM does not closely resemble the raspberry or cylinder-in-sphere morphologies of Figure 6.13 and Figure 6.14, TEM imaging does provide very similar results (nodular for the G3 template and cylindrical for G4). The AFM and TEM images obtained for the G2, G3, and G4 copolymers

investigated in film loading (G1PS-*g*-(P2VP25-*b*-PS20), G2PS-*g*-(P2VP15-*b*-PS11), and G3PS-*g*-(P2VP14-*b*-PS11), respectively) are compared in Figure 6.17.

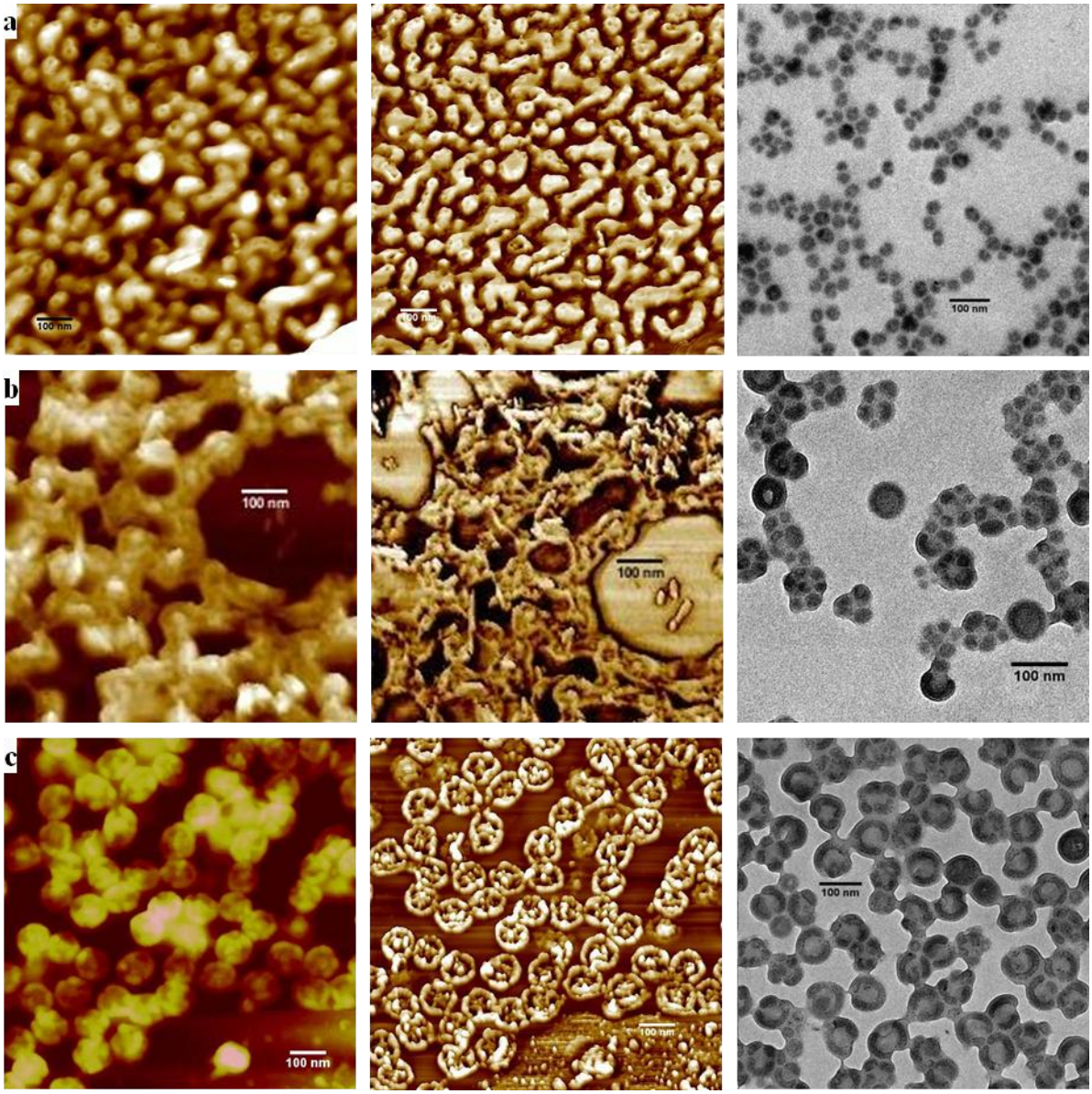

Figure 6.17 $HAuCl_4$ film-loaded arborescent copolymer films. AFM height scan on the left, AFM phase scan in the middle, and TEM on the right: (a) G1PS-*g*-(P2VP25-*b*-PS20), (b) G2PS-*g*-(P2VP15-*b*-PS11), and (c) G3PS-*g*-(P2VP14-*b*-PS11).

6.4.3.2 Phase Stability and Solvent Effects

The morphology of intermolecular micelles is known to depend on different factors including the solvency conditions used. Solvent quality variations thus represent a way to assess the stability of the morphologies resulting from phase segregation, as well as the ability to modify or control the phase structure obtained. In this investigation, the solvents used were varied and morphologies obtained were monitored for the G2, G3, and G4 templates previously discussed, as each produced distinct intramolecular phase segregation. While toluene was first examined, solvents of increased polarity such as THF and chloroform could potentially pose a problem, since $HAuCl_4$ is soluble in these solvents and preferential coordination with 2VP may not result. Free metallic salt could complicate microscopic analysis as the films would be contaminated with unbound metallic residues decreasing the contrast of the images. Fortunately, it was quickly determined that this was not an issue, and the films were exclusively populated with metal-loaded arborescent templates, in analogy to PS-*b*-P4VP micellar systems.[55]

Dilution of the toluene gold-loaded polymer solutions with an equivalent volume of THF as a non-selective solvent, to obtain a 1:1 THF:toluene mixture, resulted in no discernable change in polymer morphology for all the copolymers investigated. The addition of $CHCl_3$ likewise resulted in morphology retention, although less defined toroidal structures were observed for the G2 template. This slight change is attributed to the better solvent quality increasing chain mobility and swelling for the P2VP phase.

Loading of the same copolymers with 0.5 equiv $HAuCl_4$ in pure $CHCl_3$, a non-selective and better solvent than those previously tested, resulted in some noticeable changes in phase segregation. Provided in Figure 6.18 are TEM and AFM images for the three

copolymers loaded with 0.5 equiv of $HAuCl_4$ in $CHCl_3$. The G2 template exhibited a smaller diameter core, now having the appearance of a dimple, presumably due to enhanced swelling of the P2VP phase. This was accompanied by the formation of better defined (more fully formed) toroidal species and less topology variations. Since the species are swollen with a less defined central void, ring-like organization of the metal (as viewed by TEM imaging) is also much less obvious than for loading in toluene (compare Figure 6.10a and Figure 6.18a). The G3 template did not exhibit any noticeable change in morphology by loading in $CHCl_3$, raspberry structures being observed that were similar to those seen in toluene (Figure 6.18b). The G4 template appeared to display a morphological transition, however: The continuous cylindrical nanophases observed in toluene (a non-polar solvent) became an interpenetrating cylindrical structure in $CHCl_3$. The resulting weaved-cylinder appearance, resembling a spherical nano-cage, can be seen in Figure 6.18c. The morphological transition is attributed to increased solvency for P2VP affording a more continuous and uniform phase.

Similar cage-like micelles have recently been observed for intermolecular micelles of amphiphilic multiblock copolymers;[54] however the structures were much less defined and the morphology was not captured to the degree reported herein. The simulations of Pinna et al. for block copolymer-coated nanoparticles also yielded morphologies similar to Figure 6.18c, obtained for $HAuCl_4$-loaded G3PS-*g*-(P2VP14-*b*-PS11) in $CHCl_3$, and were referred to as "golf ball" structures (Figure 6.19).[53] While the cell dynamics simulations predicted structures close to our unimolecular system, experimental support of such polymer morphologies is limited.

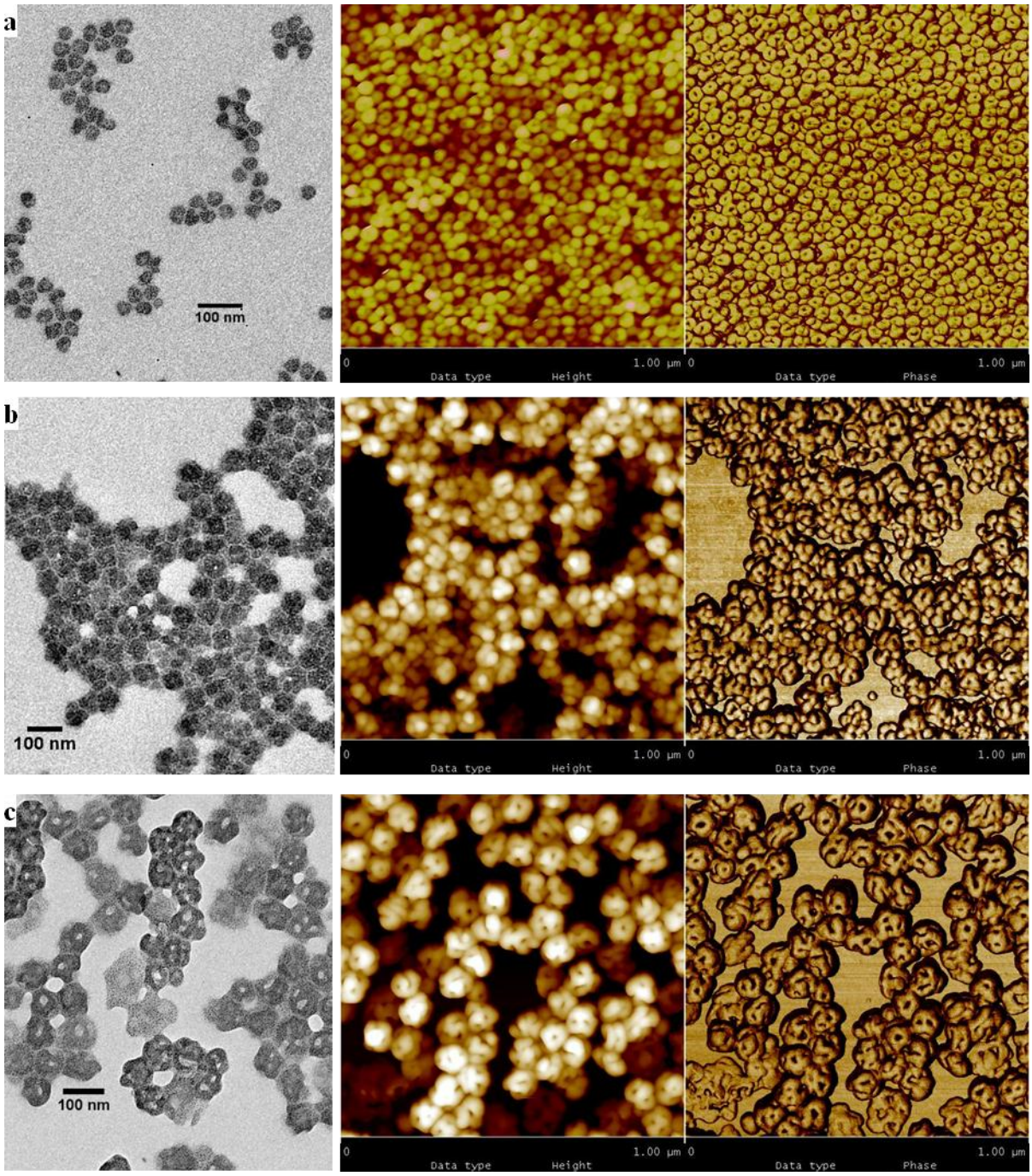

Figure 6.18 TEM and AFM images for copolymers loaded with 0.5 equiv of $HAuCl_4$ in $CHCl_3$: (a) G1PS-*g*-(P2VP25-*b*-PS20), (b) G2PS-*g*-(P2VP15-*b*-PS11), and (c) G3PS-*g*-(P2VP14-*b*-PS11).

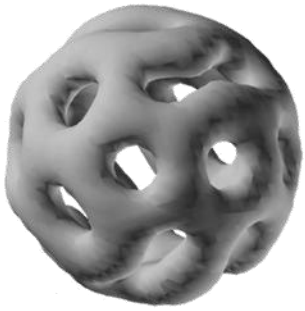

Figure 6.19 Simulation results for a nanoparticle coated with a block copolymer film resulting in a golf ball structure.[53]

In view of the previous results showing the influence on morphology of selective (toluene) and non-selective solvents (THF, $CHCl_3$) for PS, the effect of a solvent selective for P2VP was investigated next. While methanol is a non-solvent for PS, it is a known good solvent for P2VP (see Chapter 5) and the arborescent copolymers should remain soluble in low methanol content solutions. The arborescent copolymers were therefore dissolved in toluene with 2 % methanol, loaded with 0.5 equiv of $HAuCl_4$, and then analyzed by TEM and AFM. The influence of P2VP solvent selectivity was further investigated by the addition of more methanol to the gold-loaded polymer solutions until the first indication of colloidal precipitate formation (cloud-point at ca. 19 % methanol content) for the G1PS-*g*-(P2VP25-*b*-PS20) and G2PS-*g*-(P2VP15-*b*-PS11) copolymers.

The presence of methanol led to morphology changes for the G2 template displaying toroidal structures in toluene. Even at only 2 % methanol content a spherical topology was obtained, although central indentations remained for a small number of species. This dimpled sphere morphology was very similar to that seen for metal coordination in $CHCl_3$ (Figure 6.14a). Analysis by TEM provided little evidence for ring-like organization of the metal

within the template, proving that phase segregation has been altered to a significant degree from a toroidal to a spherical morphology. Figure 6.20a illustrates the spherical topology obtained with support from cross section to demonstrate the smooth contour of the surface, while Figure 6.18b confirms that phase segregation is still present, although not to the extent where ring-like organization of the metal can be observed by TEM (Figure 6.20b inset). The more uniform and spherical topology in the presence of metallic ions is therefore a direct result of P2VP phase swelling by the methanol. No additional morphology changes were observed for loading at increased methanol contents up to the pre-colloidal dispersion state: Spherical species resulted with a small phase differential in the center of the structures.

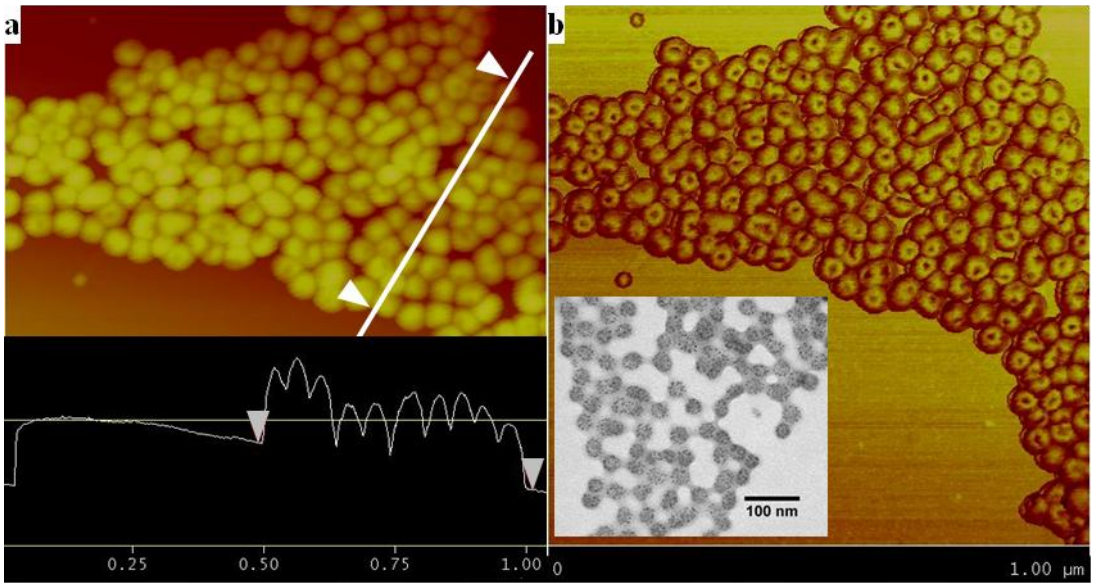

Figure 6.20 G1PS-*g*-(P2VP25-*b*-PS20) loaded with $HAuCl_4$ in toluene with 2 % methanol: (a) AFM height image with surface cross section and (b) AFM phase image with TEM inset.

The G3, G2PS-*g*-(P2VP15-*b*-PS11), and G4, G3PS-*g*-(P2VP-*b*-PS11), copolymers also showed interesting morphology changes in the presence of methanol. The G3 template, which displayed a raspberry morphology when loaded with $HAuCl_4$ in toluene or in chloroform, underwent a transition to cylindrical structures with 2 % of methanol, as seen in Figure 6.21a. With increasing methanol content, an increase in the cylinder spacing was observed. The transition to cylindrical phase segregation is attributed to enhanced phase separation between PS and P2VP resulting from P2VP swelling in methanol. The interpenetrating PS chains from the substrate, which are thought to induce nodular phase separation in toluene, should be excluded from the P2VP phase due to their incompatibility with methanol under these conditions. Enhanced phase separation between the PS and the P2VP chains within the G3 template in the presence of methanol is analogous to the situation encountered in the G4 molecules due to the preferential reaction of coupling sites on the periphery of the substrate, and likewise favors the formation of continuous cylindrical domains. In the case of the G4 template, cylinder-in-sphere morphologies were once again observed (Figure 6.21), although with increased cylinder spacing as compared to toluene alone. Interpenetration being already minimized between the PS and P2VP phases in this system, the addition of methanol had no influence on the morphology obtained.

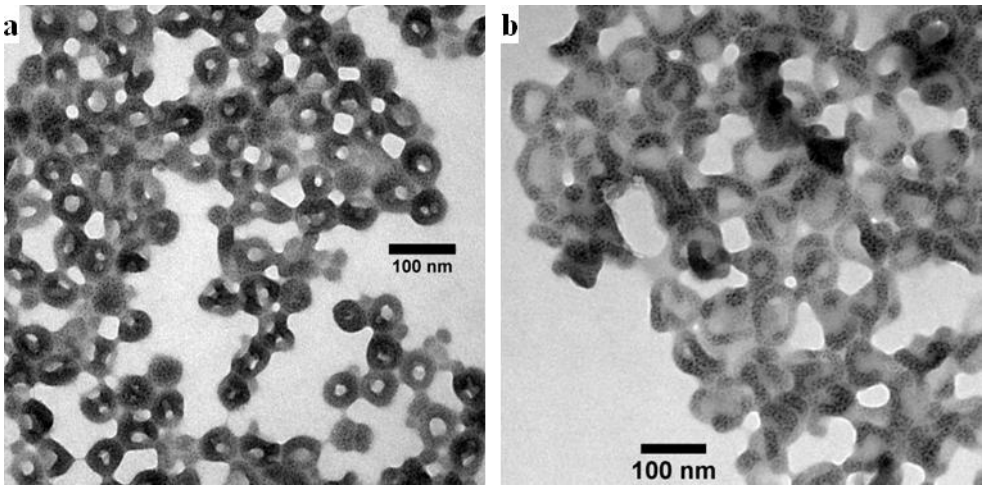

Figure 6.21 TEM images for $HAuCl_4$-loaded arborescent copolymers in toluene with 2 % methanol: (a) G2PS-*g*-(P2VP15-*b*-PS11) and (b) G3PS-*g*-(P2VP14-*b*-PS11).

The next solvent investigated was cyclohexane (CH), as it is a theta (Θ) solvent for PS and a non-solvent for P2VP, and may therefore also induce interesting phase segregation phenomena. The $HAuCl_4$-loaded copolymers were not soluble in CH alone, thus a binary solvent system was used with THF. Copolymers were loaded with $HAuCl_4$ (0.5 equiv) in THF, and then diluted with CH to either 25 % or 75 % CH content.

In solutions with 25 % CH, the G1PS-*g*-(P2VP25-*b*-PS20) arborescent copolymer lost their toroidal topology as with the addition of methanol. The topology was spherical, although a small number of structures also displayed a central depression. Toroidal phase segregation was still observed in the AFM phase scan, however. TEM analysis yielded similar findings for the metal organization within the polymer scaffold, namely a circular distribution with some templates having a lower metal concentration at the center. In the binary solvent system containing 75 % CH and 25 % THF, a spherical topology with uniform metal distribution was exclusively observed by AFM phase and TEM analysis (Figure 6.22).

Analogous observations were made for the G3 and G4 templates, with loss of nanodomains and an increased trend toward a spherical morphology with increasing CH content, as seen in Figure 6.23 and Figure 6.24.

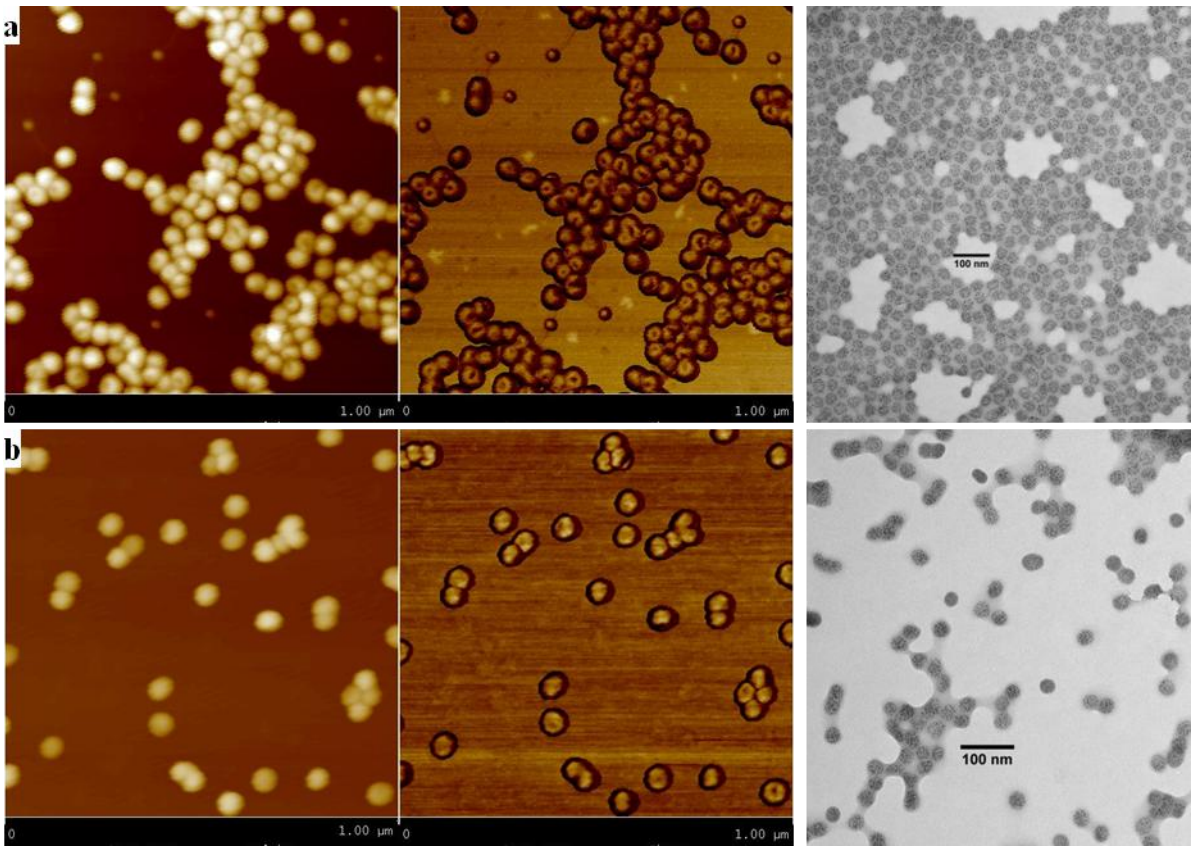

Figure 6.22 AFM height (left), phase (center), and TEM (right) images for G1PS-*g*-(P2VP25-*b*-PS20) loaded with $HAuCl_4$ in THF/cyclohexane: (a) 75:25, THF:CH and (b) 25:75, THF:CH.

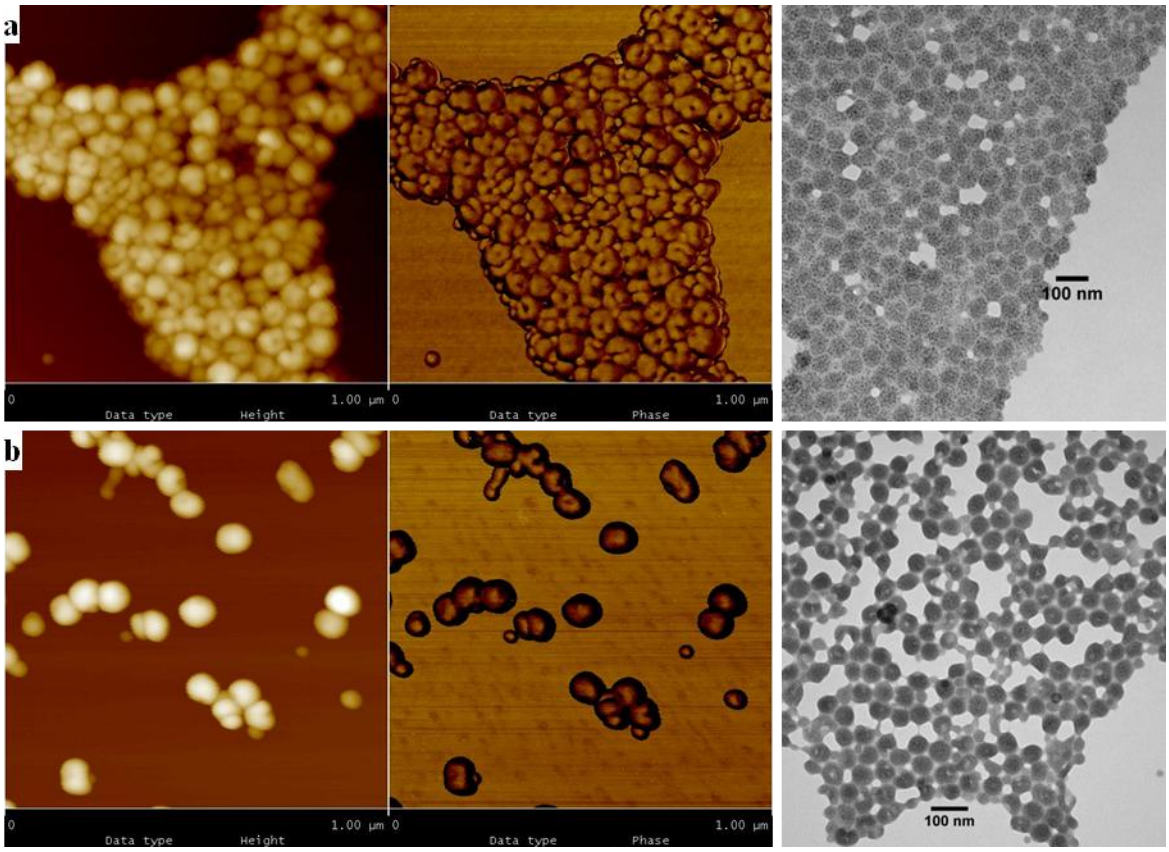

Figure 6.23 AFM and TEM images of G2PS-*g*-(P2VP15-*b*-PS11) loaded with $HAuCl_4$ in THF/cyclohexane: (a) 75:25 THF:CH and (b) 25:75 THF:CH.

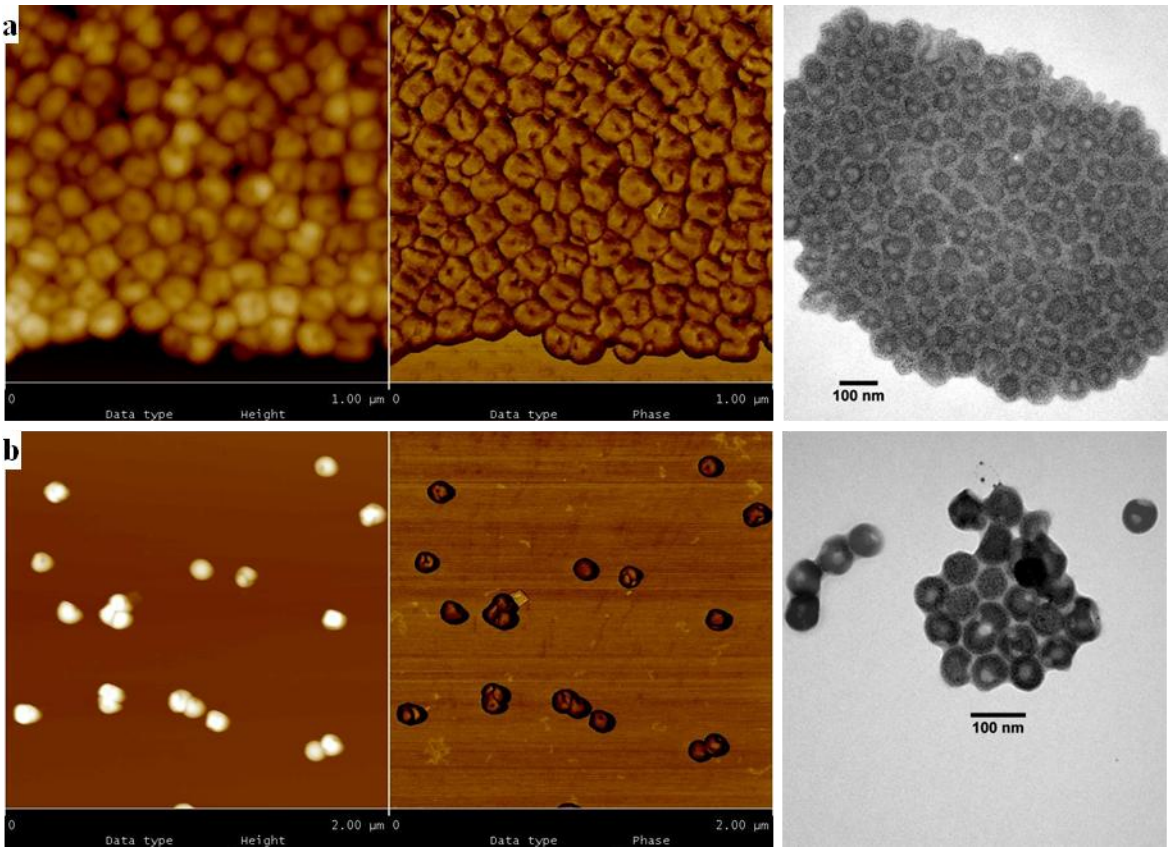

Figure 6.24 AFM and TEM images for G3PS-*g*-(P2VP14-*b*-PS11) loaded with $HAuCl_4$ in THF/cyclohexane: (a) 75:25 THF:CH and (b) 25:75 THF:CH.

6.4.3.3 Side-chain Dimension Variations

In an attempt to establish structure-property relationships and understand the phase segregation processes, the PS-*b*-P2VP side-chain length (overall and relative block length) were varied for a series of G2 and G3 copolymers. An identical block ratio was maintained while increasing the overall molecular weight for the G2 copolymers, and the relative length of the PS and the P2VP segments was varied for the G3 copolymers.

In the G2 copolymer series, the total molecular weight of the block copolymer side-chains was roughly doubled for each sample. The resulting arborescent copolymer samples

are G1PS-*g*-(P2VP5-*b*-PS6), G1PS-*g*-(P2VP11-*b*-PS11), and G1PS-*g*-(P2VP25-*b*-PS20). The G2 copolymer G1PS-*g*-(P2VP25-*b*-PS20) was already discussed in detail in this Chapter, and produced ring-like organization of gold within the template (Figure 6.10) due to toroidal phase segregation.

The G2 copolymer with the shortest side-chains, G1PS-*g*-(P2VP5-*b*-PS6), produced a spherical distribution of $HAuCl_4$ by TEM analysis in both toluene and chloroform, as seen in Figure 6.25. Unfortunately the topology and morphology of the metal-loaded templates could not be clearly visualized in toluene by AFM due to extensive aggregation, which was also observed in TEM analysis. In chloroform, the spherical distribution of the metal was better resolved, although aggregation was still prevalent. On the basis of these results, we believe that the molecular weight of the side-chains in G1PS-*g*-(P2VP5-*b*-PS6) was not large enough to trigger phase segregation of the type observed for G1PS-*g*-(P2VP25-*b*-PS20).

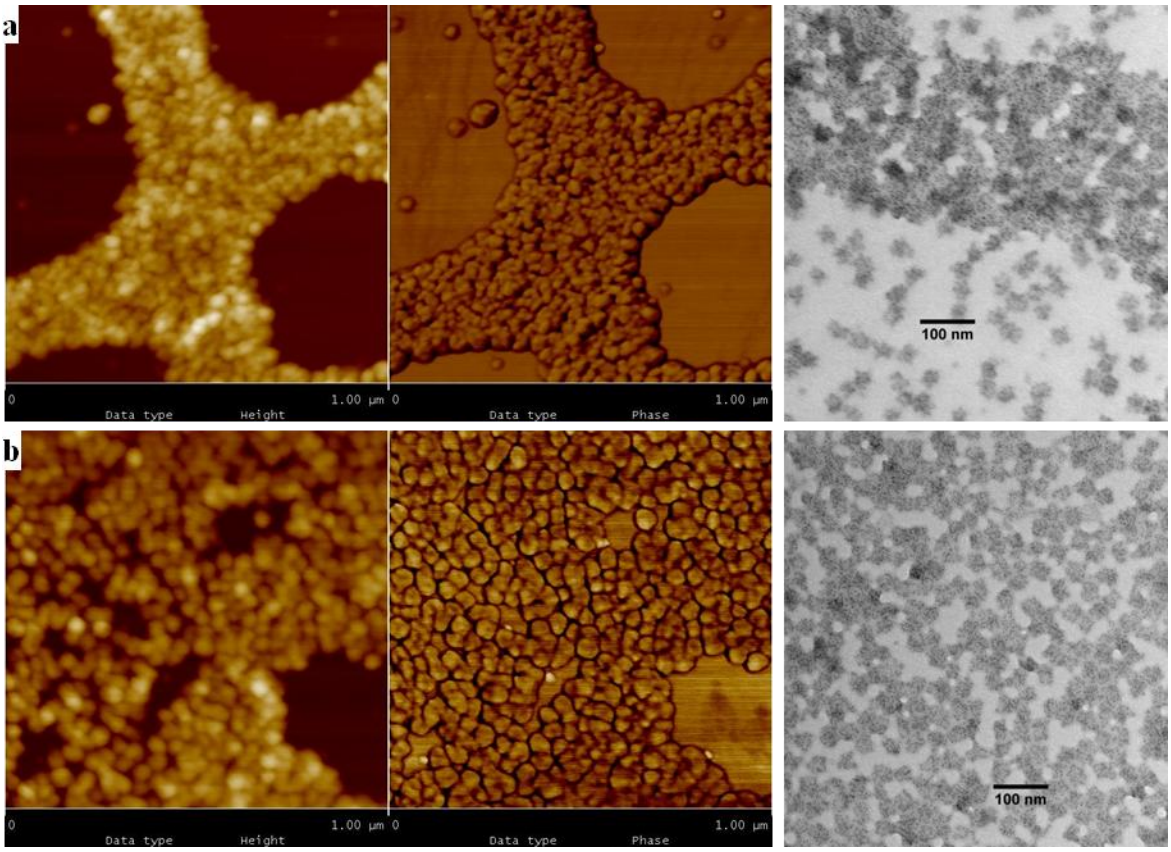

Figure 6.25 AFM and TEM images for G1PS-*g*-(P2VP5-*b*-PS6) loaded with 0.5 equiv of $HAuCl_4$ in (a) toluene and (b) $CHCl_3$.

The G2 copolymer with side-chains of intermediate length, G1PS-*g*-(P2VP11-*b*-PS11), also did not display definite signs of phase segregation but rather a spherical morphology (Figure 6.26). Aggregation was much less prevalent in this sample however, due to the longer PS coronal segment providing adequate charge shielding between the molecules. A number of species also displayed non-uniform circular organization of gold in TEM analysis, and phase differences across individual templates in AFM analysis. While this is not as prevalent or defined as for G1PS-*g*-(P2VP25-*b*-PS20) (Figure 6.10), the similarities between the two systems are obvious.

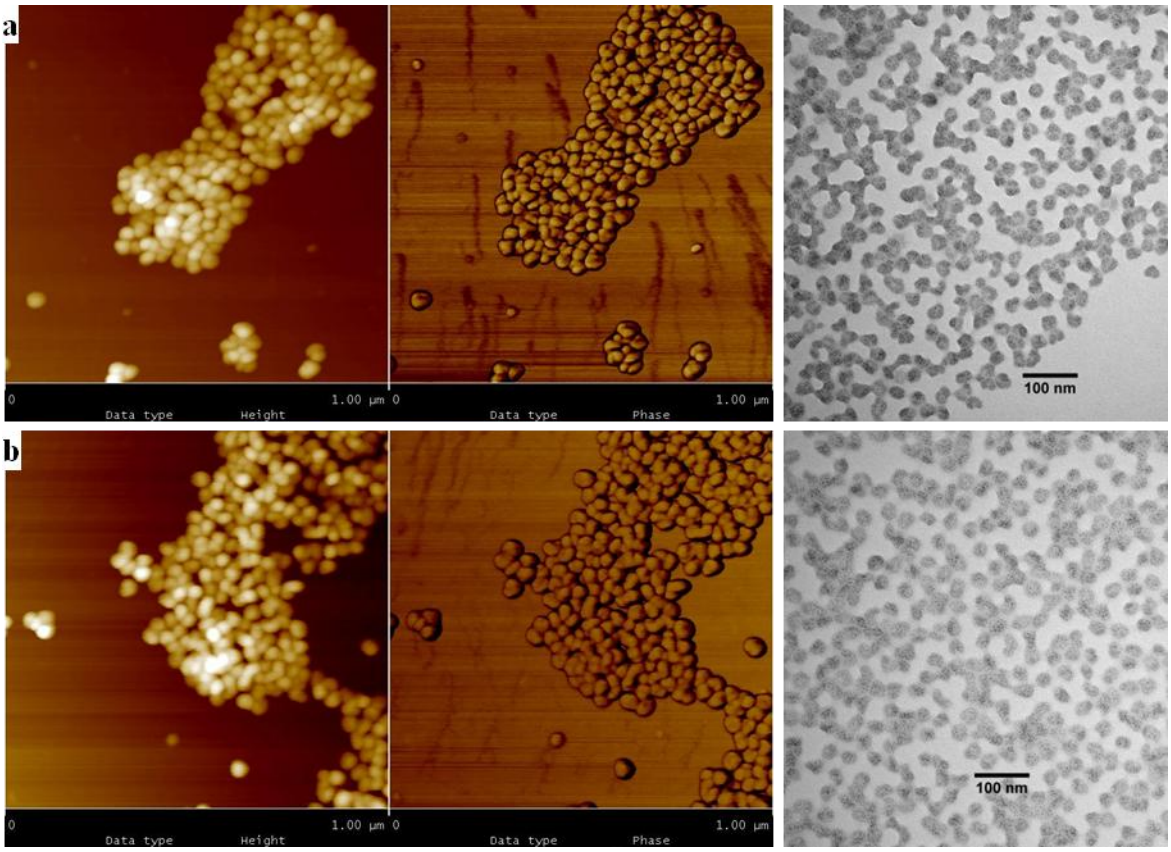

Figure 6.26 AFM and TEM images for G1PS-*g*-(P2VP11-*b*-PS11) loaded with 0.5 equiv of $HAuCl_4$ in (a) toluene and (b) $CHCl_3$.

Considering the absence of phase segregation for the arborescent copolymer with the shortest side-chains, G1PS-*g*-(P2VP5-*b*-PS6), and faint signs of non-uniform gold distribution for the copolymer G1PS-*g*-(P2VP11-*b*-PS11), it appears that a minimum P2VP molecular weight, or total block copolymer length, is required to induce phase segregation, the threshold value laying somewhere between P2VP11-*b*-PS11 and P2VP25-*b*-PS20.

For the G3 copolymer series, the length of each block was systematically varied: G2PS-*g*-(P2VP8-*b*-PS11), G2PS-*g*-(P2VP15-*b*-PS11), and G2PS-*g*-(P2VP13-*b*-PS20). While increasing the overall side-chain molecular weight, the second copolymer represents a

doubled length for the P2VP segment, while for the highest molecular weight template the size of the PS segment was doubled while holding the molecular weight of the P2VP segment relatively constant. As with the other arborescent copolymers, AFM analysis confirmed that all the G3 samples had a spherical topology in their native (unloaded) state. Once loaded with 0.5 equiv of $HAuCl_4$, phase segregation occurred in a similar fashion to that previously observed for G2PS-*g*-(P2VP15-*b*-PS11), with raspberry-type organization of the gold salt. TEM images depicting the organization of $HAuCl_4$ in both toluene and $CHCl_3$ for G2PS-*g*-(P2VP8-*b*-PS11) and G2PS-*g*-(P2VP13-*b*-PS20) are shown in Figure 6.27. Insets are also provided depicting isolated species for better illustration of the raspberry morphology.

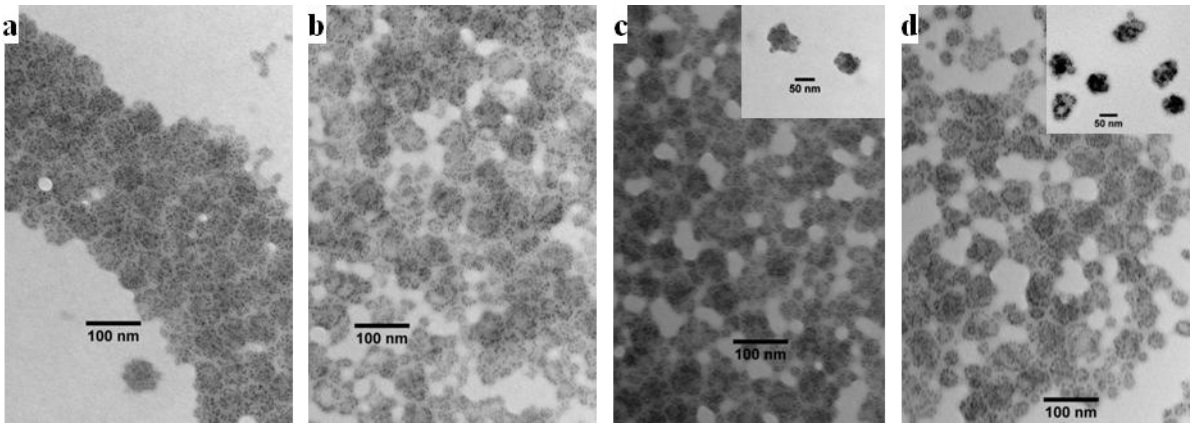

Figure 6.27 TEM images of raspberry-like morphology for $HAuCl_4$-loaded G2PS-*g*-(P2VP8-*b*-PS11) in (a) toluene and (b) $CHCl_3$, and G2PS-*g*-(P2VP13-*b*-PS20) in (c) toluene and (d) $CHCl_3$.

These results show that raspberry-type morphologies are observed independently of the length of the P2VP segments, at least within the range tested, and also independently of

the length of the PS segments in the corona. Interpenetration of the PS chains from the substrate and the P2VP in the inner shell apparently affects the extent of phase segregation similarly for all the G3 copolymers.

6.4.3.4 Influence of Loading Level

The influence of the concentration of metallic ions in the templates (i.e. the loading level) was examined, since the degree of metal coordination should affect the dynamics of phase segregation. Different morphologies may thus result at different loading levels, due to the steric effects of metallic species housed within the P2VP phase. Initial tests performed with the G0 and G2 templates showed interesting parallels to the intermolecular micelle systems:[2] With increased loading levels, the intermicellar separation increased and a more uniform dispersion of the templates was achieved. Lower loading levels often led to clustering, or the formation of 'islands' of closely packed metal-loaded templates. Similar phenomena have been reported in the literature for PS-*b*-P2VP micelles.[2] Provided in Figure 6.28 are examples of unimolecular micelle distribution and separation with varying $HAuCl_4$ loading levels (equivalents per 2VP unit) for the G0 template and two G2 templates.

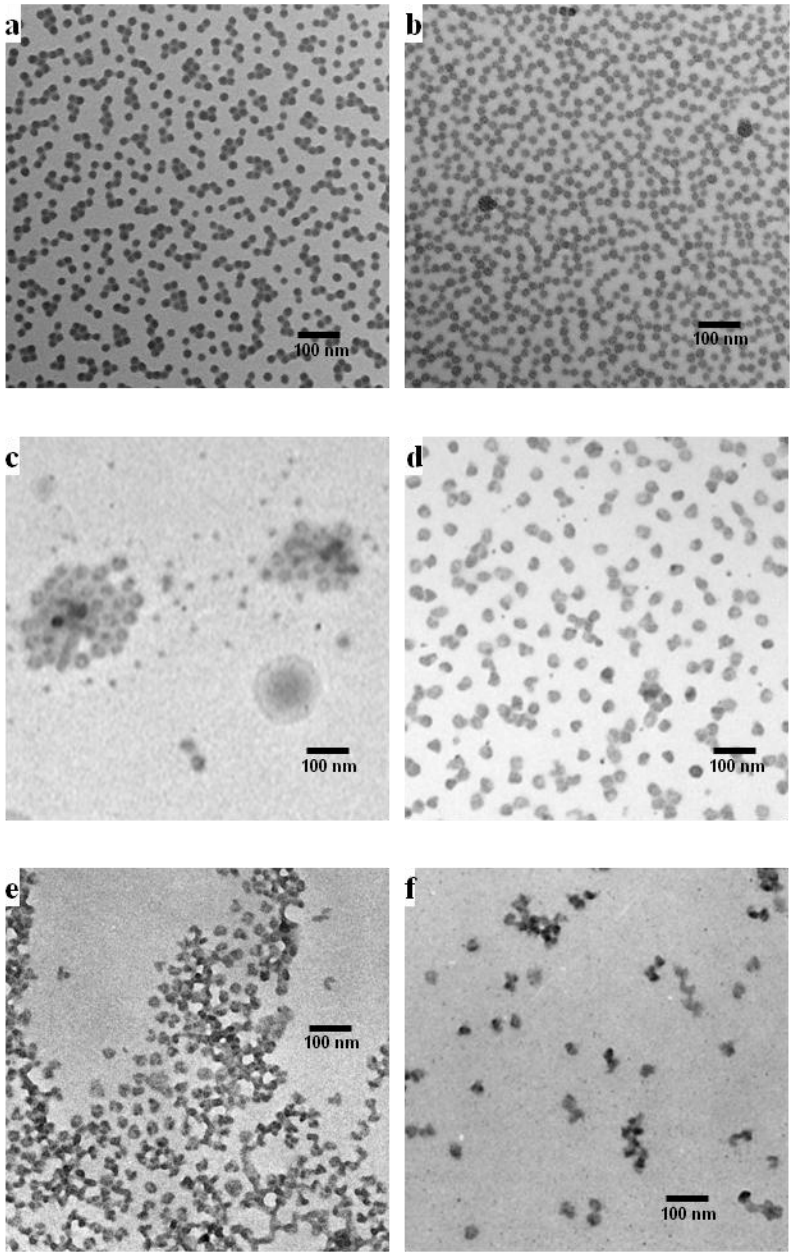

Figure 6.28 Examples of micelle distribution and separation as a function of loading level: TEM micrographs for $HAuCl_4$-loaded PS-*g*-(P2VP14-*b*-PS11) at (a) 0.125 equiv and (b) 1.0 equiv, G1PS-*g*-(P2VP11-*b*-PS11) at (c) 0.25 equiv and (d) 1.0 equiv, and G1PS-*g*-(P2VP25-*b*-PS20) at (e) 0.125 equiv, and (f) 1.0 equiv.

Stemming from these experiments, metal uptake was quantified for a G2 copolymer, G1PS-*g*-(P2VP5-*b*-PS6), as it was available in larger amounts and thus the experiment could be performed on a larger scale (50 mg template) for improved accuracy. The template was coordinated with varying amounts of $HAuCl_4$, at loading ratios (Au/2VP) from 0.1 to 1.25. The Au/polymer solutions were subjected to centrifugation (1300 × *g*, 10 min) to allow the settling of unbound $HAuCl_4$. Sediment was only detected at loading levels of 1.0 and greater. The sediment was collected and extracted with dry toluene three times in order to remove any residual polymer ($HAuCl_4$ is insoluble in toluene). The initial mass of $HAuCl_4$ added to the polymer solution was compared to the isolated gold residue and the effective loading level was calculated. It was determined that $HAuCl_4$ could be loaded up to near equivalency (ca. 0.96) to the 2VP units, in agreement with a literature report for analogous intermolecular micelle systems of PS-*b*-P4VP.[55]

For a more in-depth look at the relationship between morphology and loading level, copolymers G2PS-*g*-(P2VP15-*b*-PS11) and G3PS-*g*-(P2VP14-*b*-PS11) were used as they produced well-defined phase segregation that was easily captured by microscopic analysis, as seen earlier in Figure 6.13 and Figure 6.14. Further, the formation of intramolecular nanodomains upon metal coordination in these copolymers may arise by two different nucleation mechanisms: one at a time (sequential) or all at once (simultaneous). At loading levels as low as 0.05 equiv, phase segregation resembling the higher loading levels was observed. The morphologies, raspberry for G3 and cylinder-in-sphere for G4, were less defined at low loading levels, especially for the G4 copolymer. However, this also shows that the entire template undergoes phase segregation at once: All of the domains emerge at low loading levels, suggesting a simultaneous nucleation mechanism is operative, with increased

phase segregation (definition) at higher loading levels. Higher metal contents should enhance polymer phase incompatibility, resulting in better defined nanodomains. Provided in Figure 6.29 are AFM images depicting the raspberry and cylinder-in-sphere phase segregation observed for the G3 and G4 copolymers at 0.05 equiv loading with $HAuCl_4$ in toluene. Height scans are provided on the left, while the phase scans are seen on the right of each image.

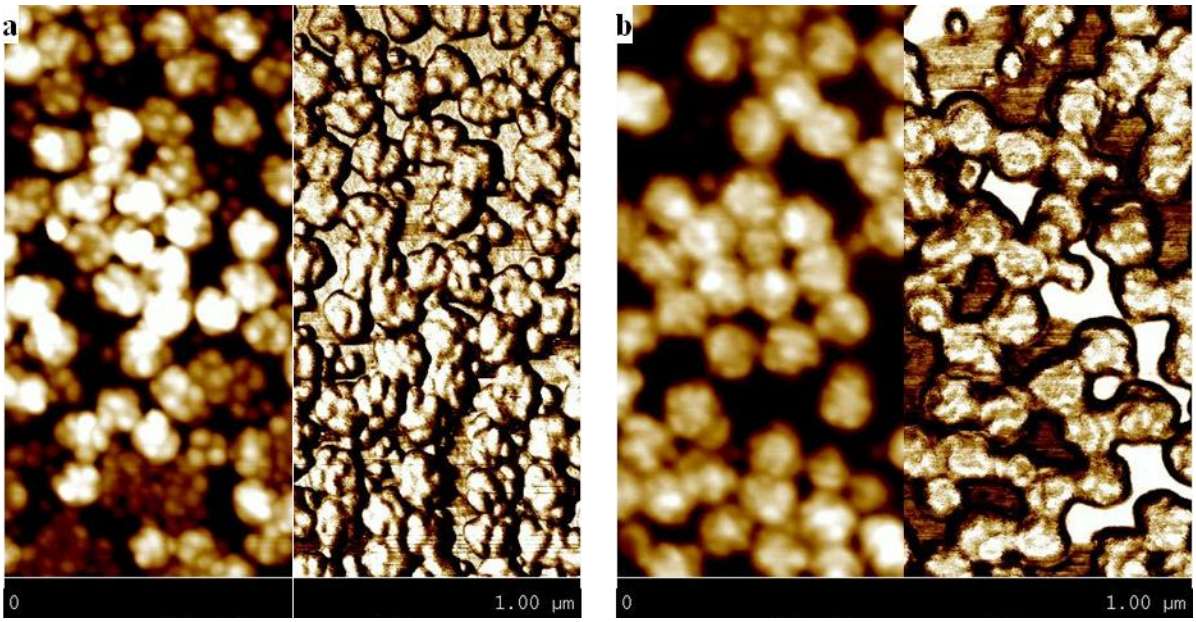

Figure 6.29 Phase segregation observed by AFM imaging for 0.05 equiv $HAuCl_4$ loading in toluene of (a) G2PS-*g*-(P2VP15-*b*-PS11) and (b) G3PS-*g*-(P2VP14-*b*-PS11).

Loading levels of 0.2, 0.5, and 1.0 equiv per 2VP unit were also examined and displayed similar features. While nanodomain definition cannot be accurately quantified, visual analysis of the AFM scans led us to the conclusion that nanodomain morphology does not change over the whole range and that the domains are no further enhanced at loading levels above 0.5 equiv. It should be noted that this may also be due to a limitation of the

AFM instrument being unable to provide adequate resolution to distinguish morphology changes within the segregated domains. A similar trend was observed for a G2 copolymer, G1PS-*g*-(P2VP25-*b*-PS20), displaying better defined toroidal phase segregation with increasing loading level.

Time-dependent loading experiments were also performed, to examine potential morphology transitions occurring over time. It was determined that significantly shorter loading times are adequate for the coordination of metals, in contrast with what the established techniques suggest.[2] For copolymers displaying intramolecular phase segregation, loading time variations could provide important information with regards to the domain nucleation mechanism. For the G0 template, PS-*g*-(P2VP14-*b*-PS11), metal coordination was evident after 30 min by TEM analysis, as revealed by a gold distribution identical to that shown in Figure 6.8a. The G2PS-*g*-(P2VP15-*b*-PS11) and G3PS-*g*-(P2VP14-*b*-PS11) copolymers were loaded with 0.5 equiv $HAuCl_4$ in $CHCl_3$, and films were cast after different time intervals (5 min, 15 min, 30 min, 1 h, 2 h, 6 h, and 24 h). Figure 6.30 depicts the gold organization observed after 30 min of loading time for the G3 and G4 copolymers, and closely resembles the results after longer equilibration times (24 h). Phase segregation had obviously already occurred after 30 min, producing morphologies similar to the ones seen previously. The deposition of gold salt within the templates appears to be fast, phase segregation being observed after as little as 5 min, and minimal changes up to 24 h.

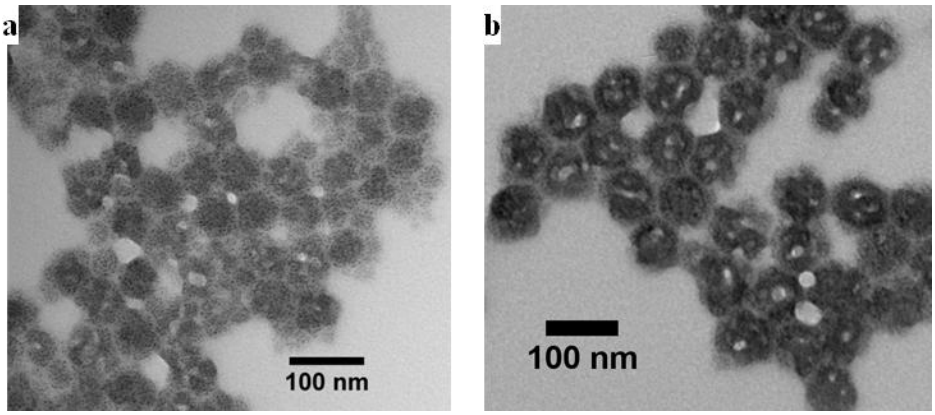

Figure 6.30 TEM images after 30 min of equilibration with $HAuCl_4$ (0.5 equiv) in $CHCl_3$: (a) G2PS-*g*-(P2VP15-*b*-PS11) and (b) G3PS-*g*-(P2VP14-*b*-PS11).

While establishing the film loading procedures, as discussed in Section 6.4.3.1, it was postulated that perhaps the ionization of P2VP was the dominant factor controlling phase segregation with no dependency on the counterion type used. Copolymers ionized with HCl by the same procedure to a 1.0 equiv loading regime (1:1 HCl:2VP) were cast into thin films and analyzed by AFM to probe phase segregation. As seen in Figure 6.31, copolymers G1PS-*g*-(P2VP25-*b*-PS20), G2PS-*g*-(P2VP15-*b*-PS11), and G3PS-*g*-(P2VP14-*b*-PS11) did not display significant phase segregation under these conditions.

The structures observed show little if any resemblance to their phase-segregated metal-loaded analogues shown previously; toroidal, raspberry, and cylinder-in-sphere morphologies were clearly not observed for the ionized species without metallic counterions. In fact, the G2 copolymer even lost its spherical shape due to strong adsorption on the mica substrate and consequent flattening of the structure. These findings show that phase segregation is induced by the metal counterion and not solely by the polymer charge. The

question then arose as to whether the morphology obtained was dependent on the type of coordinating metal used.

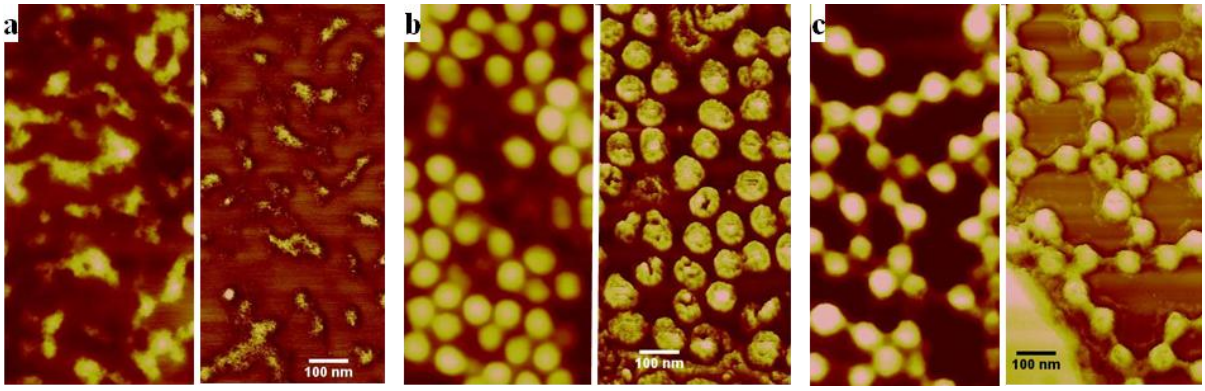

Figure 6.31 AFM images for ionized arborescent copolymer films with height scans shown on the left and phase scans on the right: (a) G1PS-*g*-(P2VP25-*b*-PS20), (b) G2PS-*g*-(P2VP15-*b*-PS11), and (c) G3PS-*g*-(P2VP14-*b*-PS11).

Again, the three copolymers displaying well-defined intramolecular nanostructures were used to investigate the effect of the metal ion type. Coordination with palladium(II) acetate, $Pd(OAc)_2$,[56] was subsequently investigated as it can coordinate without protonation (ionization) of the 2VP units. In $HAuCl_4$ coordination, the charged 2VP adduct formed clearly decreases the compatibility between the PS and P2VP phases significantly, inducing phase segregation to minimize unfavorable interactions. Shown in Figure 6.32 are TEM images depicting the organization of $Pd(OAc)_2$ within copolymers G1PS-*g*-(P2VP25-*b*-PS20), G2PS-*g*-(P2VP15-*b*-PS11), and G3PS-*g*-(P2VP14-*b*-PS11).

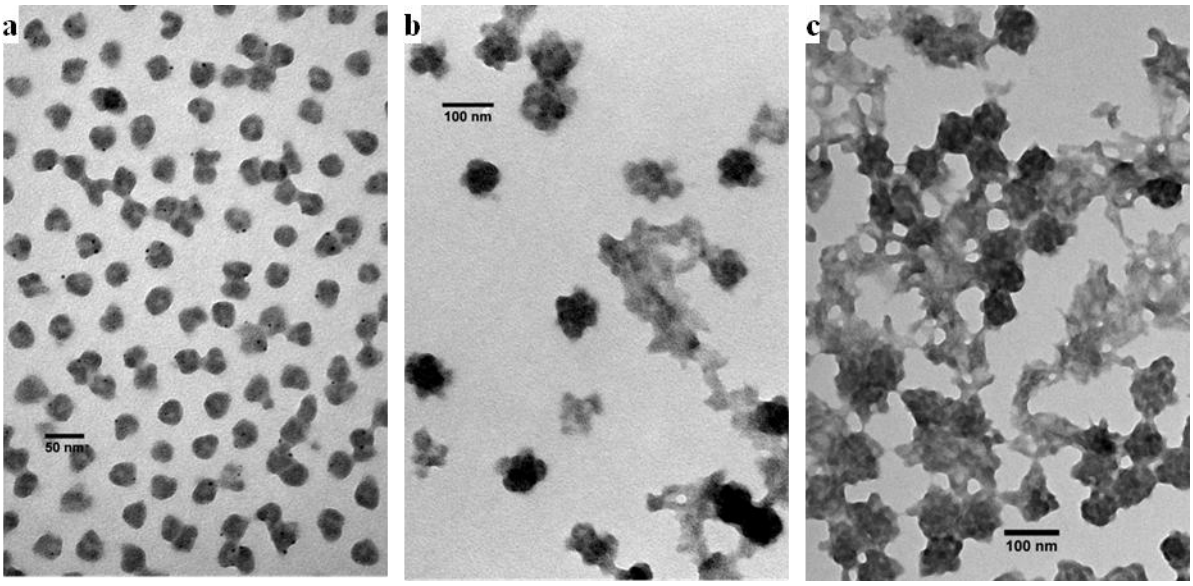

Figure 6.32 TEM images after loading with 0.5 equiv of $Pd(OAc)_2$ in toluene: (a) G1PS-*g*-(P2VP25-*b*-PS20), (b) G2PS-*g*-(P2VP15-*b*-PS11), and (c) G3PS-*g*-(P2VP14-*b*-PS11).

It is clear that the G2 and G3 copolymers display metal organization similar to the $HAuCl_4$-loaded systems, with ring-like and nodular or raspberry-like morphologies, respectively. The G4 copolymer has a significantly different morphology from the cylinder-in-sphere organization seen previously for $HAuCl_4$ coordination in toluene, however, and encroaches on the raspberry morphology seen for the G3 copolymer. This was also confirmed by AFM analysis. The primary cause for this transition to a raspberry morphology could be related to the extent of PS interpenetration from the core within the P2VP shell. Since $Pd(OAc)_2$ and the $Pd(OAc)_2$-2VP complex are more soluble in toluene as compared to $HAuCl_4$ and the $2VPH^+AuCl_4^-$ complex, chain mobility and compatibility with the PS chains from the PS substrate should be increased. This enhanced compatibility should allow the PS chains from the G3PS substrate to interpenetrate the $Pd(OAc)_2$-2VP phase to a greater extent as compared to the $2VPH^+AuCl_4^-$ complex phase. The presence of the interpenetrating chains

leads to the nodular phase segregation, in analogy to the template derived from the G2PS substrate. A similar morphology transition from cylindrical to nodular species has been reported for PS-*b*-P2VP copolymers, but this was accomplished by templating the block copolymers within cylindrical aluminum oxide nanopores and subjecting the system solvency and temperature variations.[52]

Bimetallic loading, or multi-component loading in general, is attractive due to the interesting properties which may result and the potentially broadened application spectrum for the particles, especially if some domains can be selectively loaded with specific metals. Systems such as this have potential for use as multifunctional nanoreactors or in the release of multiple agents in drug delivery applications.[57] The G4 copolymer was loaded with both $HAuCl_4$ and $Pd(OAc)_2$, in analogy to a previous investigation for PS-*b*-P4VP block copolymers.[58] Figure 6.33 depicts the raspberry morphology resulting when the G4 copolymer was loaded with $HAuCl_4$ and $Pd(OAc)_2$ in toluene (0.25 equiv each).

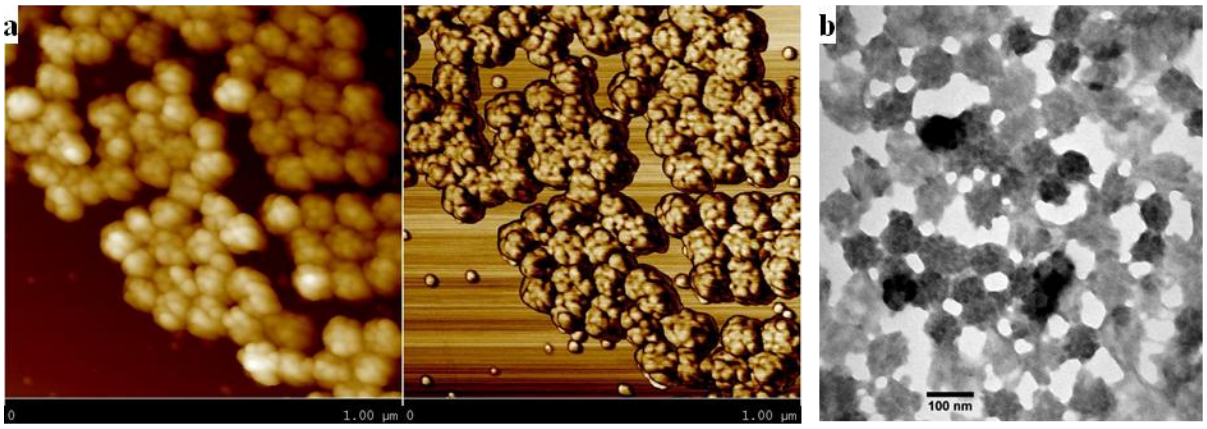

Figure 6.33 Bimetallic loading of G3PS-*g*-(P2VP14-*b*-PS11) with $HAuCl_4$ and $Pd(OAc)_2$: (a) AFM height (left) and phase (right), and (b) TEM images.

The metals were added simultaneously to the copolymer as a solution in toluene containing 0.75% of THF, to also solubilize $HAuCl_4$. Unfortunately, instrumentation which could provide mapping of the metal over the templates, such as energy-specific transmission electron microscopy,[59] was not available. Bimetallic loading was also performed in chloroform for both the G3 and G4 model copolymers, the same result (nodular phase segregation) being observed in both cases by TEM and AFM analysis. In a final bimetallic loading experiment using G3 and G4 copolymer templates, sequential loading of 0.05 equiv $HAuCl_4$ followed by hexachloroplatinic(IV) acid (H_2PtCl_6, 0.05 equiv),[56] was performed. The $HAuCl_4$ was added as a toluene solution with 0.75 % of THF for metal solubilization, while H_2PtCl_6 was added as received. Coordination of H_2PtCl_6 with 2VP occurs in similar fashion to $HAuCl_4$, by protonation of the nitrogen atom and metallic counterion association. This resulted in phase-segregated morphologies identical to $HAuCl_4$ loading in toluene, raspberry and cylinder-in-sphere structures being observed by TEM and AFM analysis for the G3 and G4 copolymers, respectively (Figure 6.34).

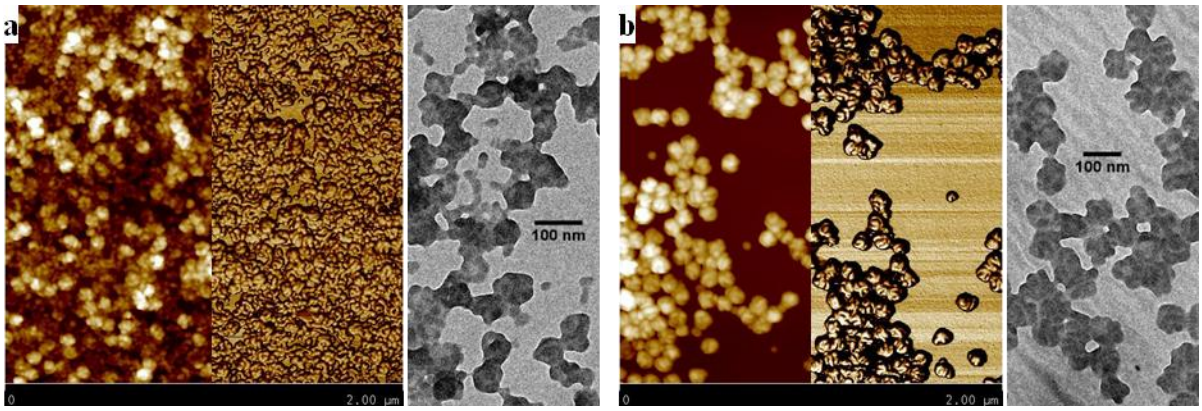

Figure 6.34 Bimetallic loading of H_2PtCl_6 (0.05 equiv) and $HAuCl_4$ (0.05 equiv) in toluene: (a) G2PS-*g*-(P2VP15-*b*-PS11) and (b) G3PS-*g*-(P2VP14-*b*-PS11).

6.4.3.5 Intermolecular Effects

Thickness measurements were performed by ellipsometry for arborescent copolymer films, before and after loading with gold, to determine the average thickness of the material deposited on the substrate. This method is somewhat crude in that the film thickness cannot be directly correlated with the molecular dimensions, since areas devoid of polymer are unaccounted for in the calculation. This technique was only applied to provide further evidence for monolayer formation. Phase segregation could potentially be induced by orthogonal polymer interactions, however if only a monolayer is present these interactions can be excluded. On the basis of the molecular dimensions determined from DLS, TEM, and AFM analysis, one would expect that for a monolayer, ellipsometry will provide a lower film thickness due to less than 100 % surface coverage as well as molecular flattening. The thickness of some of the films cast for AFM analysis was measured by ellipsometry and compared to film thickness determined by AFM analysis (Table 6.6).

Table 6.6 Film thickness measurements of native and $HAuCl_4$-loaded copolymers in toluene using ellipsometry and AFM

	Ellipsometry[a]		AFM[b]	
Sample	Native[c]	0.5 Au[d]	Native[c]	0.5 Au[d]
PS-*g*-(P2VP14-*b*-PS11)	8.3 ± 0.2	25 ± 1	–[e]	22 ± 2
G1PS-*g*-(P2VP25-*b*-PS20)	12.6 ± 0.6	23 ± 1	13 ± 2	31 ± 4
G2PS-*g*-(P2VP15-*b*-PS11)	12.9 ± 0.8	28 ± 1	19 ± 3	51 ± 3
G3PS-*g*-(P2VP14-*b*-PS11)	13.9 ± 0.2	31 ± 1	22 ± 4	60 ± 3

[a] Average film thickness, nm; [b] Height measured at substrate-polymer boundary, nm; [c] Native polymer film thickness; [d] Thickness of polymer film containing 0.5 equiv $HAuCl_4$, loaded in toluene; [e] Unable to measure, no polymer-substrate boundary present

For the measurement of film thickness by ellipsometry, aside from the G0 species which have been shown to aggregate, the film thickness increases with the generation number of the templates. The variations observed are insignificant within error limits for the G2 – G4 templates, and it is necessary to assume similar coverage for each film sample in making the comparison, however. AFM also offers the ability to quantify film thickness, provided that a bare substrate area is available as baseline. An example of such a measurement is shown in Figure 6.35 for G3PS-*g*-(P2VP14-*b*-PS11) loaded with 0.5 equiv of $HAuCl_4$ in toluene.

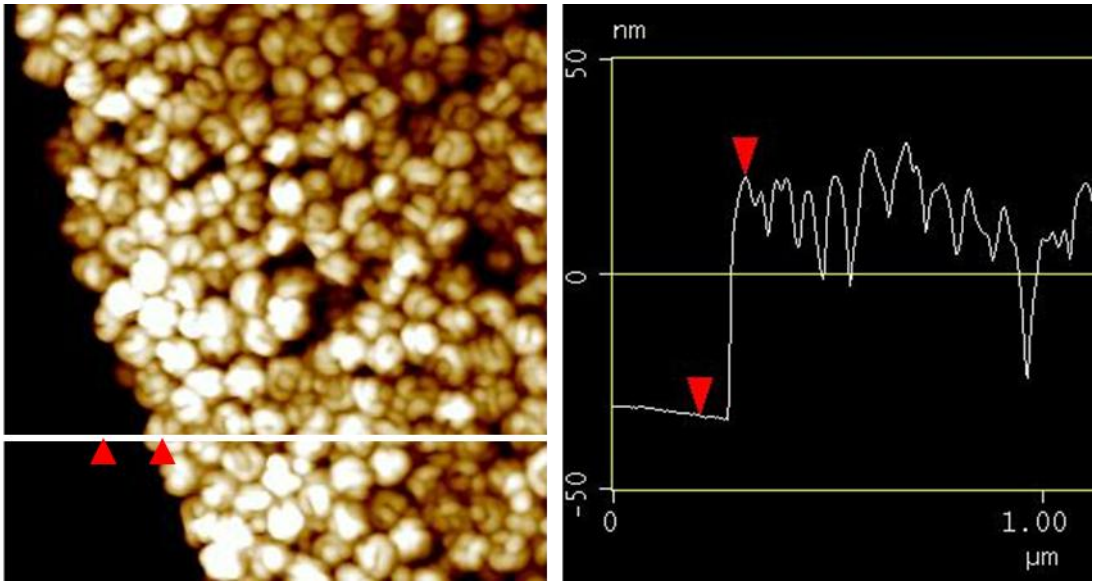

Figure 6.35 Film thickness measurement from AFM cross section analysis for $HAuCl_4$-loaded G3PS-*g*-(P2VP14-*b*-PS11).

The film thickness determined from cross section analysis provides a height difference between the substrate and the arborescent molecules of ca. 60 nm for the G3PS-*g*-(P2VP14-*b*-PS11) species, which is indicative of a monomolecular layer. Height

measurements were performed at the substrate-polymer boundary for the copolymers listed in Table 6.6 and led to similar findings: Monolayer films were adsorbed on the substrates, but multilayered sections are also apparent. The only exception to this was again the G0 species, which contained mainly multilayered areas with an average height of 20 nm. These results are in agreement with the conclusions drawn previously from the ellipsometry measurements, concerning the lack of influence of intermolecular interaction from orthogonal species to phase segregation. Additionally, similar intramolecular phase segregation is apparent for species within both mono- and multilayered areas, again in agreement with phase segregation being independent of orthogonal intermolecular or substrate interactions.

Thickness and diameter measurements from AFM analysis on both native and gold-loaded copolymers are also provided in Table 6.7. The AFM height measurements, much like ellipsometry, also show a height increase upon metal coordination. Further, molecular flattening is reduced upon coordination with $HAuCl_4$ as indicated by the larger height to diameter ratio; the gold-loaded copolymers conform to a more spherical topology.

The native G0 and G1 copolymers form continuous polymer films with no voids exposing the substrate, thus height measurements could not be performed. Further, well-defined unimolecular features were not observed in the film and thus radii could not be measured accurately, as illustrated in Figure 6.5.

Table 6.7 Analysis of molecular dimensions by AFM

	Native[a]			0.5 Au[b]		
Template	h[c]	d[d]	h/d	h[c]	d[d]	h/d
PS-*g*-(P2VP14-*b*-PS11)	–[e]	–[e]	–	22 ± 2	28 ± 1	0.8
G0PS-*g*-(P2VP8-*b*-PS8)	–[e]	–[e]	–	19 ± 2	35 ± 2	0.5
G1PS-*g*-(P2VP25-*b*-PS20)	13 ± 2	43 ± 1	0.3	31 ± 4	45 ± 4	0.7
G2PS-*g*-(P2VP15-*b*-PS11)	19 ± 3	90 ± 1	0.2	51 ± 3	69 ± 2	0.7
G3PS-*g*-(P2VP14-*b*-PS11)	22 ± 4	105 ± 2	0.2	60 ± 3	69 ± 2	0.8

[a] Native polymer in toluene; [b] Polymer containing 0.5 equiv $HAuCl_4$, loaded in toluene; [c] Height of polymer film measured at substrate-polymer boundary, nm; [d] Diameter of template molecule, nm; [e] Unable to measure, no polymer-substrate boundary present

6.4.4 Solution Properties

In the microscopic investigation of the metal-loaded polymer films, it was apparent that the nanoparticles had the tendency to self-assemble into large two-dimensional clusters. Upon investigation of the metal-loaded copolymers in solution by dynamic light scattering, however, the species were surprisingly found to be monodispersed and free of aggregation. First- and second-order analysis of the autocorrelation function yielded similar hydrodynamic radii and the measurements in toluene and chloroform were reproducible, with the exception of a few polymers (Table 6.8). These results are indicative of narrowly dispersed and non-associating species in solution. CONTIN analysis was also performed to characterize the breadth of the size distribution, as shown previously in Figure 6.4. The breadth of the distribution for these unimodal samples is also qualified in Table 6.8 to further assess aggregation.

Table 6.8 Hydrodynamic radii and size distributions of $HAuCl_4$-loaded arborescent copolymers in toluene and $CHCl_3$

Sample	Toluene			$CHCl_3$		
	r_{h1}[a]	r_{h2}[b]	Dist.[c]	r_{h1}[a]	r_{h2}[b]	Dist.[c]
PS-*g*-(P2VP14-*b*-PS11)	38 ± 1	27 ± 1	B	46 ± 1	39 ± 1	B
G0PS-*g*-(P2VP8-*b*-PS8)	53 ± 1	48 ± 1	B	45 ± 1	42 ± 1	N
G1PS-*g*-(P2VP5-*b*-PS6)	27 ± 1	26 ± 1	N	27 ± 1	26 ± 1	N
G1PS-*g*-(P2VP11-*b*-PS11)	42 ± 1	36 ± 1	B	60 ± 1	53 ± 1	B
G1PS-*g*-(P2VP25-*b*-PS20)	40 ± 1	38 ± 1	N	56 ± 1	52 ± 1	N
G2PS-*g*-(P2VP8-*b*-PS11)	54 ± 1	52 ± 1	N	51 ± 1	50 ± 1	N
G2PS-*g*-(P2VP15-*b*-PS11)	63 ± 1	60 ± 1	N	61 ± 1	59 ± 1	N
G2PS-*g*-(P2VP13-*b*-PS20)	50 ± 1	49 ± 1	N	52 ± 1	51 ± 1	N
G3PS-*g*-(P2VP14-*b*-PS11)	57 ± 1	56 ± 1	N	68 ± 1	66 ± 1	N

[a] Hydrodynamic radii (nm) from first-order analysis of the correlation function;
[b] Hydrodynamic radii (nm) from second-order analysis of the correlation function;
[c] Unimodal population distribution: broad (B) or narrow (N)

Two charts comparing the observed unimodal CONTIN size distributions obtained for narrow and broadly (aggregated) dispersed $HAuCl_4$-loaded copolymers are provided in Figure 6.36.

Templates of overall generation 2 and above formed mainly unimodal, narrowly dispersed species in solution. It was likewise not surprising to find that the G0 copolymer, PS-*g*-(P2VP14-*b*-PS11), was strongly aggregated since the native (unloaded) copolymer also exhibited similar characteristics (Table 6.4, Table 6.5).

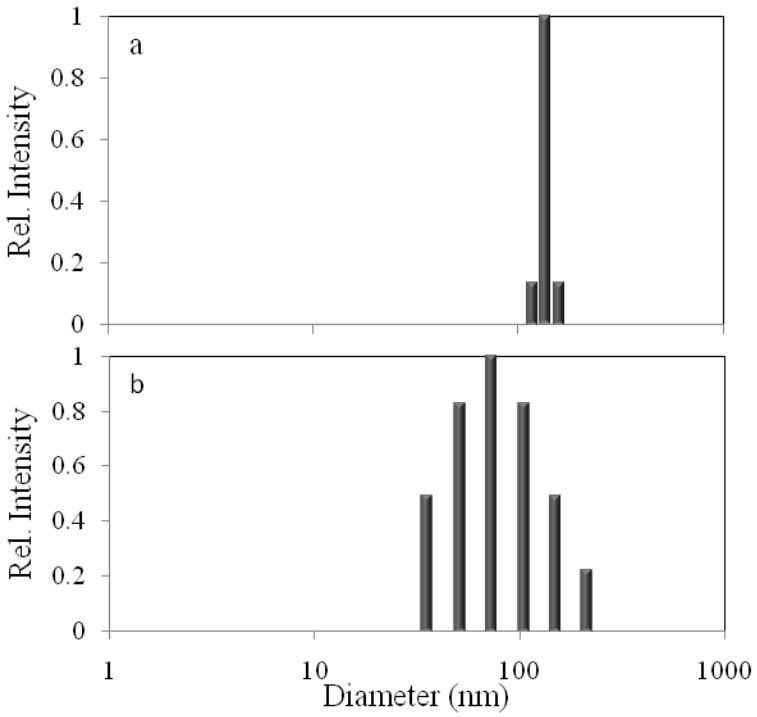

Figure 6.36 Examples of CONTIN distributions for $HAuCl_4$-loaded (0.5 equiv) copolymers: (a) monodispersed G3PS-*g*-(P2VP14-*b*-PS11) and (b) aggregated G1PS-*g*-(P2VP11-*b*-PS11).

6.4.5 Reduction to Gold Nanoparticles by Various Methods

It is understood that the gold salt ($AuCl_4^-$) contained within the arborescent copolymer molecules, shown in the TEM figures throughout this Chapter, has been reduced to elemental gold by the electron beam in TEM analysis. Reduction by the electron beam can be described by Equation 6.2.

$$2\ HAuCl_4 + 6\ e^- \rightarrow 2\ Au + 2\ HCl + 3\ Cl_2 \qquad (6.2)$$

Many reducing agents and techniques have been proposed for the reduction of gold coordinated within polymeric templates, which are more convenient for the production of

gold nanoparticles on a large scale. Scheme 6.1 provided a generic representation of gold salt reduction within coordinating P2VP systems. The type and amount of reagent, and the reduction protocol used can afford very different outcomes in terms of nanoparticle size and uniformity.[60] Analysis of the average size and/or distribution of the resultant nanoparticles can be performed by microscopic techniques such as TEM, or by spectroscopic methods. Since nanoparticles of gold salt ($AuCl_4^-$) and elemental gold (Au^0) have an absorption maximum within the visible wavelength range, UV-Vis spectroscopy can serve to monitor changes in the properties of the nanoparticles.

The yellow-colored pyridinium tetrachloroaurate complex ($2VPH^+AuCl_4^-$) solution has a characteristic absorption band at 325 nm, also observed for the unbound gold salt. Figure 6.37 depicts the absorption band for $HAuCl_4$ in solution after coordination with different arborescent CSC copolymers. The spectra are vertically shifted for improved clarity and were acquired at a concentration of ca. 0.002 % w/v copolymer (0.0024 % w/v $HAuCl_4$).

As shown in Figure 6.37, coordination does not change the electronic environment of the gold ions significantly, and no dependence of the absorption spectra on the polymer characteristics (molecular weight, generation) is observed. After reduction the yellow solution turns dark purple, irrespective of the reduction method selected. The resulting elemental gold nanoparticles have an absorption band centered near 525 nm, which is characteristic for the surface plasmon resonance of small Au nanocrystals. Shifts in the absorption maximum, or the appearance of shoulders, are indicative of particle size variations, aggregation, or pairing. An example of a red shift observed as a result of gold nanoparticle size increase is provided in Figure 6.37 and will be discussed later.

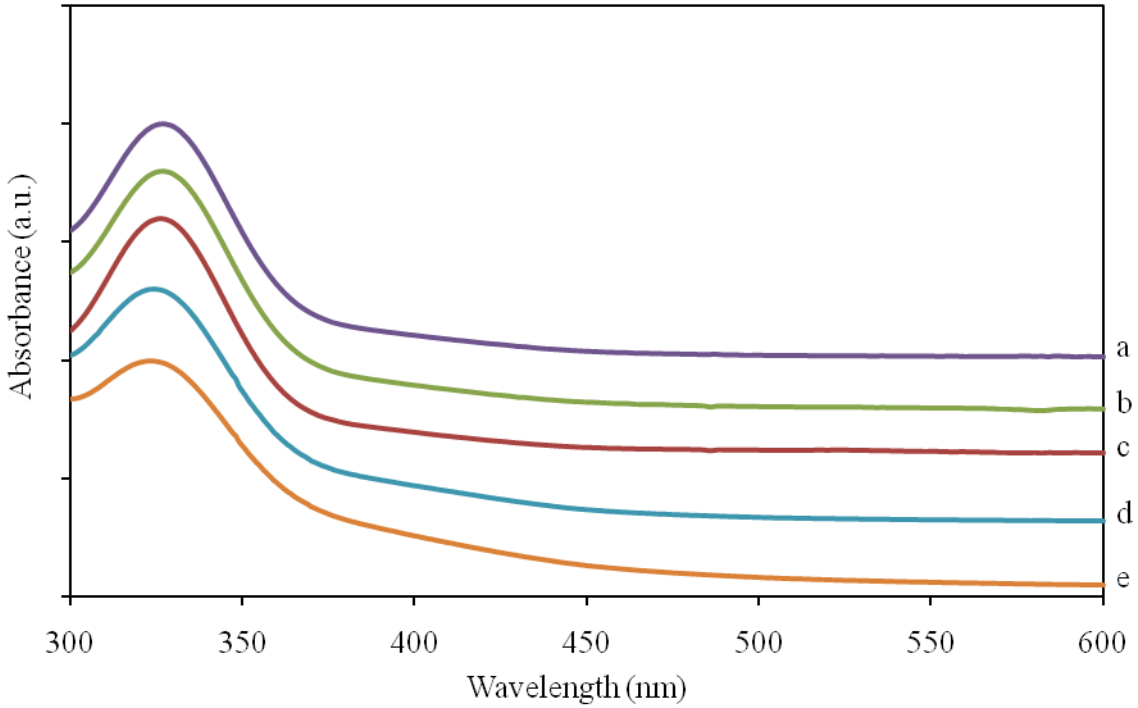

Figure 6.37 UV-Vis absorption of $AuCl_4^-$ (a) in solution and after coordination with the vinylpyridine moieties in arborescent copolymers: (b) G1PS-*g*-(P2VP5-*b*-PS6), (c) G1PS-*g*-(P2VP25-*b*-PS20), (d) G2PS-*g*-(P2VP15-*b*-PS11) and (e) G3PS-*g*-(P2VP14-*b*-PS11).

6.4.5.1 Solution Reduction with Anhydrous Hydrazine

The reduction of $HAuCl_4$ with anhydrous hydrazine in solution is described by Scheme 6.2.

The exact stoichiometry of the hydrazine reduction reaction is provided in Equation 6.3.

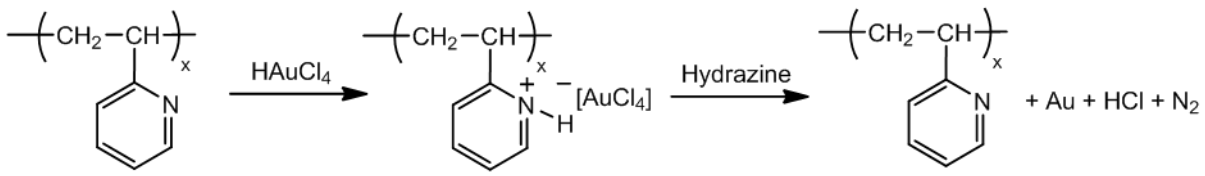

Scheme 6.2 $HAuCl_4$ coordination with poly(2-vinylpyridine) and reduction with hydrazine.

$$4\ HAuCl_4 + 3\ N_2H_4 \rightarrow 4\ Au + 3\ N_2 + 16\ HCl \qquad (6.3)$$

Reduction was examined in two different regimes for two different arborescent copolymer templates: Near equivalence and excess stoichiometry regimes for the PS-*g*-(P2VP14-*b*-PS11) and G1PS-*g*-(P2VP25-*b*-PS20) species. Since limited quantities of anhydrous hydrazine were available, and that compound poses additional risks, its use was limited to these two copolymers, as was reported in the preliminary study.[6] The excess regime (10:1 N_2H_4:Au) led to the collapse of the very small (< 1 nm) gold salt clusters into one or multiple larger, somewhat narrowly dispersed solid gold particles within each template, as shown in Figure 6.38. The size and size distribution of the collapsed nanoparticles obtained within this regime remained consistent across all loading levels for both templates, being essentially identical within error limits for the G0 (10 ± 3 nm) and G2 (8 ± 3 nm) templates. This was somewhat surprising, although similar observations have been reported for gold-loaded PAMAM dendrimers.[61]

Solution reduction in the near equivalency regime (1.2:1 N_2H_4:Au) also induced collapse of the gold particles into solid nanoparticles, but aggregation of the nanoparticles was more obvious under these conditions, as demonstrated by the larger average particle

sizes and the broader size distributions observed. This phenomenon is illustrated in Figure 6.38b and Figure 6.38d. In analogy to the excess regime, the size and size distribution of the nanoparticles was insensitive to the loading level of the templates. These results are consistent with those reported by Chiang for the preparation of gold nanoparticles within surfactant reverse micelles:[62] Larger and less uniform gold particles were obtained when the molar ratio of hydrazine to $HAuCl_4$ was decreased. It should also be noted that in the near equivalency regime, incomplete collapse of the gold into solid nanoparticles was observed since a faint shadow with a diameter similar to the non-reduced particles remained in the background. Detailed size information extracted from TEM micrograph analysis can be found in Table 6.9.

Excess reducing agent quenched nanoparticle formation from the salt adduct more efficiently, thus reducing the influence of Ostwald ripening,[63,64] a process favoring particle growth to reduce the overall surface energy of the system. It was also apparent that while excess hydrazine produced smaller and more narrowly dispersed nanoparticles, significant agglomeration and migration of the gold was prevalent. This can be deducted from the fact that some of the features did not contain measureable (dark) nanoparticle species, but rather only shadows from the gold-depleted polymer templates.

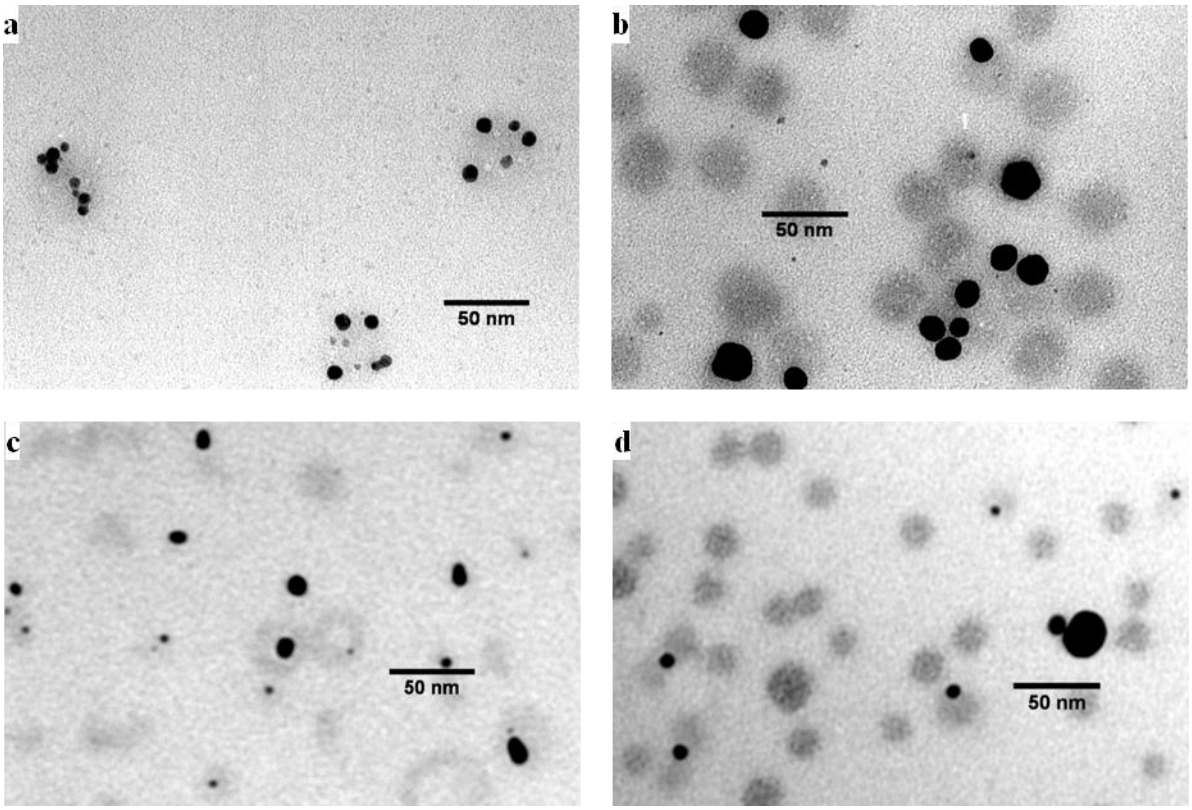

Figure 6.38 TEM analysis of gold nanoparticles obtained from anhydrous hydrazine reduction of $HAuCl_4$-loaded G1PS-*g*-(P2VP25-*b*-PS20) (a - 10:1 N_2H_4:Au, b - 1.2:1 N_2H_4:Au) and PS-*g*-(P2VP14-*b*-PS11) (c - 10:1 N_2H_4:Au, d - 1.2:1 N_2H_4:Au).

Further, grouping of the metallic nanoparticles was not consistently observed within the boundaries of each template, and the host polymers contained a variable number of nanoparticles. Intermicellar aggregation and the migration of Au upon reduction have been observed before in PS-*b*-P2VP block copolymer micelles,[2,9] so it is not surprising that this also occurs in the arborescent systems. Since the two types of polymer structures are similar, nanoparticle migration is likely the source of size dispersity and uneven distribution of nanoparticles within each arborescent copolymer template. Figure 6.39 depicts the absorbance fingerprint of elemental gold nanoparticles obtained by hydrazine solution

reduction in toluene leading to different nanoparticle sizes. The larger and more dispersed nanoparticles obtained in the near equivalency regime (1.2:1, hydrazine:Au) have a higher absorption wavelength maximum (535 nm), while particles obtained in the excess hydrazine regime (10:1, hydrazine:Au) have an absorption maximum shifted to 522 nm, which is characteristic for smaller nanoparticles.[65,66]

Table 6.9 Size analysis of TEM micrographs for gold-loaded PS-*g*-(P2VP14-*b*-PS11) and G1PS-*g*-(P2VP25-*b*-PS20) reduced with anhydrous hydrazine

Sample	Reduction Ratio (N_2H_4:Au)	Feature[b]	Diameter (nm) at Loading Level[a] 0.125	0.25	0.50	1.00
G2	none	–	31 ± 2	30 ± 3	30 ± 3	28 ± 2
G2	10:1	solid	8 ± 2	8 ± 2	8 ± 2	9 ± 3
G2	1.2:1	solid	13 ± 3	15 ± 5	17 ± 9	15 ± 7
G2	1.2:1	shadow	31 ± 3	30 ± 3	–	30 ± 2
G0	none	–	20 ± 2	22 ± 2	20 ± 3	20 ± 3
G0	10:1	solid	9 ± 2	10 ± 3	10 ± 3	11 ± 3
G0	1.2:1	solid	20 ± 8	12 ± 4	10 ± 6	21 ± 20
G0	1.2:1	shadow	18 ± 2	18 ± 2	18 ± 2	20 ± 2

[a] Equivalents of $HAuCl_4$ relative to 2VP units; [b] Refers to the feature dimensions when more than one feature is present; solid (black), shadow (grey) as seen in Figure 6.36

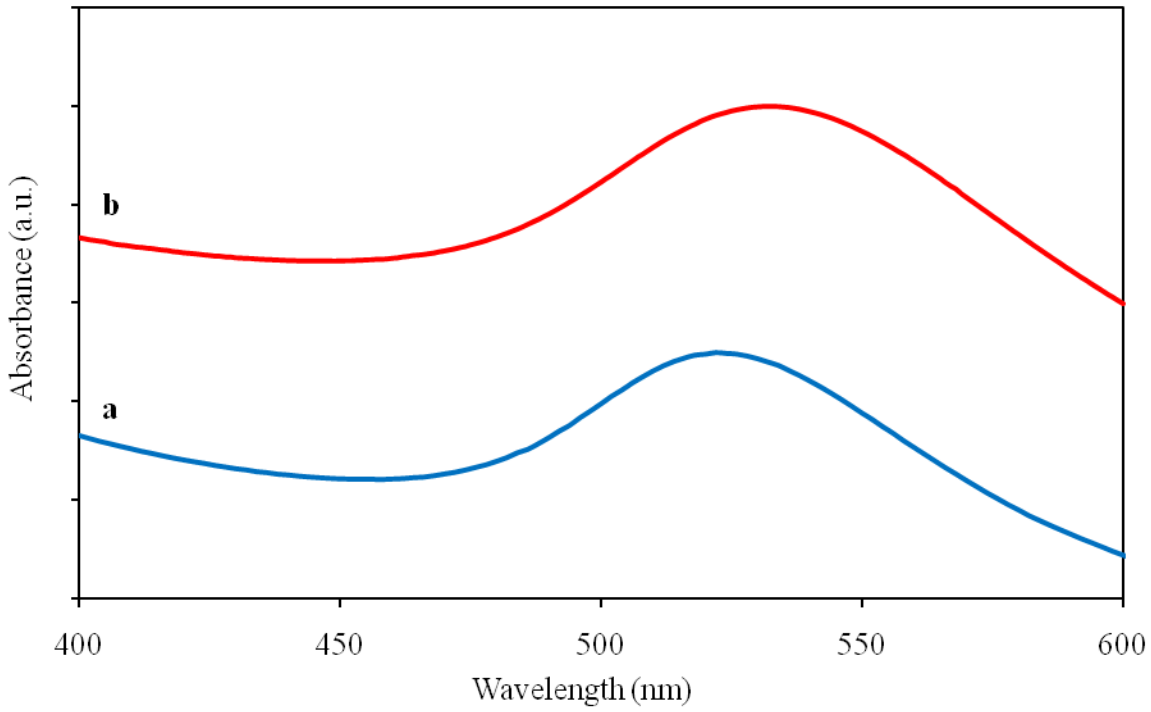

Figure 6.39 UV-Vis characterization of Au nanoparticles templated with G1PS-*g*-(P2VP25-*b*-PS20): (a) 522 nm maximum, 8 ± 2 nm diameter from excess hydrazine; and (b) 532 nm maximum, 17 ± 9 nm diameter from hydrazine reduction at near equivalency.

6.4.5.2 Reduction with Sodium Borohydride

Since hydrazine reduction led to inter-template gold particle migration and agglomeration, and ultimately to the formation of broadly dispersed nanoparticles bearing little resemblance to the polymer scaffolds from which they were derived, sodium borohydride ($NaBH_4$) was also investigated as a more powerful reducing agent than hydrazine. Stronger reducing agents induce faster reduction and can produce smaller nanoparticles that may remain localized in their original environment.[55] This effect can be explained by reduced inter-template metal migration, agglomeration, and Ostwald ripening. Sodium borohydride could therefore

represent an interesting solution to preserving the characteristics (morphology) observed for the metallic salt-loaded templates.

In each case, $NaBH_4$ was added in excess (10:1 $NaBH_4$:Au) to solutions of the arborescent copolymers loaded with 0.5 equiv of $HAuCl_4$, in an effort to ensure fast reduction and minimized agglomeration of the primary nanoparticles formed. The gold nanoparticle diameters obtained are provided in Table 6.10.

Table 6.10 Gold nanoparticle diameters by $NaBH_4$ reduction

Template	Diameter (nm)
PS-*g*-(P2VP14-*b*-PS11)	4 ± 2
G0PS-*g*-(P2VP8-*b*-PS8)	5 ± 2
G1PS-*g*-(P2VP5-*b*-PS6)	4 ± 1
G1PS-*g*-(P2VP25-*b*-PS20)	4 ± 1
G2PS-*g*-(P2VP15-*b*-PS11)	5 ± 1
G3PS-*g*-(P2VP14-*b*-PS11)	5 ± 1

As expected, the nanoparticles formed were smaller than for hydrazine reduction; however, a similar size dispersity was obtained as compared to the 10:1 hydrazine:Au reduction protocol of Table 6.9. There was virtually no discernable difference in the UV-Vis absorbance spectrum of the nanoparticles formed by $NaBH_4$ reduction of the G1PS-*g*-(P2VP25-*b*-PS20) template, with an absorption maximum at 521 nm as compared to 522 nm for hydrazine reduction (Figure 6.39). This negligible change in the absorption wavelength maximum may be due to the close proximity of the small nanoparticles derived from $NaBH_4$ reduction, as seen in Figure 6.40b, giving an absorption spectrum similar to the larger nanoparticles obtained by hydrazine reduction.

There is apparently no correlation between the template size (i.e. overall molecular weight, length of the P2VP segments, or the arborescent polymer generation) and the size of the nanoparticles obtained. This is again consistent with the findings from hydrazine reduction discussed in Section 6.4.5.1 and in Reference 6, and in agreement with the findings for gold nanoparticles templated with PAMAM-PEG dendrimers-star polymers reduced with $NaBH_4$.[61] Reductions were also performed in different solvent systems, as described for the $HAuCl_4$-loaded templates, and the nanoparticle sizes and distributions obtained were independent (within error limits) of the solvent used for template loading.

The nanoparticles derived from $NaBH_4$ reduction are much smaller than for hydrazine reduction, but they are also better confined to discrete areas defined by the polymeric template. Inter-template migration was minimized under these conditions, as indicated by the fact that nearly all features contained measureable nanoparticles. This is in contrast to hydrazine reduction, for which empty (grey shaded) templates and some with varying numbers of nanoparticles were observed. The polymeric template still remained visible as a grey shaded area in TEM analysis after $NaBH_4$ reduction, as seen in Figure 6.40.

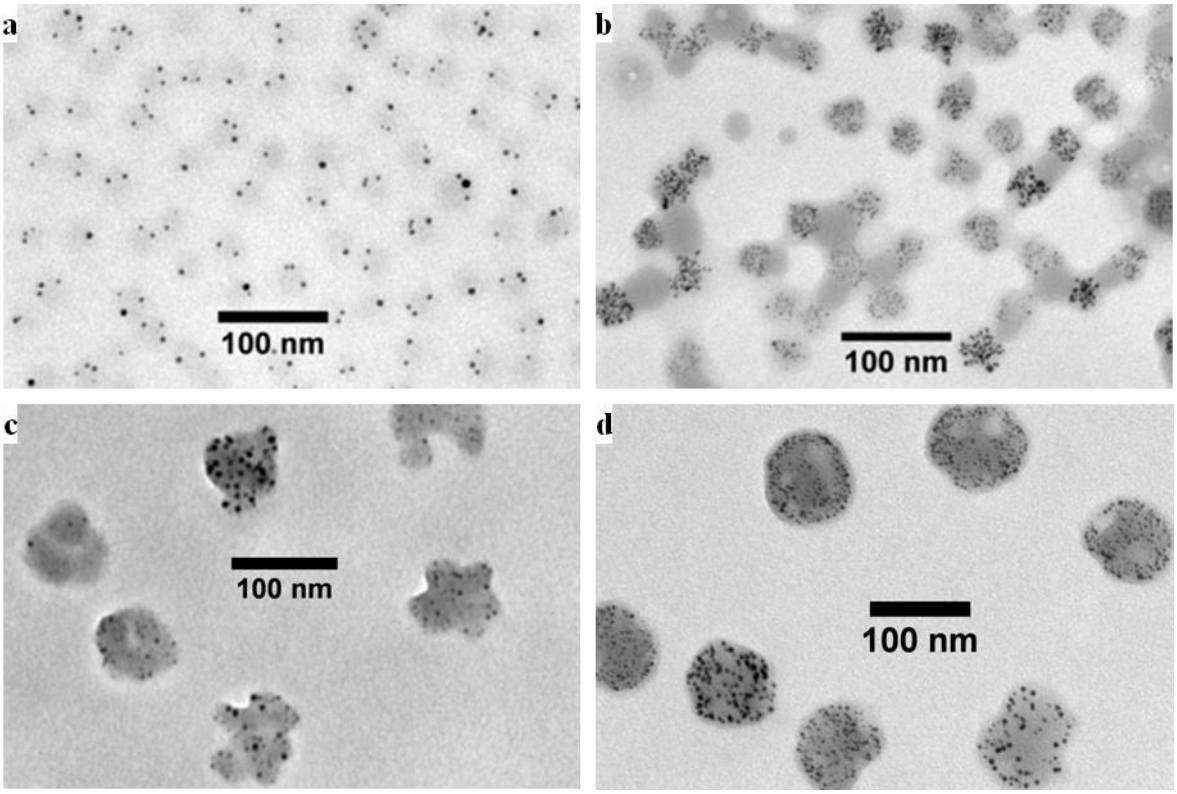

Figure 6.40 TEM images of gold nanoparticles formed by $NaBH_4$ reduction: (a) PS-*g*-(P2VP14-*b*-PS11), (b) G1PS-*g*-(P2VP25-*b*-PS20), (c) G2PS-*g*-(P2VP15-*b*-PS11), and (d) G3PS-*g*-(P2VP14-*b*-PS11).

While the reduced particles appear to maintain morphologies similar to the salt-loaded templates, as indicated by the shading pattern, nanoparticle organization within the templates does not appear to follow a unique pattern nor to encompass all the nanodomains within each template. Film reduction was also performed on the $HAuCl_4$-loaded templates for comparison, after loading in THF and cyclohexane (25:75, THF:CH) with 0.5 equiv of $HAuCl_4$, to monitor the mobility of the reduced gold and whether metal nanoparticle reorganization would take place under these conditions. TEM images for the film reduction experiments with $NaBH_4$ using the G2, G3, and G4 copolymers are shown in Figure 6.41.

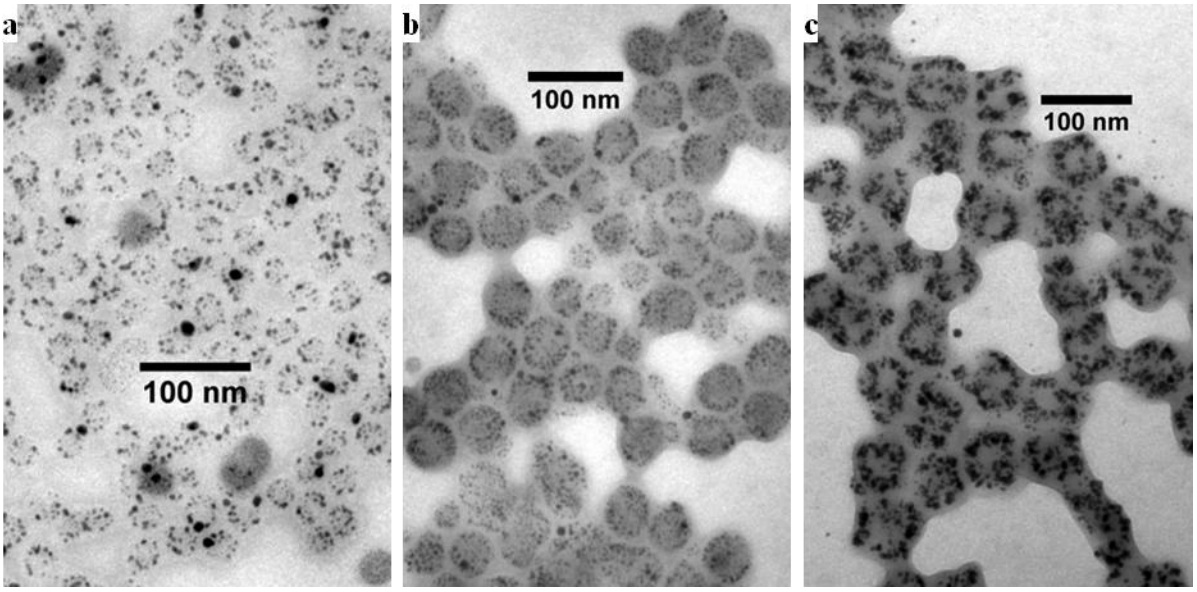

Figure 6.41 TEM images for $NaBH_4$ film reduction of $HAuCl_4$-loaded templates: (a) G1PS-*g*-(P2VP25-*b*-PS20), (b) G2PS-*g*-(P2VP15-*b*-PS11), and (c) G3PS-*g*-(P2VP14-*b*-PS11).

When compared to the non-reduced precursor, gold nanoparticle organization exists for the G2 template and noticeably more ring-like assemblies are observed than for the salt-loaded template. The gold nanoparticles within the G3 and G4 templates display organization similar to the salt, with an even distribution of particles for G3 and cylindrical patterns for G4. The corresponding salt-loaded templates can be found in Figure 6.22b, Figure 6.23b, and Figure 6.24b for G1PS-*g*-(P2VP25-*b*-PS20), G2PS-*g*-(P2VP15-*b*-PS11), and G3PS-*g*-(P2VP14-*b*-PS11), respectively. Even though the $NaBH_4$ solution can provide solvency for the ionized P2VP phase, the reduced nanoparticles within the film apparently have a low enough mobility to remain confined to the domains defined by the polymer phase.

6.4.5.3 Solid State Reduction

The reduction of $HAuCl_4$-loaded arborescent copolymer templates was also performed in the solid state as polymer films or in the powder form without solvent, as opposed to the reduction procedures previously discussed where the reducing agents were dispersed in solvents. The methods used to perform the solvent-free reductions involved hydrazine vapor,[67] UV light irradiation,[68,69] and hydrogen plasma etching,[70,71] all of which have been applied previously to intermolecular micelle systems. Particular attention focused on the same templates for which well-defined intramolecular phase segregation was observed, namely G1PS-*g*-(P2VP25-*b*-PS20), G2PS-*g*-(P2VP15-*b*-PS11), and G3PS-*g*-(P2VP14-*b*-PS11). The G0 copolymer was also investigated for comparison. Provided in Figure 6.42 are the gold nanoparticle size distributions resulting from the reduction of $HAuCl_4$-loaded G2PS-*g*-(P2VP15-*b*-PS11) films with hydrazine vapor and UV light.

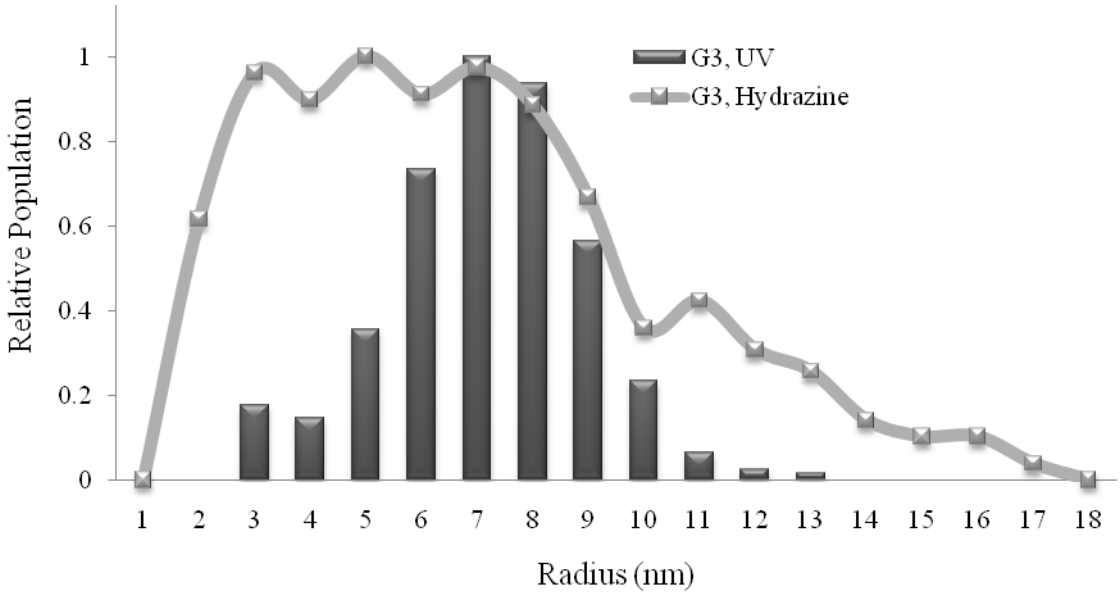

Figure 6.42 Size distribution of gold nanoparticles obtained by film reduction of G2PS-*g*-(P2VP15-*b*-PS11) with hydrazine vapor and UV light.

Similar trends were observed for the PS-*g*-(P2VP14-*b*-PS11), G1PS-*g*-(P2VP25-*b*-PS20), and G3PS-*g*-(P2VP14-*b*-PS11) templates: Hydrazine vapor reduction led to broad size distributions with a higher population of smaller radii species. TEM images for the nanoparticles resulting from the two solid state reduction methods corresponding to the distributions shown in Figure 6.42 are provided in Figure 6.43.

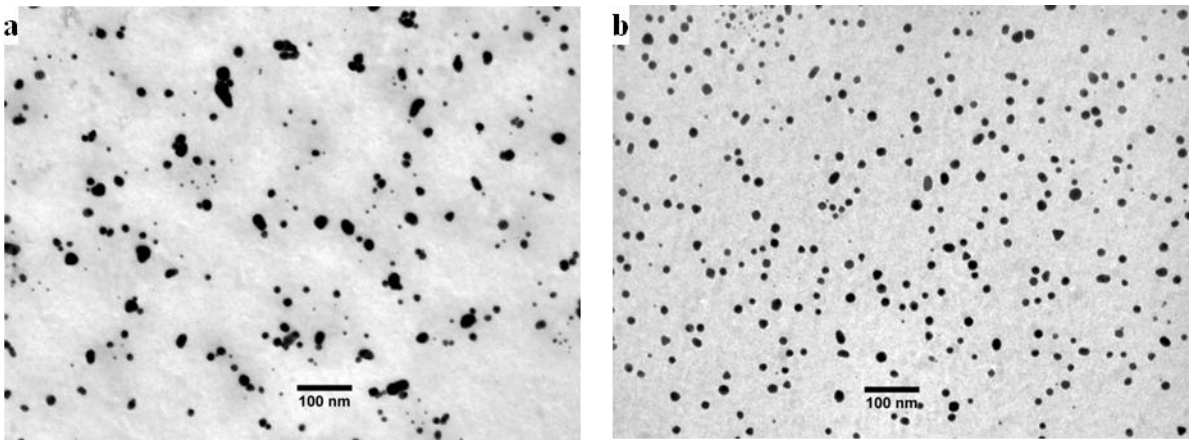

Figure 6.43 TEM images for gold nanoparticles obtained from (a) hydrazine vapor and (b) UV reduction of $HAuCl_4$-loaded G2PS-*g*-(P2VP15-*b*-PS11) film.

Additional TEM images for the PS-*g*-(P2VP14-*b*-PS11), G1PS-*g*-(P2VP25-*b*-PS20), and G3PS-*g*-(P2VP14-*b*-PS11) templates, depicting very similar nanoparticle size distributions, can be found in Appendix 6.2. The corresponding size distribution charts are provided in Appendix 6.3. Hydrazine vapor reduction of 0.5 equiv $HAuCl_4$-loaded G1PS-*g*-(P2VP25-*b*-PS20) was also performed on material in the powdered (freeze-dried) state and resulted in gold nanoparticles with a diameter of 14 ± 8 nm, nearly identical to the nanoparticles formed via vapor reduction of the film. UV-Vis absorption measurements

yielded a strong surface plasmon resonance with a maximum at 535 nm, identical with the 17 ± 8 nm nanoparticles obtained by solution reduction with 1.2 equiv of hydrazine.

Plasma reduction was also performed on the same gold-loaded copolymer films and the gold nanoparticles were viewed by scanning electron microscopy (SEM) as shown in Figure 6.44.

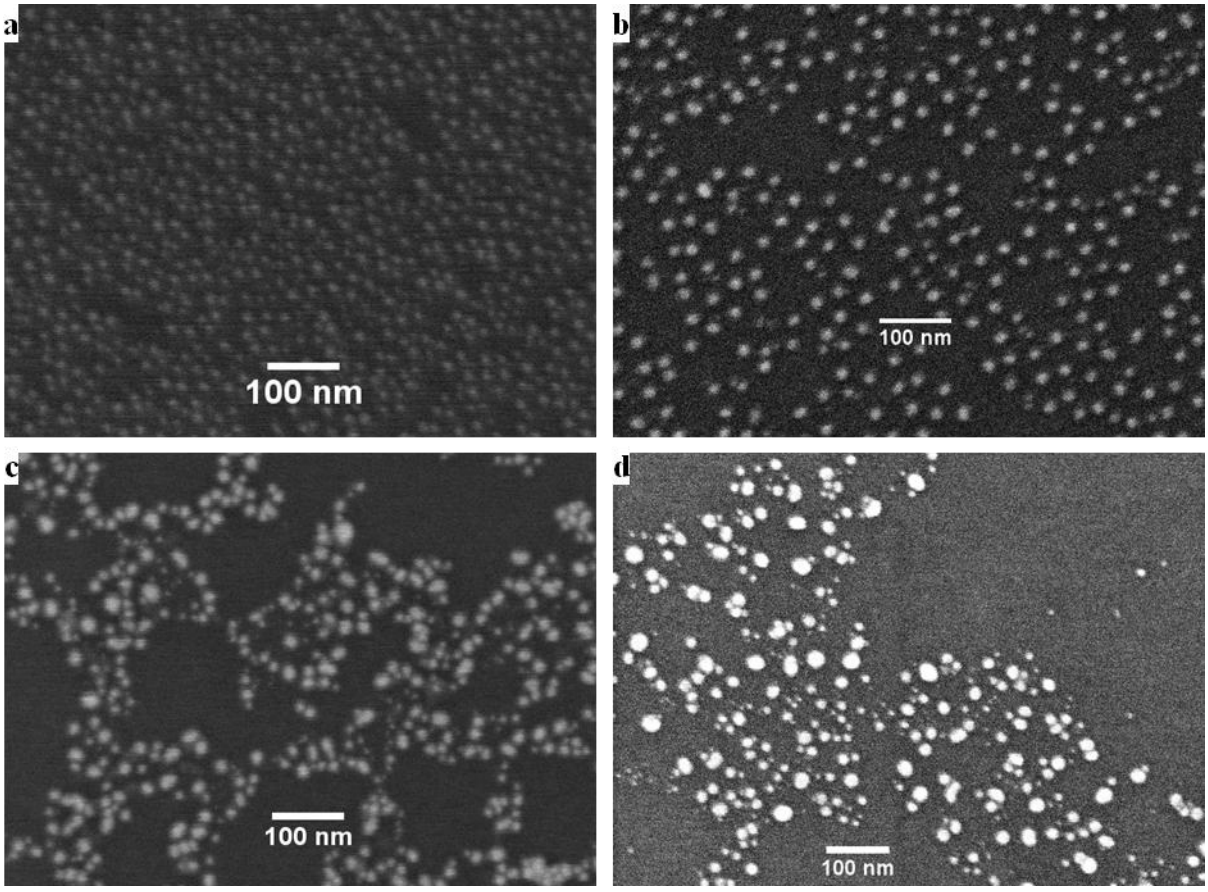

Figure 6.44 Gold nanoparticles formed by plasma reduction of copolymer films viewed by SEM: (a) PS-*g*-(P2VP14-*b*-PS11), (b) G1PS-*g*-(P2VP25-*b*-PS20), (c) G2PS-*g*-(P2VP15-*b*-PS11), and (d) G3PS-*g*-(P2VP14-*b*-PS11).

Within error limits, all three solid state reduction methods produced very similar nanoparticle sizes as seen in Table 6.11. However it is clear that hydrazine vapor produced much less defined nanoparticles with a high size polydispersity. As reported for the other solution reduction protocols, there is no correlation between the nanoparticle size and the template characteristics.

Table 6.11 Gold nanoparticle diameters by different solid state reduction methods

	Diameter (nm)		
Template	Hydrazine Vapor	UV	Plasma
PS-*g*-(P2VP14-*b*-PS11)	15 ± 7	16 ± 3	13 ± 1
G1PS-*g*-(P2VP25-*b*-PS20)	14 ± 10	13 ± 2	16 ± 2
G2PS-*g*-(P2VP15-*b*-PS11)	14 ± 7	14 ± 4	17 ± 5
G3PS-*g*-(P2VP14-*b*-PS11)	15 ± 9	18 ± 3	15 ± 3

The broadly dispersed gold nanoparticles obtained in hydrazine vapor reduction may be due to hindered diffusion of the reducing agent to the metal. To reach the metallic salt, hydrazine must diffuse through the PS corona of the template, thus inducing a non-homogeneous reduction process. A high local concentration also exists at the film surface. As the 2VP phase is swollen by hydrazine vapor, chain mobility increases and allows the aggregation of the small nanoparticles.

Hydrogen plasma can easily penetrate the polymer and react with the metal salt in a much more consistent and simultaneous manner, resulting in a more uniform size distribution. It has been shown that the plasma treatment can also degrade and remove all organic components (such as the polymeric scaffolds), thus providing nanoparticle mobility and a uniform particle size distribution.[70] In a similar fashion, UV irradiation can efficiently

reduce the metallic salt with little local concentration differentials due to uniform penetration of the beam. The proposed mechanism for $HAuCl_4$ reduction by UV light is shown in Scheme 6.3 as reported in Reference 68.

UV irradiation for 12 h under ambient conditions in air provides an adequate and consistent concentration of ozone, as evidenced by its distinct smell upon sample removal. The UV/ozone combination is known to remove organic components, including the polymeric templates.[72] While the films obtained under these conditions were not explicitly tested for residual polymer, the films looked very clean and devoid of any shaded areas indicative of polymer film remnants. This is clearly seen in the TEM images shown in Figure 6.43b and Appendix 6.2, where the background is very clear. Removal of the polymeric template enhances metallic particle mobility, allowing for the formation of uniform particles within a localized area.

$$AuX_4^- \xrightarrow{h\nu} [AuX_4^-]^*$$

$$AuX_4^{-*} \rightarrow \left[Au^{(2+)}X_3\right]^- + X$$

$$\left[Au^{(2+)}X_3\right]^- \xrightarrow{h\nu} \left[Au^{(+)}X_2\right]^- + X$$

$$\left[Au^{(+)}X_2\right]^- \xrightarrow{h\nu} Au^0 + X + X^-$$

$$nAu^0 \rightarrow Au_n$$

Scheme 6.3 Proposed mechanism for gold salt reduction by UV irradiation.

In further support of polymer scaffold removal, ellipsometry measurements performed on UV/ozone treated films displayed a drastic thickness reduction as compared to the salt-loaded copolymers. Provided in Table 6.12 are film thickness measurements

determined by ellipsometry for 0.5 equiv $HAuCl_4$-loaded copolymers before and after treatment with UV/ozone. The drastic reduction in film thickness following UV/ozone treatment can be attributed to removal of the copolymer scaffold, which amounts for the majority of material, leaving only the gold nanoparticles.

Table 6.12 Film thickness measurements by ellipsometry for $HAuCl_4$-loaded copolymers before and after UV/ozone treatment

	Thickness (nm)	
Sample[a]	$AuCl_4^-$	Au[b]
PS-*g*-(P2VP14-*b*-PS11)	25 ± 1	0.9 ± 0.5
G1PS-*g*-(P2VP11-*b*-PS11)	23 ± 1	1.3 ± 0.1
G1PS-*g*-(P2VP25-*b*-PS20)	23 ± 1	1.6 ± 0.1
G2PS-*g*-(P2VP15-*b*-PS11)	28 ± 1	1.1 ± 0.6
G3PS-*g*-(P2VP14-*b*-PS11)	31 ± 1	2.3 ± 0.1

[a] Copolymers loaded with 0.5 equiv $HAuCl_4$; [b] Thickness of residual film following UV/ozone treatment

6.5 Conclusions

Intramolecular phase segregation and intricate nanodomain formation was observed in the arborescent PS-*g*-(P2VP-*b*-PS) core-shell-corona amphipolar copolymers of generations 2 and above after coordination with various metallic salts and acids, most notably $HAuCl_4$. These unique morphologies were investigated with in-depth AFM and TEM analysis. The G0 and G1 copolymers, in contrast, exhibited spherical organization of the metals within the polymer template, much like intermolecular micelle systems. Intramolecular toroidal phase segregation was observed for the G2 template, G1PS-*g*-(P2VP-*b*-PS), with side-chain P2VP and PS molecular weights of 20,000 and 25,000 g/mol, respectively. These structures displayed ring-like organization of the metals induced by the architecture of the copolymer. Templates with shorter block copolymer side-chains did not exhibit significant phase segregation, but rather spherical morphologies resulted.

The G3 templates exhibited nodular phase segregation within each molecule, resembling a raspberry, upon coordination with $HAuCl_4$. Variations in the block copolymer ratio had limited influence on the nano-domain morphology, which remained nodular. The G4 template was characterized by cylinder-in-sphere intramolecular phase segregation, namely a spherically bound arrangement of polymer cylinders. Comparison of the G2PS and G3PS substrate characteristics used to synthesize the G3 and G4 copolymers, respectively, revealed that the intricate intramolecular self-assembly process is mainly core-mediated. The denser G3PS substrate, with reduced interpenetration of P2VP phase in the side-chains, provides enhanced phase segregation favoring the formation of the cylinder-in-sphere morphology. Template molecules derived from the G2PS analogue, having further interpenetration of the P2VP segments into the core, had a greater tendency to break up into

smaller nodular domains. The intramolecular nanodomains arising from phase segregation were somewhat sensitive to solvent variations; various phase transitions were observed. Most interestingly, a spherical nano-cage morphology was discovered for the G4 copolymer once loaded with $HAuCl_4$ in chloroform.

Solution reduction using anhydrous hydrazine or $NaBH_4$ revealed that the size and uniformity of the gold nanoparticles obtained was independent of the template generation, but rather reliant on the amount and the strength of the reducing agent used. Excess hydrazine (10:1 N_2H_4:Au) limited the aggregation and led to a more uniform size distribution for the gold nanoparticles as compared to a near equivalency reduction regime (1.2:1 N_2H_4:Au). Reduction with a stronger reducing agent (10:1 $NaBH_4$:Au) resulted in very small and relatively monodispersed gold nanoparticles. The nanoparticles clearly remained located within the polymer template boundaries in this case, and there was limited inter-template nanoparticle migration and agglomeration of the type observed for hydrazine reduction. Solid state reduction of gold-loaded polymer films was also performed. Hydrazine vapor treatment resulted in broadly dispersed nanoparticles, while UV and plasma treatment produced well-defined nanoparticles. Vapor reduction presumably induces localized mobility and large reducing agent concentration gradients across the template molecules, both of which disfavor the formation of narrowly dispersed species. UV and plasma treatment removes the polymer template and provides nanoparticle mobility allowing localized coalescence and the production of narrowly dispersed but larger nanoparticles.

6.6 Appendices

Appendix 6.1 Synthesis of anhydrous hydrazine and experimental apparatus

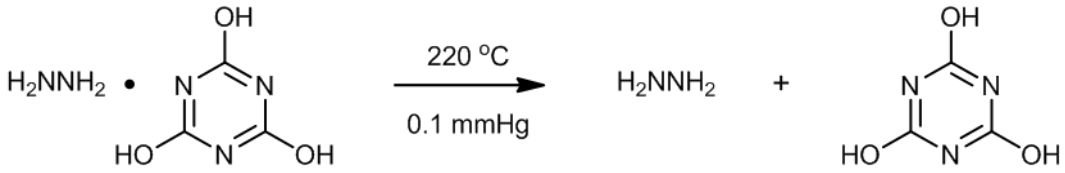

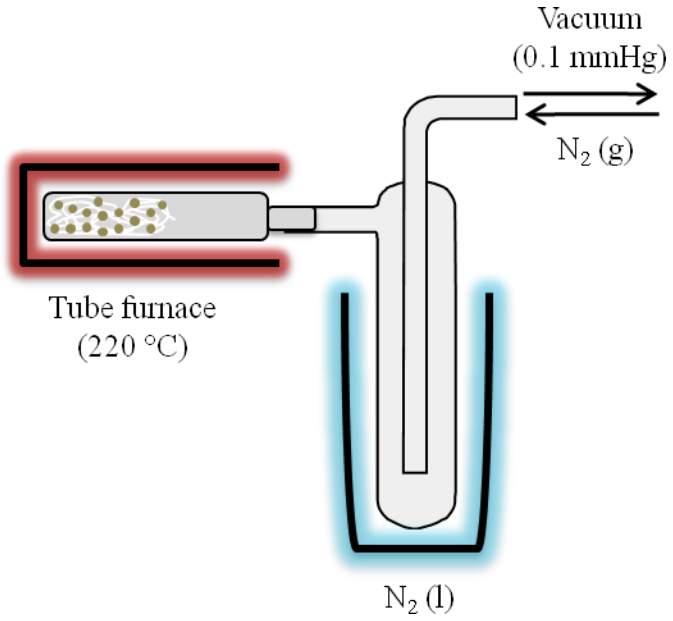

Appendix 6.2 TEM images for gold nanoparticles obtained by reduction with hydrazine vapor (left) and UV light (right) from various templates: (a) PS-*g*-(P2VP14-*b*-PS11), (b) G1PS-*g*-(P2VP25-*b*-PS20), and (c) G3PS-*g*-(P2VP14-*b*-PS11)

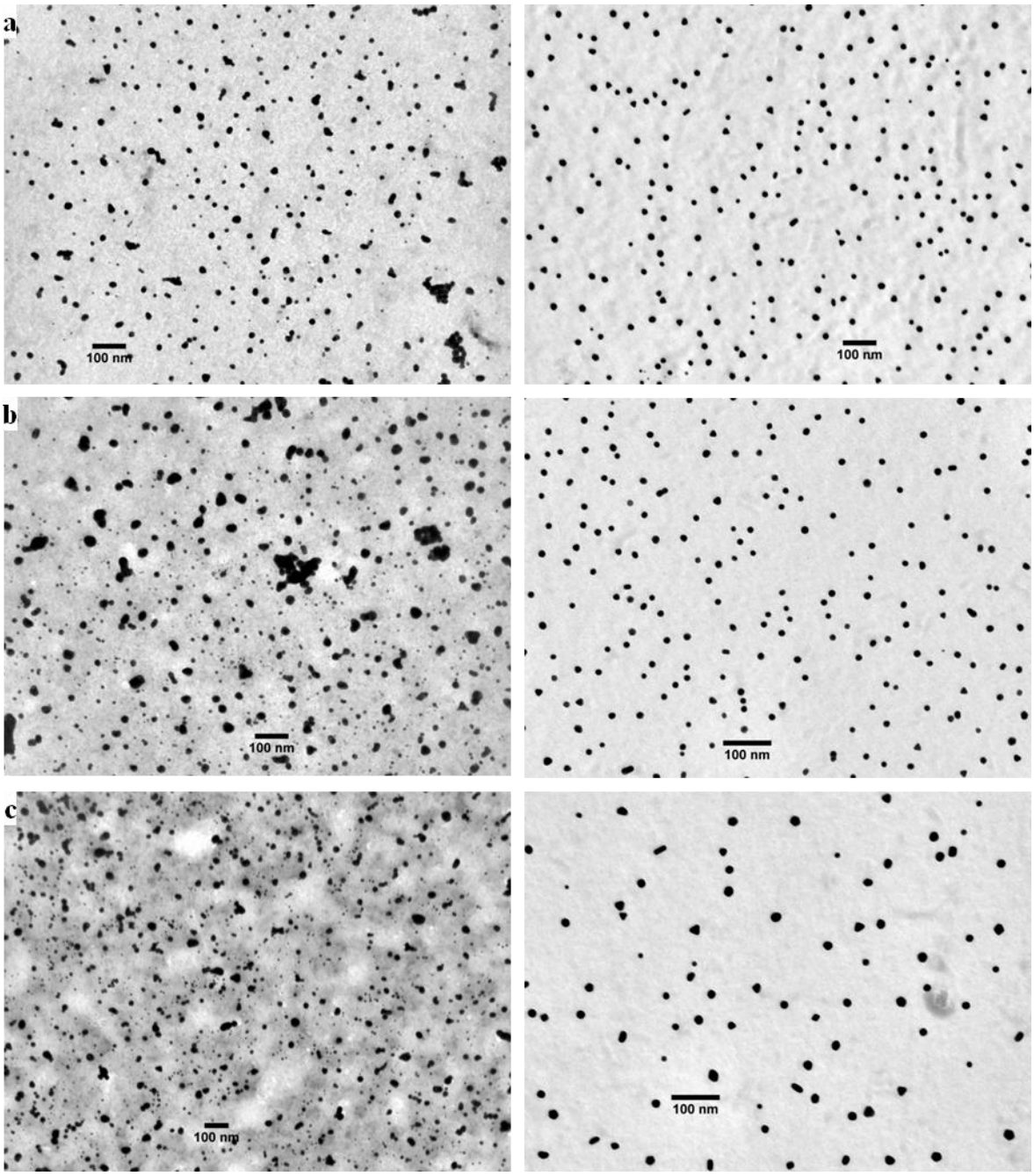

Appendix 6.3 Gold nanoparticle size distributions obtained by hydrazine vapor and UV light reduction of various arborescent copolymer films

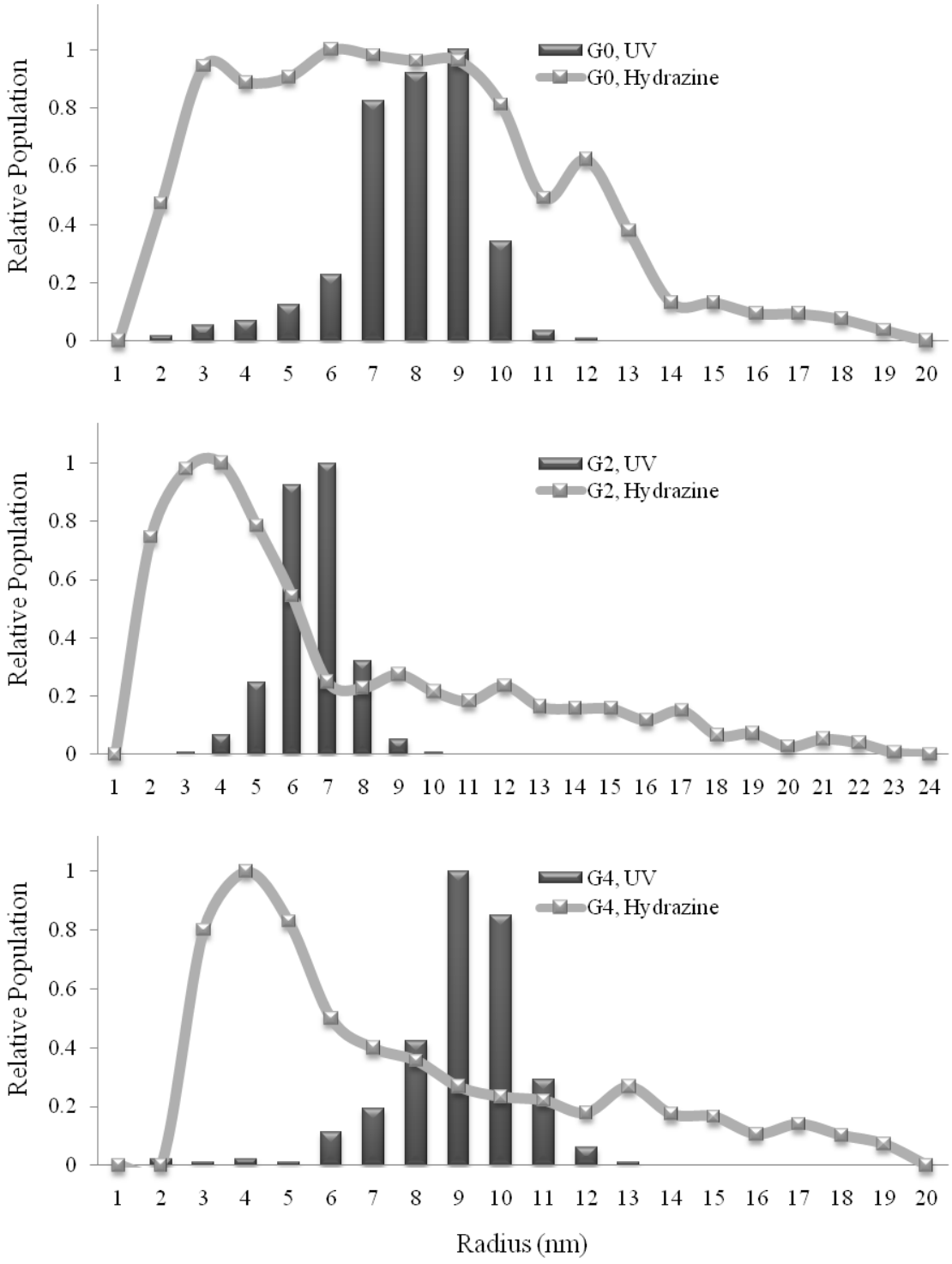

Chapter 7

Concluding Remarks

7.1 Arborescent Core-Shell Copolymers: PS-*g*-P2VP

7.1.1 Summary and Contributions to Knowledge

Arborescent copolymers with amphipolar properties were synthesized and examined for their polyelectrolyte properties and their application as scaffolds for the preparation of metallic nanoparticles. The synthesis of some of the copolymers was achieved previously,[1] by grafting poly(2-vinylpyridine), P2VP, side-chains onto linear and arborescent polystyrene (PS) substrates randomly functionalized with acetyl groups. The PS substrates (linear, and branched polymers of generations G0, G1, and G2) were grafted with P2VP side-chains having a molecular weight of either 5000 g/mol or 30,000 g/mol to afford unimolecular micelles with a hydrophobic PS core encased in a shell of P2VP chains. To provide aqueous solubility to the PS-*g*-P2VP arborescent copolymers with a core-shell (CS) morphology, the P2VP component was protonated with HCl. The extent of solubilization of the arborescent polyelectrolytes was investigated by dynamic light scattering using two dissolution protocols: direct dissolution in 0.1 N HCl, and dissolution in THF followed by dilution with HCl.

Arborescent copolymers of generations G1 and above existed as unimolecular species, while the G0 molecules (linear PS-*g*-P2VP) with M_n = 5000 g/mol or 30,000 g/mol side-chains displayed significant differences in hydrodynamic radii determined from first- and second-order analysis of the correlation function, which is indicative of intermolecular association. Further, large radius variations were observed within a series of measurements, especially for the PS-*g*-P2VP copolymers with M_n = 5000 g/mol side-chains. It was found that the radii distribution and reproducibility of the analysis were improved by dissolving the copolymers in THF prior to protonation. Size distributions were assessed by applying the

CONTIN algorithm to the correlation function, and the results were consistent with the hydrodynamic radii analysis results: Bimodal distributions (2 size populations) were observed for the G0 copolymer (PS-*g*-P2VP), while upper generation arborescent polyelectrolytes were characterized by one population with a narrow size distribution, particularly for dissolution in THF prior to ionization. The results of these solution property measurements have been published previously.[1]

The arborescent copolymer polyelectrolytes were also examined as scaffolds to construct metallic nanoparticles in aqueous environments, for comparison to other methods reported previously. The nitrogen atom within the pyridine moiety allows the complexation of polar compounds such as metallic salts and acids. In the case of $HAuCl_4$, the nitrogen atom is protonated and the metallic counterion completes the ion pair. The direct uptake of $HAuCl_4$ by the native polymer did not provide stable solutions, but pre-ionization of the copolymers by dilution of a THF solution with HCl allowed the successful loading of the polymer in aqueous solutions of $HAuCl_4$. The upper generation copolymers were able to effectively coordinate the metal without showing signs of aggregation or precipitation. Spherical organization of the metal within the templates, matching the polymer topology, was observed by TEM analysis.

Upon reduction of the metallic salt with hydrazine monohydrate or sodium borohydride ($NaBH_4$), the metal-polymer complexes became unstable in solution and precipitation was observed. Microscopic analysis still confirmed that $NaBH_4$ produced smaller nanoparticles than hydrazine reduction, as previously reported in the literature, due to the increased reducing power of $NaBH_4$ as compared to hydrazine.

Palladium, in the form of $Pd(OAc)_2$, was likewise investigated as a metallic compound, as it can complex with the lone pair electrons of the nitrogen atom within the pyridine moiety but does not protonate it as does $HAuCl_4$. This system was investigated in THF and was characterized by colloidal precipitate formation upon complexation. TEM analysis revealed that distinct spherical species were present within long chain-like assemblies resembling a pearl necklace.

In summary, the work with the amphipolar CS arborescent copolymers demonstrated that PS-*g*-P2VP copolymers can exist as unimolecular species in aqueous solutions, and can house metallic salts and acids while maintaining some degree of solubility.

7.1.2 Suggestions for Future Work

The colloidal stability of the metal-loaded species could be further investigated with dynamic light scattering techniques, to provide a more accurate picture of the degree of aggregation of the metal-loaded templates. These copolymers are also interesting in terms of their ability to host and release hydrophobic compounds. Indeed, some work has been performed on the *in vitro* loading and release of hydrophobic drugs from these molecules.[2] In such drug delivery applications, the ability to label the polymeric container with a species having a high electron density provides an intramolecular tracking device which can be monitored by various techniques. Embedding metallic species in the PS-*g*-P2VP copolymers may also alter the loading and release kinetics of hydrophobic compounds, so extending the previous research to include the *in vitro* loading and release of metal-coordinated PS-*g*-P2VP materials would be advisable.

The work on metallic loading of PS-*g*-P2VP arborescent copolymers focused mainly on loading at one coordination level (4:1 ratio of 2VP:Au), but it would be advantageous to investigate lower loading levels in more details. As reported in Chapter 4, extensive precipitation was observed upon reduction of the metallic salt within the copolymer scaffold. If these systems are to be investigated further as model devices for drug delivery with tracking ability, the drug-loaded polymer-metal complex must remain soluble in aqueous environments. To achieve this goal, lower metal loading levels should be examined. As mentioned in Chapter 6, loading levels as low as 0.05 equiv $HAuCl_4$ relatively to 2VP units still provide adequate contrast for microscopic visualization.

7.2 Arborescent Core-Shell-Corona Copolymers: PS-*g*-(P2VP-*b*-PS)

7.2.1 Summary and Contributions to Knowledge

Arborescent copolymers with a layered core-shell-corona (CSC) architecture have also been synthesized and used as templates for the construction of metallic nanoparticles. The copolymers, amphipolar in nature, were synthesized by grafting block copolymers of PS and P2VP, obtained by anionic polymerization, onto linear or arborescent PS substrates. Using a sequential monomer addition procedure in the block copolymer synthesis, the 2VP monomer being added second, the living end is located at the P2VP end of the side-chain. Grafting of these living side-chains onto acetyl- or chloromethyl-functionalized PS substrates affords the desired PS-*g*-(P2VP-*b*-PS) arborescent copolymers. These copolymers have a core of PS, a shell of P2VP, and a corona of PS chains. The arborescent CSC copolymers synthesized spanned generations from G0 to G4, including a series of G2 and G3 copolymers where the PS-*b*-P2VP molecular weights and the ratio of block lengths were systematically varied.

Analogous grafting reactions have been reported for the preparation of various arborescent homo- and copolymers,[3–5] but these reactions involved the grafting of homopolymer side-chains in all cases. In the current investigation, we grafted copolymer (PS-*b*-P2VP) side-chains onto the PS substrates. It was quickly realized that this grafting process did not proceed as efficiently as for homopolymer side-chains (e.g. PS-*g*-PS or PS-*g*-P2VP). Using light scattering analysis, it was shown that the PS-*b*-P2VP side-chains formed aggregates under the conditions used for the synthesis. This produced large species having living ends buried or hindered, and therefore unable to react with the coupling sites on the substrate. As a result, low grafting yields and coupling efficiencies were obtained.

Further, the low grafting yield and the amphipolar nature of the CSC copolymers and the side-chains made it difficult to isolate the graft material from the linear side-chain contaminant in the crude reaction product. A cloud-point centrifugation procedure was developed whereby the crude product was dissolved in a non-selective solvent (THF) and brought to a colloidal precipitate state by the addition of a solvent selective for P2VP (methanol). After the onset of an opalescent appearance, the solutions were centrifugated to collect the grafting product. Pure graft copolymers, free of PS-*b*-P2VP side-chains, were isolated after several purification cycles, some samples requiring a final purification step by preparative size exclusion chromatography.

Loading of the arborescent CSC copolymers with $HAuCl_4$ was successfully performed by a procedure similar to that previously reported for intermolecular micelle systems of PS-*b*-P2VP, namely polymer dissolution and the addition of the metallic acid. The results obtained were very different for some of the arborescent scaffolds as compared to other polymeric nanoparticle templates, however. Generation (G) 0, PS-*g*-(P2VP14-*b*-PS11), and G1, G0PS-*g*-(P2VP8-*b*-PS8), templates had similar templating characteristics to intermolecular micelles, yielding a spherical topology and metal organization. There appeared to be no influence of the hydrophobic PS core (unable to coordinate metals and ill-defined due to its flexibility) in these systems. Templates of generations 2 and above displayed significant transitions from the spherical topology, also characterizing the native templates, after coordination with $HAuCl_4$ in toluene. Intramolecular phase segregation was observed, producing unique and intricate polymer self-assembly within the boundaries of each individual copolymer molecule. Sample G1PS-*g*-(P2VP25-*b*-PS20) formed cylinders with circular orientation resembling toroids, although not all molecules formed complete

toroidal structures. The metal was concentrated within the cylindrical phase, as demonstrated by ring-like organization of the metal in TEM analysis. The G2PS-*g*-(P2VP15-*b*-PS11) template was characterized by a multicompartment morphology: Intramolecular phase segregation produced nodular domains resembling a raspberry, with metal distributed amongst the multiple spherical nanodomains within the template volume. Lastly, sample G3PS-*g*-(P2VP14-*b*-PS11) produced cylindrical phase segregation within each copolymer template. The arrangement of the coiled cylinders resembled a nano-brain or intestine and is referred to as a cylinder-in-sphere morphology. The morphologies of the intramolecular phase-segregated templates were relatively stable to changes in solvent quality although drastic changes in solvent selectivity, namely with addition of methanol or cyclohexane, resulted in some morphological transitions. In $CHCl_3$ as a non-selective solvent, a unique spherical nano-cage structure was observed for the G4 copolymer upon metal coordination. Illustrations of the various morphologies formed by intramolecular phase segregation of the arborescent copolymers upon metal loading are shown in Figure 7.1. The illustrations depicting the cylinder-in-sphere and spherical nano-cage morphologies in Figures 7.1c and 7.1d, respectively, were adapted from Reference 6.

The observed morphologies and gold organization appear to be mediated primarily by the characteristics of the PS cores. The G0 and G1 templates have small, flexible PS cores leading to a spherical morphology, as mentioned previously. The G2 template displayed intramolecular phase segregation for the copolymer with significantly long P2VP segments, G1PS-*g*-(P2VP25-*b*-PS20), while the other copolymers in the G2 series displayed spherical structures for the most part. The molecular weight of the P2VP segments must apparently exceed a critical size to display significant phase segregation. The G2PS and G3PS cores had

identical dimensions but vastly different molecular weights. Side-chain grafting onto the denser G3PS core is expected to result in a more distinct core-shell phase boundary with less interpenetration of PS from the core and the P2VP segments in the side-chains. The consequence of this is a better defined and more continuous phase-separated morphology leading to the formation of the intramolecular cylindrical structures observed. The PS chains of the G2PS core, on the other hand, have a less defined core-shell morphology leading to the formation of multiple spherical or nodular domains.

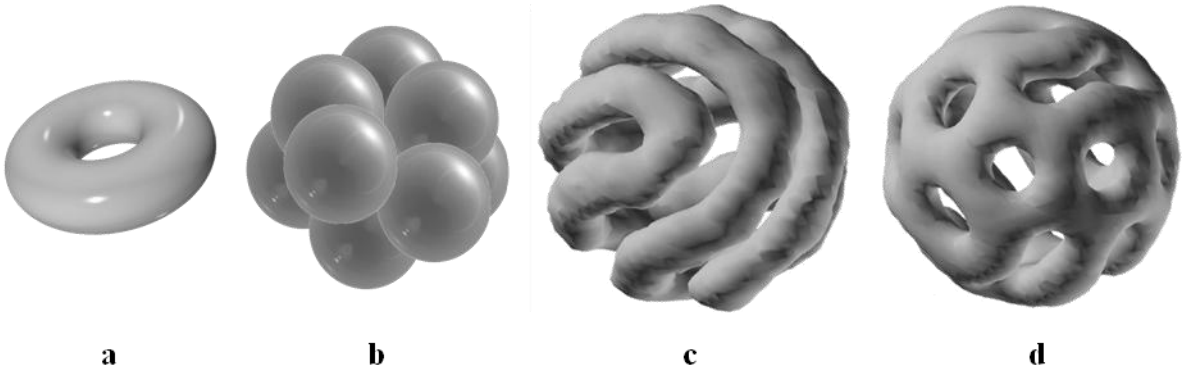

Figure 7.1 Graphical representations of phase segregated morphologies observed in various arborescent CSC copolymers upon metal loading in different solvents: (a) Toroid, G1PS-*g*-(P2VP25-*b*-PS20) in toluene; (b) raspberry, G2PS-*g*-(P2VP15-*b*-PS11) in toluene; (c) cylinder-in-sphere, G3PS-*g*-(P2VP14-*b*-PS11) in toluene; and (d) spherical nano-cage, G3PS-*g*-(P2VP14-*b*-PS11) in $CHCl_3$.

Upon reducing the metallic salt complexes in solution, it was realized that the polymeric scaffolds had little influence on the size and dispersity of the nanoparticles obtained: For a specific reducing agent, the radius and polydispersity of the particles were essentially identical within error limits for all the copolymers investigated. The nanoparticle

size rather depended on the strength and the amount of reducing agent used. When comparing hydrazine to the stronger reducing agent $NaBH_4$, much smaller gold nanoparticles were observed for $NaBH_4$, in agreement with previous reports.[7] Further, an excess of reducing agent produced smaller and more narrowly dispersed nanoparticles. The solid state reduction of $HAuCl_4$-loaded polymer films with UV irradiation in air or hydrogen plasma provided larger nanoparticles with a well-defined size distribution, which is attributed to increased nanoparticle mobility after the removal of the polymer template. The reduction of metal-loaded copolymers in the film state led to better retention of the phase-segregated morphology: the metals remained within the boundaries of the intramolecular domains.

In summary, the coordination of arborescent CSC copolymers with metallic salts and acids has highlighted the unique properties of these unimolecular micelles. Further, the resultant morphologies observed are very unusual. While some of these morphologies have been observed in intermolecular micelle systems, they have not achieved the extent of definition reported herein. Some of these results have been published in a preliminary report (Communication) and can be found in Reference 8.

7.2.2 Suggestions for Future Work

The intramolecular phase segregation phenomenon exhibited by amphipolar arborescent CSC copolymers of generations G2 and above represents an extremely intriguing topic deserving further investigation. The synthesis of a more comprehensive library of arborescent CSC copolymers would provide a better understanding of the phase segregation process and the influence of composition on the morphologies obtained. A specific composition of interest would be obtained by grafting PS-*b*-P2VP with significantly longer P2VP segments onto the

G2 PS substrate. Since nodular phase segregation is attributed to the PS interpenetration effect of the core, longer P2VP segments would also produce a more distinct P2VP phase and should therefore produce a morphology similar to G3PS-*g*-(P2VP14-*b*-PS11). Conversely, a G4 copolymer with shorter P2VP segments would be interesting to investigate in terms of morphological transitions.

Expanding the work on bimetallic loading should include elemental mapping to provide more details on the loading process, namely whether individual nano-compartments are loaded with each metal or are alloys formed within each domain. The G3 copolymers would be of particular interest for bimetallic loading investigations, as these copolymers are characterized by multiple intramolecular domains analogous to multicompartment intermolecular micelles.

While there was significant focus on morphology analysis of the metallic salt-loaded templates, AFM analysis after reduction was not attempted, but this would provide a great extension to the current work. Further, the influence of multiple loading cycles should be investigated by characterizing the polymer morphology and nanoparticle characteristics obtained at each step. Modeling phase segregation has been performed for a number of different systems, but the focus of these investigations has been on predicting morphologies in intermolecular micelle systems.[9] Developing a model to predict phase segregation in unimolecular systems such as the arborescent amphipolar copolymers would nicely complement the current work.

References

Chapter 1

1. Gauthier, M.; Li, J.; Dockendorff, J. *Macromolecules* **2003**, *36*, 2642–2648.
2. Dockendorff, J.; Gauthier, M.; Mourran, A.; Möller, M. *Macromolecules* **2008**, *41*, 6621–6623.
3. Spatz, J. P.; Sheiko, S.; Möller, M. *Macromolecules* **1996**, *29*, 3220–3226.

Chapter 2

1. Buhleier, E.; Wehner, W.; Vögtle, F. *Synthesis* **1978**, *2*, 155–158.
2. Tomalia, D. A.; Fréchet, J. M. J. *J. Polym. Sci. Part A: Polym. Chem.* **2002**, *40*, 2719–2728.
3. Maciejewski, M. *J. Macromol. Sci. A Chem.* **1982**, *17*, 689–703.
4. de Gennes, P. G.; Hervet, H. *J. Physique-Lett.* **1983**, *44*, 351–360.
5. Tomalia, D. A.; Baker, H.; Dewald, J.; Hall, M.; Kallos, G.; Martin, S.; Roeck, J.; Ryder, J.; Smith, P. *Polym. J.* **1985**, *17*, 117–132.
6. Newkome, G. R.; Yao, Z.-q.; Baker, G. R.; Gupta, V. K. *J. Org. Chem.* **1985**, *50*, 2003–2004.
7. Hawker, C. J.; Fréchet, J. M. J. *J. Am. Chem. Soc.* **1990**, *112*, 7638–7647.
8. Miller, T. M.; Neenan, T. X. *Chem. Mater.* **1990**, *2*, 346–349.
9. Gunatillake, P. A.; Odian, G.; Tomalia, D. A. *Macromolecules* **1988**, *21*, 1556–1562.
10. Kim, Y. H.; Webster, O. W. *J. Am. Chem. Soc.* **1990**, *112*, 4592–4593.
11. Hawker, C. J.; Lee, R.; Fréchet, J. M. J. *J. Am. Chem. Soc.* **1991**, *113*, 4583–4588.
12. Gauthier, M.; Möller, M. *Macromolecules* **1991**, *24*, 4548–4553.
13. Tomalia, D. A.; Hedstrand, D. M.; Ferritto, M. S. *Macromolecules* **1991**, *24*, 1435–1438.
14. Tomalia, D. A.; Fréchet, J. M. J. *Dendrimers and Other Dendritic Polymers*. Fréchet, J. M. J.; Tomalia, D. A. Eds.; Wiley: New York, 2001; p. 34.
15. Tomalia, D. A.; Hall, B. M.; Hedstrand, D. M. *Macromolecules* **1987**, *20*, 1164–1167.

16. Naylor, A. M.; Goddard III, W. A.; Kiefer, G. E.; Tomalia, D. A. *J. Am. Chem. Soc.* **1989**, *111*, 2339–2341.

17. Wörner, C.; Mülhaupt, R. *Angew. Chem. Int. Ed. Engl*. **1993**, *32*, 1306–1308.

18. De Brabander-van den Berg, E. M. M.; Meijer, E. W. *Angew. Chem. Int. Ed. Engl*. **1993**, *32*, 1308–1311.

19. Inoue, K. *Prog. Polym. Sci.* **2000**, *25*, 453–571.

20. Zhao, M.; Sun, L.; Crooks, R. M. *J. Am. Chem. Soc.* **1998**, *120*, 4877–4878.

21. Balogh, L.; Tomalia, D. A. *J. Am. Chem. Soc.* **1998**, *120*, 7355–7356.

22. Gröhn, F.; Bauer, B. J.; Akpalu, Y. A.; Jackson, C. L.; Amis, E. J. *Macromolecules* **2000**, *33*, 6042–6050.

23. Scott, R. W. J.; Ye, H.; Henriquez, R. R.; Crooks, R. M. *Chem. Mater.* **2003**, *15*, 3873–3878.

24. Gu, Y.; Xie, H.; Gao, J.; Liu, D.; Williams, C. T.; Murphy, C. J.; Ploehn, H. J. *Langmuir* **2005**, *21*, 3122–3131.

25. Peng, Z.; Zhang, J.; Sun, X.; Yang, J.; Diao, J. *Colloid Polym. Sci.* **2009**, *287*, 609–614.

26. Atwater, J. E.; Akse, J. R.; Holtsnider, J. T. *Materials Letters* **2008**, *62*, 3131–3134.

27. Scott, R. W. J.; Wilson, O. M.; Oh, S.-K.; Kenik, E. A.; Crooks, R. M. *J. Am. Chem. Soc.* **2004**, *125*, 15583–15591.

28. Gu, Y.; Wu, G.; Hu, X. F.; Chen, D. A.; Hansen, T.; zur Loye, H.-C.; Ploehn, H. J. *J. Power Sources* **2010**, *195*, 425–434.

29. Newkome, G. R.; He, E.; Moorefield, C. N. *Chem. Rev*. **1999**, *99*, 1689–1746.

30. Cuadrado, I.; Morán, M.; Casado, C. M.; Alonso, B.; Losada, J. *Coord. Chem. Rev.* **1999**, *193–195*, 395–445.

31. Berger, A.; Gebbink, R. J. M. K.; van Koten, G. *Top. Organomet. Chem.* **2006**, *20*, 1–38.

32. (a) King, A. S. H.; Twyman, L. J. *J. Chem. Soc., Perkin Trans.* **2002**, *1*, 2209–2218. (b) van Heerbeek, R.; Kamer, P. C. J.; van Leeuwen, P. W. N. M.; Reek, J. N. H. *Chem. Rev.* **2002**, *102*, 3717–3756. (c) Ribaudo, F.; van Leeuwen, P. W. N. M.; Reek, J. N. H. *Top. Organomet. Chem.* **2006**, *20*, 39–59.

33. Knapen, J. W. J.; van der Made, A. W.; de Wilde, J. C.; van Leeuwen, P. W. N. M.; Wijkens, P.; Grove, D. M.; van Koten, G. *Nature* **1994**, *372*, 659–663.

34. Reetz, M. T.; Lohmer, G.; Schwickardi, R. *Angew. Chem. Int. Ed. Engl*. **1997**, *36*, 1526–1529.

35. Bourque, S. C.; Maltais, F.; Xiao, W.-J.; Tardif, O.; Alper, H.; Arya, P.; Manzer, L. E. *J. Am. Chem. Soc.* **1999**, *121*, 3035–3038.

36. Oosterom, G. E.; van Haaren, R. J.; Reek, J. N. H.; Kamer, P. C. J.; van Leeuwen, P. W. N. M. *Chem. Commun.* **1999**, *12*, 1119–1120.

37. Albrecht, M.; Hovestad, N. J.; Boersma, J.; van Koten, G. *Chem. Eur. J.* **2001**, *7*, 1289–1294.

38. Fischer, M.; Vögtle, F. *Angew. Chem. Int. Ed.* **1999**, *38*, 884–905.

39. Navarro, G.; de ILarduya, C. T. *Nanomedicine: Nanotechnology, Biology, and Medicine* **2009**, *5*, 287–297.

40. Bielinska, A.; Kukowska-Latallo, J. F.; Johnson, J.; Tomalia, D. A.; Baker Jr., J. R. *Nucleic Acids Research* **1996**, *24*, 2176–2182.

41. Jansen, J. F. G. A.; Meijer, E. W. *J. Am. Chem. Soc.* **1995**, *117*, 4417–4418.

42. (a) Malik, N.; Evagorou, E. G.; Duncan, R. *Anticancer Drugs* **1999**, *10*, 767–776 (b) Howell, B. A.; Fan, D. *Proc. R. Soc. A* **2010,** *466*, 1515–1526.

43. Cheng, Y.; Li, M.; Xu, T. *Eur. J. of Med. Chem.* **2008**, *43*, 1791–1795.

44. Shaunak, S.; Thomas, S.; Gianasi, E.; Godwin, A.; Jones, E.; Teo, I.; Mireskandari, K.; Luthert, P.; Duncan, R.; Patterson, S.; Khaw, P.; Brocchini, S. *Nature Nanobiotechnology* **2004**, *22*, 977–984.

45. (a) Devadoss, C.; Bharathi, P.; Moore, J. S. *J. Am. Chem. Soc.* **1996**, *118*, 9635–9644. (b) Adronov, A.; Fréchet, J. M. J. *Chem. Commun*. **2000**, *18*, 1701–1710. (c) Nantalaksakul, A.; Reddy, D. R.; Bardeen, C. J.; Thayumanavan, S. *Photosynthesis Research* **2006**, *87*, 133–150. (d) Lo, S.-C.; Burn, P. L. *Chem. Rev.* **2007**, *107*, 1097–1116.

46. Flory, P. J. *J. Am. Chem. Soc.* **1952**, *74*, 2718–2723.

47. Yan, D.; Müller, A. H. E.; Matyjaszewski, K. *Macromolecules* **1997**, *30*, 7024–7033.

48. Hölter, D.; Burgath, A.; Frey, H. *Acta Polym.* **1997**, *48*, 30–35.

49. Erlander, S.; French, D. *J. Polym. Sci. Part A: Polym. Chem.* **1956**, *20*, 7–28.

50. Burchard, W. *Macromolecules* **1972**, *5*, 604–610.

51. Hanselmann, R.; Hölter, D.; Frey, H. *Macromolecules* **1998**, *31*, 3790–3801.

52. Bharathi, P.; Moore, J. S. *Macromolecules* **2000**, *33*, 3212–3218.

53. Gong, C.; Miravet, J.; Fréchet, J. M. J. *J. Polym. Sci. Part A: Polym. Chem.* **1999**, *37*, 3193–3201.

54. Schallausky, F.; Erber, M.; Komber, H.; Lederer, A. *Macromol. Chem. Phys.* **2008**, *209*, 2331–2338.

55. Radke, W.; Litvinenko, G.; Müller, A. H. E. *Macromolecules* **1998**, *31*, 239–248.

56. Yan, D.; Zhou, Z.; Müller, A. H. E. *Macromolecules* **1999**, *32*, 245–250.

57. Gao, C.; Yan, D. *Prog. Polym. Sci.* **2004**, *29*, 183–275.

58. Miller, T. M.; Neenan, T. X.; Kwock, E. W.; Stein, S. M. *J. Am. Chem. Soc.* **1993**, *115*, 356–357.

59. Wooley, K. L.; Hawker, C. J.; Lee, R.; Fréchet, J. M. J. *Polym. J.* **1994**, *26*, 187–197.

60. Spindler, R.; Fréchet, J. M. J. *Macromolecules* **1993**, *26*, 4809–4813.

61. Mathias, L. J.; Carothers, T. W. *J. Am. Chem. Soc.* **1991**, *113*, 4043–4044.

62. Bolton, D. H.; Wooley, K. L. *Macromolecules* **1997**, *30*, 1890–1896.

63. Yoon, K.; Son, D. Y. *Macromolecules* **1999**, *32*, 5210–5216.

64. Miravet, J. F.; Fréchet, J. M. J. *Macromolecules* **1998**, *31*, 3461–3468.

65. Hawker, C. J.; Fréchet, J. M. J.; Grubbs, R. B.; Dao, J. *J. Am. Chem. Soc.* **1995**, *117*, 10763–10764.

66. Fréchet, J. M. J.; Henmi, M.; Gitsov, I.; Aoshima, S.; Leduc, M. R.; Grubbs, R. B. *Science* **1995**, *269*, 1080–1083.

67. (a) Paulo, C.; Puskas, J. E. *Macromolecules* **2001**, *34*, 734–739. (b) Puskas, J. E.; Dos Santos, L. M.; Kaszas, G.; Kulbaba, K. *J. Polym. Sci. Part A: Polym. Chem.* **2009**, *47*, 1148–1158.

68. Foreman, E.; Puskas, J. E.; Kaszas, G. *J. Polym. Sci. Part A: Polym. Chem.* **2007**, *45*, 5847–5856.

69. Liu, M. L.; Vladimirov, N.; Fréchet, J. M. J. *Macromolecules* **1999**, *32*, 6881–6884.

70. Sunder, A.; Hanselmann, R.; Frey, H.; Mülhaupt, R. *Macromolecules* **1999**, *32*, 4240–4246.

71. Magnusson, H.; Malmström, E.; Hult, A. *Macromol. Rapid Commun.* **1999**, *20*, 453–457.

72. Suzuki, M.; Li, A.; Saegusa, T. *Macromolecules* **1992**, *25*, 7071–7072.

73. Jikei, M.; Chon, S.-H.; Kakimoto, M.-a.; Kawauchi, S.; Imase, T.; Watanebe, J. *Macromolecules* **1999**, *32*, 2061–2064.

74. Emrick, T.; Chang, H.-T.; Fréchet, J. M. J. *Macromolecules* **1999**, *32*, 6380–6382.

75. Tanaka, S.; Takeuchi, K.; Asai, M.; Iso, T.; Ueda, M. *Synthetic Metals* **2001**, *119*, 139–140.

76. Mendez, J. D.; Schroeter, M.; Weder, C. *Macromol. Chem. Phys.* **2007**, *208*, 1625–1636.

77. Pérignon, N.; Mingotaud, A.-F.; Marty, J.-D.; Rico-Lattes, I.; Mingotaud, C. *Chem. Mater.* **2004**, *16*, 4856–4858.

78. Salazar, R.; Fomina, L.; Fomine, S. *Polymer Bulletin* **2001**, *47*, 151–158.

79. Slagt, M. Q.; Stiriba, S.-E.; Gebbink, R. J. M. K.; Kautz, H.; Frey, H.; Van Koten, G. *Macromolecules* **2002**, *35*, 5734–5737.

80. Slagt, M. Q.; Stiriba, S.-E.; Kautz, H.; Gebbink, R. J. M. K.; Frey, H.; Van Koten, G. *Organometallics* **2004**, *23*, 1525–1532.

81. Krämer, M.; Pérignon, N.; Haag, R.; Marty, J.-D.; Thomann, R.; Viguerie, N. L-d.; Mingotaud, C. *Macromolecules* **2005**, *38*, 8308–8315.

82. Yang, J.; Lin, H.; He, Q.; Ling, L.; Zhu, C.; Bai, F. *Langmuir* **2001**, *17*, 5978–5983.

83. Lee, J.-C.; Lee, W.; Han, S.-H.; Kim, T. G.; Sung, Y.-M. *Electrochem. Commun.* **2009**, *11*, 231–324.

84. Häußler, M.; Lam, J. W. Y.; Zheng, R.; Dong, H.; Tong, H.; Tang, B. Z. *J. Inorg. Organomet. Polym. Mater.* **2005**, *15*, 519–526.

85. Onitsuka, K.; Ohshiro, N.; Fujimoto, M.; Takei, F.; Takahashi, S. *Mol. Cryst. Liq. Cryst.* **2000**, *342*, 159–166.

86. Hagihara, N.; Sonogashira, K.; Takahashi, S. *Adv. Polym. Sci.* **1981**, *41*, 149–179.

87. Takahashi, S.; Onitsuka, K.; Takei, F. *Macromol. Symp.* **2000**, *156*, 69–77.

88. Frey, H.; Haag, R. *Rev. Mol. Biotechnol.* **2002**, *90*, 257–267.

89. Cosulich, M. E.; Russo, S.; Pasquale, S.; Mariani, A. *Polymer* **2000**, *41*, 4951–4956.

90. Boulares-Pender, A.; Prager-Duschke, A.; Elsner, C.; Buchmeiser, M. R. *J. Appl. Polym. Sci.* **2009**, *112*, 2701–2709.

91. Muthukrishnan, S.; Nitschke, M.; Gramm, S.; Özyürek, Z.; Voit, B.; Werner, C.; Müller, A. H. E. *Macromol. Biosci.* **2006**, *6*, 658–666.

92. Puskas, J. E.; Dos Santos, L. M.; Fischer, F.; Götz, C.; El Fray, M.; Altstädt, V.; Tomkins, M. *Polymer* **2009**, *50*, 591–597.

93. Puskas, J. E.; Chen, Y.; Dahman, Y.; Padavan, D. *J. Polym. Sci. Part A: Polym. Chem.* **2004**, *42*, 3091–3109.

94. (a) Puskas, J. E.; Chen, Y.; Antony, P.; Kwon, Y.; Kovar, M.; Harbottle, R. R; de Jong, K.; Norton, P. R.; Cadieux, P.; Burton, J.; Reid, G.; Beiko, D.; Watterson, J. D.; Denstedt, J. *Polym. Adv. Technol*. **2003**, *14*, 763–770. (b) Foreman, E.; Puskas, J. E.; El Fray, M.; Prowans, P.; Piątek, M. *Polymer Preprints* **2008**, *49*, 822–823.

95. Cadieux, P.; Watterson, J. D.; Denstedt, J.; Harbottle, R. R.; Puskas, J.; Howard, J.; Gan, B. S.; Reid, G. *Colloid Surf. B: Biointerf.* **2003**, *28*, 95–105.

96. Freeman, A. W.; Fréchet, J. M. J. *Dendrimers and Other Dendritic Polymers*. Fréchet, J. M. J.; Tomalia, D. A. Eds.; Wiley: New York, 2001; p. 209–236.

97. Li, J.; Gauthier, M. *Macromolecules* **2001**, *34*, 8918–8924.

98. Kee, R. A.; Gauthier, M. *Macromolecules* **2002**, *35*, 6526–6532.

99. Gauthier, M.; Li, J.; Dockendorff, J. *Macromolecules* **2003**, *36*, 2642–2648.

100. Kee, R. A.; Gauthier, M. *Macromolecules* **1999**, *32*, 6478–6484.

101. Kee, R. A.; Gauthier, M. *J. Polym. Sci. Part A: Polym. Chem.* **2008**, *46*, 2335–2346.

102. Dockendorff, J.; Gauthier, M.; Mourran, A.; Möller, M. *Macromolecules* **2008**, *41*, 6621–6623.

103. Zhang, L.; Eisenberg, A. *J. Am. Chem. Soc.* **1996**, *118*, 3168–3181.

104. Gauthier, M.; Möller, M.; Burchard, W. *Macromol. Symp.* **1994**, *77*, 43–49.

105. Yun, S. I.; Lai, K.-C.; Briber, R. M.; Teertstra, S. J.; Gauthier, M.; Bauer, B. J. *Macromolecules* **2008**, *41*, 175–183.

106. Yin, R.; Swanson, D. R.; Tomalia, D. A. *Polym. Mater. Sci. Eng.* **1995**, *73*, 277–278.

107. Six, J.-L.; Gnanou, Y. *Macromol. Symp.* **1995**, *95*, 137–150.

108. Hirao, A.; Sugiyama, K.; Tsunoda, Y.; Matsuo, A.; Watanabe, T. *J. Polym. Sci. Part A: Polym. Chem.* **2006**, *44*, 6659–6687.

109. Trollsås, M.; Hedrick, J. L. *J. Am. Chem. Soc.* **1998**, *120*, 4644–4651.

110. Walach, W.; Kowalczuk, A.; Trzebicka, B.; Dworak, A. *Macromol. Rapid Commun.* **2001**, *22*, 1272–1277.

111. Klok, H.-A.; Rodriguez-Hernandez, J. *Macromolecules* **2002**, *35*, 8718–8723.

112. Grubbs, R. B.; Hawker, C. J.; Dao, J.; Fréchet, J. M. J. *Angew. Chem. Int. Ed. Engl.* **1997**, *36*, 270–272.

113. Cheng, G.; Böker, A.; Zhang, M.; Krausch, G.; Müller, A. H. E. *Macromolecules* **2001**, *34*, 6883–6888.

114. Yuan, Z.; Gauthier, M. *Macromolecules* **2006**, *39*, 2063–2071.

115. Yuan, Z.; Gauthier, M. *Macromol. Chem. Phys.* **2007**, *208*, 1615–1624.

116. Gauthier, M.; Tichagwa, L.; Downey, J. S.; Gao, S. *Macromolecules* **1996**, *29*, 519–527.

117. Knauss, D. M.; Al-Muallem, H. A.; Huang, T.; Wu, D. T. *Macromolecules* **2000**, *33*, 3557–3568.

118. Knauss, D. M.; Al-Muallem, H. A. *J. Polym. Sci. Part A: Polym. Chem.* **2000**, *38*, 4289–4298.

119. Knauss, D. M.; Huang, T. *Macromolecules* **2002**, *35*, 2055–2062.

120. Njikang, G. N.; Gauthier, M.; Li, J. *Polymer* **2008**, *49*, 5474–5481.

121. Gauthier, M.; Lin, W.-Y.; Teertstra, S. J.; Tzoganakis, C. *Polymer* **2010**, *51*, 3123–3129.

122. Li, J.; Gauthier, M. *Macromolecules* **2001**, *34*, 8918–8924.

123. Puskas, J. E.; Kaszas, G. *Prog. Polym. Sci.* **2000**, *25*, 403–452.

124. Note: Patent search results from an ‘advanced search’ performed at http://patft.uspto.gov/ on July 13, 2010. Query included appropriate Issue Date and keyword search of “dendrimer or arborescent or dendrigraft or hyperbranched”

within the abstract. An example of a query string was as follows: ISD/1/1/2000->7/13/2010 and ABST/(dendrimer or arborescent or dendrigraft or hyperbranched)

Chapter 3

1. Botha, S. S.; Brijoux, W.; Brinkmann, R.; Feyer, M.; Hofstadt, H.-W.; Kelashvili, G.; Kinge, S.; Matoussevitch, N.; Nagabhushana, K. S.; Wen, F. *Appl. Organometal. Chem.* **2004**, *18*, 566–572.
2. Klingelhöfer, S.; Heitz, W.; Greiner, A.; Oestreich, S.; Förster, S.; Antonietti, M. *J. Am. Chem. Soc.* **1997**, *119*, 10116–10120.
3. Spatz, J. P.; Mössmer, S.; Hartmann, C.; Möller, M.; Herzog, T.; Krieger, S.; Boyen, H.-G.; Ziemann, P.; Kabius, B. *Langmuir* **2000**, *16*, 407–415.
4. Grubbs, R. B. *Polym. Rev.* **2007**, *47*, 197–215.
5. Jiang, X.; Wei, G.; Zhang, X.; Zhang, W.; Zheng, P.; Wen, F.; Shi, L. *J. Mol. Catal. A: Chem.* **2007**, *277*, 102–106.
6. Ohno, K.; Koh, K.; Tsujii, Y.; Fukuda, T. *Macromolecules* **2002**, *35*, 8989–8993.
7. Wong, M. S.; Cha, J. N.; Choi, K.; Deming, T. J.; Stucky, G. D. *Nano Letters* **2002**, *2*, 583–587.
8. Mössmer, S.; Spatz, J. P.; Möller, M.; Aberle, T.; Schmidt, J.; Burchard, W. *Macromolecules* **2000**, *33*, 4791–4798.
9. Gao, Z.; Varshney, S. K.; Wong, S.; Eisenberg, A. *Macromolecules* **1994**, *27*, 7923–7927.
10. Spatz, J. P.; Sheiko, S.; Möller, M. *Macromolecules* **1996**, *29*, 3220–3226.
11. Sidorov, S.; Bronstein, L. M.; Kabachii, Y. A.; Valetsky, P. M.; Soo, P. L.; Maysinger, D.; Eisenberg, A. *Langmuir* **2004**, *20*, 3543–3550.
12. Zhang, L.; Shen, H.; Eisenberg, A. *Macromolecules* **1997**, *30*, 1001–1011.
13. Mayer, A. B. R.; Mark, J. E. *Colloid Polym. Sci.* **1997**, *275*, 333–340.

14. Förster, S.; Plantenberg, T. *Angew. Chem. Int. Ed.* **2002**, *41*, 688–714.

15. Youk, J. H.; Park, M.-K.; Locklin, J.; Advincula, R.; Yang, J.; Mays, J. *Langmuir* **2002**, *18*, 2455–2458.

16. Gauthier, M.; Li, J.; Dockendorff, J. *Macromolecules* **2003**, *36*, 2642–2648.

17. Dockendorff, J.; Gauthier, M.; Mourran, A.; Möller, M. *Macromolecules* **2008**, *41*, 6621–6623.

18. Hansen, C. R.; Westerlund, F.; Moth-Poulsen, K.; Ravindranath, R.; Valiyaveettil, S.; Bjørnholm, T. *Langmuir* **2008**, *24*, 3905–3910.

19. Burchard, W. *Macromol. Symp.* **1996**, *101*, 103–113.

20. Förster, S.; Antonietti, M. *Adv. Mater.* **1998**, *10*, 195–217.

21. Zhang, L.; Yu, K.; Eisenberg, A. *Science* **1996**, *272*, 1777–1779.

22. Yu, G.; Eisenberg, A. *Macromolecules* **1998**, *31*, 5546–5549.

23. Gohy, J.-F.; Willet, N.; Varshney, S.; Zhang, J.-X.; Jérôme, R. *Angew. Chem. Int. Ed.* **2001**, *40*, 3214–3216.

24. Erhardt, R.; Böker, A.; Zettl, H.; Kaya, H.; Pyckhout-Hintzen, W.; Krausch, G; Abetz, V.; Müller, A. H. E. *Macromolecules* **2001**, *34*, 1069–1075.

25. (a) Zheng, W.; Wang, Z.-G. *Macromolecules* **1995**, *28*, 7215–7223. (b) Stadler, R.; Auschra, C.; Beckmann, J.; Krappe, U.; Voight-Martin, I.; Leibler, L. *Macromolecules* **1995**, *28*, 3080–3097. (c) Bates, F.; Fredrickson, G. *Physics Today* **1999**, *52*, 32–38. (d) Abetz, V.; Goldacker, T. *Macromol. Rapid Commun.* **2000**, *21*, 16–34. (e) Bailey, T. S.; Pham, H. D.; Bates, F. S. *Macromolecules* **2001**, *34*, 6994–7008. (f) Zheng, R.; Liu, G.; Yan, X. *J. Am. Chem. Soc.* **2008**, *127*, 15358–15359. (g) Hu, J.; Liu, G.; Njikang, G. *J. Am. Chem. Soc.* **2008**, *130*, 3236–3237. (h)

Dupont, J; Liu, G.; Niihara, K.-i.; Kimoto, R.; Jinnai, H. *Angew. Chem. Int. Ed.* **2009**, *48*, 6144–6147.

26. Antonietti, M.; Heinz, S.; Schmidt, M.; Rosenauer, C. *Macromolecules* **1994**, *27*, 3276–3281.
27. Antonietti, M.; Wenz, M.; Bronstein, L.; Seregina, M. *Adv. Mater.* **1995**, *7*, 1000–1005.
28. Spatz, J. P.; Mössmer, S.; Möller, M. *Angew. Chem. Int. Ed.* **1996**, *35*, 1510–1512.
29. Krishnamoorthy, S.; Pugin, R.; Brugger, J.; Heinzelmann, H.; Hoogerwerf, A. C.; Hinderling, C. *Langmuir* **2006**, *22*, 3450–3452.
30. Sohn, B.-Y.; Yoo, S.-I.; Seo, B.-W.; Yun, S.-H.; Park, S.-M. *J. Am. Chem. Soc.* **2001**, *123*, 12734–12735.
31. Pietsch, T.; Gindy, N.; Fahmi, A. *Polymer* **2008**, *49*, 914–921.
32. Discher, D. E.; Eisenberg, A. *Science* **2002**, *297*, 967–973.
33. Spatz, J. P.; Roescher, A.; Möller, M. *Adv. Mater.* **1996**, *8*, 337–340.
34. Kei, L.; Gohy, J.-F.; Willet, N.; Zhang, J.-X.; Varshney, S.; Jérôme, R. *Macromolecules* **2004**, *37*, 1089–1094.
35. Talingting, M. R.; Munk, P.; Webber, S. E. *Macromolecules* **1999**, *32*, 1593–1601.
36. Schacher, F.; Walther, A.; Ruppel, M.; Drechsler, M.; Müller, A. H. E. *Macromolecules* **2009**, *42*, 3540–3548.
37. Quirk, R. P.; Yoo, T.; Lee, Y.; Kim, J.; Lee, B. *Adv. Poylm. Sci.* **2000**, *153*, 67–162.
38. Schacher, F.; Walther, A.; Müller, A. H. E. *Langmuir* **2009**, *25*, 10962–10969.
39. Schacher, F.; Betthausen, E.; Walther, A.; Schmalz, H.; Pergushov, D.; Müller, A. H. E. *ACS Nano* **2009**, *3*, 2095–2102.

40. Gorodyska, G.; Kiriy, A.; Minko, S.; Tsitsilianis, C.; Stamm, M. *Nano. Lett.* **2003**, *3*, 365–368.

41. Voulgaris, D.; Tsitsilianis, C.; Grayer, V.; Esselink, F. J.; Hadziioannou, G. *Polymer* **1999**, *40*, 5879–5889.

42. Tsitsilianis, C.; Voulgaris, D. *Macromol. Chem. Phys.* **1997**, *198*, 997–1007.

43. Du, J.; Chen, Y. *Macromolecules* **2004**, *37*, 3588–3594.

44. Kricheldorf, H. R.; Kreiser-Saunders, I.; Stricker, A. *Macromolecules* **2000**, *33*, 702–709.

45. Baek, K.-Y.; Kamigaito, M.; Sawamoto, M. *Macromolecules* **2001**, *34*, 215–221.

46. Terashima, T.; Kamigaito, M.; Baek, K.-Y.; Ando, T.; Sawamoto, M. *J. Am. Chem. Soc.* **2003**, *125*, 5288–5298.

47. Baek, K.-Y.; Kamigaito, M.; Sawamoto, M. *Macromolecules* **2002**, *35*, 1493–1498.

48. Filali, M.; Meier, M. A. R.; Schubert, U. S.; Gohy, J.-F. *Langmuir* **2005**, *21*, 7995–8000.

49. Schmatloch, S.; Meier, M. A. R.; Schubert, U. S. *Macromol. Rapid Commun*. **2003**, *24*, 33–46.

50. Meier, M. A. R.; Gohy, J.-F.; Fustin, C.-A.; Schubert, U. S. *J. Am. Chem. Soc.* **2004**, *126*, 11517–11512.

51. Fustin, C.-A.; Colard, C.; Filali, M.; Guillet, P.; Duwez, A.-S.; Meier, M. A. R.; Schubert, U. S.; Gohy, J.-F. *Langmuir* **2006**, *22*, 6690–6695.

52. Meier, M. A. R.; Filali, M.; Gohy, J.-F.; Schubert, U. S. *J. Mater. Chem.* **2006**, *16*, 3001–3006.

53. Zhang, L.; Nui, H.; Chen, Y.; Liu, H.; Gao, M. *J. Colloid Interface Sci*. **2006**, *298*, 177–182.

54. Tomalia, D. A.; Baker, H.; Dewald, J.; Hall, M.; Kallos, G.; Martin, S.; Roeck, J.; Ryder, J.; Smith, P. *Polym. J.* **1985**, *17*, 117–132.

55. Tomalia, D. A.; Hall, B. M.; Hedstrand, D. M. *Macromolecules* **1987**, *20*, 1164–1167.

56. Zhao, M.; Sun, L.; Crooks, R. M. *J. Am. Chem. Soc.* **1998**, *120*, 4877–4878.

57. Balogh, L.; Tomalia, D. A. *J. Am. Chem. Soc.* **1998**, *120*, 7355–7356.

58. Ottaviani, M. F.; Bossmann, S.; Turro, N. J.; Tomalia, D. A. *J. Am. Chem. Soc.* **1994**, *116*, 661–671.

59. Abe, H.; Tesche, C. B.; Schulze, W. *Chem. Phys.* **1982**, *68*, 137–141.

60. Gröhn, F.; Bauer, B. J.; Akpalu, Y. A.; Jackson, C. L.; Amis, E. J. *Macromolecules* **2000**, *33*, 6042–6050.

61. Scott, R. W. J.; Ye, H.; Henriquez, R. R.; Crooks, R. M. *Chem. Mater.* **2003**, *15*, 3873–3878.

62. Gu, Y.; Xie, H.; Gao, J.; Liu, D.; Williams, C. T.; Murphy, C. J.; Ploehn, H. J. *Langmuir* **2005**, *21*, 3122–3131.

63. Peng, Z.; Zhang, J.; Sun, X.; Yang, J.; Diao, J. *Colloid Polym. Sci.* **2009**, *287*, 609–614.

64. Atwater, J. E.; Akse, J. R.; Holtsnider, J. T. *Materials Letters* **2008**, *62*, 3131–3134.

65. Scott, R. W. J.; Wilson, O. M.; Oh, S.-K.; Kenik, E. A.; Crooks, R. M. *J. Am. Chem. Soc.* **2004**, *125*, 15583–15591.

66. Gu, Y.; Wu, G.; Hu, X. F.; Chen, D. A.; Hansen, T.; zur Loye, H.-C.; Ploehn, H. J. *J. Power Sources* **2010**, *195*, 425–434.

67. Scott, W. J.; Wilson, O. M.; Crooks, R. M. *J. Phys. Chem. B* **2005**, *109*, 692–704.

68. Crooks, R. M.; Zhao, M.; Sun, L.; Chechik, V.; Yeung, L. K. *Acc. Chem. Res.* **2001**, *34*, 181–190.

69. Hedden, R. C.; Bauer, B. J. *Macromolecules* **2003**, *36*, 1829–1835.

70. Hedden, R. C.; Bauer, B. J.; Smith, P. A.; Gröhn, F.; Amis, E. *Polymer* **2002**, *43*, 5473–5481.

71. Pérignon, N.; Mingotaud, A.-F.; Marty, J.-D.; Rico-Lattes, I.; Mingotaud, C. *Chem. Mater.* **2004**, *16*, 4856–4858.

72. Sun, Y.; Wang, D.; Gao, J.; Zheng, Z.; Zhang, Q. *J. Appl. Polym. Sci.* **2007**, *103*, 3701–3705.

73. Sun, Y.; Liu, Y.; Guizhe, Z.; Zhang, Q. *J. Polym. Res.* **2008**, *15*, 269–273.

74. Sunder, A.; Hanselmann, R.; Frey, H.; Mülhaupt, R. *Macromolecules* **1999**, *32*, 4240–4246.

75. Wan, D.; Fu, Q.; Huang, J. *J. Appl. Polym. Sci.* **2006**, *101*, 509–514.

76. Brust, M.; Walker, M.; Bethell, D.; Schiffrin, D. J.; Whyman, R. *J. Chem. Soc. Chem. Commun.* **1994**, *7*, 801–802.

77. Dziezok, P.; Sheiko, S. S.; Fischer, K.; Schmidt, M.; Möller, M. *Angew. Chem.* **1997**, *109*, 2894–2897.

78. Djalali, R.; Li, S.-Y.; Schmidt, M. *Macromolecules* **2002**, *35*, 4282–4288.

79. Djalali, R.; Hugenberg, N.; Fischer, K.; Schmidt, M. *Macromol. Rapid Commun.* **1999**, *20*, 444–449.

80. Tsubaki, K.; Ishizu, K. *Polymer* **2001**, *42*, 8387–8393.

81. Ishizu, K.; Tsubaki, K.; Uchida, S. *Macromolecules* **2002**, *35*, 10193–10197.

82. Cheng, G.; Böker, A.; Zhang, M.; Krausch, G.; Müller, A. H. E. *Macromolecules* **2001**, *34*, 6883–6888.

83. Zhang, M.; Breiner, T.; Mori, H.; Müller, A. H. E. *Polymer* **2003**, *44*, 1449–1458.

84. Zhang, M.; Dreschler, M.; Müller, A. H. E. *Chem. Mater.* **2004**, *16*, 537–543.

85. Zhang, M.; Estournès, C.; Bietsch, W.; Müller, A. H. E. *Adv. Funct. Mater.* **2004**, *14*, 871–882.

86. Zhang, M.; Teisser, P.; Krekhova, M.; Cabuil, V.; Müller, A. H. E. *Progr. Colloid Polym. Sci.* **2004**, *126*, 35–39.

Chapter 4

1. Gohy, J.-F. *Adv. Polym. Sci.* **2005**, *190*, 65–136.
2. Förster, S.; Antonietti, M. *Adv. Mater.* **1998**, *10*, 195–217.
3. Zhang, L.; Yu, K.; Eisenberg, A. *Science* **1996**, *272*, 1777–1779.
4. (a) Tomalia, D. A.; Baker, H.; Dewald, J.; Hall, M.; Kallos, G.; Martin, S.; Roeck, J.; Ryder, J.; Smith, P. *Polym. J.* **1985**, *17*, 117–132. (b) Newkome, G. R.; Yao, Z.-q.; Baker, G. R.; Gupta, V. K. *J. Org. Chem.* **1985**, *50*, 2003–2004. (c) Gunatillake, P. A.; Odian, G.; Tomalia, D. A. *Macromolecules* **1988**, *21*, 1556–1562. (d) Hawker, C. J.; Fréchet, J. M. J. *J. Am. Chem. Soc.* **1990**, *112*, 7638–7647. (e) Miller, T. M.; Neenan, T. X. *Chem. Mater.* **1990**, *2*, 346–349. (f) Kim, Y. H.; Webster, O. W. *J. Am. Chem. Soc.* **1990**, *112*, 4592–4593. (g) Hawker, C. J.; Lee, R.; Fréchet, J. M. J. *J. Am. Chem. Soc.* **1991**, *113*, 4583–4588.
5. Gauthier, M.; Möller, M. *Macromolecules* **1991**, *24*, 4548–4553.
6. Tomalia, D. A.; Hedstrand, D. M.; Ferritto, M. S. *Macromolecules* **1991**, *24*, 1435–1438.
7. Gauthier, M.; Li, J.; Dockendorff, J. *Macromolecules* **2003**, *36*, 2642–2648.
8. Njikang, G. N.; Gauthier, M.; Li. J. *Polymer* **2008**, *49*, 5474–5481.
9. Eastoe, J.; Hollamby, M. J.; Hudson, L. *Adv. Colloid Interface Sci.* **2006**, *128*, 5–15.
10. Spatz, J. P.; Sheiko, S.; Möller, M. *Macromolecules* **1996**, *29*, 3220–3226.
11. (a) Filali, M.; Meier, M. A. R.; Schubert, U. S.; Gohy, J.-F. *Langmuir* **2005**, *21*, 7995–8000. (b) Koh, H.-D.; Kang, N.-G.; Lee, J.-S. *Langmuir* **2007**, *23*, 11425–11429. (c) Hansen, C. R.; Westerlund, F.; Moth-Poulsen, K.; Ravindranath, R.; Valiyaveettil, S.; Bjørnholm, T. *Langmuir* **2008**, *24*, 3905–3910.

12. (a) Crooks, R. M.; Zhao, M.; Sun, L.; Chechik, V.; Yeung, L. K. *Acc. Chem. Res.* **2001**, *34*, 181–190. (b) Gohy, J.-F.; Willet, N.; Varshney, S.; Zhang, J.-X.; Jérôme, R. *Angew. Chem. Int. Ed.* **2001**, *40*, 3214–3216. (c) Sidorov, S.; Bronstein, L. M.; Kabachii, Y. A.; Valetsky, P. M.; Soo, P. L.; Maysinger, D.; Eisenberg, A. *Langmuir* **2004**, *20*, 3543–3550. (d) Zhou, Y.; Jiang, K.; Chen, Y.; Liu, S. *J. Polym. Sci. Part A: Polym. Chem.* **2008**, *46*, 6518–6531.
13. Daniel, M.-C.; Astruc, D. *Chem. Rev.* **2004**, *104*, 293–346.
14. Grzelczak, M.; Pérez-Juste, J.; Mulvaney, P.; Liz-Marzán, L. M. *Chem. Soc. Rev.* **2008**, *37*, 1783–1791.
15. Tsai, S.-W.; Chen, Y.-Y.; Liaw, J.-W. *Sensors* **2008**, *8*, 2306–2316.
16. Munam, A. *Ph. D. Thesis*, University of Waterloo, Waterloo, 2008.
17. Li, J.; Gauthier, M. *Macromolecules* **2001**, *34*, 8918–8924.
18. Munam, A.; Gauthier, M. *J. Polym. Sci. Part A: Polym. Chem.* **2008**, *46*, 5742–5751.
19. Kestin, J.; Sokolov, M.; Wakeham, W. A. *J. Phys. Chem. Ref. Data* **1978**, *7*, 941–948.
20. Abramoff, M. D.; Magelhaes, P. J.; Ram, S. J. *Biophotonics International* **2004**, *11*, 36–42.
21. Zhang, L.; Eisenberg, A. *J. Am. Chem. Soc.* **1996**, *118*, 3168–3181.
22. Schmidt, M.; Burchard, W.; Ford, N. C. *Macromolecules* **1978**, *11*, 452–454.
23. (a) Provencher, S. W. *Makromol. Chem.* **1979**, *180*, 201–209. (b) Provencher, S. W. *Comput. Phys. Commun.* **1982**, *27*, 213–227. (c) Provencher, S. W. *Comput. Phys. Commun.* **1982**, *27*, 229–242.

24. Gauthier, M.; Möller, M.; Burchard, W. *Macromol. Symp.* **1994**, *77*, 43–49.

25. (a) Zhao, M.; Sun, L.; Crooks, R. M. *J. Am. Chem. Soc.* **1998**, *120*, 4877–4878. (b) Balogh, L.; Tomalia, D. A. *J. Am. Chem. Soc.* **1998**, *120*, 7355–7356. (c) Balogh, L.; deLeuze-Jallouli, A. M.; Dvornic, P. R.; Owen, M. J.; Perz, S. V.; Spindler, R. U.S. Patent 5938934, 1999. (d) Gröhn, F.; Bauer, B. J.; Akpalu, Y. A.; Jackson, C. L.; Amis, E. J. *Macromolecules* **2000**, *33*, 6042–6050. (e) Dvornic, P. R.; Hu, J.; Reeves, S. D.; Owen, M. J. *Silicon Chem*. **2002**, *1*, 177–193. (f) Seo, Y.-S.; Kim, K.-S.; Shin, K.; White, H.; Rafailovich, M.; Sokolov, J.; Lin, B.; Zhang, C.; Balogh, L. *Langmuir* **2002**, *18*, 5927–5932. (g) Dvornic, P. R.; Bubeck, R. A.; Reeves, S. D.; Li, J.; Hoffman, L. W. *Silicon Chem.* **2003**, *2*, 207–216. (h) Bubeck, R. A.; Dvornic, P. R.; Hu, J.; Hexemer, A.; Li, X.; Keinath, S. E.; Fischer, D. A. *Macromol. Chem. Phys.* **2005**, *206*, 1146–1153. (i) Wan, D.; Fu, Q.; Huang, J. *J. Appl. Polym. Sci.* **2006**, *101*, 509–514. (j) Zhang, J.; Meng, L.; Zhao, D.; Fei, Z.; Lu, Q.; Dyson, P. J. *Langmuir* **2008**, *24*, 2699–2704.

26. Roiter, Y.; Minko, S. *J. Phys. Chem. B* **2007**, *111*, 8597–8604.

27. Chiu, J. J.; Kim, B. J.; Kramer, E. J.; Pine, D. J. *J. Am. Chem. Soc.* **2005**, *127*, 5036–5037.

28. Dockendorff, J.; Gauthier, M.; Mourran, A.; Möller, M. *Macromolecules* **2008**, *41*, 6621–6623.

29. Dong, R.; Yu, L. E. *Environ. Sci. Technol.* **2003**, *37*, 2813–2819.

30. Njikang, G. N.; Cao, L.; Gauthier, M. *Macromol. Chem. Phys.* **2008**, *209*, 907-918.

31. Sheiko, S. S.; Gauthier, M.; Möller, M. *Macromolecules* **1997**, *30*, 2343–2349.

32. Samal, A. K.; Sreeprasad, T. S.; Pradeep, T. *J. Nanopart. Res.* **2010**, *12*, 1777–1786.

33. Nachbaur, E.; Leiseder, G. *Monatsh. Chem.* **1971**, *102*, 1718–1723.

34. Bowker, M. *Nat. Mater.* **2002**, *1*, 205–206.

35. Luo, Y. *Mater. Lett.* **2007**, *61*, 1039–1041.

36. (a) Klingelhöfer, S.; Heitz, W.; Greiner, A.; Oestreich, S.; Förster, S.; Antonietti, M. *J. Am. Chem. Soc.* **1997**, *119*, 10116–10120. (b) Seregina, M. V.; Bronstein, L. M.; Platonova, O. A.; Chernyshov, D. M.; Valetsky, P. M. *Chem. Mater.* **1997**, *9*, 923–931. (c) Spatz, J. P.; Mössmer, S.; Hartmann, C.; Möller, M. *Langmuir* **2000**, *16*, 407–415. (d) Meier, M. A. R.; Filali, M.; Gohy, J.-F.; Schubert, U. S. *J. Mater. Chem.* **2006**, *16*, 3001–3006.

37. Jiang, X.; Wei, G.; Zhang, X.; Zhang, W.; Zheng, P.; Wen, F.; Shi, L. *J. Mol. Catal. A: Chem.* **2007**, *277*, 102–106.

Chapter 4 Appendix

1. Koppel, D. E. *J. Chem. Phys.* **1972**, *57*, 4814–4820.

2. Burchard, W. *Chimia* **1985**, *39*, 10–18.

3. Mössmer, S.; Spatz, J.; Möller, M.; Aberle, T.; Schmidt, J.; Burchard, W. *Macromolecules* **2000**, *33*, 4791–4798.

4. Demas, J. N. *Excited State Lifetime Measurements.* Academic Press: New York, NY, **1983**. p. 135–137.

5. (a) Provencher, S. W. *Makromol. Chem.* **1979**, *180*, 201–209. (b) Provencher, S. W. *Comput. Phys. Commun.* **1982**, *27*, 213–227. (c) Provencher, S. W. *Comput. Phys. Commun.* **1982**, *27*, 229–242.

Chapter 5

1. Kee, R. A.; Gauthier, M. *Macromolecules* **1999**, *32*, 6478–6484.
2. Kee, R. A.; Gauthier, M. *Macromolecules* **2002**, *35*, 6526–6532.
3. Gauthier, M.; Li, J.; Dockendorff, J. *Macromolecules* **2003**, *36*, 2642–2648.
4. Gauthier, M.; Tichagwa, L.; Downey, J. S.; Gao, S. *Macromolecules* **1996**, *29*, 519–527.
5. Njikang, G. N.; Cao, L.; Gauthier, M. *Macromol. Chem. Phys.* **2008**, *209*, 907–918.
6. Tomalia, D. A.; Hedstrand, D. M.; Ferritto, M. S. *Macromolecules* **1991**, *24*, 1435–1438.
7. Gauthier, M.; Möller, M. *Macromolecules* **1991**, *24*, 4548–4553.
8. Li, J.; Gauthier, M. *Macromolecules* **2001**, *34*, 8918–8924.
9. Dockendorff, J.; Gauthier, M.; Mourran, A.; Möller, M. *Macromolecules* **2008**, *41*, 6621–6623.
10. Burchat, A. F.; Chong, J. M.; Neilsen, N. *J. Organomet. Chem.* **1997**, *542*, 281–283.
11. (a) Frank, R. *M. Sc. Thesis*, University of Waterloo, Waterloo, 1995. (b) Teertstra, S. J. *Ph. D. Thesis*, University of Waterloo, Waterloo, 2006. (c) Munam, A. *Ph. D. Thesis*, University of Waterloo, Waterloo, 2008.
12. Quirk, R. P.; Yoo, T.; Lee, Y.; Kim, J.; Lee, B. *Adv. Polym. Sci.* **2000**, *153*, 67–162.
13. Teertstra, S. J.; Gauthier, M. *Prog. Polym. Sci.* **2004**, *29*, 277–327.
14. Collum, D. B. *Acc. Chem. Res.* **1992**, *25*, 448–454.
15. Yuan, Z.; Gauthier, M. *Macromolecules* **2005**, *38*, 4124–4132.
16. Gauthier, M.; Li, W.; Tichagwa, L. *Polymer* **1997**, *38*, 6363–6370.

17. Mössmer, S.; Spatz, J.; Möller, M.; Aberle, T.; Schmidt, J.; Burchard, W. *Macromolecules* **2000**, *33*, 4791–4798.

18. (a) Provencher, S. W. *Makromol. Chem.* **1979**, *180*, 201–209. (b) Provencher, S. W. *Comput. Phys. Commun.* **1982**, *27*, 213–227. (c) Provencher, S. W. *Comput. Phys. Commun.* **1982**, *27*, 229–242.

19. Burchard, W. *Adv. Poly. Sci.* **1999**, *143*, 113–194.

20. Schmidt, M.; Burchard, W.; Ford, N. C. *Macromolecules* **1978**, *11*, 452–454.

21. Nordmeier, E.; Lechner, M. D. *Polym. J.* **1989**, *21*, 623–632.

22. Zimm, B. H. *J. Chem. Phys.* **1948**, *16*, 1093–1099.

23. Schulz, V. G. V.; Baumann, H. *Die Makromol. Chemie* **1968**, *114*, 122–138.

24. Stacy, C. J.; Kraus, G. *J. Polym. Sci: Polym. Phys. Ed.* **1979**, *17*, 2007–2012.

Chapter 5 Appendix

1. Mie, G. *Ann. Physik* **1908**, *25*, 377–445.

2. Zimm, B. H. *J. Chem. Phys.* **1948**, *16*, 1093–1099.

Chapter 6

1. (a) Schimpf, S.; Lucas, M.; Mohr, C.; Rodemerck, U.; Brückner, A.; Radnik, J.; Hofmeister, H.; Claus, P. *Catalysis Today* **2002**, *72*, 63–78. (b) Jain, P. K.; Huang, X.; El-Sayed, I. H.; El-Sayed, M. A. *Plasmonics* **2007**, *2*, 107–118. (c) Xu, C.; Sun, S. *Polym. Int.* **2007**, *56*, 821–826. (d) Bhattacharya, R.; Patra, C. R.; Earl, A.; Wang, S.; Katarya, A.; Lu, L.; Kizhakkedathu, J. N.; Yaszemski, M. J.; Greipp, P. R.; Mukhopadhyay, D.; Mukherjee, P. *Nanomed. Nanotechnol. Biol. Med.* **2007**, *3*, 224–238. (e) Garnett, E. C.; Liang, W.; Yang, P. *Adv. Mater.* **2007**, *19*, 2946–2950. (f) Nilsson, C.; Birnbaum, S.; Nilsson, S. *J. Chromatogr. A* **2007**, *1168*, 212–224. (g) Tsuchiya, K.; Nagayasu, S.; Okamoto, S.; Hayakawa, T.; Hihara, T.; Yamamoto, K.; Takumi, I.; Hara, S.; Hasegawa, H.; Akasaka, S.; Kosikawa, N. *Opt. Express* **2008**, *16*, 5362–5371. (h) Qian, X.-M.; Nie, S. M. *Chem. Soc. Rev.* **2008**, *37*, 912–920. (i) Azarmi, S.; Roa, W. H.; Löbenberg, R. *Adv. Drug Deliv. Rev*. **2008**, *60*, 863–875. (j) Podsiadlo, P.; Sinani, V. A.; Bahng, J. H.; Kam, N. W. S.; Lee, J.; Kotov, N. A. *Langmuir* **2008**, *24*, 568–574. (k) Gannon, C. J.; Patra, C. R.; Bhattacharya, R.; Mukherjee, P.; Curley, S. A. *J. Nanobiotechnology* **2008**, *6*:2.
2. Spatz, J. P.; Sheiko, S.; Möller, M. *Macromolecules* **1996**, *29*, 3220–3226.
3. (a) Filali, M.; Meier, M. A. R.; Schubert, U. S.; Gohy, J.-F. *Langmuir* **2005**, *21*, 7995–8000. (b) Koh, H.-D.; Kang, N.-G.; Lee, J.-S. *Langmuir* **2007**, *23*, 11425–11429.
4. Hansen, C. R.; Westerlund, F.; Moth-Poulsen, K.; Ravindranath, R.; Valiyaveettil, S.; Bjørnholm, T. *Langmuir* **2008**, *24*, 3905–3910.

5. (a) Zhao, M.; Sun, L.; Crooks, R. M. *J. Am. Chem. Soc.* **1998**, *120*, 4877–4878. (b) Balogh, L.; Tomalia, D. A. *J. Am. Chem. Soc.* **1998**, *120*, 7355–7356. (c) Balogh, L.; deLeuze-Jallouli, A. M.; Dvornic, P. R.; Owen, M. J.; Perz, S. V.; Spindler, R. U.S. Patent 5938934, 1999. (d) Gröhn, F.; Bauer, B. J.; Akpalu, Y. A.; Jackson, C. L.; Amis, E. J. *Macromolecules* **2000**, *33*, 6042–6050. (e) Dvornic, P. R.; Hu, J.; Reeves, S. D.; Owen, M. J. *Silicon Chem*. **2002**, *1*, 177–193. (f) Seo, Y.-S.; Kim, K.-S.; Shin, K.; White, H.; Rafailovich, M.; Sokolov, J.; Lin, B.; Zhang, C.; Balogh, L. *Langmuir* **2002**, *18*, 5927–5932. (g) Dvornic, P. R.; Bubeck, R. A.; Reeves, S. D.; Li, J.; Hoffman, L. W. *Silicon Chem*. **2003**, *2*, 207–216. (h) Bubeck, R. A.; Dvornic, P. R.; Hu, J.; Hexemer, A.; Li, X.; Keinath, S. E.; Fischer, D. A. *Macromol. Chem. Phys.* **2005**, *206*, 1146–1153. (i) Wan, D.; Fu, Q.; Huang, J. *J. Appl. Polym. Sci.* **2006**, *101*, 509–514. (j) Zhang, J.; Meng, L.; Zhao, D.; Fei, Z.; Lu, Q.; Dyson, P. J. *Langmuir* **2008**, *24*, 2699–2704.

6. For a preliminary report on this work, see Dockendorff, J.; Gauthier, M.; Mourran, A.; Möller, M. *Macromolecules* **2008**, *41*, 6621–6623.

7. (a) Daniel, M.-C.; Astruc, D. *Chem. Rev.* **2004**, *104*, 293–346. (b) Sperling, R. A.; Gil, P. R.; Zhang, F.; Zanella, M.; Parak, W. J. *Chem. Soc. Rev.* **2008**, *37*, 1896–1908. (c) Yong, K.-T.; Swihart, M. T.; Ding, H.; Prasad, P. N. *Plasmonics* **2009**, *4*, 79–83. (d) Sardar, R.; Funston, A. M.; Mulvaney, P.; Murray, R. W. *Langmuir* **2009**, *25*, 13840–13851.

8. Klingelhöfer, S.; Heitz, W.; Grenier, A.; Oestreich, S.; Förster, S.; Antonietti, M. *J. Am. Chem. Soc.* **1997**, *119*, 10116–10120.

9. Förster, S.; Antonietti, M. *Adv. Mater.* **1998**, *10*, 195–217.

10. Yu, G.; Eisenberg, A. *Macromolecules* **1998**, *31*, 5546–5549.

11. Gohy, J.-F.; Willet, N.; Varshney, S.; Zhang, J.-X.; Jérôme, R. *Angew. Chem. Int. Ed.* **2001**, *40*, 3214–3216.

12. Erhardt, R.; Böker, A.; Zettl, H.; Kaya, H.; Pyckhout-Hintzen, W.; Krausch, G; Abetz, V.; Müller, A. H. E. *Macromolecules* **2001**, *34*, 1069–1075.

13. Zheng, R.; Liu, G.; Yan, X. *J. Am. Chem. Soc*. **2008**, *127*, 15358–15359.

14. Hu, J.; Liu, G.; Njikang, G. *J. Am. Chem. Soc*. **2008**, *130*, 3236–3237.

15. Dupont, J; Liu, G.; Niihara, K.-i.; Kimoto, R.; Jinnai, H. *Angew. Chem. Int. Ed*. **2009**, *48*, 6144–6147.

16. Zhang, L.; Yu, K.; Eisenberg, A. *Science* **1996**, *272*, 1777–1779.

17. Schacher, F.; Walther, A.; Ruppel, M.; Drechsler, M.; Müller, A. H. E. *Macromolecules* **2009**, *42*, 3540–3548.

18. Li, Z.; Hillmyer, M. A.; Lodge, T. P. *Macromolecules* **2006**, *39*, 765–771.

19. Li, Z.; Kesselman, E.; Talmon, Y.; Hillmyer, M. A.; Lodge, T. P. *Science* **2004**, *306*, 98–101.

20. Lutz, J.-F.; Laschewsky, A. *Macromol. Chem. Phys.* **2005**, *206*, 813–817.

121. Walther, A.; Barner-Kowollik, C.; Müller, A. H. E. *Langmuir* **2010**, *26*, 12237–12246.

22. Cadena, L.-E. S.; Gauthier, M. *Polymer* **2010**, *2*, 596–622.

23. Nelson, P. H.; Rutledge, G. C.; Hatton, T. A. *J. Chem. Phys.* **1997**, *107*, 10777–10781.

24. Charlaganov, M.; Borisov, O. V.; Leermakers, F. A. M. *Macromolecules* **2008**, *41*, 3668–3677.

25. Liu, D.; Zhong, C. *Polymer* **2008**, *48*, 1407–1413.

26. Zhong, C.; Liu, D. *Macromol. Theory Simul.* **2007**, *16*, 141–157.

27. Chou, S.-H.; Tsao, H.-K.; Sheng, Y.-J. *J. Chem. Phys.* **2006**, *125*, 194903-1–194903-6.

28. Ko, M. J.; Kim, S. H.; Jo, W. H. *Fiber. Polym.* **2003**, *4*, 15–19.

29. Xin, J.; Liu, D.; Zhong, C. *J. Phys. Chem. B* **2009**, *113*, 9364–9372.

30. Nachbaur, E.; Leiseder, G. *Monatsh. Chem.* **1971**, *102*, 1718–1723.

31. Abramoff, M. D.; Magelhaes, P. J.; Ram, S. J. *Biophotonics International* **2004**, *11*, 36–42.

32. Schmitz, C.; Mourran, A.; Keul, H.; Möller, M. *Macromol. Chem. Phys.* **2008**, *209*, 1859–1871.

33. Schmitz, C.; Mourran, A.; Keul, H.; Möller, M.; Keerl, M.; Richtering, W. *Colloid Polym. Sci.* **2009**, *287*, 1183–1193.

34. Albrecht, K.; Mourran, A.; Zhu, X.; Markkula, T.; Groll, J.; Beginn, U.; de Jeu, W. H.; Moeller, M. *Macromolecules* **2008**, *41*, 1728–1738.

35. (a) Provencher, S. W. *Makromol. Chem.* **1979**, *180*, 201–209. (b) Provencher, S. W. *Comput. Phys. Commun.* **1982**, *27*, 213–227. (c) Provencher, S. W. *Comput. Phys. Commun.* **1982**, *27*, 229–242.

36. Sheiko, S.; Gauthier, M.; Möller, M. *Macromolecules* **1997**, *30*, 2343–2349.

37. Njikang, G. N.; Cao, L.; Gauthier, M. *Macromol. Chem. Phys.* **2008**, *209*, 907–918.

38. Gauthier, M.; Möller, M.; Burchard, W. *Macromol. Symp.* **1994**, *77*, 43–49.

39. Mössmer, S.; Spatz, J. P.; Möller, M.; Aberle, T.; Schmidt, J.; Burchard, W. *Macromolecules* **2000**, *33*, 4791–4798.

40. Cui, H.; Chen, Z.; Wooley, K. L.; Pochan, D. J. *Soft Matter* **2009**, *5*, 1269–1278.

41. Kong, W.; Li, B.; Jin, Q.; Ding, D.; Shi, A.-C. *Langmuir* **2010**, *26*, 4226–4232.

42. He, P.; Li, X.; Kou, D.; Deng, M.; Liang, H. *J. Chem. Phys.* **2010**, *132*, 204905-1–204905-6.

43. Kubowicz, S.; Baussard, J.-F.; Lutz, J.-F.; Thünemann, A. F.; Berlepsch, H. v.; Laschewsky, A. *Angew. Chem. Int. Ed.* **2005**, *44*, 5262–5265.

44. Gohy, J.-F.; Khousakoun, E.; Willet, N.; Varshney, S. K.; Jérôme, R. *Macromol. Rapid Commun.* **2004**, *25*, 1536–1539.

45. Zhang, M.; Dreschler, M.; Müller, A. H. E. *Chem. Mater.* **2004**, *16*, 537–543.

46. Zhang, M.; Estournès, C.; Bietsch, W.; Müller, A. H. E. *Adv. Funct. Mater.* **2004**, *14*, 871–882.

47. Zhang, M.; Teisser, P.; Krekhova, M.; Cabuil, V.; Müller, A. H. E. *Progr. Colloid Polym. Sci.* **2004**, *126*, 35–39.

48. Khanna, K.; Varshney, S.; Kakkar, A. *Polym. Chem.* **2010**, *1*, 1171–1185.

49. Saito, N.; Liu, C.; Lodge, T. P.; Hillmyer, M. A. *ACS Nano* **2010**, *4*, 1907–1912.

50. Saito, N.; Liu, C.; Lodge, T. P.; Hillmyer, M. A. *Macromolecules* **2008**, *41*, 8815–8822.

51. Berlepsch, H. v.; Böttcher, C.; Skrabaniab, K.; Laschewsky, A. *Chem. Commun.* **2009**, *17*, 2290–2292.

52. Wang, Y.; Gösele, U.; Steinhart, M. *Nano Lett.* **2008**, *8*, 3548–3553.

53. Pinna, M.; Hiltl, S.; Guo, X.; Böker, A.; Zvilindovsky, A. V. *ACS Nano* **2010**, *4*, 2845–2855.

54. Du, B.; Mei, A.; Yong, Y.; Zhang, Q.; Wang, Q.; Xu, J.; Fan, Z. *Polymer* **2010**, *51*, 3493–3502.

55. Antonietti, M.; Wenz, M.; Bronstein, L.; Seregina, M. *Adv. Mater.* **1995**, *7*, 1000–1005.

56. Spatz, J. P.; Mössmer, S.; Hartmann, C.; Möller, M.; Herzog, T.; Krieger, S.; Boyen H.-G.; Ziemann, P.; Kabius, B. *Langmuir* **2000**, *16*, 407–415.

57. Lodge, T. P.; Rasdal, A.; Li, Z.; Hillmyer, M. A. *J. Am. Chem. Soc.* **2005**, *127*, 17608–17609.

58. Seregina, M. V.; Bronstein, L. M.; Platonova, O. A.; Chernyshov, D. M.; Valetsky, P. M. *Chem. Mater.* **1997**, *9*, 923–931.

59. Langlois, C. T.; Oikawa, T.; Bayle-Guillemaud, P; Ricolleau, C. *J. Nanopart. Res.* **2008**, *10*, 997–1007.

60. Papp, S.; Kőrösi, L.; Gool, B.; Dederichs, T.; Mela, P.; Möller, M.; Dékány, I. *J. Therm. Anal. Calorim.* **2010**, *101*, 865–872.

61. Hedden, R. C.; Bauer, B. J.; Smith, P. A.; Gröhn, F.; Amis, E. *Polymer* **2002**, *43*, 5473–5481.

62. Chiang, C. *J. Colloid Interface Sci.* **2001**, *239*, 334–341.

63. Bowkler, M. *Nat. Mater.* **2002**, *1*, 205–206.

64. Luo, Y. *Mater. Lett.* **2007**, *61*, 1039–1041.

65. Spatz, J. P.; Roescher, A.; Möller, M. *Adv. Mater.* **1996**, *8*, 337–340.

66. Link, S.; El-Sayed, M. A. *J. Phys. Chem. B* **1999**, *103*, 8410–8426.

67. Dai, C.-A.; Yu, Y.-L.; Lee, Y.-H.; Chang, C.-J.; Su, W.-F. *J. Cryst. Growth* **2006**, *288*, 128–136.

68. Miranda, O. R.; Ahmadi, T. S. *J. Phys. Chem. B* **2005**, *109*, 15724–15734.

69. Djalali, R.; Li, S.-Y.; Schmidt, M. *Macromolecules* **2002**, *35*, 4282–4288.

70. Gorzolnik, B.; Mela, P.; Moeller, M. *Nanotechnology* **2006**, *17*, 5027–5032.

71. Aizawa, M.; Buriak, J. M. *Chem. Mater.* **2007**, *19*, 5090–5101.

72. Liu, Y.; Fu, Q.; Pan, D.; Ding, L.; Liu, J.; Lu, J. *J. Phys. Chem. C* **2010**, *114*, 5767–5772.

Chapter 7

1. Gauthier, M.; Li, J.; Dockendorff, J. *Macromolecules* **2003**, *36*, 2642–2648.
2. Njikang, G. N.; Gauthier, M.; Li, J. *Polymer* **2008**, *49*, 5474–5481.
3. Sheiko, S.; Gauthier, M.; Möller, M. *Macromolecules* **1997**, *30*, 2343–2349.
4. Li, J.; Gauthier, M.; Teertstra, S. J.; Xu, H.; Sheiko, S. *Macromolecules* **2004**, *37*, 795–802.
5. Njikang, G. N. *Ph. D. Thesis*, University of Waterloo, Waterloo, 2006.
6. Pinna, M.; Hiltl, S.; Guo, X.; Böker, A.; Zvilindovsky, A. V. *ACS Nano* **2010**, *4*, 2845–2855.
7. Antonietti, M.; Wenz, M.; Bronstein, L.; Seregina, M. *Adv. Mater.* **1995**, *7*, 1000–1005.
8. Dockendorff, J.; Gauthier, M.; Mourran, A.; Möller, M. *Macromolecules* **2008**, *41*, 6621–6623.
9. (a) Nelson, P. H.; Rutledge, G. C.; Hatton, T. A. *J. Chem. Phys.* **1997**, *107*, 10777–10781. (b) Ko, M. J.; Kim, S. H.; Jo, W. H. *Fiber. Polym.* **2003**, *4*, 15–19. (c) Li, Z.; Kesselman, E.; Talmon, Y.; Hillmyer, M. A.; Lodge, T. P. *Science* **2004**, *306*, 98–101. (d) Li, Z.; Hillmyer, M. A.; Lodge, T. P. *Macromolecules* **2006**, *39*, 765–771. (e) Chou, S.-H.; Tsao, H.-K.; Sheng, Y.-J. *J. Chem. Phys*. **2006**, *125*, 194903-1–194903-6. (f) Zhong, C.; Liu, D. *Macromol. Theory Simul.* **2007**, *16*, 141–157. (g) Charlaganov, M.; Borisov, O. V.; Leermakers, F. A. M. *Macromolecules* **2008**, *41*, 3668–3677. (h) Liu, D.; Zhong, C. *Polymer* **2008**, *48*, 1407–1413. (i) Xin, J.; Liu, D.; Zhong, C. *J. Phys. Chem. B* **2009**, *113*, 9364–9372. (j) Pinna, M.; Hiltl, S.; Guo, X.; Böker, A.; Zvilindovsky, A. V. *ACS Nano* **2010**, *4*, 2845–2855.